The Design and Analysis of a Micro Squeeze Flow Rheometer

By

David Cheneler

A thesis submitted to
The University of Birmingham
for the degree of
DOCTOR OF PHILOSOPHY

Department of Mechanical Engineering
College of Engineering and Physical Sciences
The University of Birmingham
September 2009

ABSTRACT

This thesis describes the analysis and design of a micro squeeze flow rheometer.

The need to analyse the rheology of complex liquids occurs regularly in industry and during research. However, frequently the amount of fluid available is too small, precluding the use of conventional rheometers. Conventional rheometers also tend to have the disadvantage of being too massive, preventing them from operating effectively at high frequencies. The investigation carried out in this thesis has revealed that current microrheometry techniques also have their own disadvantages.

The proposed design is a stand-alone device capable of measuring the dynamic properties of nanolitre volumes of viscoelastic fluid at frequencies up to the kHz range, an order of magnitude greater than conventional rheometers.

The device uses a single piezoelectric component to both actuate and sense its own position. Thorough analytical analysis of the microrheometer has been carried out. The capillary effects, including contact angle hysteresis, and viscoelasticity associated with the liquid has been combined with the dynamics and electrical response of the rheometer itself to form a complete and consistent model.

The validity of the model has been proven through fabrication and testing of the rheometer.

CONTENTS

List of Figures

List of Tables

Nomenclature

d	Gap between capacitive plates
$\boldsymbol{d}$	Piezoelectric coupling coefficients for Strain-Charge form
d_{11}	Piezoelectric coupling coefficient
$\overrightarrow{dl}$	Segment length of conductor
$\boldsymbol{dh}$	Small change in gap
$\boldsymbol{dr}$	Small change in radius
$\boldsymbol{dt}$	Small change in time
emf	Electromotive force
$f(z,t)$	Form of velocity profile
$\boldsymbol{g}$	Piezoelectric coupling coefficients for Strain-Voltage form
h	Bridge gap
$\bar{h}$	Mean bridge gap
h_{max}	Maximum allowable gap
h_p	Effective thickness of plate
h^*	Nondimensional gap
h^*_{max}	Maximum nondimensional gap
h^*_{min}	Minimum nondimensional gap

i	Current
$\boldsymbol{i}$	Square root of minus one
r	Radial direction
$\boldsymbol{s}$	Compliance coefficients
t	Time
t_q	Thickness of piezoelectric layer
$\boldsymbol{q}$	Piezoelectric coupling coefficients for Stress-Voltage form
$\boldsymbol{u}$	Radial fluid velocity
$\boldsymbol{u_0}$	Lateral deflection of plate
$\boldsymbol{v}$	Tangential fluid velocity
$\boldsymbol{v_{in}}$	Induced voltage
v_{out}	Output voltage actually measured
$\boldsymbol{w}$	Axial fluid velocity
$\boldsymbol{w_0}$	Transverse deflection of plate
x	Displacement of platen
x_c	Characteristic length
z	Axial direction
A	Area of plate
$\vec{A}$	Swept area

$\boldsymbol{A}$ Extensional stiffness matrix

A_{Vout} Amplitude of induced voltage

$\vec{B}$ Magnetic flux density vector

$\boldsymbol{B}$ Extensional-bending coupling stiffness matrix

C_1 Viscous constant due to viscoelasticity of fluid

Cq Capacitance of piezoelectric layer

C_O Input capacitance of oscilloscope

D Constant pertaining to material properties of membrane

$\boldsymbol{D}$ Bending stiffness matrix

$\boldsymbol{D_i}$ Charge-density displacement matrix

E Young's modulus

$\boldsymbol{E}$ Electric field matrix

$\vec{F}$ Magnetic force vector

$F_{Applied}$ Applied force

$F_{Capillary}$ Capillary force

F_{CT} Toroidal approximation of capillary force

$F_{Elastic}$ Elastic component of viscoelastic force

$F_{Stiffness}$ Force due to the stiffness of the rheometer

$F_{Viscous}$ Viscous component of viscoelastic force

F_0 Amplitude of effective force due to applied voltage

G Shear modulus

G' Storage modulus

G'' Loss modulus

$\boldsymbol{G^*}$ Complex shear modulus

H^* Dimensionless curvature

$\boldsymbol{K}$ Kinetic energy of plate

K_1 Elastic constant due to viscoelasticity of fluid

$\boldsymbol{K_{max}}$ Maximum kinetic energy of plate

K_{Cap} Stiffness constant associated with the capillary force

K_{Plate} Stiffness of rheometer

M Effective mass of rheometer

$\boldsymbol{M}$ Net moment on plate

$\boldsymbol{M_r}$ Net moment in radial direction

$\boldsymbol{M_\theta}$ Net moment in tangential direction

$\boldsymbol{M_r^P}$ Net moment due to piezoelectric layer in radial direction

$\boldsymbol{M_\theta^P}$ Net moment due to piezoelectric layer in tangential direction

$\boldsymbol{N}$ Net body force on plate

$\boldsymbol{N_r}$ Net force in radial direction

$\boldsymbol{N_\theta}$ Net force in tangential direction

$\boldsymbol{N_r^P}$ Net force due to piezoelectric layer in radial direction

$\boldsymbol{N_\theta^P}$ Net force due to piezoelectric layer in tangential direction

$Nh*$ Normalised dimensionless gap

$\boldsymbol{P}$ Fluid pressure

P_0 Resisting force due to fluid

Q Plane stress-induced stiffness matrix

$\boldsymbol{Q_r}$ Radial flow rate

$\boldsymbol{Q_z}$ Axial flow rate

R Nondimensional radial coordinate

$\bar{R}$ Mean fluid radius

R_c Contact line radius

R_{cmin} Minimum allowable contact radius

Re Reynolds number

R_C Nondimensional contact line radius

R_{Cyl} Radius of equivalent cylinder

R_L Resistance due to losses in wiring etc.

R_N Neck radius

R_O Input resistance of oscilloscope

R_0 Nondimensional neck radius

R_α, R_β, R_γ, R_δ Radii of the different sections of the rheometer

RMS Root mean square of the profile of the bridge

$\boldsymbol{S}$ Strain matrix

$\boldsymbol{T}$ Stress matrix

$\boldsymbol{T_{zz}}$ Extra stress

$\boldsymbol{U}$ Magnitude of radial fluid velocity

$\boldsymbol{U_{max}}$ Maximum potential energy of plate

V Applied potential difference

$\boldsymbol{W}$ Magnitude of axial fluid velocity

X Amplitude of oscillations

Z Nondimensional axial coordinate

Zq impedance of piezoelectric layer

Z_O Input impedance of oscilloscope

Vol Volume of liquid

α Phase of resisting force

$\boldsymbol{\alpha_1 \ldots \alpha_n}$ Constants for linear viscoelasticity

β Phase of induced voltage

$\boldsymbol{\beta_1 \ldots \beta_n}$ Constants for linear viscoelasticity

$\boldsymbol{\delta}$ Phase difference between stress and strain

$\boldsymbol{\gamma}$ Strain

$\boldsymbol{\gamma_0}$ Amplitude of strain

$\boldsymbol{\gamma_{LV}}$ Liquid/vapour surface tension

$\boldsymbol{\gamma_{SL}}$ Solid/liquid surface tension

$\boldsymbol{\gamma_{SV}}$ Solid/vapour surface tension

$\dot{\boldsymbol{\gamma}}$ Strain rate

$\dot{\boldsymbol{\gamma}}_{\boldsymbol{E}}$ Strain rate of elastic component

$\dot{\boldsymbol{\gamma}}_{\boldsymbol{V}}$ Strain rate of viscous component

ε Mechanical amplitude

$\boldsymbol{\varepsilon_{rr}^{0}}$ Radial strain of neutral plane

$\boldsymbol{\varepsilon_{\theta\theta}^{0}}$ Tangential strain of neutral plane

ε_0 Permittivity of dielectric

$\boldsymbol{\kappa_r^0}$ Radial curvature of neutral plane

$\boldsymbol{\kappa_\theta^0}$ Tangential curvature of neutral plane

ζ Correction factor for toroidal approximation

η Shear viscosity

$\boldsymbol{\eta'}$ Dynamic viscosity

1 INTRODUCTION

In this thesis, the development and the theoretical analysis of a microrheometer is described. This chapter examines what rheometry is and why a microrheometer is required, as well as discussing why existing technologies do not satisfy the need. Following this, the theory behind the proposed method of analysis will be discussed. This analysis will provide the required specification and the basic principles behind the design. Finally, the thesis structure is outlined.

1.1 The Need for Microrheology

Microrheology is rheology on the micron scale. In order to ascertain why a microrheometer is required it is necessary to first understand what rheology is and why conventional methods of studying rheology are not sufficient. The shortfalls in conventional rheometry will then be used to derive a specification for the microrheometer and so justify the project.

Rheology is the study of the viscoelasticity of materials. Viscoelasticity is the property of materials that exhibit both viscous and elastic characteristics when undergoing deformation. Neglecting inertial effects, Newtonian viscous materials, like honey, resist shear flow and strain linearly with time when a stress is applied. The ratio of stress to strain rate is called viscosity and is a measure of the ‘slipperiness’ of a fluid. Alternatively, Hookean elastic materials strain instantaneously when deformed and just as quickly return to their original state once the stress is removed. If the material is stretched, then the ratio of stress to strain is known as the Young’s modulus. If the material is sheared then the

ratio is known as the shear modulus. Viscoelastic materials have both viscous and elastic elements and, as such, exhibit time-dependent strain [1].

Therefore it is clear that as most materials have a complex structure and can be described as viscoelastic, rheology is an important subject. Specifically, rheology extends the classical disciplines of elasticity and Newtonian fluid mechanics which are concerned only with materials that can be completely described by its elastic moduli or viscosity respectively to materials which cannot be described thus. These complex materials can be defined in terms of how they store and dissipate energy. In this thesis we will be concerned with materials that can be described in terms of their storage modulus (G' – a measure of how the material stores elastic energy) and their loss modulus (G" – a measure of how the material dissipates energy). These properties are not constants like their Newtonian or Hookean counterparts and will be shown later to be frequency dependent.

Microrheology extends the field further still by considering the measurement of these storage and loss moduli for very small volumes of material. This allows for the study of phenomenon that occurs at the micrometre or sub-micrometre level [2] and at very small time scales. Historically there has been a distinct biological bias in the field, since cells are of the micrometre scale, providing a strong impetus to drive the research [3]. The theory of microrheology has been widely extended to include the field of complex fluids, in particular fluids such as polymer melts, colloidal suspensions and other biological materials which also demonstrate viscoelastic behaviour.

The industrial applications of complex fluids are vast. For example, foods are complex structural materials and may consist of mixtures of solid and fluid components. Therefore rheology has many applications in the fields of food acceptability, food processing and food handling [4, 5]. Also the rheological properties of cosmetics affect their spreadability and consistency and in turn the sensation their application causes [6]. The rheological properties of a material also affects the acceptability of shampoos, the performance of a drug delivery system and how a fruit cake changes as it undergoes multiple phase transitions during cooking [7]. Therefore there are a wide range of fields that will benefit from the current research.

Microfluidics, which is primarily concerned with the flow of relatively simple fluids, and considers such phenomena as those involved in ink jet printing, microelectrophoresis on a chip and microvalves, is closely connected to the field of microrheology [8]. The change of emphasis, which separates the two fields, is the inclusion of viscoelastic effects in microrheology. The overlap is thus quite strong and the fluid mechanics of materials in confined geometries is a common area to the two research fields.

To analyse the rheological properties of a material, conventional bulk rheometers such as cone and plate rheometers etc. are widely used [9]. However, these rheometers due to their size are only able to measure the macroscopic properties of fluids and so can only give limited information about a material, restricting their usefulness. They usually require a relatively large volume of fluid to be able to perform the analysis and so are of limited use in fields (such as the analysis of biological fluids in medicine, or the prototyping of new

compounds in the pharmaceutical industry) where the amount of fluid available for analysis is small.

The inertia of such rheometers precludes the probing of complex fluids at high frequencies. High frequency rheometry, which is possible with a microrheometer, is useful in measuring the properties of materials at very high velocities and provides details about very short time scale relaxation processes within the molecular structure of the material. This allows for the measurement of the suspension stability in colloidal suspensions and the chain stiffness and molecular architecture in polymers etc. [10]. This information is very useful in many applications such as paint and drug synthesis and the lubrication of high speed components. This thesis will therefore focus upon microrheometry.

1.2 Project Goal

It was shown in the last section that rheology is an extensive subject with far reaching implications. It was also shown that industry, especially companies involved in research and development in chemicals such as Unilever and ICI, require high through-put, high frequency characterisation of small volumes of complex liquids. However it was also shown that the capabilities of conventional rheometers are limited, in essence by their sheer size. The goal of this work is therefore to develop a microrheometer. The device has to facilitate the analysis of small (nanolitre) volumes of a wide range of different types of fluid and soft materials but specifically materials that can be described as viscoelastic. The rheometer has to be small enough so that it is sensitive to such small volumes of liquid and

to have low enough inertia as to allow operation at high frequencies (i.e. greater than 100Hz).

Given this specification it is now necessary to ascertain what sort of rheometry will give the most useful results when scaled down to the micron scale. To achieve this all current methods and technologies used in rheometry will be reviewed. This review will cover both conventional rheometry and more modern micro-scale methods and will highlight the issues associated with these methods and show why the method chosen is the most beneficial.

1.3 Review of Conventional Rheometric Experimental Techniques

While it has been stated that conventional rheometers have limited capabilities and usefulness, much of the theory and data used in microrheology has its basis in conventional rheometry. Therefore, in order to better understand current technology and theory, traditional techniques will be briefly discussed.

1.3.1 Origins of Rheology

When discussing the development of technology, it is often beneficial to put the advancements in context. For this reason the chronological development of rheology is given first. Then the various technologies and methods available for conventional rheometry will be discussed.

Rheology is one of the few disciplines whose origins can be precisely traced. While being formally born in 1929, the theory of rheology is based on theories dating back centuries as this short chronology shows:

1678 Robert Hooke considered elastic behaviour and proposed that 'the power of any spring is in the same proportion with the tension thereof'.

1687 Isaac Newton observed that in liquids 'the resistance which arises from the lack of slipperiness originating in a fluid – other things being equal – is proportional to the velocity by which parts of the fluid are being separated from each other'.

1845 Navier-Stokes equations developed enabling the complete mathematical characterisation of Newtonian liquids.

1867 Maxwell postulated his famous first-order empirical differential equation relating the shear stress to the deformation and the accompanying simple exponential stress relaxation (the Maxwell model).

1878 Boltzmann arrived at his 'principle of superposition': 'the value of a characteristic function of a system is equal to the sum of all changes induced in the system by the driving functions which have been applied to it throughout its history'. Thus an integral generalisation of linear viscoelasticity was created.

1888 Thomson introduces the concept of a distribution of relaxation times thus extending the Maxwell model.

1890 Schwedoff's experimental work on colloidal gelatine solutions using a Couette device (see sliding plate rheometry below) was one of the first results on non-Newtonian systems.

1902 Poynting and Thomson introduce the well-known 'spring-and-dashpot' analogy for the Maxwell model.

1922 Bingham proposed a 'yield stress' to describe the flow of paints to explain the apparent plasticity of certain fluids.

1929 (April 29th to be exact): The study of rheology was created as a specific science by a committee chaired by Eugene Bingham.

1950 Oldroyd formalised the basic requirements for the mathematical models of rheology.

1956 The network theory for rubber-like fluids was developed by Lodge.

1978 The Doi-Edwards model extends the reptation theory to explain the effects of entanglements in polymer melts.

1.3.2 Conventional Rheometry

Now it is known how recently rheology has come into existence and how quickly the theory has developed, it is a good juncture to see what conventional methods and technologies are used to perform rheometry and to see where development is required.

1.3.2.1 Sliding Plate Rheometry

Sliding plate rheometry is the simplest form of shear rheometry. Here a fluid is contained between two flat platens which are moved laterally to each other maintaining a constant gap and parallelism between the platens (see Fig. 1.1) [13]. In this way a shear flow (Couette flow – see Fig. 1.1) is generated within the fluid. The advantage of this method is that it is not subject to the flow instabilities caused by turbulence that limit the use of rotational rheometers to shear rates often below $1s^{-1}$ [14]. Issues of secondary flow (deviations in flow away from Couette flow) and slip (where fluid at a solid-fluid interface moves at a different velocity to the solid) must be addressed to obtain reliable data using a sliding plate rheometer [15].

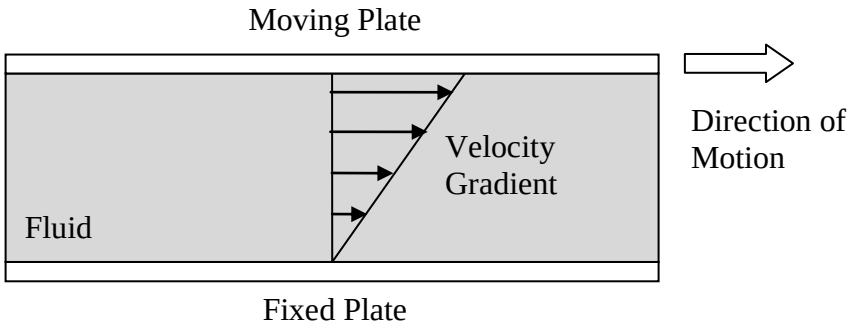

Fig. 1.1: A schematic of sliding plate rheometry. The velocity gradient caused by the shear flow is known as Couette flow.

Despite its apparent simplicity, this is not a common method of rheometry. Practical issues often arise as difficulties in maintaining a constant gap is non-trivial [16]. Nevertheless a number of fluids have been tested with reasonable accuracy [16, 17]. However shear flow is a convenient configuration that allows for accurate analysis hence its frequent discussion in rheology. In microrheology, instead of sliding-plate rheology, squeeze flow rheology is occasionally employed to induce shear flow. Squeeze flow will be described in full later in this chapter.

1.3.2.2 Cone and Plate

In cone and plate rheometry, the liquid is placed on horizontal plate and a shallow truncated cone placed into it (see Fig. 1.2). Instead of a cone, two parallel plates could be used however the cone ensures the flow is homogenous and has a constant shear rate. The angle between the surface of the cone and the plate is of the order of 1 degree. Typically the cone is rotated (either with angular velocity Ω, or to an angular displacement φ and held) and the force, F, and the torque, M, on the plate measured, (see Fig. 1.2) [11]. In a stress-controlled cone and plate rheometer, a constant torque is applied to the drive shaft of the cone, and the rotation of the cone that results is measured with an optical encoder [12]. In either case the velocity field in the liquid is expected to be identical on a local level to rectilinear simple shear (Couette) flow (described above).

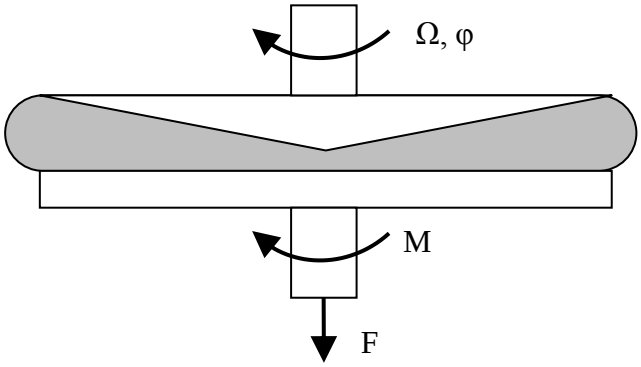

Fig. 1.2: A schematic of cone and plate rheometry.

A well-known version of this instrument is the Weissenberg Rheogoniometer, in which the movement of the cone is resisted by a thin piece of metal which twists—known as a torsion bar. The known response of the torsion bar and the degree of twist give the shear stress, while the rotational speed and cone dimensions give the shear rate. In principle the Weissenberg Rheogoniometer is an absolute method of measurement providing it is accurately set up. Other instruments operating on this principle may be easier to use but

require calibration with a known fluid. Cone and plate rheometers can also rotate the cone sinusoidally to measure elastic properties, or in combined rotational and sinusoidal modes.

1.3.2.3 Rotational Coaxial Cylinder

In a coaxial-cylinder system, the liquid is placed within the annulus of one cylinder inside another (see Fig. 1.3). The inner cylinder is often referred to as a bob, and the external one as a cup. One of the cylinders is rotated at a set speed. This determines the shear rate inside the annulus. The liquid tends to drag the other cylinder round, and the force it exerts on that cylinder (torque) is measured. The shear stress is calculated from the torque and the geometrical dimensions [18]. This design is supposed to create the same Couette flows described above as the cylinders can emulate infinite flat plates moving relative to each other. The curvature inherent in these devices gives rise to increased drag in the wall region [19] but generally it is assumed that if the cylinders have large radii compared to the fluid thickness, where the outer cylinder has only a slightly larger radius, then this effect can be neglected locally.

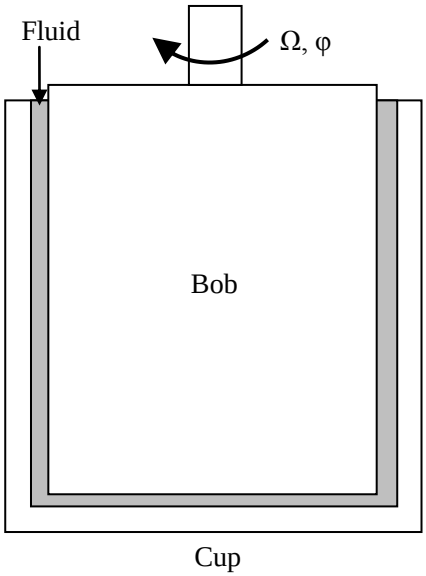

Fig. 1.3: A schematic of coaxial cylinder rheometry.

1.3.2.4 Capillary Tube Rheometer

In capillary tube rheometers, a fluid is forced to flow through a thin cylindrical tube by means of a pressure difference across the two ends of the rheometer [20]. The premise is if the tube is long enough to negate entrant effects (instabilities caused by change in geometry of the tube at the entrance) and the flow velocity is low enough, the flow will be laminar and steady in the sense that it will have a constant velocity distribution over the cross-section of the tube, independent of the distance along the tube [21]. The fluid properties are then calculated by measuring the flow rate due to the pressure difference from elementary pipe flow theory [22].

Capillary tubes are used for a number of reasons. The main reason is that the flow induced during an experiment emulates those found in typical polymer processing methods such as die-drawing, extrusion and injection moulding [23]. They can also emulate organic systems such as blood vessels [24] and nano-tubes [25] and other processes [26]. Additionally capillary tube rheometry is easy to set up and interpret.

However, a number of issues exist in capillary tube rheometry. Certain types of fluid cannot be tested because of problems with obliteration, in that the fluids structure is destroyed changing its properties. This is especially true of water-based hydraulic fluids of the emulsion type [20]. In addition, some of these fluids can contain solid contaminants making it nearly impossible to clean the system. Also the elementary theory only applies if the assumptions it is based on hold true. The main assumption that needs correcting for is the no-slip condition where it is assumed that the fluid has zero velocity next to the solid boundary [24, 26]. Other effects such as elastic effects, colloidal suspension effects etc.

have to be corrected for [22]. It is for these reasons that fluids are commonly tested in rheometers with moving boundaries.

1.3.2.5 Acoustic Rheometer

The acoustic rheometer employs a piezo-electric crystal that launches waves of extensions and contractions into the fluid. In this way it applies an oscillating extensional stress. Acoustic rheometers measure the speed of the sound wave and the attenuation of ultrasound waves up to 2MHz. The speed of sound is a measure of the material's elasticity and density and can also be used to calculate the fluid's compressibility. The attenuation of the wave is a measure of the viscous properties of the material. In the case of Newtonian liquids, attenuation yields information on the volume viscosity, which is only useful when fluid compressibility is significant [27]. Also, this method can produce significant heating effects on the liquid's properties due to internal friction.

1.3.3 Summary of Conventional Techniques

While conventional rheometry has been proven very useful for characterising fluids they do have limitations. In the techniques above, the rheometers used are generally large and heavy. This means that they require relatively large volume samples of liquid in order to produce meaningful results. It also means that their inherent inertia prevents them operating at high frequencies. This suggests that methods which utilise smaller scale technologies will be beneficial. It is for these reasons that microrheometry techniques need to be investigated.

1.4 Review of Microrheometric Experimental Techniques

As was stated previously, microrheology can provide a number of advantages. However several techniques already exist and so it is necessary to see why these methods are not satisfactory and why further development is required. At the end of this section it should be apparent what the basic premise behind the proposed microrheometer must be.

Microrheology is the study of the viscoelasticity in soft materials at the micrometre or sub-micrometre level. Microrheology has long been identified with the resolution limit of an optical microscope operating at its largest degree of magnification, $\approx 0.5\mu m$, and optical techniques continue to dominate the field. However, the area is rapidly enlarging and advancing with a series of technical and theoretical barriers being overcome. Within this enlargement there has been the creation of new sub-fields which are discussed below.

1.4.1 Origins of Microrheology

Microrheology has been around for a long time but its development has not been a steady progression. However as analytical technology has increased giving us the ability to probe further into complex fluids, and as the need for more highly specific requirements in the fluids has increased, the development of microrheology has become more and more intense. To give context to the following discussions in the types of microrheology, here is a simple chronology of the development of microrheology:

1827 Robert Brown observed that pollen grains moved incessantly on the surface of water and posed the question: what is the origin of the force driving this motion?

1879 Hannay published the paper entitles ‘On the Microrheometer’. It is the first indication of a technique that can be used to probe the nature of fluids on the microscale. He noticed that Poiseiulle’s theory on the rate of flow through a tube didn’t work for very small diameter tubes and discussed the possibility of the effect of a fluid’s structure on its properties.

1905 Albert Einstein theoretically analysed Robert Brown’s problem and established the molecular nature of matter by explaining Brown’s results in terms of a statistical analysis of the collisions of pollen with the surrounding solvent molecules.

1924 Seifriz suggested that an active magnetic microrheometer may be able to manipulate micrometre-sized ferromagnetic particles and be used to measure the properties of liquids.

1925 Oseen worked on anisotropic liquid crystalline polymers.

1934 Kuhn developed the first molecular model characterising the configuration of polymer molecules using a random coil model.

1944 Treloar performed first biaxial and planar extension experiments.

1948 Jean Baptiste Perrin painstakingly demonstrated quantitatively Einstein’s theory by showing the mean-square-displacement of 0.37 μm gutta-percha particles in water are directly proportional to time with a constant of proportionality that describes the frictional dissipation of the particles.

1950 Crick and Hughes created active magnetic rheometer.

1986 Ashkin developed optical tweezers and used them to manipulate a sphere submerged in a fluid and uses the response to characterise the fluid.

1986 AFM invented.

1993 Weitz extended dynamic light scattering to create diffusing wave spectroscopy.

1997 Mason uses particle tracking video-microrheology for the first time for rheological purposes.

This chronology shows that there are a plethora of different approaches to measuring material properties at the micron scale. These methods can be grouped into three types. These include interfacial microrheometers, which concentrate on the fluid surface, passive microrheometers, which tend to use optical methods and active microrheometers which manipulate the fluid sample directly. These methods will be discussed in turn in order to see where the new design can offer a better solution.

1.4.2 Interfacial Microrheometry

Interfacial rheology is the field of science that studies the response of fluid surfaces to deformation [28]. It is used to measure the properties of fluid just next to an interface (such as local viscosity – the viscosity next to an interface is different due to absorption and other surface effects). Traditionally, free fluid surfaces were considered purely to specify an appropriate boundary condition for bulk fluid flow problems [29]. This is because a precise knowledge of the normal stress boundary condition is often unnecessary for a basic understanding of the bulk-fluid motion. Hence, if the fluid surface-to-volume ratio, or specific surface, is small for the particular system under consideration (as is the case for most microrheological techniques), a rigorous formulation of the normal stress condition at fluid boundaries is generally unnecessary. Therefore interfacial microrheometry is only

useful for systems with a high fluid surface-to-volume ratio and can be considered an extreme of microrheology – see Fig. 1.4.

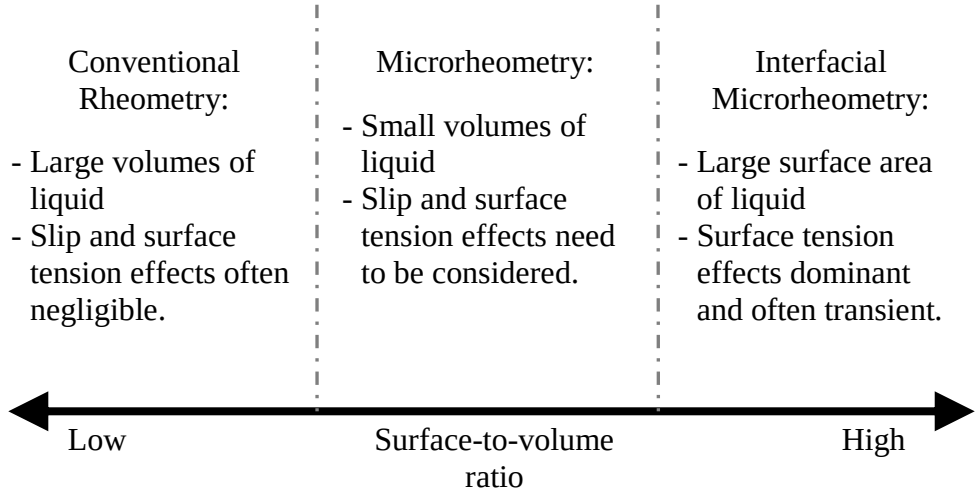

Fig. 1.4: The relationship between the different types of rheometry and the surface-to-volume ratio.

However in circumstances for which the fluid system under study possesses a large specific surface, as occurs in many fluid-fluid colloidal dispersions (e.g. emulsions and foams), interfacial rheometrical knowledge may prove indispensable for understanding bulk hydrodynamic behaviour, for example in dynamic phase mixing [28]. Interfacial rheometry seeks, amongst other things, to determine the shape of a dynamic free fluid interface, the nature of the interfacial response to deformation, and the quantitative influence that interfacial stress imparts upon hydrodynamic motion in contiguous phases.

Several different devices have been proposed to measure the forces required to deform these surfaces including canal devices [30, 31], rotating discs and rings [32-34], knife edge devices [35,36] and Langmuir troughs [37,38]. Canal devices or deep-channel surface viscometers usually consist of two concentric cylinders in a pool of liquid (see Fig. 1.5).

The dish is rotated with a known angular velocity and the mid-channel surface motion of the interface within the channel formed by the two cylinders is monitored by a small micron sized particle. This device allows for sensitive measurements of the interfacial shear viscosity but the inclusion of the particle can affect the interfacial properties, especially local curvature [30, 31].

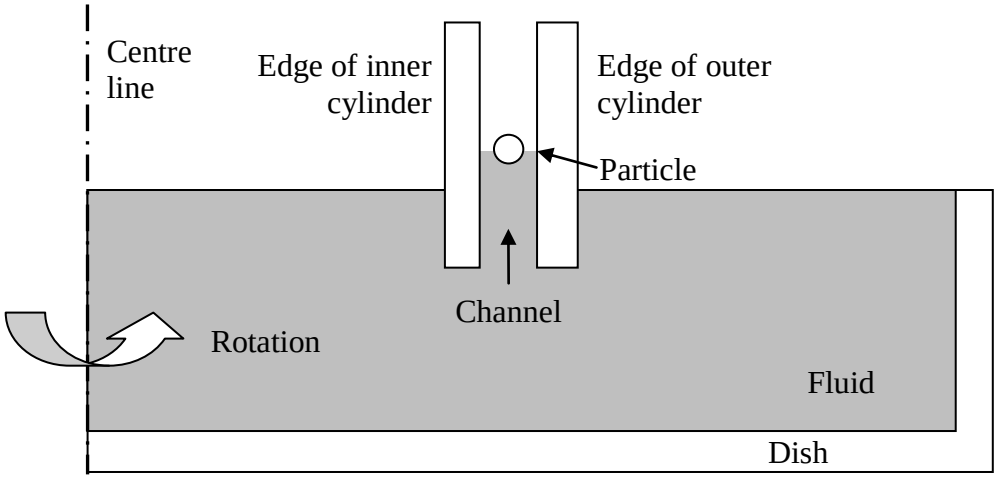

Fig. 1.5: A schematic of canal surface rheometers.

In another configuration, discs and rings are floated on the surface [32-34] or alternatively knife edge surface viscometers consist of a knife edge bob suspended on a torsional wire such that the circular knife use touches the interface of a surfactant solution contained within a circular cup (see Fig. 1.6). In all cases, the cup is rotated and the torsional stress on the bob is measured to determine the interfacial shear viscosity [35, 36].

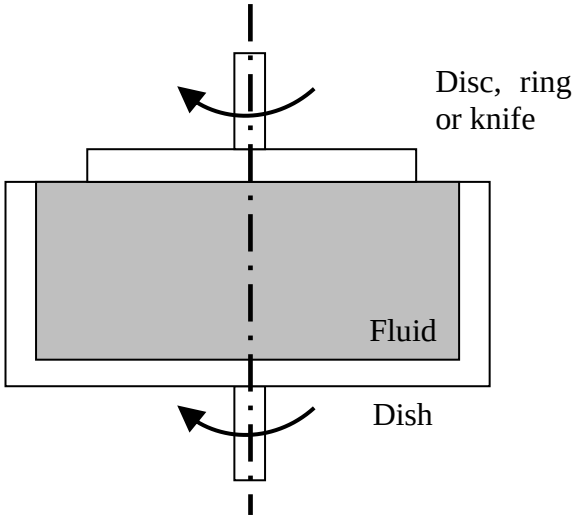

Fig. 1.6: A schematic of rotating disc, ring and knife rheometry. In all devices the dish is rotated and the torque exerted on the floating object is monitored to measure interfacial viscosity.

In the Langmuir trough method, a surfactant monolayer is spread upon a gas-liquid surface (see Fig. 1.7). A barrier is moved from one side of the trough to the other, sweeping the monolayer to one compartment of the trough leaving a clean solvent interface in the other compartment. This causes a surface pressure force to act on the barrier which can be measured and used to determine a relationship between area per molecule and surface pressure [37, 38]. These methods are only applicable to very specific fluid problems. If the dynamic properties of fluids are required other microrheometry methods have to be used.

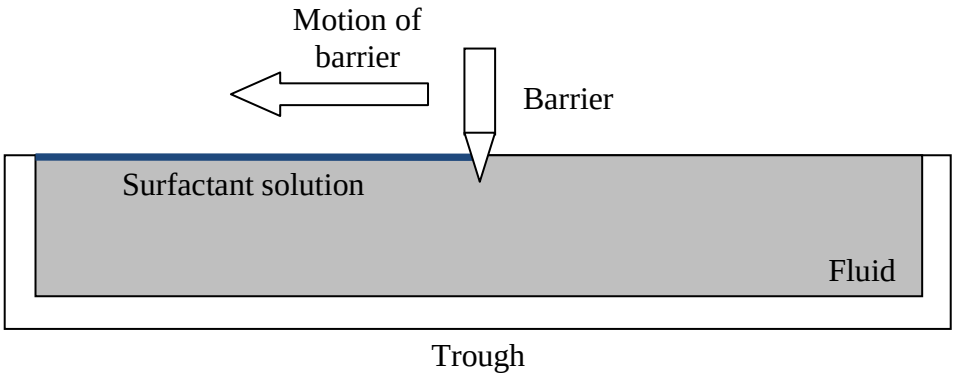

Fig. 1.7: A schematic of a Langmuir trough.

When the fluid surface-to-volume ratio is small for the particular system under consideration, surface effects tend to become negligible (see Fig. 1.4). This situation, which occurs frequently, means that rheology is specifically concerned with the structure and properties of fluids away from the interface need to be utilised. To this end several methods have been investigated:

1.4.3 'Passive' Microrheometers

Passive rheometers are frequently used in microrheometry to measure fluid properties. Passive rheometers are those that are concerned with the motion of particles or molecules within the fluid, rather than the motion of the fluid itself. These rheometers use optical methods and use image processing to monitor the fluid (as compared to active rheometers which use mechanical methods). The advantage of these methods is that the perturbation of the fluid is minimised allowing for the accurate analysis of the fluid's structure.

1.4.3.1 Optical Tweezers

Optical tweezers, also known as optical traps or laser tweezers were first described in the 1980s by Ashkin et al. [39]. They permit the non-invasive micromanipulation of inert and biological objects by means of optical radiation alone [40]. Optical tweezers use the forces generated when light interacts with matter to trap objects near the point of focus of an objective lens. The premise is that, when photons are absorbed, reflected or refracted by an object, the momentum they possess is changed i.e. the photon exerts a force on the object. Optical tweezers require an intense laser light source, tightly focused by an objective lens of high numerical aperture. They produce forces in the pico-Newton range that are

sufficient to trap microscopic particles (from whole cells down to particles of a few tens of nanometres in size) and move them relative to their surroundings (provided the particle has a refractive index significantly higher than its surroundings) [40].

More frequently used in biophysics as a means to manipulate cells and organelles [41] optical tweezers have played a role in molecular motor mechanochemistry [42, 43], DNA transcription [44] and cytoskeletal-membrane interactions [45]. Experimental approaches based on optical tweezers also offer the ability to probe the structure and response of complex fluids at nanometre-to-micrometre length scales. Optical tweezers are especially useful for applications in complex fluidics when combined with real-space imaging, such as video and confocal microscopy [46]. For instance, Chu et al. introduced single polymer visualization and manipulation to understand polymer dynamics in dilute and entangled solutions of DNA [47-49].

The dynamic capabilities of laser tweezers can also be used for microrheological measurements [46]. Several unique advantages are often cited including minimal mechanical perturbation, and a temporal range that spans many decades (10^{-6} to >100s). Inertial effects, in which the propagation of deformation becomes on the order of the probe size, occur at approximately megahertz frequencies, far above that of mechanical rheometers [50]. However the light beams used are very intense and may heat and damage the sample and so careful monitoring is required.

1.4.3.2 Single/dual Particle Techniques

For this technique a micron-sized probe particle is introduced inside a rheologically complex fluid (like a polymer melt) and its Brownian fluctuations are noted [51]. The properties of the fluid are then determined from the measured diffusion coefficient using a generalised Stokes-Einstein relationship. The principal advantages of this technique are that it can be used for the detailed study of materials that cannot be produced in bulk quantities and that it can be used to probe rheologically inhomogeneous materials [52]. This method can also be used to probe soft biomaterials that are too delicate to be analysed using conventional rheometry [53, 54]. Typically the position of the probe particles is measured either by light scattering [53], laser interferometry [54] or by direct real-space imaging [55]. The exact physics of this method is contentious as experiments have shown that discrepancies exist between microrheological and bulk measurements of the shear modulus of fluids in certain systems [52]. The issue is that, large probes perturb the medium by reducing the polymer network density in the vicinity of the probe. To deal with this issue researchers have considered dual particle techniques. In this situation it has been shown that the interparticle position (the particles relative position as compared to the absolute position of each probe) is insensitive to the local particle environment and therefore provides a more reliable probe of the properties of the bulk material than do single-particle techniques [55].

The inspiration for using such a technique is that suspensions of particles dispersed in a viscoelastic complex fluid matrix are ubiquitous in chemical and materials processing [56]. For example, colloidal latex particles dispersed in associative polymeric thickeners are the basis of water-borne paints and coatings [57]. Also at certain stages of processing,

pharmaceutical formulations are well described as drug particulates embedded in a polymer matrix. In addition, polymer melts have long been compounded with micrometer-sized particulate fillers to improve mechanical properties and reduce costs [58]. The result has been the emergence of polymer nanocomposites as a new class of filled polymeric materials [59]. However these materials are only analogous to the systems used in single or dual particle techniques provided the dispersed particles are relatively large; if this is not the case diffusing wave spectroscopy may be more advantageous.

1.4.3.3 Dynamic Light Scattering and Diffusing Wave Spectroscopy

Dynamic Light Scattering (DLS) is a method used to determine the size distribution profile of small particles in solution [60]. Basically when light hits small particles the light scatters in all directions (Rayleigh scattering) so long as the particles are small compared to the wavelength (< 250 nm). If the light source is a laser, and thus is monochromatic and coherent, then one observes a time-dependent fluctuation in the scattering intensity. These fluctuations are due to the fact that the small molecules in solutions are undergoing Brownian motion and so the distance between the scatterers in the solution is constantly changing with time. This scattered light then undergoes either constructive or destructive interference by the surrounding particles and within this intensity fluctuation, information is contained about the movement of the scatterers [60, 61].

Diffusing Wave Spectroscopy (or DWS) is essentially an extension of DLS [61]. DWS extends DLS to very strongly scattering media, where the propagation of light is described by the diffusion approximation, allowing the distribution of the light paths to be determined [61]. Interference between these light paths results in a speckle pattern of

scattered light intensity that fluctuates over time due to the relative motion of the individual scattering elements. Since many scatterers participate, very small displacements of these scatterers give rise to discorrelation of the intensity of scattered light [62]. Therefore compared to DLS, DWS is sensitive to fluctuations of the media on length-scales much smaller than the wavelength of light. Moreover these fluctuations can be probed over a very wide range of timescales (10^{-8} to 10^{5}s) [63].

DWS can be used to study the transient nature of hydrodynamic interactions between a particle and the surrounding fluid [61]. It can also be used to measure the viscoelastic properties of complex fluids [64-65]. It has been shown that the response of the fluid to thermal fluctuations, as probed by the average motion of small particles dispersed within the fluid, provides a close representation of the response of the bulk fluid to an imposed shear strain. Good agreement has been found when comparing results to those obtained by more conventional boundary driven rheometers, with the added advantage of being able to probe much higher frequencies.

Passive rheometers are very useful for a number of systems. However, the inclusion of particles into the fluid inherently changes its structure and hence its properties. It can therefore be argued that using these techniques have a built-in inaccuracy. These techniques are also generally limited to transparent and lower viscosity fluids due to the difficulties that arise in the detection and introduction of particles. The main reason, however, why these techniques are not being considered further is that they are complicated techniques and require a lot of equipment to operate. For these reasons active microrheometers will now be investigated.

1.4.4 'Active' Microrheometers

Boundary driven or active rheometers are rheometers that mechanically manipulate the fluid itself. This usually involves using a moving plate to induce a flow within the fluid. The fluid properties are then calculated by measuring the resultant fluid velocity or displacement and comparing it to the applied force (alternatively it could be a velocity that is applied to the fluid and the resultant force that is measured). The subsequent rheometers are those that follow this basic premise:

1.4.4.1 μCaBER and FiSER

In Capillary Break-up Extensional Rheometry (μCaBER) and conventional Filament-Stretching Rheometry (FiSER), a cylindrical liquid bridge is formed between two circular end-plates that are separated in a prescribed manner, such that the fluid sample is subjected to a strong extensional deformation [66]. This generates a uniaxial extensional flow at the filament centre. This filament stretching is a common example of extensional flow which has wide applications in the study of polymer solutions and melts. In addition, it is a common technique employed to quantify certain material fluid properties, via quantitative measurements of the thinning process within fluid filaments [67]. The difference between FiSER and μCaBER is that in FiSER it is common practice to impose an exponentially increasing velocity upon the fluid formed between the plates [68]. Typically, the subsequent development of the mid-filament diameter is monitored during the process of necking down. In contrast, μCaBER is based on the formation of an unstable fluid filament by imposing a rapid axial step-strain of prescribed magnitude. The filament is then allowed to relax until it breaks up under the action of viscous, elastic, gravitational and capillary

forces [69], and as with FiSER-procedures, the evolution of the mid-filament diameter is again monitored.

The associated progressive thinning and break-up of a fluid filament into numerous small beads/droplets occurs in many commercial operations, such as printing, paint applications, roll-coating of adhesives, and under food processing. Extensional flows are also encountered in applications such as coatings, enhanced oil recovery, lubrication, turbulent drag reduction and atomization [70-72]. This method however can only measure extensional properties, not shear properties which often of more use as most flows exhibit shear stresses.

1.4.4.2 Atomic Force Microscope Extensional Flow

The atomic force microscope (AFM) belongs to a series of scanning probe microscopes developed in the 1980s. These are the scanning tunnelling microscope (STM), which allows the imaging of surfaces of conducting and semiconducting materials, the scanning near-field optical microscope (SNOM), which allows microscopy with light below the optical resolution limit, and the AFM itself, which allows the imaging of the topography of conducting and insulating materials, in some cases with atomic resolution [73]. From this data the molecular structure of fluids can be found [74]. It is also used to study the properties of systems ranging from polymer networks, to cells and membranes, to single polymer filaments [75, 76].

In an AFM force measurement, the sample is moved up and down by applying a voltage to the piezoelectric transducer (onto which the sample is mounted). Forces are measured when a small micromachined tip is deflected when placed in contact with a surface. Sensitive measurement of the tip motion is made possible by monitoring the deflection of a laser. AFMs can be used to apply rather large forces by using small tips, making them ideal to study stiff elastic materials with elastic moduli of order 1 GPa [77-80]. Recent AFM experiments have also explored the viscoelastic properties of polymer solutions and melts. Two distinct modes of AFM have been widely used to locally test viscoelastic properties of various materials. The first is the force mapping method and the other is the force modulation method (see below).

In the force mapping method [81], the tip of the AFM is slowly brought into contact to indent the material at a certain point and then retracted. The tip is retracted at various velocities and the force that acts on the tip due to the fluid is mapped from point to point in time. In this way the elastic and viscous forces can be deduced and the fluid properties calculated [82]. However, uncertainties in the tip geometry and cantilever stiffness make it difficult to be quantitative in practice. Furthermore, adhesive and wetting forces between the tip and the surface need to be known as they determine the geometry of the bridge and so affect the calculation of the fluid properties. While this method can theoretically be used to measure both shear and extensional fluid properties, the results are often inconsistent. In order to calculate dynamic properties, an oscillatory method is required.

1.4.4.3 Oscillating AFM Probes

In the force modulation method (or dynamic force microscopy) the sample (or the base of the tip) is vibrated to invoke a known strain normal to the surface and the amplitude and phase of the tip response is monitored. Usually the tip moves sinusoidally and the displacement is resolved into an in-phase and out-of-phase response [83]. Often, the in-phase or amplitude responses are interpreted as elasticity, and the out-of-phase or phase-shift responses are interpreted as viscosity. For example, Overney et al. [84] have generated an "elasticity map" of a lipid bilayer with molecular resolution by measuring the spatially-resolved amplitude response of the AFM tip during a two-dimensional scan of the film. Also, Akari et al. [85] have imaged mixed self-assembled monolayers containing dodecanethiol and a thiol-terminated polystyrene on gold by measuring the amplitude of the tip response as the tip was rastered across the surface.

Again, unfortunately, the contact geometry is not generally known for these systems, nor is the cantilever spring constant known to any great precision. Furthermore, the compliance of the AFM cantilever can lead to a viscous response that is largely in-phase, causing it to be confused with elasticity.

Alternatively the AFM can be excited using thermal noise [86]. In either case, the response of the system to the strain is analyzed in the frequency domain for extracting the viscoelastic response of the materials. In a method described by Ma [87] called Brownian fluctuation spectroscopy, the local viscous or viscoelastic behaviour is obtained from an analysis of the power spectrum of the thermal fluctuations of the probe. To do this, usually a Langevin formalism in either Laplace or Fourier space [88] is used to interpret the data.

It has been shown that the AFM can theoretically be used to measure dynamic shear properties. However, because of the ambiguities involved in AFM rheometry, it is necessary to use a microrheometer with a more precisely defined geometry. This will improve the accuracy and consistency of results and negate the need to use an AFM which is not amenable to high-throughput testing.

1.4.4.4 Squeeze Flow Rheometry

In squeeze flow rheology, a fluid is trapped between two plates which are kept parallel and inline axially and a small distance apart (see Fig. 1.8). The gap is varied by displacing either plate thus generating a squeezing flow (a biaxial extensional flow). It is of particular interest to study this type of flow because it appears in a wide variety of situations such as machine bearings, human joints and manufacturing processes such as compression moulding [89]. If used in a steady shearing mode, such as in a parallel plate plastimeter, certain properties such as shear modulus can be deduced. However, squeeze flow is much more frequently used to find the dynamic properties (storage and loss modulus) of viscoelastic materials [90]. Generally experiments consist of measuring the normal force on the top plate as a function of time whilst it is moving with a prescribed sinusoidal motion [91].

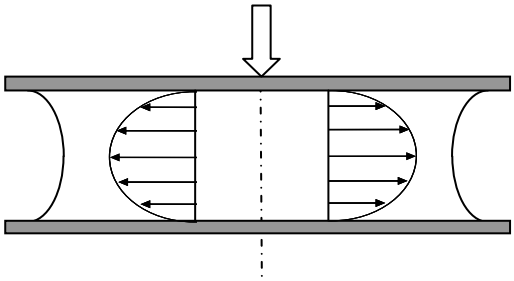

Fig. 1.8: A schematic of squeeze flow rheometry. The velocity gradient is an example of a biaxial extensional flow.

At present very few commercially available rheometers exist. Exceptions include the MFR2001 that is manufactured by GBC, in Melbourne, Australia [92]. This device is called a micro-Fourier rheometer and uses random squeezing to measure the complex modulus of viscoelastic materials [89, 93]. This rheometer is capable of measuring the viscoelastic properties of small quantities of fluid (a few millilitres) over a frequency range of 1-100 Hz in 4 s or less [94]. This frequency range is typical of most conventional rheometry techniques. However, as explained above, complex fluids exhibit relaxation times that range over many orders of magnitude. Therefore measurements of the rheological properties such as the storage and loss modulus must cover an enormous scale in the time or frequency domain in order to capture all the relaxation processes that occur in these materials [95]. In view of this Pechhold et al. recently introduced a new device named a piezoelectric axial vibrometer [96]. It consists of a dynamic press with a thin gap in which the fluid is confined. A squeeze flow is generated by a piezoelectric drive and monitored by piezosensors and has a frequency range between 10 and 4000 Hz. The gap can be varied between 20 and 200 μm and the required sample volume is 100 μL [97]. This allows for the measurements on fluid with viscosity range between 1 and 2000 mPa s. The device seems to be very promising; however, the volume of liquid required is still too large and the viscosity that can be measured is too low to satisfy a number of industrial needs.

Other squeeze flow rheometers do exist but are usually limited in their abilities [98]. It seems apparent that a device capable of measuring properties of fluids into the kHz range and operating on sub-μL volumes and sub-20 μm gaps has yet to be developed. A device with these capabilities would be able to measure the properties and perhaps the change in structure of the fluid in thin films – a non-trivial task.

1.4.5 Summary of Current Rheometric Techniques

This review has shown that conventional techniques are too large and heavy to measure the properties of small volumes of liquid at high velocities. It has shown that interfacial microrheometry doesn't measure properties that are particularly relevant for most applications and that passive microrheometers frequently require expensive optical systems, difficult analysis and usually do not facilitate high through-put processing. Active microrheometers were shown to offer a number of advantages in that they measure the pertinent dynamic properties using a relatively simple set-up. However it was shown that most active microrheometry methods still require expensive equipment and there are few devices available specifically for active microrheometry. In terms of which type of active microrheometry to focus on, it is apparent that squeeze flow is a very useful type of rheometry as it emulates a vast number of natural processes and so the data generated will be directly applicable. Therefore a micro squeeze flow rheometer will be designed. Existing devices generally require a number of actuators and sensors in a complicated arrangement making them expensive to produce. And as squeeze flow often occurs in micro-devices (often in the form of damping) it seems a natural progression to utilise micro system technology (MST) to create such a device. There are other advantages to using MST to fabricate a micro rheometer. With MST it is possible to produce large numbers of microrheometers cheaply, making it feasible to create arrays of disposable microrheometers facilitating high-throughput analysis on an industrial scale. It is to this end that the rest of this thesis is dedicated.

In order to maximise the capabilities of the micro squeeze flow rheometer, it is necessary to fully understand squeeze flow theory. In the following section existing squeeze flow theory will be discussed to see where further development is required.

1.5 Review of Existing Squeeze Flow Theory

In the previous section we saw that the use of squeeze flow rheology has a number of advantages that have not been exploited fully. To this end, this field will be investigated in depth within this thesis. In order to give this investigation a good foundation, it is necessary to understand what developments have occurred within squeeze flow theory previously. This will highlight the areas which require further development.

1.5.1 Origins of Squeeze Flow Theory

As technology has improved, especially micro systems technology, the need for more accurate and more specific theories on squeeze flow has increased. To see how the theory has developed so far, consider the following chronology:

1874 Stefan publishes his seminal paper on the force required to separate two plates with a fluid in-between them, thus starting interest in squeeze flow.

1886 Reynolds conducts a theoretical investigation into squeeze flow and validates Stefan's results and creates the infamous Stefan-Reynolds equation.

1931 Scott develops his parallel-plate plastimeter and his power-law fluid theory.

1933 Eisenschitz and Philippoff conduct the first small-strain dynamic studies of polymers and polymer solutions.

1965 Tanner investigates the effect of viscoelastic non-Newtonian fluids in inertia-less squeeze flow.

1975 Walters publishes 'Rheometry' which details the simplification of the Maxwell model by using a complex viscosity for sinusoidal rheology.

1985 Phan-Thien finds a computational solution of the complete flow field.

2006 Walters publishes for the first time a full treatment of the effect of fluid inertia on viscoelastic squeeze flow.

1.5.2 The Development of Squeeze Flow Theory

There are many aspects to squeeze flow. In order to create a comprehensive accurate theory, researchers have investigated many facets of squeeze flow using a myriad of techniques from theoretical analysis, to numerical through to empirical examinations of a range of systems with variable success. To see where development is required consider the following review:

1.5.2.1 Geometries Found in Squeeze Flow Theory

Before a theoretical investigation can commence it is first necessary to define the experiment, and so choose an arrangement that is the most convenient and the most useful. In squeeze flow there are a number of possible configurations. This is true even though we are only going to consider squeeze flow between parallel plates (squeeze flow between

spheres and other shapes are of high importance but is a geometry not conveniently realisable using MST therefore this possibility is outside the scope of this thesis). The main possibilities include:

1. In Stefan's classic study [99] he considered platens that were *fully submerged* in the fluid (see Fig. 1.9). This is a technique that has found little application though it was used by Chatraei et al. [100]. This technique is only feasible when the tested fluid is of low or medium viscosity or if it can be submerged in another liquid without creating unwanted interactions, and is therefore not applicable to many materials.

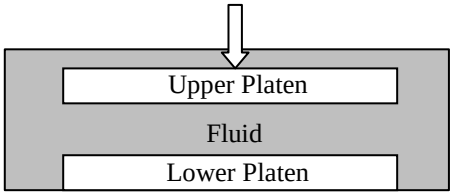

Fig. 1.9: A schematic of submerged squeeze flow rheometry.

2. Another method is the so-called '*imperfect squeezing flow*' and is the penetration of a platen into a 'lake' of fluid (see Fig. 1.10). This means that sample preparation is simple for materials with low viscosity and low relaxation times. However the flow is asymmetric (the top and bottom contact areas between platens and fluid are of different size) and the boundary conditions at the edge of the plate are not known [101-103].

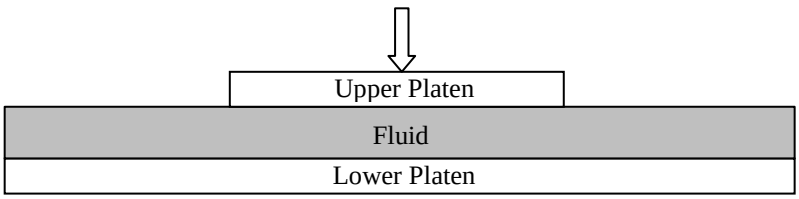

Fig. 1.10: A schematic of imperfect squeeze flow rheometry. Note how the platens have different radii.

3. A more common geometry is the *constant area* geometry. Here the sample radius is the same or larger than that of the platens and the sample flows out during squeezing (see Fig. 1.11). This has the advantage that the contact area is known at all times, and that the sample position errors are limited, which minimises losses of parallelism due to additional torque. Disadvantages include the amount of fluid needed to fill the initial gap is higher and more importantly, the unknown boundary conditions at the edges of the platens. This is because material accumulates outside the platen causing an additional variable pressure, which is difficult to predict. This phenomenon particularly affects results when material viscosity is high or when compression speed is low [104].

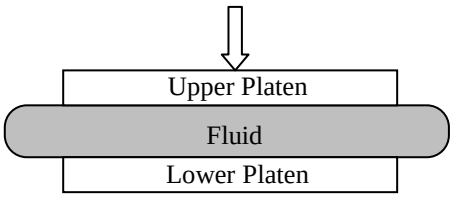

Fig. 1.11: A schematic of constant area squeeze flow rheometry. Note how the platens have smaller radii than the fluid.

4. The last geometry is known as *constant volume* geometry. Here the platens are larger than the sample and the radial interface is free (see Fig. 1.12). The advantages of this geometry are that the stresses (not the shape) at the sample edges are more clearly defined, which minimises additional pressure build-up around the edges. This geometry is also closer to industrial compression moulding processes. The disadvantages are that the sample contact area needs to be calculated or recorded and that the wetting behaviour at the plate/sample/air interface may affect the data.

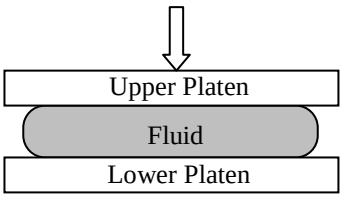

Fig. 1.12: A schematic of constant volume squeeze flow rheometry. Note how the platens have larger radii than the fluid.

From the arguments above it is apparent that it is the constant volume geometry that is most likely to give the most accurate and relevant results, provided that the geometry of the liquid bridge is carefully considered along with surface tension effects. Therefore, in this thesis, it is this geometry that will be used.

1.5.2.2 Inertial Effects in Squeeze Flow

Early work in this field was concerned with Newtonian fluids in creeping flow using the now-classical lubrication approximation [99, 105]. However sample inertia becomes relevant at high plate speeds and complicates the analysis of experimental data considerably. Later works attempted to correct for inertia by using a perturbation method or by solving the Navier-Stokes equations numerically [106]. These methods are inconvenient however and so a first order closed form solution was sought and found by Phan-Thien et al. [107]. It was not until very recently when a full solution for the Navier-Stokes including inertial terms was found by Bell et al. [108]. This solution is very useful not only in that it gives a closed form solution for the inertia but it verified the assumption that inertial effects can be ignored when the Reynolds number is less than unity.

1.5.2.3 Slip Effects in Squeeze Flow

Relative motion between a solid surface and the material in contact with it (wall slip) is a phenomenon observed in many materials such as concentrated suspensions [109]. It disturbs the rheological characterisation by shear rheometry, which is the purpose of squeeze flow. Stokes in 1845 was the first to establish the no-slip condition at solid walls and further theoretical investigations were carried out in the 1930's by Schofield and Mooney. Pearson and Petrie in 1968 showed conclusively that for slip to occur, the molecular size must be greater than the wall roughness scale [110]. The amount of slip therefore depends not only on the roughness of the plate but also on the fluid. Thus if there is evidence of slip, a friction model may be required to separate the characterisation of slip and rheological behaviour. Laun [111] took slip into account by assuming a slip velocity at the boundary comparable to the Mooney analysis for capillary rheometry; similarly Hassager [111] uses a slip coefficient to modify the shear stress boundary condition at the wall. However both the slip velocity and the slip coefficient can only be found empirically.

1.5.2.4 More Complex Constitutive Models

Traditional studies in squeeze flow mainly concentrated on Newtonian fluids due to the ease of analysis. This meant the theory was very limited because only a small number of fluids can be truly described as Newtonian. The first deviation from this trend was by Scott who considered power-law fluids (a type of generalised Newtonian fluid) and began the investigation into more comprehensive models that were valid for a wide range of fluids [112]. These investigations delved into a wide range of materials that were more immediately useful in industry. They included perfectly plastic materials that were of importance in the area of metal forging, viscoplastic materials were investigated by Scott

[112] and Peek [113] who used the lubrication approximation and assumed two yield surfaces within the material. Lipscomb and Denn [114] showed that this method led to kinematic inconsistencies in Bingham fluids leading to further developments [115].

Adams obtained an asymptotic solution for Herschel-Bulkley materials, which are fluids that exhibit a yield stress, and studies into Mooney-type and neo-Hookean (non-linear) elastic materials are numerous [116]. Naturally there have also been considerable investigations into viscoelastic materials. For example, Tanner in 1965 assumed a nonlinear Maxwell model [117], Kramer used another Maxwell model (the Lodge model for rubber-like fluid) [118] and Phan-Thien used a Maxwell model in 1983 [107]. There are of course numerous other examples although these are the most important. Traditionally the flow of viscoelastic fluids has been investigated in three different ways:

1. By assuming that the flow field is not substantially influenced by elasticity and computing the viscoelastic stresses from an integral constitutive model on the basis of the viscous velocity field obtained from a nearly parallel flow approximation [119].
2. By assuming a specific form of the velocity field with or without employing the lubrication approximation where it is assumed the flow is predominately shear [106, 107, 120], which usually leads to a set of PDEs. For example, in case of an upper-convected Maxwell model, Phan-Thien and Tanner [107] obtained five coupled PDEs that they solved by using a perturbation in the Reynolds and Weissenberg numbers.
3. By numerical methods, such as finite elements or boundary elements [121, 122].

However, recently Bell et al. [108] have been able to perform a full analysis of sinusoidal squeeze flow for Maxwell fluids taking inertia into account. This led to a closed form solution for the constant area geometry. It is this method which is the most convenient and will be used in the subsequent analysis upon conversion to the constant volume geometry.

1.5.2.5 Free Surface Boundary Conditions

At the interface between the platens and the sample, the no-slip condition is to be used as discussed previously, but these are not the only boundary conditions that need to be considered. At the free surface (i.e. at the sample/air interface) the boundary conditions are more complicated. In the traditional analysis of Reynolds and Stefan it was assumed that the material filled the space between the platens completely and so had no free surface. This meant that surface tension (see Chapter 4) was effectively ignored. It should be noted however that the material described in such an analysis may still have a free surface outside the flow domain, which may affect the evolution of the stress and velocity profile at the plate edges. In this case, strains and stresses are not uniform throughout the sample and so an assumption about the pressure or normal stress at the edges is usually made (i.e. it is usually assumed that the pressure in the sample at the edge of the platen is equal to atmospheric pressure and so extra stresses are neglected).

If the free surface is contained within the platens, the form of the free surface depends on the axial direction and changes with time. The normal stresses are now equal to the capillary pressure caused by surface tension (see Chapter 4). This means the squeeze flow

velocity/stress profile is a function of the radius of curvature of the profile making it cumbersome to find an exact solution and a free boundary condition is thus rarely used except in some numerical analyses [121-123].

1.5.3 Summary of the Status of Squeeze Flow Theory

It is apparent that in order to develop a theory for squeeze flow that will be consistent for use in a future micro squeeze flow rheometer, an investigation into the effects of constant volume geometry and the edge effects caused by having a free surface will have to be carried out. The effects of slip and inertia will initially be ignored in the current investigation as their effects are easily made negligible through controlled experimentation, i.e. ensuring the amplitude is sufficiently small – see later chapters for details.

1.6 Conclusion

This chapter has shown that microrheometry is of industrial interest. There is a need in several different fields and yet it has been shown that existing technologies do not fulfil all requirements. It has been shown that the theory of squeeze flow, whilst maturing, is still not complete and that further analysis is necessary. It has also been shown that squeeze flow rheometry can be incorporated into a MEMS design. The rest of this thesis will therefore concentrate on the design, fabrication and analysis of a micro squeeze flow rheometer capable of measuring the dynamic shear properties (specifically G' and G") of small volumes of fluid at high frequencies.

1.7 Structure of the Thesis

This thesis comprises nine chapters. Following the conclusions ascertained in this first chapter, chapter two discusses the advantages of micro system technology and the type of actuation that this technology makes possible. This discussion explains why the actuation method used was chosen. Chapter three discusses a simplified overview of the design and principle operation to facilitate the development of the theory in subsequent chapters. The next three chapters each discuss a specific area of theory that needs to be dealt with separately before it is consolidated. Chapter four discusses surface tension theory and the effects of contact angle hysteresis which affects the boundary conditions of the fluid flow. Chapter five then deals with the fluid flow itself and incorporates the viscoelasticity of the fluid. Chapter six combines the effects of the fluid and the mechanics of the rheometer, including the effects of piezoelectricity, induced voltages and other electrical considerations. The fabrication of the rheometer is described in Chapter seven. This is followed by chapter eight which details the various experiments that have taken place and discusses the implications and the conclusions that were drawn from the project. The thesis is then finished off with chapter nine where the conclusion is stated and future work and potential development of the rheometer is discussed.

2 DESIGN OPTIONS

In the preceding chapter, the need for rheology and the methods of measuring viscoelastic properties were discussed. This investigation has led to the conclusion that a micro squeeze flow rheometer capable of measuring the dynamic shear properties (specifically the storage and loss modulus) of small volumes of fluid at high frequencies is required. This specification suggests that micro fabrication techniques as used in microsystems technology (MST) should yield the desired device. This chapter will discuss MST and possible actuation methods for the rheometer that these techniques make possible.

2.1 Microsystems Technology

MST devices (or Micro Electromechanical Systems (MEMS)) are characterised by the integration of multiple devices, usually consisting of sensors, actuators and integrated electronics on a single substrate. This allows for the simultaneous mass-manufacture of complex structures at a lower cost than using conventional technology.

Early developments in this technology were led by the silicon based microelectronics industry with the miniaturisation of transistors in integrated circuits. MEMS technologies emerged out of the fabrication of silicon ICs in the early 1990's. Consequently the majority of MEMS devices are still fabricated out of, or on, silicon wafers using photolithographic processing techniques. The material properties of silicon based materials (crystalline silicon, polycrystalline silicon, silicon nitride etc.) are very attractive to designers and the ability to deposit and pattern metal and polymer layers on them gives a great variety to the devices fabricated using this technology.

One of the fundamental reasons for using MEMS technology to create miniaturised mechanical devices is to take advantage of the associated scaling laws. Whilst the fundamental laws of physics don't change in the micro-domain, their relative influence can change drastically due to scaling. For example, consider two cubes. The first is a 'macro-cube' where each side has a length of 10 units, and the second a 'micro-cube' where each side has a length of 1 unit. While the macro-cube will have a volume of 1000, a surface area of 600 and a surface area to volume ratio of 0.6, the micro-cube will have a volume of 1, a surface area of 6 and therefore a surface area to volume ratio of 6. Therefore we can see that as a device is scaled down, any forces that are related to the surface area of the device, such as surface tension, will have a much greater effect than one that is related to the volume, such as mass. These scaling laws mean that a MEMS device, being smaller than that which can be created using conventional technologies, will have less inertia (allowing it to vibrate at higher frequencies) and generally a higher compliance giving it higher sensitivity to external factors such as pressure.

The use of micro system technology (and the associated scaling laws) allow for fabrication of many different devices in various configurations. There are several methods of actuation made available by considering MEMS technology. Next the main methods of actuation that are most pertinent in the design of a micro squeeze flow rheometer are described. This investigation will reveal what the best method of actuation is and suggest the design of the rheometer.

2.2 Actuation Methods

2.2.1 Electrostatics

One of the most commonly used modes of actuation in micromechanical devices is electrostatic actuation. Here a potential difference is placed between two separate surfaces which results in a build up of charge on the surfaces (see Fig. 1.1). This causes an attractive force to act between the surfaces, therefore if one of the surfaces is free, it will move towards the other.

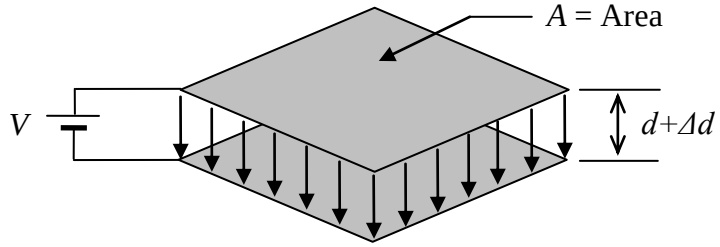

Fig. 2.1: A schematic of a basic parallel plate electrostatic actuator.

In the case of two parallel plates, Coulomb's law defines the force as [124]:

$$F = \frac{1}{2}\varepsilon_0 A\left(\frac{V}{d+\Delta d}\right)^2 \tag{2.1}$$

Here the terms are defined in Fig. 2.1, except ε_0 which is the permittivity of the material between the plates, which is assumed to be air. Simultaneously, a high frequency signal can be applied across the surfaces and used to measure the capacitance and so the gap between the surfaces. This can be challenging however as the static values of capacitance are generally in the pico Farad range while the changes are in the femto Farad range [125]. There are a number of configurations that may be investigated; for example, consider the following designs:

(a)

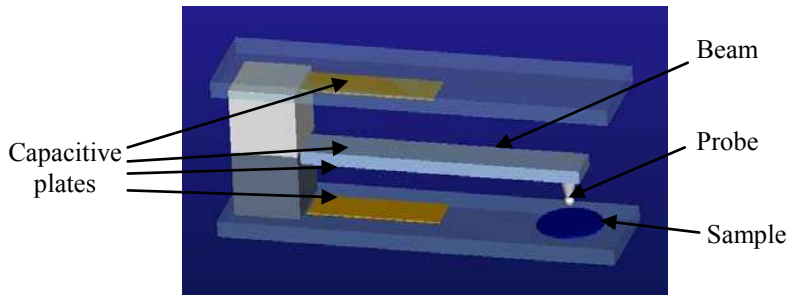

(b)

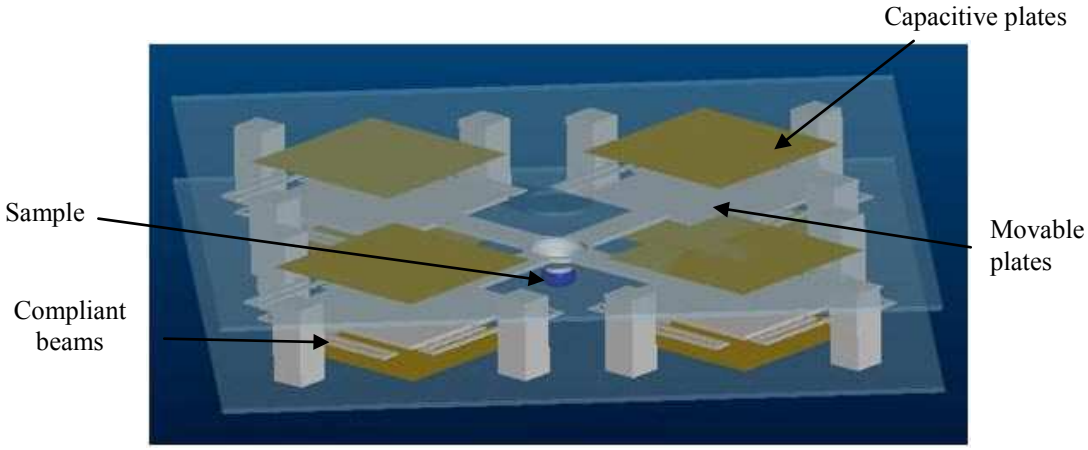

Fig. 2.2: Examples of electrostatically actuated rheometers. (a) Here the rheometer is cantilever based with the sample is the end. (b) This one is actuated using four movable capacitive plates suspended by beams. Here the sample is at the centre.

The device in Fig. 2.2a consists of a compliant beam with a spherical probe at the end. As the electrostatic force is always attractive, when a potential is applied across the lower capacitive plates the beam is pulled down squeezing the sample. There are then two ways to proceed:

1. The potential can be reduced allowing the stiffness of the beam to pull the probe back up. In order for the beam to be able to stretch the sample, it would have to be very stiff.

Therefore, in order to pull the beam down as it squeezes the sample, a very high voltage would need to be applied to the capacitive plates.

2. The cantilever can be actively pulled up by the upper capacitive plates. This would mean the force to stretch the fluid would be supplied by the electrostatic plates rather than the cantilever, but control of the applied voltage of the device will be challenging. This is because it will be necessary to ensure the electrostatic force balances the squeeze flow force of the liquid in such a way as to ensure the displacement of the tip is sinusoidal to get good rheometry data.

Both methods of operation would mean that calculating the force applied to the sample is difficult as the force is actually applied to the cantilever and so will be dependent of the deflection and shape of the cantilever. Similarly, as it is the position of the cantilever that is measured rather than the position of the probe, the evolution in the shape of the cantilever as it oscillates will probably result in inaccurate measurements. For instance, it can be imagined that if the cantilever was being pulled up but the tip was stuck down, the bulk of the cantilever will be close to the sensor giving the impression of having a large gap, when in fact the converse is true. Similarly, if the cantilever was oscillating at a frequency whereupon the mode shape was dominated by the second mode shape, at its peak the sensor will measure large amplitude even though the tip will actually be moving much less than expected.

Fig. 2.2b represents an alternative design based on electrostatic actuation. This design negates the effects of having to apply a force to a compliant beam. Instead the sample is held centrally between four rigid plates suspended by twelve beams. This means that the

electrostatic plates are always parallel simplifying analysis. However in simplifying analysis, the fabrication difficulties are increased. The operation of such a device would also be challenging as the complexity makes it difficult to load the cell.

2.2.2 Magnetomotive Actuation

Magnetomotive actuation is based on the Lorentz force effect. It involves a moveable current-carrying conductor placed within a fixed permanent magnetic field. The magnitude and direction of the force on the conductor is given by the following relationship:

$$\vec{F} = i\int d\vec{l} \times \vec{B} \tag{2.2}$$

where *i* is the current passing through the segment length *dl* of the conductor placed in the magnetic flux density of *B*. This force is independent of the displacement of the conductor (assuming a uniform magnetic field) making the force linear w. r. t. displacement and thus an attractive possibility for a potential design [126].

Sensing using a magnetic transducer is done through the exploitation of electromagnetic induction. The Faraday-Lenz law of induction defines the induced *emf* as:

$$emf = -\frac{d\Phi}{dt} \tag{2.3}$$

where Φ is the magnetic flux passing through a finite area. When a conductor sweeps through an area *A* of magnetic flux density *B*, the emf induced across the sensor is defined by:

$$emf = -\frac{d}{dt}\int \vec{B} \cdot d\vec{A} \tag{2.4}$$

where the negative sign, given by Lenz's Law, indicates that the induced emf opposes the motion that is causing it, and the dot product indicates that it is the area normal to the magnetic field. It should be mentioned that even though magnetic sensing is a possibility, the use of magnetic actuation does not preclude the use of electrostatic sensing.

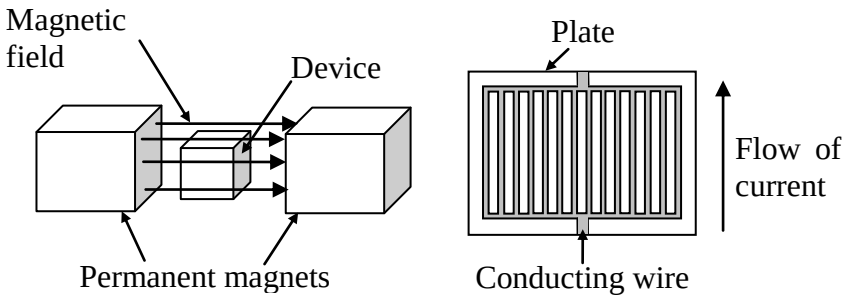

Fig. 2.3: A schematic of a possible magnetically actuated design. Note the plate will actually be horizontal in this design. This means the magnetic field will be parallel to the surface and the resulting force will deflect the plate upwards.

Fig. 2.3 shows a potential magnetically actuated design. Here a compliant structure, such as a fixed-fixed plate, is placed between two permanent magnets such that it experiences a constant magnetic flux. On this plate is deposited a grid of wires constructed so that the current flows in a direction perpendicular to the magnetic flux lines. As shown in eq. 2.2, when an AC current is passed through the wires the plate will be forced to deflect up and down. If there were two platens beneath the plate (one attached to the plate, one to a fixed surface) with a fluid in-between, it can be seen that the fluid would be dynamically squeezed.

The issue with this design is the fabrication of the magnets. While magnets can be deposited directly onto the substrate through sputtering or electroplating, it is not a simple process [127]. Also the magnetic remanence of such magnets is not particularly high (of

the order of 200mT), and so as the magnetic flux density decreases rapidly with distance, the size of the structure becomes limited [128]. This limits the amount of material that can be analysed and makes operation more difficult. Magnets machined from a bulk rare-earth material allow for much larger magnetic flux densities but are incompatible with full integration or batch fabrication [129], although this is a possible method whilst prototyping.

2.2.3 Piezoelectricity

Piezoelectric actuators are based on the piezoelectric effect. For actuation, a voltage is applied to an asymmetric crystal lattice resulting in deformation in a certain direction. For sensing the converse effect is utilised: deformation of the crystal material induces a voltage. The most common implementation of piezoelectric transduction is based upon piezoelectric films in bimorph structures. Piezoelectric actuation can be used to supply very high forces, but the fabrication processes for piezo materials require further development, in particular the deposition of piezo films on silicon substrates is particularly challenging [130]. However, the main advantage of using piezoelectricity is that a single piezoelectric crystal can be used as a sensor and actuator simultaneously greatly simplifying operation and fabrication.

2.3 Proposed Rheometer Design

In the previous section various actuation methods commonly used in MST were discussed. The investigation suggested that piezoelectric transducers can provide the high force and displacements necessary to squeeze a liquid and can simultaneously sense its own

deformation. Therefore it is apparent that piezoelectric actuation should provide the best basis for a microrheometer design. The analysis of the device may not be straight forward due to the coupled constitutive equations for piezoelectric devices, but should be possible. Similarly, the fabrication issues should be surmountable given the large range of appropriate piezoelectric materials available. Therefore, the rest of this thesis will be concerned with the design and analysis of a piezoelectrically actuated microrheometer. The design concept will be covered in detail in the next chapter.

2.4 Conclusion

In this chapter various designs were considered with the intent of discovering one with a high potential of being able to achieve the goals of the project. This analysis has shown that electrostatic devices will likely to be difficult to control and give inaccurate results and magnetic devices are likely to be difficult to manufacture. Therefore it is apparent that a piezoelectrically actuated design has the most advantages.

3. COMPLETE SYSTEM MODEL

This chapter explains the concept behind the design of the micro-rheometer. The basic dynamics and operation of the rheometer and the assumptions used in its analysis are introduced to be dealt with in more depth in subsequent chapters. An example of a typical experiment is also described.

3.1. Specification

There are a number of features that the micro-rheometer should have. The rheometer should be able to:

- Squeeze a drop of viscoelastic fluid.
- Oscillate at frequencies greater than 100Hz.
- Accommodate nanolitre volumes of fluid.
- Produce an output signal related to the properties of the fluid.
- Be fabricated using current MEMS technology in a cost-effective manner.
- Measure storage and loss moduli in the range of 0-1000000 Pa.

3.2. Design

The device must be capable of supplying a large force (~100N) over a small distance (~10nm) to manipulate small volumes of stiff/viscous liquids and will need to have a sensor integrated into the device to monitor its response. Also, the flow profile inside the fluid needs to be simple in order to allow the analysis to be meaningful. This can be achieved by squeezing the fluid axially between two parallel platens (see Fig. 3.1). A number of methods designed to squeeze the fluid (for example electrostatic actuation)

were investigated, but practicalities meant that these methods were unsuitable (see Chapter 2 for details).

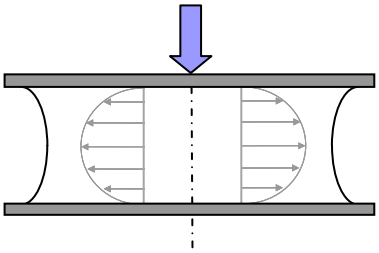

Fig. 3.1: Axial squeezing of the fluid as opposed to squeezing it between spheres or at an angle. The horizontal arrows indictate velocity profile.

In the end, a piezoelectrically actuated device was chosen as not only does it supply the necessary force and displacements, but it also allows for the easy integration of the sensor. This is because the reverse piezoelectric effect can now be utilised to monitor the response. The device comprises of a disc of piezoelectric material bonded onto a thin silicon membrane (see Fig. 3.2).

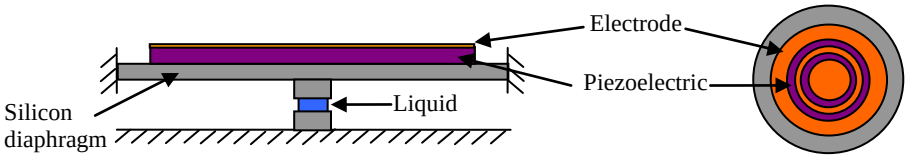

Fig. 3.2: Schematic of the MEMS device showing both profile and bird eye views.

The piezoelectric material is orientated in such a way as to cause it to expand radially when a voltage is applied across it. This causes the silicon membrane to distort and deflect, thus moving the platen up and down as the voltage changes. This movement imposes a force onto the fluid thus squeezing it. If the fluid is removed, applying a voltage to the piezoelectric material induces a particular strain field within it. This in turn induces a voltage in the areas where the input voltage is not being applied in the piezoelectric

material. This gives us a measure pertaining to a specific deflection of the membrane. When the fluid is replaced it resists this deflection and the strain field is altered, and a different voltage is induced. Therefore if the change in the induced voltage is measured, we are able to calculate the force resisting the deflection. Since the resisting force is a function of the fluid's properties, so the induced voltage is also a function of the fluid's properties.

3.3. Dynamic model

The full mechanics of the MEMS device is quite complex. However it will be shown that the system can be approximated (in the limit of small amplitudes) by a simple lumped mass system (see Fig. 3.3). This facilitates the analysis of the device and in turn the measuring of the fluid's properties.

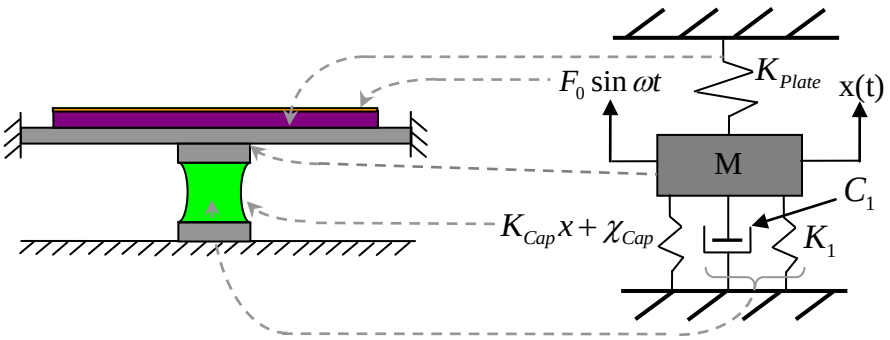

Fig. 3.3: A schematic of the rheometer (not to scale) and a lumped-mass representation. Arrows indicate what part of the rheometer is being represented by each part of the dynamic model.

From Newton's second law we can write the equations of motion for the mass as shown in eq. 3.1. Here we represent the piezoelectric material, the upper platen and the membrane as a mass (M) on a spring (K_{Plate}). The applied voltage is represented as an equivalent

sinusoidal force ($F_0 sin\omega t$). The viscoelastic forces are represented as a spring and dashpot (K_1 and C_1 respectively). The inertia of the fluid is neglected as it only becomes significant at very high frequencies – see section 5.8 for details. The capillary force due to surface tension is also represented by a spring (a modified spring with an additional constant – $K_{Cap}x + \chi_{Cap}$).

$$M\frac{d^2x(t)}{dt^2} = F_{Applied} - \left(F_{Viscous} + F_{Elastic} + F_{Capillary} + F_{Stiffness}\right) \tag{3.1}$$

To simplify analysis it will be assumed that the 'spring' forces are directly proportional to the displacement of the mass and that the 'dashpot' forces are directly proportional to the velocity of the mass. These assumptions will be validated and the pertinent constants will be determined in the subsequent chapters and mean that the device's dynamics can be modelled as a simple linear differential equation as given in eq. 3.2:

$$M\frac{d^2x}{dt^2} + C_1\frac{dx}{dt} + K_1x + K_{Plate}x - K_{Cap}x + \chi_{Cap} = F_0\sin\omega t \tag{3.2}$$

The solution of eq. 3.2 is given in eq. 3.3:

$$x(t) = \sqrt{\frac{F_0^2}{(B^2 + \omega^2 C_1^2)}}\sin\left(\omega t + \tan^{-1}\left(\frac{\omega C_1}{B}\right)\right) - \frac{\chi_{Cap}}{K_{Plate} - K_{Cap}} \tag{3.3}$$

Where:

$$B = -\omega^2 M + K_1 + K_{Plate} - K_{Cap} \tag{3.4}$$

From eq. 3.3 it can be seen that the amplitude (ε) and phase (φ) of the response can be shown to be:

$$\varepsilon = \sqrt{\frac{F_0^2}{(B^2 + \omega^2 C_1^{\,2})}} \tag{3.5}$$

$$\varphi = \tan^{-1}\left(\frac{\omega C_1}{B}\right) \tag{3.6}$$

By equating the in-phase components and out-of-phase components of eq. 3.3, the dynamic properties of the liquid are then given as:

$$G' = \frac{2\bar{h}^3\left(\frac{F_0}{\varepsilon}\cos\varphi + \omega^2 m - K_{Plate} + K_{Cap}\right)}{3\pi\bar{R}^4} \tag{3.7}$$

$$G'' = \frac{2\bar{h}^3 F_0 \sin\varphi}{3\pi\varepsilon\bar{R}^4} \tag{3.8}$$

Where $\bar{h}$ and $\bar{R}$ are the fluid's mean height and radius. *G'* and *G''* are the fluid's storage and loss moduli respectively. These properties are a function of the fluid's viscosity and elastic shear moduli and so characterise the fluid.

We do not measure the amplitude and the phase of the response directly but rather the amplitude and phase of the induced voltage. We know that the induced voltage is a function of the applied voltage and the resisting force. Therefore at a given instant of time we can calculate the magnitude of the force necessary to induce the output voltage measured at that instant. From the phase of the output voltage we can calculate the phase of the resisting force and in turn the phase of the response as used in eqs. 3.7 and 3.8. Knowing the functions of the input voltage and the resisting force, we can then calculate the amplitude of the response again used in eqs. 3.7 and 3.8 and so calculate the dynamic properties of the fluid.

3.4. Device Parameters

To further clarify what will happen during the use of the rheometer, a typical experiment will be described here. First a description of the rheometer:

- The silicon diaphragm
    - The diaphragm is made out of single crystal silicon and has a low resistivity (~0.001Ωcm) and also acts as the ground electrode for the piezoelectric material.
    - The diaphragm has a radius of 11.5mm and is 50μm thick. This is large to ensure it has a low stiffness and because the quartz disc has a diameter of 10mm and 100μm thick which is a commercially available size.
- The piezoelectric material
    - This is made out of X-cut quartz
    - It has been cut into a disc with a 10mm diameter and 100μm thickness.
    - It is assumed that it has a Young's modulus of 40.14GPa, Poisson's ratio of 0.33 (see Appendix A for details) and a piezoelectric coupling coefficient (d_{11}) of -2.3×10^{-12} C/N.
- The electrodes
    - The electrodes comprise of a 10nm e-beam evaporated layer of titanium (for adhesion) under a 200nm layer of thermally evaporated gold.
    - The electrodes have been deposited onto the quartz in five concentric circles:
        - The inner electrode is an active electrode in that the input voltage will be directly applied to it. It is a circle of radius 3mm.

    - The second electrode is a ground electrode to shield the sensing electrode from the applied electric field. It will be an annulus of inner radius 3.25mm and outer radius 3.75mm.
    - The third electrode is the sensing electrode. It is an annulus of inner radius 4mm and outer radius 6mm.
    - The fourth electrode is another ground electrode. It is an annulus with inner radius 6.25mm and outer radius 6.75mm.
    - The last electrode is another active electrode. It is an annulus of inner radius 7mm and outer radius 10mm.
- The platens have a radius of 250μm and have been coated with a fluorinated polymer so that the fluid will form a sessile drop upon depositing and not flow off the platen. The initial gap between the platens is 20 μm.
- The test sample is polydimethylsiloxane (PDMS). It is a linear Maxwell fluid and has a dynamic viscosity of 29.25 Pas, a density of 975 kgm^{-3}, shear modulus of 15 kPa and surface tension 20.5mNm^{-1}. The PDMS has a static contact angle of 40° on the fluorinated platens, a receding contact angle of 35° and an advancing contact angle of 83°.

3.5. A Typical Experiment

Now the parameters and the design of the device are known, the information will be used to explain what will happen during a typical experiment. Placing a drop of PDMS onto the lower platen causes it to form a spherical cap with the same radius as the platen. When the upper platen is brought into contact with the drop during the assembly of the device, there will not be enough space for this much liquid and the excess will be forced off the platen,

so the actual volume of liquid in the bridge will be 3.7 nL. The static capillary force pulls down the membrane so that the static liquid bridge height will be 19.6 μm.

A voltage with magnitude 50 V and frequency 50 Hz is applied to the active electrodes. This is equivalent to applying a sinusoidal force, F_0, with magnitude 0.55 mN with the same frequency. The membrane and quartz has a combined stiffness of 5252 Nm^{-1} which would mean that if the device was run without any liquid in it, the amplitude of the response would be approximately 105 nm. With the fluid in the rheometer, the amplitude of the response is reduced and shifted by a phase angle (see Fig. 3.4). At this frequency the fluid's storage modulus should be 4 kPa and its loss modulus should be 6.7 kPa and so the amplitude of the response will be 58nm with a phase difference of 0.69 rad.

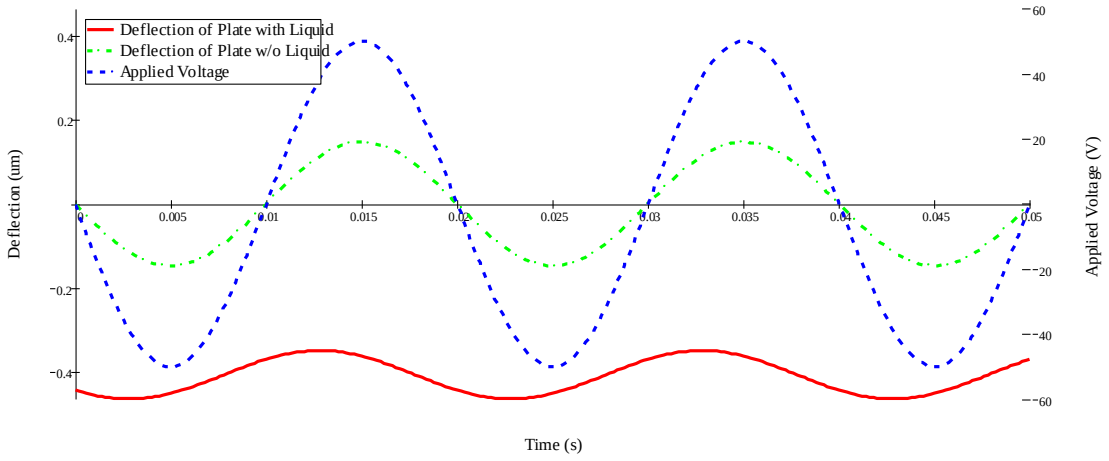

Fig. 3.4: The simulated mechanical response of the rheometer with and without liquid.

Again the mechanical response is not measured directly, only the induced voltage. This can be seen in Fig. 3.5.

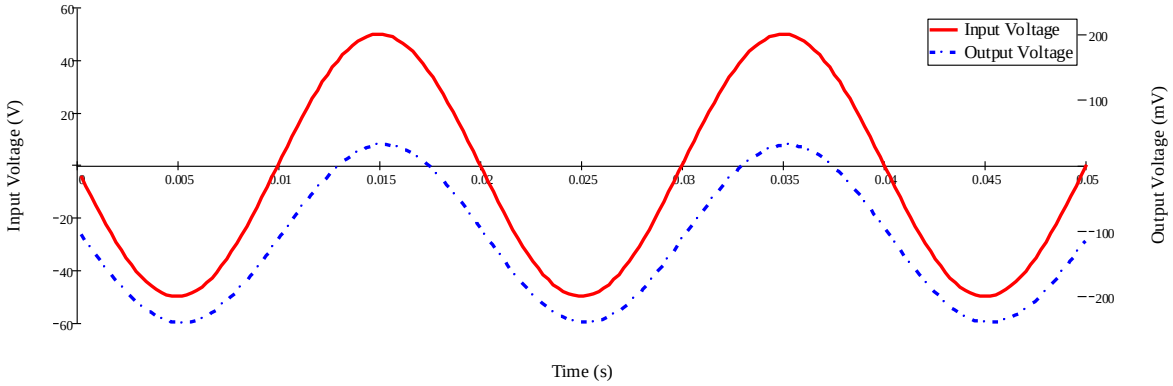

Fig. 3.5: The simulated electrical output of the rheometer.

The output voltage has an amplitude (A_{Vout}) of 136 mV and a phase (β) of 0.073 rad. As the applied force is known, this new information can be used to calculate the total resisting force, P_0, due to the fluid. This is done by using the input voltage at the instant that the output voltage is at a maximum, and calculating the induced voltages for a range of applied forces (see Fig. 3.6). When the calculated induced voltage equals the maximum measured induced voltage, the resisting force is found.

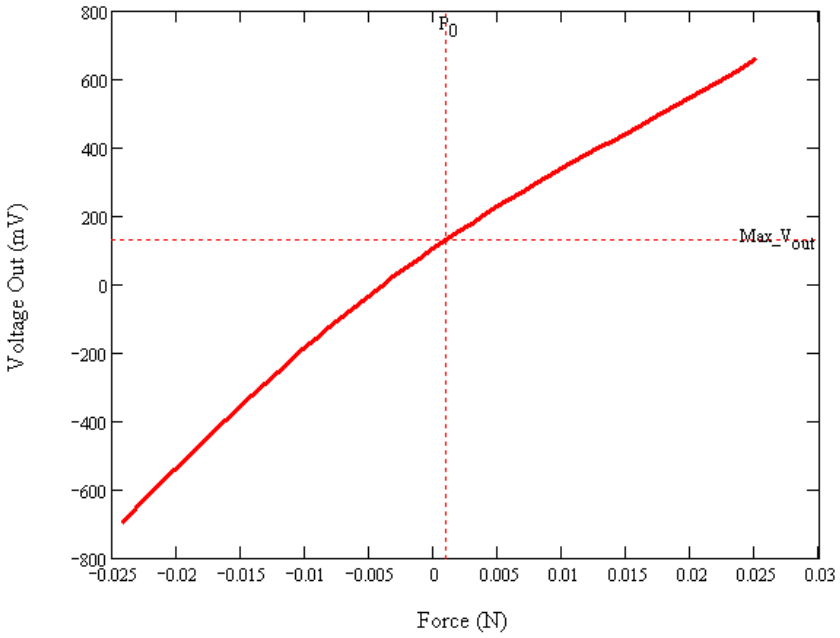

Fig. 3.6: Graph depicting the simulated induced voltage as a function of applied force for a given input voltage – see Chapter 6 for details.

Using this value, the magnitude and the phase of the output voltage gives the phase, α, of the resisting force as seen in eq. 3.9.

$$\alpha = \sin^{-1}\left(\frac{A_{Vout}\sin\beta}{4.85\times10^{9}t_q\left(\frac{DP_0}{4\pi}\right)}\right) \tag{3.9}$$

Where t_q is the thickness of the quartz and D is a constant pertaining to the material properties of the membrane and quartz (see Chapter 6). This value can then be used to calculate the phase of the response (i.e. φ as used in eq. 3.7 and 3.8) using eq. 3.10.

$$\varphi = \tan^{-1}\left(\frac{P_0\sin\alpha}{F_0 + P_0\cos\alpha}\right) \tag{3.10}$$

The input voltage and the resisting force in now completely known and so the deflection of the membrane can be found. Therefore the storage and loss modulus can be calculated.

3.6. Flow diagram of solution

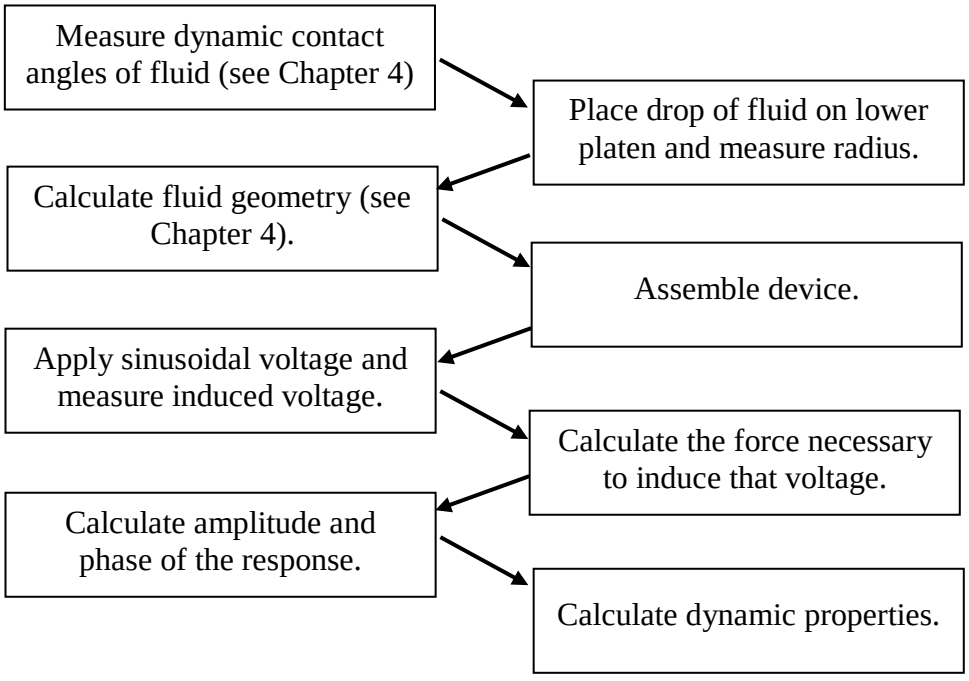

3.7. Capabilities of the Rheometer

It is now known that the voltage induced during the operation of the rheometer is related to the properties of the fluid. The issue now is given the phase and magnitude of the induced voltage, are the calculated storage and loss moduli unique or is there some other combination of storage and loss moduli that can cause the same voltage signal to be induced? This will of course mean that there will be ambiguities in any results obtained rendering them useless. Fortunately this is not the case. Let us assume the rheometer is being operated with a sinusoidal voltage of 50V at 50Hz. If a range of fluids with different storage and loss moduli are put into the rheometer, it can be seen in Figs. 3.7 and 3.8 that there is not an instance where both the phase and amplitude of the induced voltage are the same for two fluids until we reach very high viscosity levels.

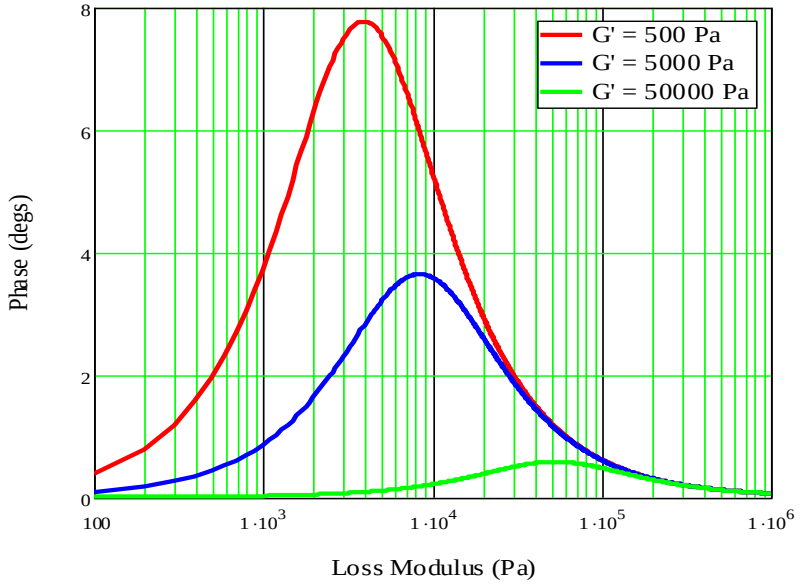

Fig. 3.7: Graph depicting the phase of the induced voltage for fluids with a range of storage and loss moduli.

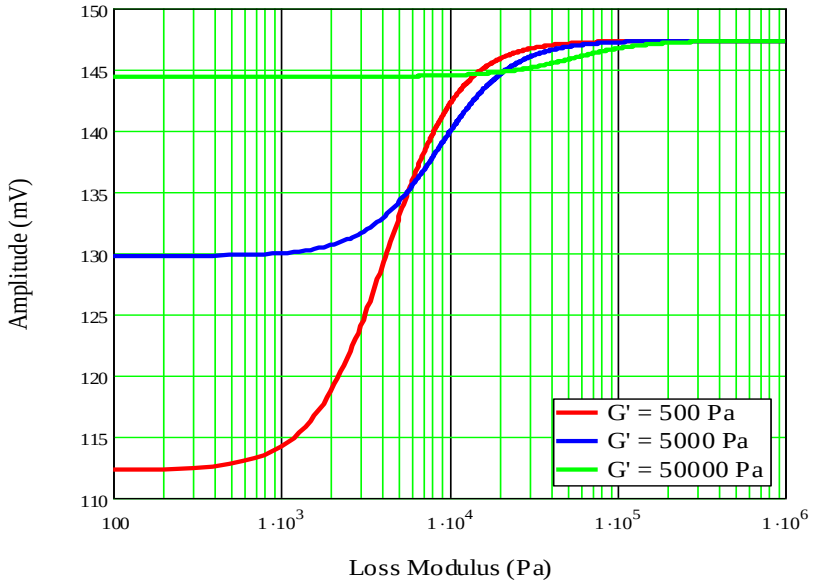

Fig. 3.8: Graph depicting the magnitude of the induced voltage for fluids with a range of storage and loss moduli.

Looking at the mechanical response of the rheometer under the influence of these fluids it can be seen why the rheometers capabilities are limited. In Fig. 3.9 it can be seen that the response of the rheometer is dominated by viscous forces for fluids with high loss moduli, as denoted by the response having a phase difference of 90°. The phase cannot go beyond 90° and therefore will not change if a fluid with a higher loss modulus is put into the rheometer. Similarly, it can be seen in Fig. 3.10 that the magnitude of the response tends to zero if the fluid is particularly viscous/stiff. This is of course, because a much larger force is needed to squeeze these fluids any appreciable distance. The result of this again means that any further increase in viscosity will not be measured.

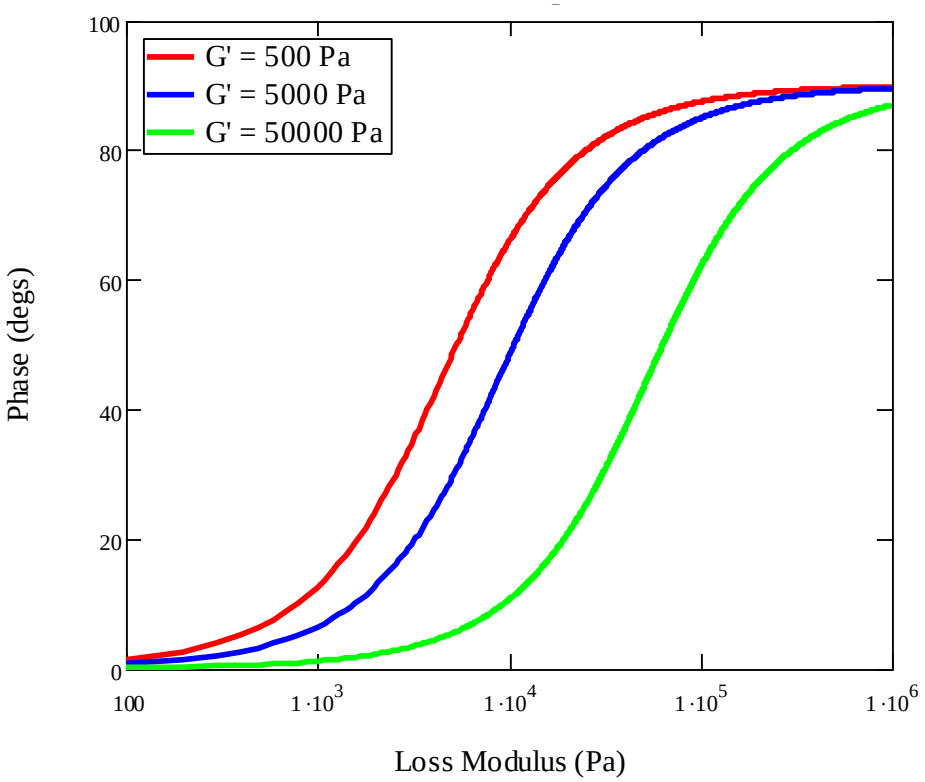

Fig. 3.9: Graph depicting the phase of the response for fluids with a range of storage and loss moduli.

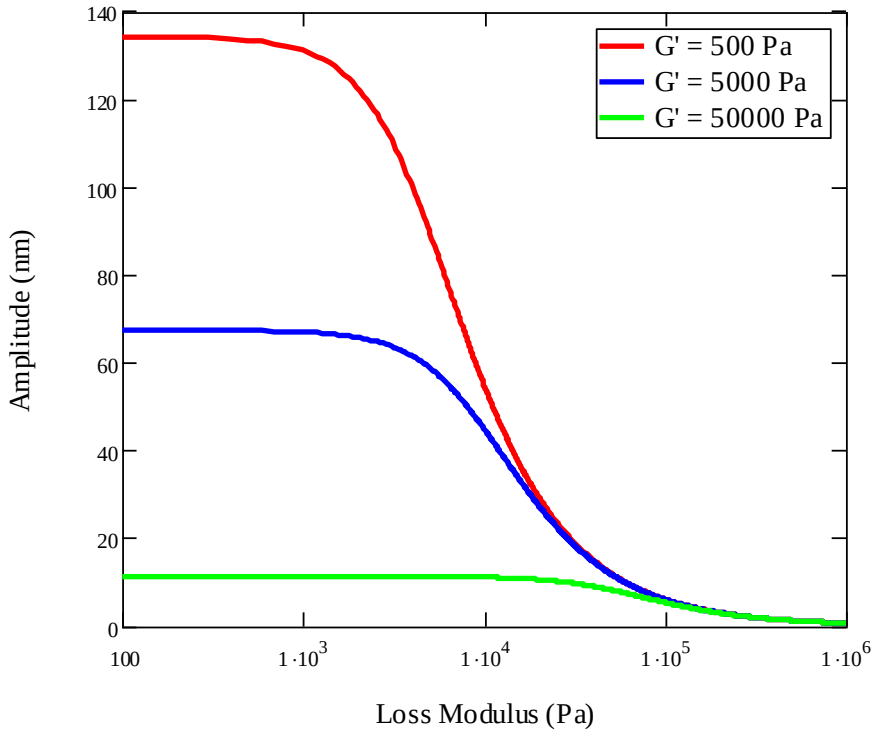

Fig. 3.10: Graph depicting the magnitude of the response for fluids with a range of storage and loss moduli.

3.8. Conclusion

In this chapter, a MEMS device comprised of a quartz disc bonded onto a silicon membrane and modelled as a lumped mass system is described with the intent to use it to measure the dynamic properties of a fluid. The details of the physics behind the device and the assumptions made are now fully developed and explained below. The analysis in the subsequent chapters will produce the constants used in the model.

4. CAPILLARY EFFECTS

In this chapter the effect of capillary (or surface tension) forces is discussed. The importance of surface tension in terms of the associated phenomena such as contact angle hysteresis, wetting etc. are investigated. A closed form description of all the relevant geometries and forces is derived. The theory is then linearised for inclusion into the equation of motion as discussed in the previous chapter.

4.1. Surface Tension

Surface tension is a phenomenon caused when two immiscible substances meet. As the name implies, surface tension is a measure of the force required to increase the area of the surface of a substance. This tension is due to the imbalance of forces that act on individual molecules that reside at the surface. As the surface on the micro-scale is in constant thermal flux with molecules from both substances diffusing into the other, the surface tension that is actually measured is a statistical mean of all the forces averaged over a sufficiently long time.

There are in fact many forces that act on a molecule whether it is near a surface or not. These include London dispersion forces, hydrogen bonds, dipole-dipole interactions, dipole-induced dipole interactions, π-bonds, donor-acceptor bonds, and electrostatic interactions [131] and may include others. How these forces interact with the molecules and each other is complex and not completely understood. This is because they depend very much on the substances under investigation and so many conclusions are based on empirical relationships [132]. Nevertheless, we can ignore the individual contribution of

all these forces and simply consider the total effect in order to get a sensible picture of what is going on.

Fig. 4.1 shows a diagram of the forces acting on particles in a fluid near a fluid/vapour interface. The interactions on a molecule in the liquid sufficiently away from the surface are balanced on all sides by equal forces acting in all directions. Molecules situated on the surface of the liquid experience an imbalance of forces. This is because the vapour is less dense, and so fewer molecules on the vapour side of the surface will exert forces on the molecules in the fluid. The result of this imbalance is the presence of free energy at the surface. The excess energy is known as surface free energy when measured as energy per unit area but known as surface tension (or line tension) when measured as force per unit length [133]. This excess energy always exists at the interface between two separate mediums (such as liquid and vapour, liquid-liquid, liquid-solid and solid-vapour).

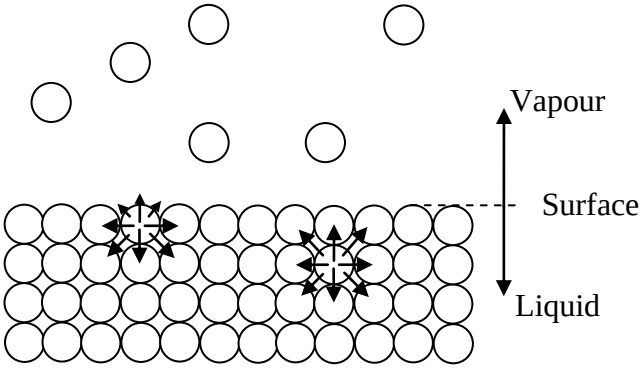

Fig. 4.1: A schematic of the vapour-liquid interface. The size of the arrows on the particles denotes the relative size of the forces acting on them.

As the molecules at the surface have unbalanced forces acting on them, they are attracted inwards towards the bulk of the liquid. This action (which is eventually balanced by the resistance of the liquid to compression) causes the surface area of the liquid to be

minimised. Increasing the surface area increases the number of molecules at the surface. This in turn increases the free energy of the system, which acts like a force resisting the increase in surface area.

This phenomenon is important in the context of this thesis because the liquid is constrained by surface tension (or capillary) forces and therefore exerts an additional force on the rheometer. It is also important to know how this force varies throughout the operation of the rheometer as it determines the geometry of the liquid bridge and affects the response of the rheometer.

4.2. Contact Angles

The level of complexity increases when this liquid/vapour interface meets a solid surface (this point is known as the contact line) as seen in Fig. 4.2. The geometry of the interface is determined by considering the thermodynamic equilibrium condition at this point. Essentially at equilibrium, the potential energy of the three phases should be equal [133]. This condition is characterised by the Young equation and is given as:

$$\gamma_{SV} = \gamma_{SL} + \gamma_{LV} \cos\theta \tag{4.1}$$

This equation can be better understood if one resolves the surface tension forces per unit length in the horizontal direction (see Fig. 4.2).

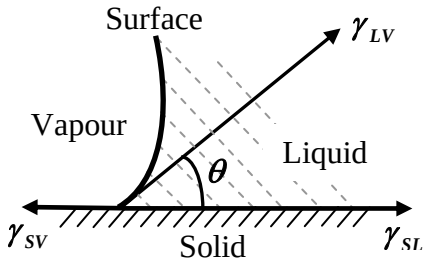

Fig. 4.2: A schematic of the three-phase contact line where the vapour, liquid and the solid surface meet. Note how the contact is characterised by a contact angle.

This contact angle in part describes the geometry of the liquid bridge and also describes the spreadability of the fluid, or the ability of the fluid to wet the solid surface. This spreadability depends on the relative magnitudes of the various surface energies (as denoted by the contact angle – see Fig. 4.2). If the contact angle is large, the fluid will form a compact droplet on the surface (see Fig. 4.3a). Conversely if the contact angle is small, the fluid will spread to cover a large area of the solid i.e. it has high spreadability (see Fig. 4.3b).

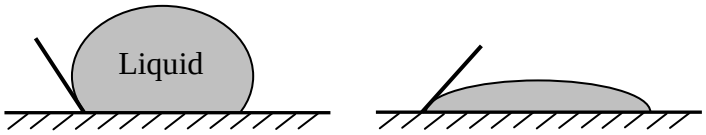

Fig. 4.3: A schematic of how contact angles can be used to describe spreadability. (a) The liquid has a high contact angle and forms a sessile drop on the surface. (b) The liquid has a low contact angle and spreads across the solid.

4.3. Contact Angle Hysteresis

This definition of the contact angle only works under static equilibrium conditions. When the contact line is in motion, such as when the liquid in the bulk phase is flowing, as in

during squeeze flow, different mechanics apply. Many aspects of this dynamic wetting are poorly understood and the subject is of great scientific interest [134]. What is known is that when the contact line moves due to flow within the bulk of the liquid, hysteresis is observed in the contact angle. It is shown in [135] that as the contact line moves towards the vapour; the contact angle will become larger than the equilibrium angle; this is known as the advancing contact angle. Similarly, the contact angle will decrease if the contact line contracts (this is known as a receding contact angle).

It has been found that the contact line does not move smoothly, but instead pins and slips [135]. This is because there is a transition period as the contact angle varies between its advancing and receding state. In the context of the rheometer, this contact line will undergo four stages of motion:

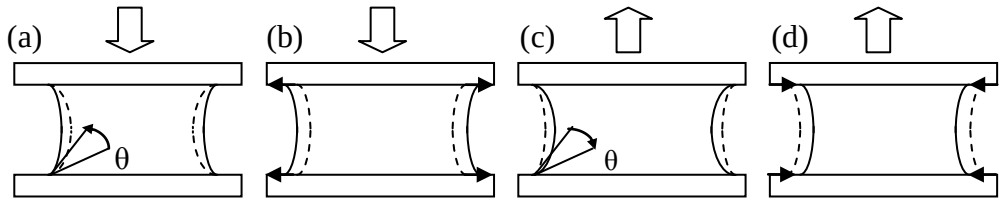

Fig. 4.4: A schematic of the four stages of contact line motion during contact angle hysteresis.

1) When the platen moves downwards and the gap decreases, initially the contact line remains stationary until the contact angle equals the advancing contact angle (see Fig. 4.4a). This is known as pinning.

2) If the gap decreases further, the contact angle remains at the advancing angle and the contact line expands (see Fig. 4.4b). This is known as slipping.

3) When the gap increases, the contact angle first decreases while the contact line remains still (pins - see Fig. 4.4c).

4) When the contact angle reaches the receding angle, provided the gap is still increasing, it will remain at that angle while the contact line declines (slips - see Fig. 4.4d). And so on.

4.4. The No-slip Condition

It may seem as if a contradiction is being caused by the moving contact line. When dealing with viscous fluid flow, it is assumed that the fluid in contact with the solid surface does not move - the no-slip condition. The moving contact line seems to induce infinite shear stresses within the fluid. This of course is not the case.

In reality the fluid flows towards the contact line from the bulk of the fluid and not along the solid surface [136]. This means the actual fluid flow in the vicinity of the contact line is very complicated and it is not a trivial matter to treat the effect of the surface consistently [137-138]. However, one of the assumptions that are prevalent in this thesis is that the gap to neck radius ratio of the fluid is very small (see Fig. 4.5).

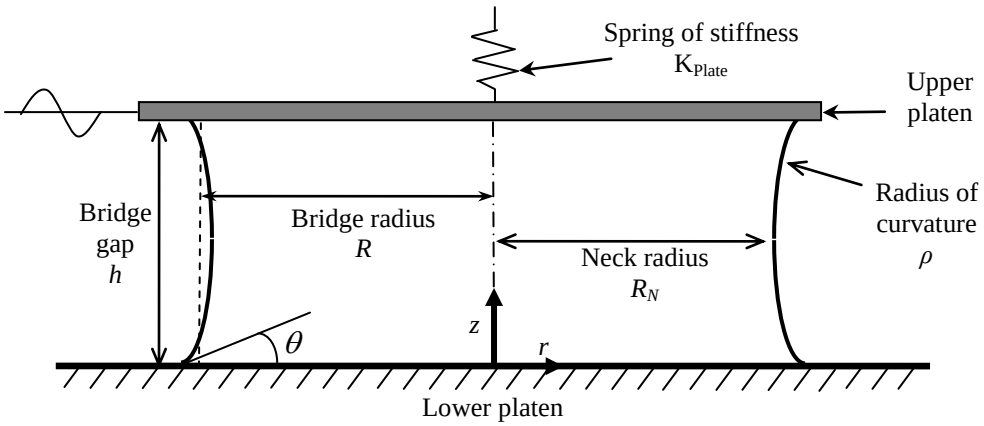

Fig. 4.5: A schematic of the geometry of the liquid bridge.

This means that the vast majority of the flow is unaffected by the presence of the surface. Therefore the fluid flow and surface are treated independently and their contributions are combined only in the equations of motion in Chapter 3. The only deviation from this rule is that the geometry used to define the fluid flow is determined by consideration of the surface tension forces.

4.5. Modification of Surface Chemistry

It was shown in the previous chapter that in order to permit analysis, the liquid must form a liquid bridge between the platens (see Fig. 3.1). It was also stated that the platens were made from silicon and the test fluid was PDMS (polydimethylsiloxane). Normally this would not be possible (especially for low viscosity PDMS) as the PDMS wets silicon perfectly and the surface tension would cause the PDMS to flow off the platen completely, preventing a bridge from being formed. To prevent this, the platens were coated with plasma polymerised octofluorocyclobutane, hereafter referred as C_4F_8. C_4F_8 has the advantage of being a fluorinated polymer with wetting properties similar to Teflon®.

Therefore, as will be confirmed in Chapter 8, PDMS forms a finite contact angle with C_4F_8 and will form a liquid bridge inside the rheometer.

Another reason to use C_4F_8 is that the plasma polymerisation of gaseous octafluorocyclobutane (C_4F_8) to yield C_4F_8 films is frequently used in the manufacture of MEMS devices during the DRIE process as described in full in Chapter 7. This process allows deep features and structures with high aspect ratios to be etched into silicon using a method known as the Bosch process. The DRIE process utilises inductively coupled power (ICP) technology to create a plasma that enhances the etch rate and also improves the passivation of the process. During the passivation step, C_4F_8 is deposited using plasma-enhanced chemical vapour deposition (PECVD), which uses electrical energy to generate the plasma, with gaseous C_4F_8 being converted into reactive radicals, ions and neutral molecules. Instead of the plasma colliding and reacting with and etching the substrate surface, the interactions occur in the gas phase resulting in the deposition of polymerised C_4F_8 onto the substrate surface. Under such conditions, film formation occurs at relatively low temperatures whilst providing strong adhesion, low pinhole density, effective step coverage and high surface uniformity. This makes it convenient to use C_4F_8 to coat the microrheometer platens and change their surface chemistry.

4.6. The Young-Laplace Equation

Surface tension acts to minimise the surface area of an interface. This minimisation of the surface area using the Euler-Lagrange equation leads to the Young-Laplace equation [133]. This equation describes the pressure difference across the interface between two

fluids due to surface tension and the curvature of the surface (see eq. 4.2) – refer to Fig. 4.5 for definition of terms.

$$\Delta P = \gamma_{LV} \cdot \left(\frac{1}{R_N} + \frac{1}{\rho} \right) \tag{4.2}$$

We then use this pressure difference to calculate the force that will act on the rheometer due to surface tension (see Fig. 4.6).

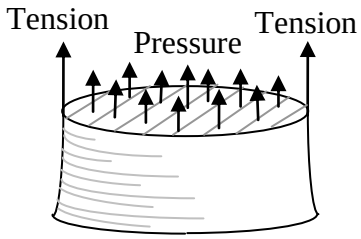

Fig. 4.6: A schematic of the lower half of the liquid bridge. The arrows at the edge indicate the forces due to the tension at the liquid-vapour interface and the arrows in the centre represent the force due to the pressure difference.

Surface tension forces acting on the rheometer as defined at the neck plane can be given as:

$$F_{Capillary} = 2\pi R_N \gamma_{LV} - \pi {R_N}^2 \gamma_{LV} \cdot \left(\frac{1}{R_N} - \frac{1}{\rho} \right) \tag{4.3}$$

It is easy to see that this equation is the sum of the tension acting on the surface, denoted by surface tension multiplied by the circumference of the liquid bridge, and the resultant pressure difference acting on the cross-sectional area.

It is assumed that the capillary forces are in equilibrium; therefore all the forces acting at one point in the liquid bridge should equal the forces acting on another point. This means

we can choose where we resolve the forces, and for convenience we resolve the forces at the neck (the plane of symmetry) of the liquid bridge (see Fig. 4.5).

Eq. 4.2 cannot be solved analytically except in a few special circumstances, such as planar and cylindrical geometries [139]. It is now common practice to use numerical methods to find the solution [140]. The numerical solution used in this thesis is similar to that used in [140]. As we are dealing with an axisymmetric problem, the Young-Laplace equation is first non-dimensionalised by dividing all the relevant gaps and radii by eq. 4.4 and rephrased into the form as given in eq. 4.5.

$$x_C = \sqrt[3]{Vol} \tag{4.4}$$

$$\frac{\Delta P x_C}{2\gamma_{LV}} = H^* = \frac{\frac{d^2R}{dZ^2}}{\left(1+\frac{dR}{dZ}^2\right)^{3/2}} + \frac{1}{R\left(1+\frac{dR}{dZ}^2\right)^{1/2}} \tag{4.5}$$

The solution of this equation gives the profile of the liquid bridge which can be approximated by a truncated Taylor series:

$$R_{i+1} \simeq R_i + (Z_{i+1} - Z_i)\frac{dR}{dZ}_i + \frac{1}{2}(Z_{i+1} - Z_i)^2 \frac{d^2R}{dZ^2}_i \qquad i = 0,1,2,... \tag{4.6}$$

Eq. 4.5 can be integrated to give:

$$\frac{R}{\left(1+\frac{dR}{dZ}^2\right)^{1/2}} + H^* R^2 = C \tag{4.7}$$

Where:

$$C = R_C \sin\theta + H^* R_C \tag{4.8}$$

where R_C is the dimensionless contact radius. Therefore the first and second differential as used in eq. 4.6 can be given as:

$$\frac{dR}{dZ_i} = \sqrt{\left(\frac{R_i}{C - H^* R_i^2}\right)^2 - 1} \tag{4.9}$$

$$\frac{d^2R}{dZ^2{}_i} = \frac{1 + \frac{dR^2}{dZ_i}}{R_i} + 2H^* \left(1 + \frac{dR^2}{dZ_i}\right)^{3/2} \tag{4.10}$$

Given the following boundary conditions (R_0,R_n), Eq. 4.6 can be solved::

$$R_0 = \begin{cases} C & if \quad H^* = 0 \\ \dfrac{-1 + \sqrt{1 + 4H^* C}}{2H^*} & if \quad H^* \neq 0 \end{cases} \tag{4.11}$$

$$R_n = R_C \tag{4.12}$$

$$\frac{dR}{dZ_n} = \cot\theta \tag{4.13}$$

However it can be seen that in the solution of eq. 4.6 a choice of curvature, and contact line radius has to be made as these are unknown. Therefore to get the correct solution it is required that the resultant volume of the liquid bridge is met. The method used to find the geometry of the bridge is to calculate the volume of the bridge for a range of curvatures for each contact line radius or contact angle. Given this range of possible solutions, we interpolate to find the correct curvature. This in turn defines the gap. Therefore, if the

procedure is repeated for each contact line radius we obtain the geometry of the liquid bridge for a range of gaps (see Fig. 4.7).

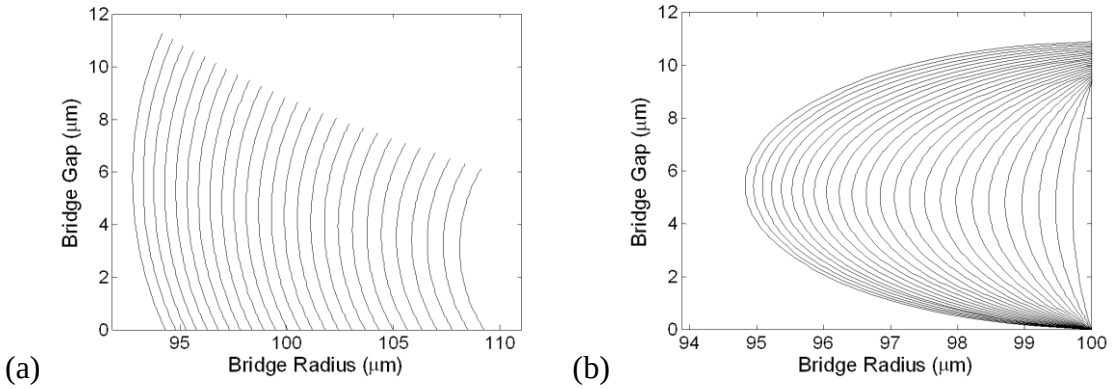

Fig. 4.7: How the geometry of a typical liquid bridge varies with the gap as given by eq. 4.6. (a) The contact angle is constant; (b) the contact angle varies.

Given the geometry for a range of gaps means the curvature and neck radius is known, allowing the solution of eq. 4.3 (see Fig. 4.8).

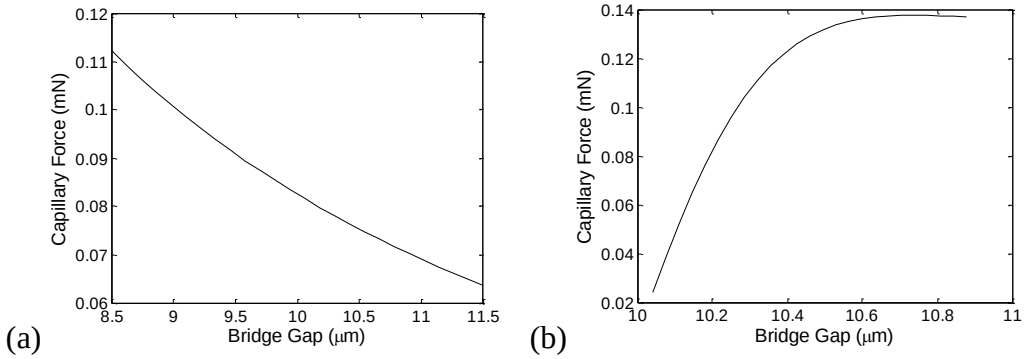

Fig. 4.8: How the capillary force varies with the gap as given by eq. 4.3. (a) The contact angle is constant; (b) the contact angle varies.

This solution is the exact solution for eq. 4.3. However, it is not in a convenient form for use in the dynamic equation eq. 3.2. Its use would mean having to run a program prior to each use of the rheometer which is inconvenient. It is useful however in that it serves as a

check for any subsequent calculations but it is apparent that a closed form solution will be of much more use.

4.7. Toroidal Approximation

A few closed form solutions exist. These include the gorge approximation [140], a parabolic approximation [141] and the toroidal approximation [142]. Because the parabolic approximation requires direct physical measurement of the liquid bridge (which is impractical in this case) and the gorge method leads to high inaccuracies [140], it is decided that the toroidal approximation is the best option. It can be shown that this method is applicable because if we consider the curves shown in Fig. 4.7 and superimpose a circular arc on top, we can easily see that the arc is a good approximation to the exact solution:

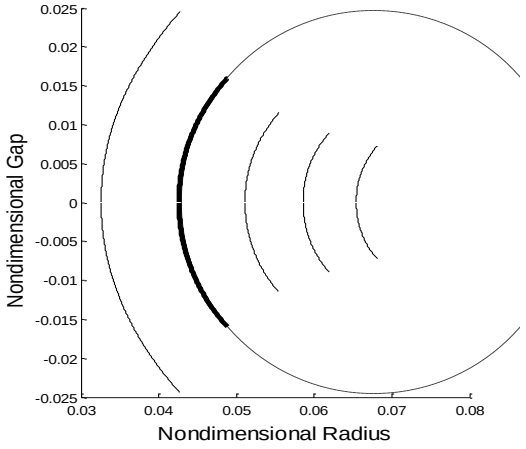

Fig. 4.9: A comparison between the geometry of the bridge as given by eq. 4.6 (solid lines) and a circular arc (dashed line).

We can also check that this assumption is valid. If we take a sample video capture of a liquid bridge (see Fig. 4.10) we can see that the circular arc is indeed a good approximation to the actual geometry of the bridge. It is necessary to remember however

that the geometry is not actually a circular arc. In order for the geometry to be valid, the curvature has to be constant at all points on the surface of the bridge. This is not true of circular arc geometry where the curvature varies along the axis of the bridge suggesting that a pressure difference exists within the bridge. This of course cannot happen or else the fluid will flow to negate the pressure difference. This means the bridge is not circular, but it is still a close approximation. The toroidal approximation is used to describe the geometry of liquid bridges between spheres [143] but hasn't really been solved completely to deal with the flat on flat geometry as is of interest here.

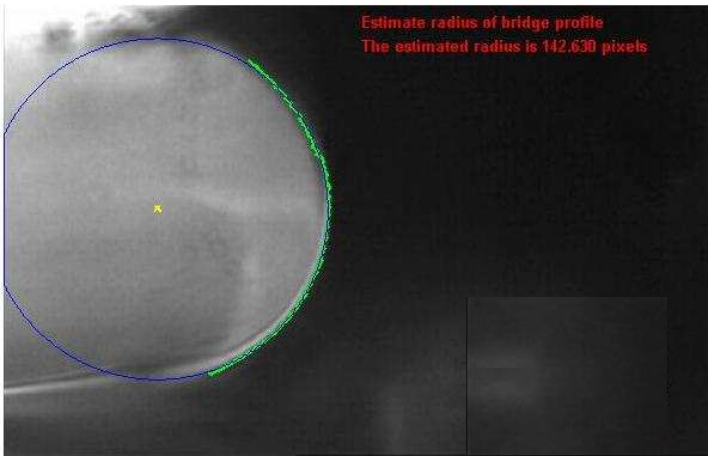

Fig. 4.10: A video still of a liquid bridge. Note how the circular arc closely approximates the actual shape of the bridge profile. The dark area indicates the liquid.

To use the toroidal approximation, consider the geometry given in Fig. 4.11:

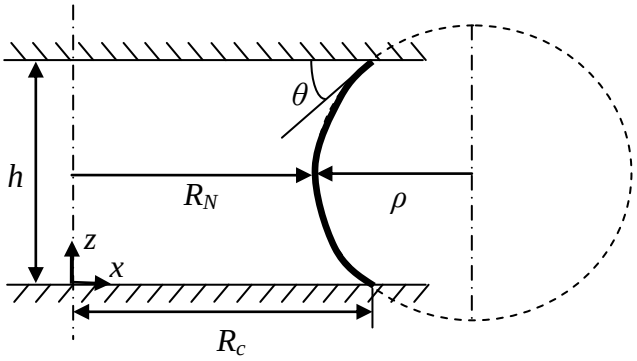

Fig. 4.11: A schematic of the liquid bridge represented by toroidal geometry.

From simple geometry it can be seen that the bridge profile represented by the thick black line can be expressed by the equation:

$$r(z) = R_c + \frac{h}{2}\tan(\theta) - \sqrt{\left(\frac{h}{2\cos\theta}\right)^2 - \left(\frac{h}{2} - z\right)^2} \tag{4.14}$$

Where the radius of curvature of the bridge profile is defined as:

$$\rho = \frac{h}{2\cos\theta} \tag{4.15}$$

And the neck radius becomes:

$$R_N = R_c + \frac{h}{2}\tan(\theta) - \frac{h}{2\cos\theta} \tag{4.16}$$

By using the disc method for calculating the volume of a revolution, the volume of the liquid bridge is shown to be:

$$Vol = \int_0^h \pi\left(R_N + \rho - \sqrt{\rho^2 - \left(\frac{h}{2} - z\right)^2}\right)^2 dz \tag{4.17}$$

We can solve eq. 4.17; and so for a given gap, contact angle and volume, the neck and contact radii for the bridge can be shown to be:

$$R_N = \frac{1}{2}\sqrt{\frac{hA}{\cos^2\theta}\left(\frac{hA}{4\cos^2\theta} + \frac{h}{2}\tan(\theta)\right) + \frac{4Vol}{\pi h} + \frac{h^2}{12} - 3\rho^2} - \left(\rho - \frac{h}{4}\tan(\theta) - \frac{\rho^2 A}{h}\right) \tag{4.18}$$

$$R_c = \frac{1}{2}\sqrt{\frac{hA}{\cos^2\theta}\left(\frac{hA}{4\cos^2\theta} + \frac{h}{2}\tan(\theta)\right) + \frac{4Vol}{\pi h} + \frac{h^2}{12} - 3\rho^2} - \left(\frac{h}{4}\tan\theta - \frac{\rho^2 A}{h}\right) \tag{4.19}$$

Where: $A = \arcsin\left(\frac{h}{2\rho}\right)$

This means we can calculate the capillary force as a function of gap for a given volume and contact angle. As mentioned above, the toroidal approximation does not give an exact

answer. To maintain the accuracy of the exact solution shown in Fig. 4.8, a scale factor, ζ, needs to be added to the toroidal approximation solution.

If the capillary force is defined as:

$$F_{CT} = 2\pi R_N \gamma_{LV} - \pi {R_N}^2 \gamma_{LV} \cdot \left(\frac{1}{R_N} - \frac{1}{\rho} \right) \tag{4.20}$$

Here the neck radius and the radius of curvature are those approximately given by eq. 4.18 and 4.19. The more accurate solution is given by:

$$F_C \simeq \zeta F_{CT} \tag{4.21}$$

Where ζ is a scaling factor found through curve fitting:

$$\zeta = 0.695 \sqrt{\pi - \sqrt[3]{\sin\left(\sqrt{\theta}\right)}} \tag{4.22}$$

It can be seen in Fig. 4.12 that eq. 4.21 does indeed give an accurate answer:

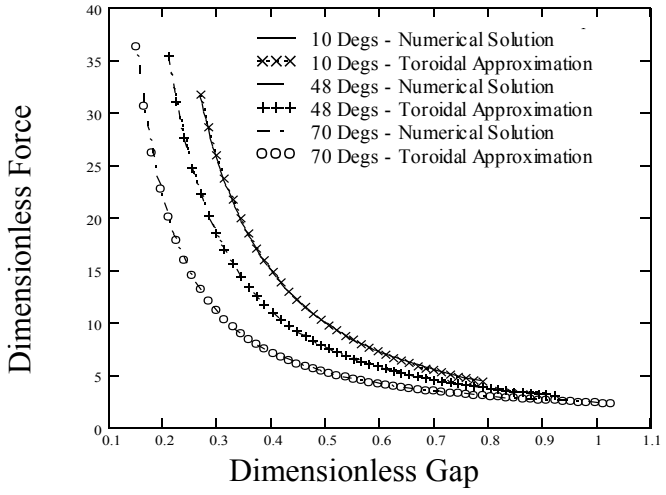

Fig. 4.12: A comparison between the exact numerical solution and the approximate solution for the capillary force (as given in eq. 4.21) for a range of contact angles.

4.8. Toroidal Approximation for Contact Angle Hysteresis

The liquid bridge may exhibit contact angle hysteresis, but it was assumed in the derivation of the above equations that the contact angle remains constant and that the contact line radius was free to change as a function of gap.

To deal with the situation where the contact angle varies and the contact line radius remains constant, we would need to solve eq. 4.17 for θ as a function of the gap. This is not trivial and a solution cannot be derived. To find a solution, a numerically derived expression needs to be found. It is easy to see that the variation of the contact angle as a function of the gap will depend on the volume of the bridge and the contact line radius. Therefore in order to obtain a single expression which will cover all situations it is prudent to first non-dimensionalise the pertinent equations with respect to the volume by using eq. 4.4.

It is also necessary to normalise the gap. To do this, consider the theoretical extreme gaps for a liquid bridge with constant contact line radius and volume. These extremes correspond to the situation where the contact angle is at a maximum (180°) or a minimum (0°). These cases relate to the minimum gap (where any further decrease would cause the contact line to slip) and the maximum gap (where any further increase would cause the contact line to slip) respectively (see Fig. 4.13). A real liquid will generally oscillate between limits in-between the theoretical limits.

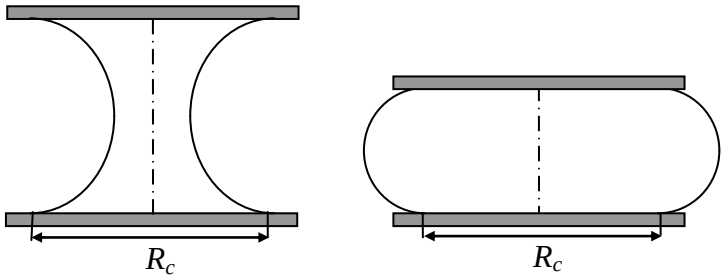

Fig. 4.13: A schematic of the two extreme cases. Note in both cases the contact line radii and volumes are equal. Only the gap and contact angle have changed.

These extreme gaps can be found by solving eq. 4.17 for the gap and setting the contact angle to its relevant value. The extreme gaps in their non-dimensional form can be given as:

$$h^*_{\min} = \frac{B}{2\pi} - \left(4 - \frac{\pi^2}{2}\right)\frac{\pi R_C{}^2}{B} - \frac{\pi R_C}{2} \tag{4.23}$$

Where: $B = \sqrt[3]{\left(12-\pi^2\right)\pi^4 R_C{}^3 + 24\pi^2 + 4\pi^2\sqrt{\left(32-3\pi^2\right)\pi^2 R_C{}^6 + \left(36-3\pi^2\right)\pi^2 R_C{}^3 + 36}}$

$$h^*_{\max} = \left(4 - \frac{\pi^2}{2}\right)\frac{\pi R_C{}^2}{C} - \frac{C}{2\pi} + \frac{\pi R_C}{2} \tag{4.24}$$

Where: $C = \sqrt[3]{\left(12-\pi^2\right)\pi^4 R_C{}^3 - 24\pi^2 + 4\pi^2\sqrt{\left(32-3\pi^2\right)\pi^2 R_C{}^6 + \left(3\pi^2-36\right)\pi^2 R_C{}^3 + 36}}$

There is also another case of special interest, which corresponds to a contact angle of 90°. When this is the case, the bridge assumes the shape of a cylinder, and is the point where the profile changes from being concave to convex and visa versa. It is useful to note that this case represents a singularity in the solution of eq. 4.17, as it means that eq. 4.15 equals

infinity (i.e. the bridge profile is straight). The relationship between the extreme gaps and the contact line radius is shown in Fig. 4.14.

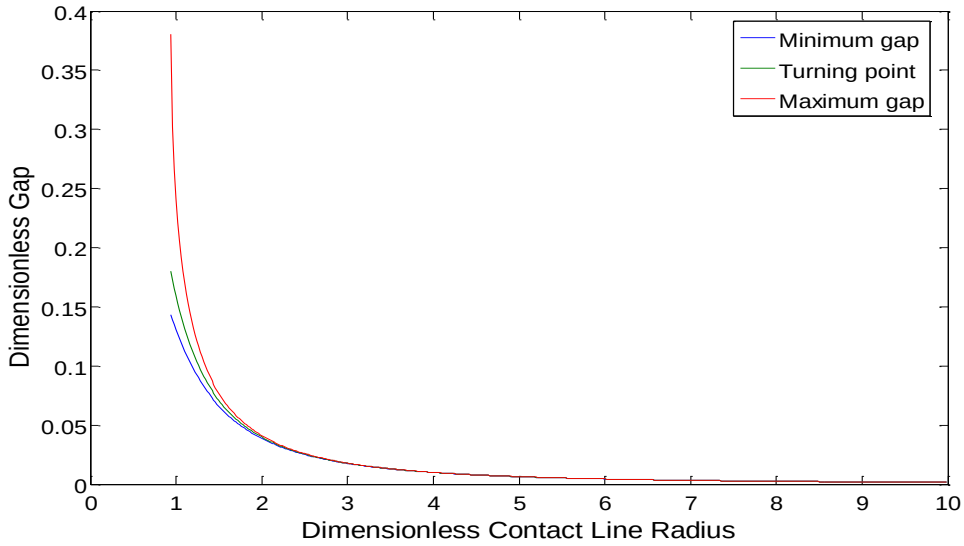

Fig. 4.14: Dimensionless extreme gaps as a function of contact line radius.

We can now normalise the gap with respect to these extremes so that we know that any gap we consider is a possible value (the normalised dimensionless gap has to lie between 0 and 1 or else it is a value outside the extreme values hence impossible).

The normalised dimensionless gap is defined thus:

$$Nh^* = \frac{h^* - h^*_{\min}}{h^*_{\max} - h^*_{\min}} \tag{4.25}$$

It appears that when the dimensionless contact line radius is less than 0.94 (see Fig. 4.14) the only solutions correspond to the geometry of a potentially unstable bridge. If we consider Fig. 4.15, the effect is more obvious. Here the contact angle is set to 0° and the curves show how the dimensionless volume changes as the gap is increased for a range of

contact line radii. Remembering that the correct dimensionless volume equals one, every time the curve equals one, the gap given corresponds to a real solution.

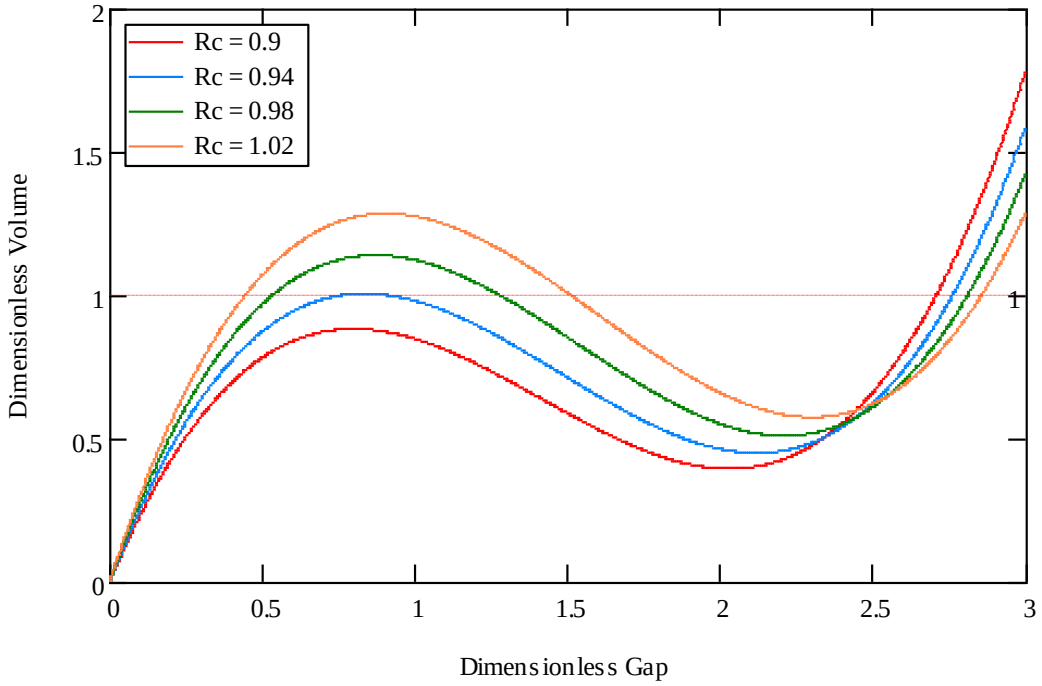

Fig. 4.15: Range of solutions for the maximum gap for various contact line radii.

It can be seen that there are multiple solutions but the solution that occurs at the smallest gap is the one that corresponds to that of the most stable bridge. The other solutions may be achievable in practice but this would be unlikely due to gravity effects. The point is when the dimensionless contact line radius is less than 0.94 there are only 'unstable' solutions where the smallest correct gap is much larger than that given for bridges with larger contact line radii.

For expediency it is necessary to just consider the case where the dimensionless contact line radius is greater than 0.94. We are interested in how the contact angle varies as the gap changes between the extreme values. As was mentioned before, due to the intractability of

the solution of eq. 4.17 the contact angle as a function of gap can only be found numerically. The solution can be seen in Fig. 4.16.

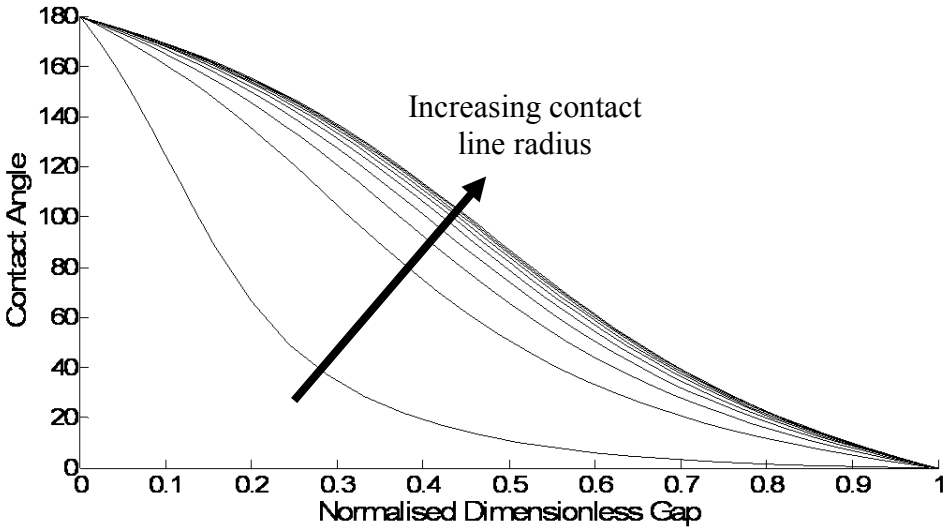

Fig. 4.16: Change in contact angle as a function of the normalised dimensionless gap. Each curve represents the result for a different dimensionless contact radius for the range of 0.94 to 3.

It can be shown that the solution depends on the dimensionless contact line radius, but converges as the dimensionless contact line radius reaches about 2.8. This is interesting but still not very useful in that if a numerical solution was sufficient we might as well use the exact equation rather than using the toroidal approximation. However, Fig. 4.16 is useful in that we now know what form the solution will take.

The curves in Fig. 4.16 have the shape of a generalised logistic curve, which has the form of eq. 4.26.

$$\theta\left(R_C\right) = A + \frac{C}{\left(1 + Te^{-B\left(0.5Nh^* - M\right)}\right)^{1/T}} \tag{4.26}$$

Where A is the lower asymptote, C is the upper asymptote minus A, M is the time of maximum growth, B is the growth rate and T affects near which asymptote maximum growth occurs. It can be seen from Fig. 4.15 that A, C, M, B and T are functions of R_C. B is given in terms of a polynomial and A, C, M and T can be given by Gompertz curves as:

$$B = \begin{matrix} 200.4557R_C^{\,4} - 968.45R_C^{\,3} + 1757.8R_C^{\,2} - 1420.7R_C + 435.63 \,|\, R_C < 1.3 \\ -0.0097R_C^{\,4} + 0.1519R_C^{\,3} - 0.8938R_C^{\,2} + 2.3783R_C + 2.4239 \,|\, R_C > 1.3 \end{matrix}$$

$$A = 198.0365e^{-18.170098e^{-5.694151R_C}}$$

$$C = -405.897e^{-2.4651e^{-3.70624R_C}} + 191.0749$$

$$M = 4.709296e^{-0.672116e^{-2.26707R_C}} - 4.21509$$

$$T = 6.683049e^{-1.90651e^{-2.23444R_C}} - 5.675506 \qquad (4.27)$$

The coefficients for A, C, M, B and T were all found by using a curve fitting algorithm. The results of substituting eq. 4.27(a-e) into eq. 4.26 is seen in Fig. 4.17.

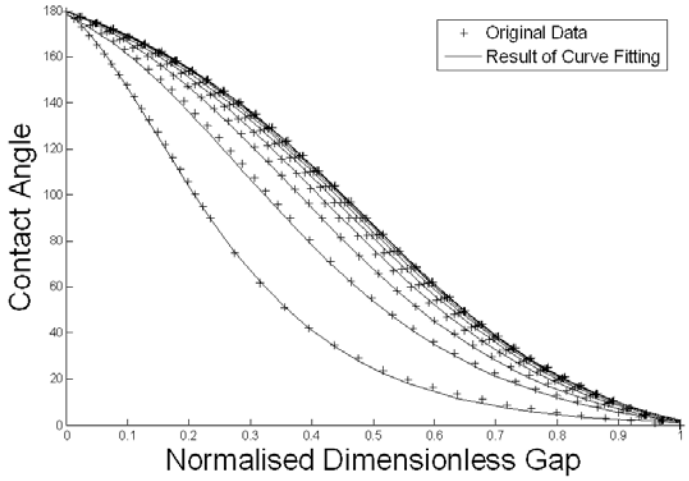

Fig. 4.17: Comparison between the approximate numerical answer and the closed form solution given by eq. 4.26.

Above $R_C^* = 1$, the results of eqs 4.17 and 4.26 can be seen to be in good agreement with the desired results. This means that they can be used as working equations when dealing with the effects of contact angle hysteresis. Below $R_C = 1$ the results do diverge but the error is never greater than 5%. Because eqs 4.27(a-e) converge to a single value as R_C increases beyond 2.8, eq. 4.26 can be simplified to:

$$\theta = 200.93 + \left. \frac{-210.55}{\left(1 + 1.4424 e^{-5.7099\left(Nh^* - 0.50805\right)}\right)^{0.6933}} \right| R_C > 2.8 \qquad (4.28)$$

At this juncture we can now calculate the geometry of a liquid bridge undergoing a change in height for the two circumstances, namely when the contact line slips and when it pins. The procedure for any subsequent calculations would be as follows:

- State initial conditions
    - We need to know four things: gap, equilibrium contact angle, contact line radius and volume.
    - Gap is a design/experimental parameter and is known, equilibrium (and dynamic for later) contact angle is a fluid property and can be found easily before hand.
    - The volume or the contact line radius needs to be measured. The other can be calculated using eqs 4 or 6 respectively. However they only need to be measured once. The values can then be used throughout the calculation.
- Change the gap
    - It is assumed that subsequent motion will be continuous and no relaxation towards equilibrium conditions is observed.
    - The change in geometry depends on the direction the upper platen is moved.
    - If it is moving upwards, initially the receding contact angle will be lower than the equilibrium contact angle. Here the contact line radius (given) will stay constant until the instantaneous contact angle (given by eq. 4.26) equals the receding contact angle. If the motion continues to increase, the contact angle stays constant and the contact line radius changes according to eq. 4.19.
- Change the direction
    - At this point the contact angle equals the receding contact angle and the contact line radius is known. Decreasing the gap, the contact line radius will remain constant and the contact angle will increase as in eq. 4.26 until it reaches the advancing contact angle. Decreasing the gap further will mean

the contact angle stays at the advancing angle and the contact line radius changes.

Using this procedure the capillary forces can be found as seen in Fig. 4.18.

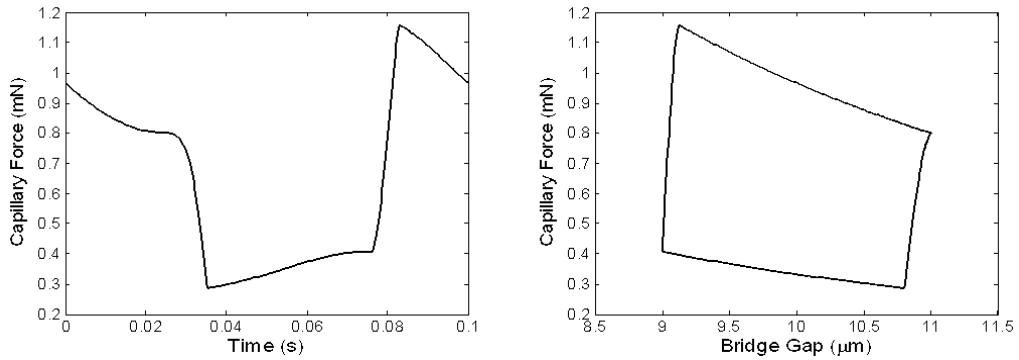

Fig. 4.18: Capillary force hysteresis effects for a typical liquid bridge undergoing sinusoidal motion (amplitude is 1μm, frequency is 10 Hz, advancing contact angle is 20° and receding contact angle is 70°).

In this case the contact line radius and contact angle vary as a function of gap thus:

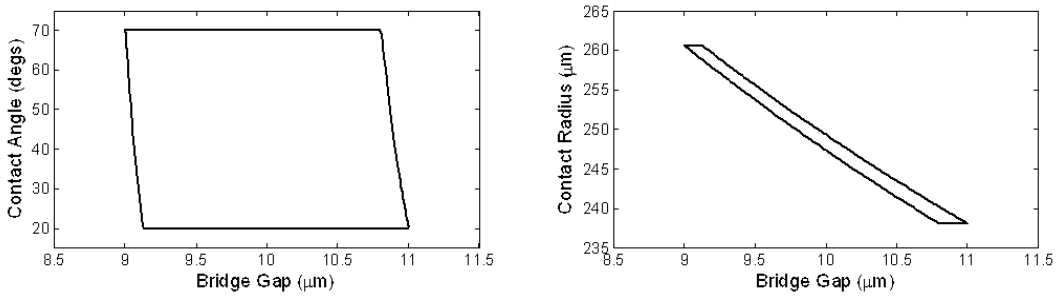

Fig. 4.19: Variation of contact angle and contact line radius as a function of gap.

This relationship may be better appreciated as a function of time:

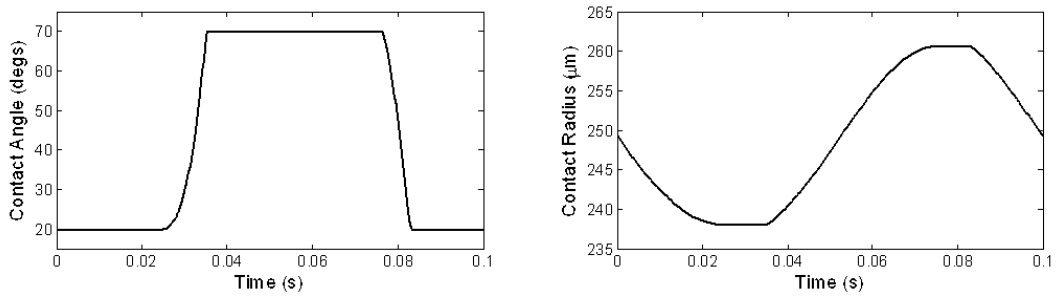

Fig. 4.20: Variation of contact angle and contact line radius as a function of time.

4.9. Squeeze Flow

To relate this theory back to squeeze flow theory, it is necessary to recall two assumptions: 1) that the fluid is assumed to have a cylindrical shape and 2) that the gap to radius ratio is very small. The first assumption seems to be at odds with the idea that surface tension causes the bridge to have a curved profile. This is because dealing with the boundary conditions in an exact manner is not a trivial matter. This inconsistency is dealt with by the second assumption. If the gap to radius ratio is small, the effect the surface tension has on the fluid flow is also small. With this in mind, the theory established in this chapter is to be used only to define the radius as used in the squeeze flow calculations and to give the additional force due to surface tension. It is intended to reduce the error caused by introducing the assumption that the capillary effects and the hydrodynamics of the fluid can be separated by ensuring that the two theories are consistent.

This is done by ensuring that the volumes of fluid used in both theories are the same. To do this, the radius of fluid used in the squeeze flow theory has to be the root mean square of the radius of the bridge given in eq. 4.14, or:

$$RMS = \sqrt{\frac{1}{h}\int_0^h r(z)^2 dz} \tag{4.29}$$

To see why this is consistent, recall that the volume of the bridge is defined as:

$$Vol = \int_0^h \pi r(z)^2 dz \tag{4.30}$$

And the volume of a cylinder is defined as:

$$Vol = \pi R_{Cyl}^2 h \tag{4.31}$$

If the definition of the root mean square radius is substituted into eq. 4.31 as the radius of the cylinder, it can be seen that eq. 4.30 and eq. 4.31 are in fact the same (see eq. 4.32).

$$Vol = \pi\left(\sqrt{\frac{1}{h}\int_0^h r(z)^2 dz}\right)^2 h = \int_0^h \pi r(z)^2 dz \tag{4.32}$$

Therefore matching the '*RMS*' value for the radius does ensure the volume of liquid used in both theories are consistent. We can now use this theory to ensure that the second assumption (that the gap to radius ratio is small) is also satisfied. This is done by ensuring the following inequality based on the limits of the lubrication approximation is satisfied:

$$RMS > 10h \tag{4.33}$$

Recalling the definition of the volume:

$$Vol = \pi h\left(RMS\right)^2 \tag{4.34}$$

Therefore the maximum gap is given as:

$$h_{\max} = \sqrt[3]{\frac{Vol}{100\pi}} \tag{4.35}$$

Substituting eqs 4.33 and 4.34 into eq. 4.19 gives the inequality:

$$R_c \geq \frac{1}{2}\sqrt{\frac{h_{\max}A}{\cos^2\theta}\left(\frac{h_{\max}A}{4\cos^2\theta}+\frac{h_{\max}}{2}\tan(\theta)\right)+\frac{4801h_{\max}^{\ 2}}{12}-3\rho^2}-\left(\frac{h_{\max}}{4}\tan\theta-\frac{\rho^2 A}{h_{\max}}\right) \quad (4.36)$$

This gives the minimum contact line radius that satisfies the lubrication approximation for any contact angle. The absolute minimum occurs when the contact angle is zero and this is the value that should be used to ensure that the lubrication approximation is always satisfied. In this case eq. 4.36 becomes:

$$R_{c\min} = \frac{\sqrt{3}h}{24}\sqrt{3\pi^2+19168}+\frac{\pi h}{8} \quad (4.37)$$

If eqs 4.35 and 4.37 are satisfied, the lubrication approximation is satisfied. Even though we now have a closed form expression for the capillary forces and all the geometry for the squeeze flow theory (to be used in the subsequent chapter), the model is still not in a form that can be used in the dynamic model introduced in Chapter 3.

4.10. Linearisation of the Capillary Force

To find the constants for eq. 3.2, the capillary force curve needs to be linearised. To do this the change in the gap has to be sufficiently small as to not cause the contact line radius to slip. This eliminates the contact angle hysteresis effect, and while the capillary force curve is still non-linear, if the change in gap is small enough this nonlinearity will be small. This means the capillary force can be approximated by a linear relationship given by eq. 4.38 as seen in Fig. 4.21.

$$F_{Capillary} = K_{Cap}x + \chi_{Cap} \quad (4.38)$$

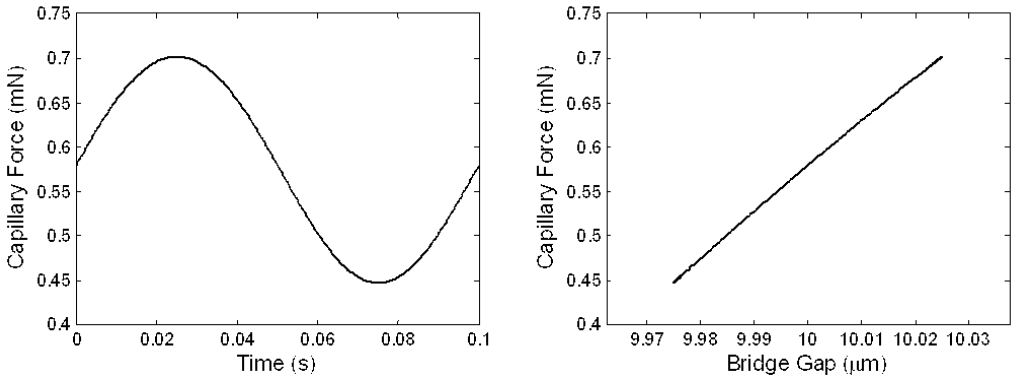

Fig. 4.21: Linearised capillary force. Note that the amplitude has been reduced to 25 nm and as the contact radius is not able to slip, the capillary force is linear.

It can be seen that the coefficients to be used in eq. 3.2-3.4 and eq. 3.7 in Chapter 3 are:

$$K_{Cap} = \frac{d\left(\zeta F_{CT}\left(\bar{h}\right)\right)}{d\bar{h}} \tag{4.39}$$

And:

$$\chi_{Cap} = \zeta F_{CT}\left(\bar{h}\right) - K_{Cap}\bar{h} \tag{4.40}$$

While these expressions are difficult to solve analytically, they are solved numerically very easily.

4.11. Conclusion

In this chapter the geometry of the liquid bridge has been defined and related to the squeeze flow theory to be discussed in Chapter 5. During the derivation of the geometry the capillary forces acting on the rheometer have been defined. The result was a hysteresis force curve which was then linearised to form the coefficients that will be used in eq. 3.2 in Chapter 3.

5. VISCOELASTICITY

In this chapter the viscoelastic aspects of the model is discussed and the constants C_1 and K_1 from eq. 3.2 will be found. An effective viscosity coefficient is derived and used in the Navier-Stokes equations. This is then solved in order to find the force required to squeeze a fluid sinusoidally. This force is spilt into its viscous and elastic components to define the viscoelastic coefficients to be used in the equations of motion (eq. 3.2) in Chapter 3.

5.1. Viscoelasticity

Classically, materials were defined in terms of two models; they were either an elastic solid or a viscous liquid [144]. Elastic solids were defined by Hooke's law which stated that in elastic solids, stress is directly proportional to strain during small deformations but is independent of the rate of strain. Similarly, Newton's law for viscous liquids stated that the stress is directly proportional to the rate of strain but independent of the strain itself. Both laws are idealisations because while there are materials whose behaviour can be modelled using the above laws under certain conditions, there are many more materials that are more accurately described as being viscoelastic.

Being viscoelastic means that a material can exhibit both viscous and elastic properties simultaneously. The specific response will depend on the time-scale of the experiment relative to the time it takes the material to relax. This means that if the experiment is relatively slow; the material will appear to be viscous, whereas if the experiment was fast the material will seem to be elastic. At intermediate time-scales a mixed, viscoelastic response will be observed. Examples include bodies that are soft solids and therefore do

not maintain a constant deformation under constant stress and so creep with time. Alternative examples may include particles which are not quite liquid which may, while flowing under constant stress, store some of the energy input, and instead of dissipating it as heat, recover part of its deformation when the stress is removed (elastic recoil) [144].

Therefore it is not unreasonable to assume that the majority of materials can be considered to be viscoelastic and will exhibit either elastic or viscous properties (or both) given the right situation. In this chapter we will only consider linear viscoelasticity. This is because rheological properties are very sensitive to the molecular structure of the material. So when finite strains and/or strain rates are applied to a material, the stress-strain relationship is very complicated (it can exhibit non-Hookean deformation and/or non-Newtonian flow [144]) as it causes the molecular structure of the material to vary significantly. This means that measurement of the material properties is much more complicated then if infinitesimal strains/strain rates were applied. Therefore in a bid to ensure that the results obtained in an experiment are as meaningful and as mathematically tractable as possible, a linear model of the viscoelasticity will be assumed.

As shown in [145] the theory of linear viscoelasticity is based on a superposition principle. This principle states that the response (e.g. strain) is directly proportional to the cause (e.g. stress). It is therefore implied that the response to a series of small step strains will be simply the sum of the responses to each step, where the same relaxation modulus governs the response. This means the differential equations governing the theory are also linear, and the corresponding coefficients are constants. These constants are material properties such as viscosity and shear modulus which are assumed not to change with changes in

variables such as strain or strain rate. Therefore the time derivatives are ordinary partial derivatives, thus restricting the theory to be applicable to small changes in the variables only i.e. only infinitesimal strains and strain rates can be applied to the material in order to keep the model valid.

The general differential equation for linear viscoelasticity is [144]:

$$\left(1+\alpha_1\frac{\partial}{\partial t}+\alpha_2\frac{\partial^2}{\partial t^2}+\cdots+\alpha_n\frac{\partial^n}{\partial t^n}\right)\sigma=\left(\beta_0+\beta_1\frac{\partial}{\partial t}+\beta_2\frac{\partial^2}{\partial t^2}+\cdots+\beta_m\frac{\partial^m}{\partial t^m}\right)\gamma \quad (5.1)$$

where σ is the stress and γ is the strain. α_i, β_i are material constants.

5.2. The Maxwell Model

A popular way of describing linear viscoelastic behaviour is by using mechanical models. These one-dimensional models consist of springs and dashpots arranged in such a way so that the system behaves in a manner similar to a real material. This allows the main features of the behaviour of the material to be inferred from an appropriate model rather having to develop complex mathematical models that may be intractable.

A simple but common model for linear viscoelastic fluids is the Maxwell model. Here the elastic term is represented by a Hookean (linear) spring and the viscous term is represented by a Newtonian dashpot in series (see Fig. 5.1).

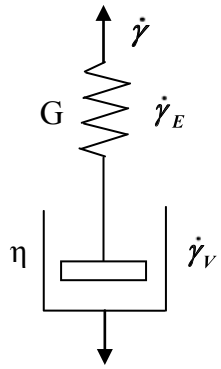

Fig. 5.1: A schematic of a Maxwell element comprised of a spring and a dashpot in series.

The differential equation for the Maxwell model is given as:

$$\sigma + \tau_m \dot{\sigma} = \eta \dot{\gamma} \tag{5.2}$$

This is equivalent to making α_1 in eq. 5.1 equal τ_m (defined as η / G) which is the natural time constant for a Maxwell fluid and β_1 equal η which is the shear viscosity. These are the only non-zero terms in eq. 5.1. To see the significance of the time constant, we consider the situation where a strain rate which has had a constant value for t < 0, has been applied to a material and suddenly removed at $t = 0$. It can be shown that the solution of eq. 5.2 for $t \geq 0$ gives the stress in the material as (see Fig. 5.2):

$$\sigma = \eta \dot{\gamma} e^{-\frac{t}{\tau_m}} \tag{5.3}$$

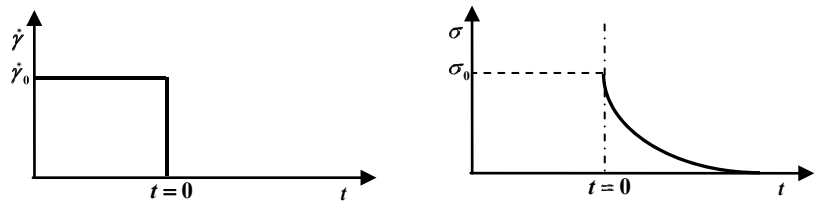

Fig. 5.2: (a) Graph depicting the variation in strain rate with respect to time and (b) the corresponding stress relaxation as given in eq. 5.3.

From Fig. 5.2 and eq. 5.3, it can be seen that the stress relaxes exponentially from its equilibrium value to zero at a rate proportional to τ_m. For this reason we call the time constant τ_m the relaxation time for the material.

To calculate the properties of the fluid, it is usual to impose a known strain/strain rate onto the fluid and measure the stress which will be proportional to those properties. A common way of determining viscoelastic behaviour (and the method used in this thesis) is to measure the fluid's response to small-amplitude oscillatory shear. To illustrate this for a Maxwell fluid let:

$$\gamma(t) = \gamma_0 \cos \omega t \tag{5.4}$$

Thus the strain rate is:

$$\dot{\gamma}(t) = -\omega\gamma_0 \sin \omega t \tag{5.5}$$

Substituting into eq. 5.2, a linear first order differential equation is obtained which gives the solution:

$$\sigma = \frac{\eta\omega\gamma_0}{\left(1+\omega^2{\tau_m}^2\right)}\left(\omega\tau_m \cos \omega t - \sin \omega t\right) \tag{5.6}$$

It can be seen that part of the stress is in phase with the applied strain and can be written as $G'\gamma(t)$. G' is the storage modulus (or dynamic rigidity) for the liquid. It is a measure of how much elastic potential energy is stored in the fluid. The part of the stress which is out of phase is written as $(G''/\omega)\dot{\gamma}(t)$. Here G'' is the loss modulus of the fluid. This is a measure of how much energy is being dissipated in the form of heat due to viscous losses (or internal friction).

The storage and loss modulus are defined respectively as [145]:

$$G' = \frac{\eta \tau_m \omega^2}{1 + \omega^2 \tau_m{}^2} \quad \textit{and} \quad G'' = \frac{\eta \omega}{1 + \omega^2 \tau_m{}^2} \tag{5.7}$$

Using a simple trigonometric identity it can be seen that the solution for the stress can be recast into a more convenient form, namely:

$$\sigma(t) = \sigma_0 e^{i(\omega t + \delta)} \tag{5.8}$$

Where:

$$\tan \delta = \frac{G''}{G'} \tag{5.9}$$

Therefore if we normalise eq. 5.8 (or eq. 5.6) and plot it against the normalised applied strain we can determine the fluid properties ***G'*** and ***G"*** (see Fig. 5.3).

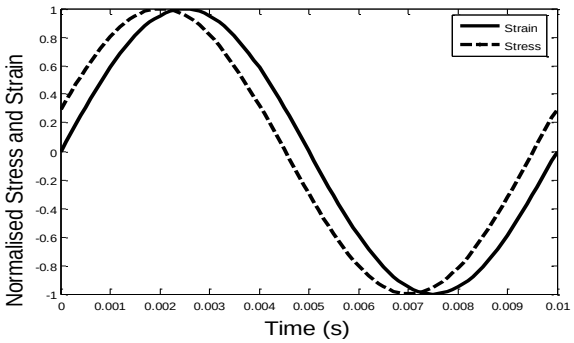

Fig. 5.3: Typical stress/strain curves for a sinusoidal experiment.

It is easy to see that if the fluid was purely viscous the phase would be 90° and if it was purely elastic the phase would be 0°. It should therefore be obvious that if the phase angle and amplitude of the response was measured at various frequencies, the storage and loss moduli for the fluid would be known for different strain rates.

5.3. The Generalised Maxwell Model

This model, as it stands, can only accurately describe simple fluids with a single relaxation time. However, because of the many processes that occur when a complex fluid is subject to a deformation, many fluids exhibit multiple relaxation times. However, while more complicated models exist, Roscoe [146] showed that all models irrespective of their complexity can be reduced to two simple canonical forms. These include the generalised Kelvin model (pertaining to viscoelastic solids) and the generalised Maxwell model (for viscoelastic liquids), and it can be shown that these two models are also equivalent. The general Maxwell model is made up of a number of Maxwell elements in parallel (see Fig. 5.4), where each element has a different relaxation time and shear modulus.

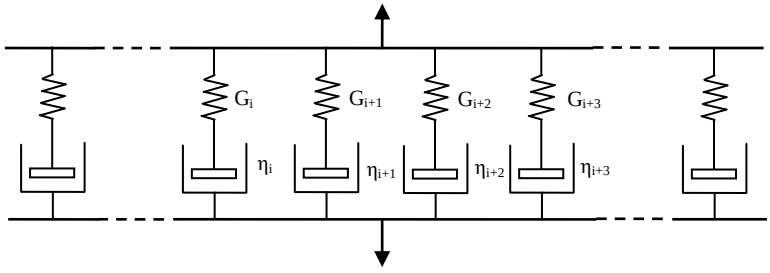

Fig. 5.4: A schematic of the generalised Maxwell model showing many elements in parallel.

It was shown by [147] that the full differential equation (eq. 5.1) and the mechanical model shown in Fig. 5.4 are equivalent. The implication of this is that complex fluid behaviour can be modelled by superimposing a series of linear responses rather than having to deal with more difficult models. Given the pertinent data, we can tell how best to model the fluid. For example in Fig. 5.5, the rheometry data is best described by a linear single-element Maxwell model, whereas in Fig. 5.6, the data is best described by a five-element Maxwell model. The number of elements is decided by what the curve fitting method gives as the best fit.

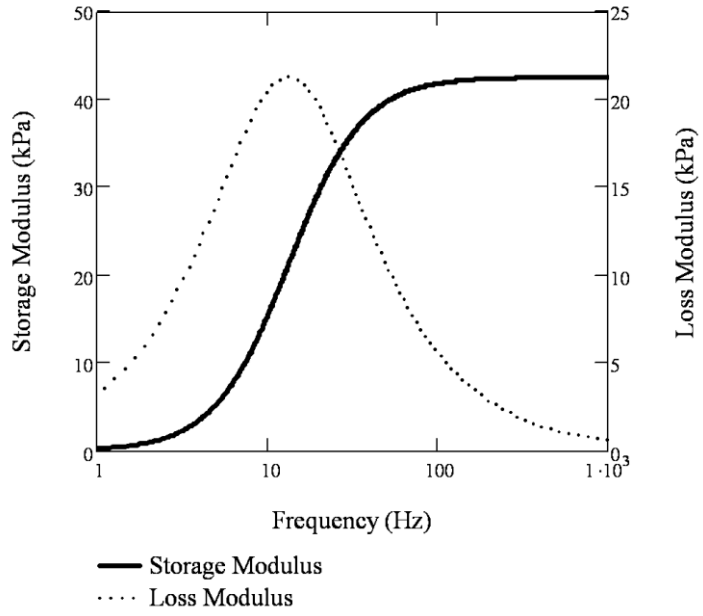

Fig. 5.5: Rheometry data best described by the single-element Maxwell model.

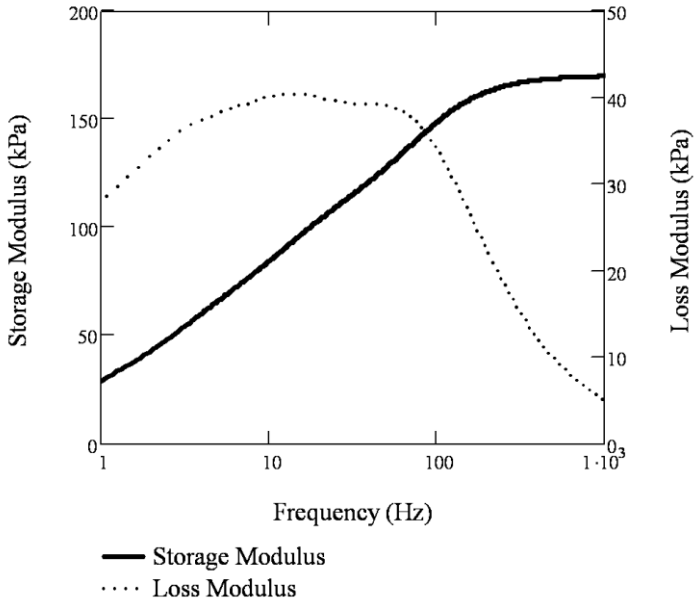

Fig. 5.6: Rheometry data best described by a five-element Maxwell model.

This may seem like an unnecessary complication, as it seems like we now have to build in an unknown number of spring and dashpots into the dynamic model (eq. 3.2). In fact this is not the case. From Figs. 5.5 and 5.6, it is clearly seen that regardless of how complicated

the response is, there is still only one value for the storage and loss moduli for each frequency as shown in eq. 5.10 and hence can be modelled as a single Maxwell element. The only real difference between the simple Maxwell model and the generalised Maxwell model is how these moduli vary with frequency (see eq. 5.10).

$$G' = \sum_{i=0}^{n} \frac{\eta_i \tau_{mi} \omega^2}{1 + \omega^2 \tau_{mi}^{\ 2}} \quad \textit{and} \quad G'' = \sum_{i=0}^{n} \frac{\eta_i \omega}{1 + \omega^2 \tau_{mi}^{\ 2}} \tag{5.10}$$

5.4. The Relaxation Spectrum

From eq. 5.10 it can be seen that once the storage and loss moduli have been measured, the shear viscosities and relaxation times can be calculated. With this information, the relaxation spectrum for the fluid can be obtained. The relaxation spectrum shows how a fluid 'softens' with time. From eq. 5.2 it can be seen that if we apply a constant strain to the material, the stress response can be given as:

$$\sigma(t) = G\gamma_0 e^{-\frac{t}{\tau_m}} \tag{5.11}$$

The relaxation modulus can therefore be defined as:

$$G(t) = Ge^{-\frac{t}{\tau_m}} \tag{5.12}$$

This information gives a picture of the molecular structure of the material. How this is done is complex and is outside the scope of this thesis – it is only necessary to know that we can calculate these properties.

For completeness the relaxation modulus for the fluid shown in Fig. 5.6 can be seen to be:

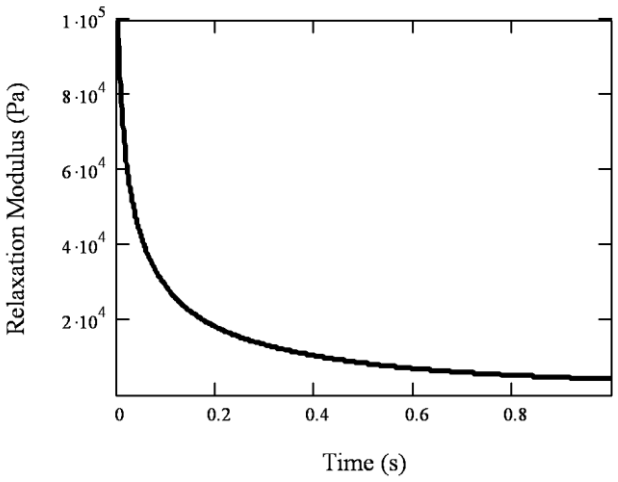

Fig. 5.7: The relaxation modulus for the fluid described by the rheological data given in Fig. 5.6.

5.5. Equivalent Viscosity Coefficient

When dealing with storage and loss moduli, it is customary to write [145]:

$$G^* = G'' + iG' \tag{5.13}$$

Here G^* is the complex shear modulus of the fluid, where:

$$\sigma(t) = G^*(\omega)\gamma(t) \tag{5.14}$$

Instead of this form we can define the stress in eq. 5.8 to be:

$$\sigma(t) = \eta^*(\omega)\dot{\gamma}(t) \tag{5.15}$$

Where η^* is the complex viscosity and is given as:

$$\eta^* = \eta' - i\eta'' \tag{5.16}$$

η' is the dynamic viscosity but the parameter η'' has no special name but is related to the storage modulus through $G' = \eta''\omega$ [145].

The physical interpretation of this is easily observed if we consider a linear dynamic spring-dashpot system with an equation of motion like:

$$\eta' \frac{dx}{dt} + G' x = F_0 e^{i\omega t} \tag{5.17}$$

And if we let:

$$x = Xe^{i\omega t} \tag{5.18}$$

This can be rearranged thus:

$$\left(\eta' - i\frac{G'}{\omega}\right) X = F \tag{5.19}$$

Comparing to eq. 5.16 shows that the complex viscosity can be used as an effective viscosity coefficient (see [148]). As well as being elegant, this idea also has practical applications. It is well known that the stresses and velocities in a Newtonian fluid are completely described by the Navier-Stokes equations. Unfortunately, simple equivalent expressions for viscoelastic fluids do not exist, but by using this effective viscosity (eq. 5.16) we can use the Navier-Stokes equations to analyse complex fluids [148].

5.6. The Oscillatory Stefan-Reynolds Equation

For the current situation (i.e. squeeze flow) we need to consider the Navier-Stokes equations in polar coordinates (using the equivalent viscosity coefficient):

$$\rho\left(\frac{\partial u}{\partial t}+u\frac{\partial u}{\partial r}+\frac{v}{r}\frac{\partial u}{\partial \theta}+w\frac{\partial u}{\partial z}-\frac{v^2}{r}\right)=-\frac{\partial P}{\partial r}+\eta^*\left[\frac{1}{r}\frac{\partial\left(r\frac{\partial u}{\partial t}\right)}{\partial r}+\frac{1}{r^2}\frac{\partial^2 u}{\partial \theta^2}+\frac{\partial^2 u}{\partial z^2}-\frac{u}{r^2}-\frac{2}{r^2}\frac{\partial v}{\partial \theta}\right]$$

$$\rho\left(\frac{\partial v}{\partial t}+u\frac{\partial v}{\partial r}+\frac{v}{r}\frac{\partial v}{\partial \theta}+w\frac{\partial v}{\partial z}+u\frac{v^2}{r}\right)=-\frac{\partial P}{\partial \theta}+\eta^*\left[\frac{1}{r}\frac{\partial\left(r\frac{\partial v}{\partial t}\right)}{\partial r}+\frac{1}{r^2}\frac{\partial^2 v}{\partial \theta^2}+\frac{\partial^2 v}{\partial z^2}-\frac{v}{r^2}+\frac{2}{r^2}\frac{\partial u}{\partial \theta}\right]$$

$$\rho\left(\frac{\partial w}{\partial t}+u\frac{\partial w}{\partial r}+\frac{v}{r}\frac{\partial w}{\partial \theta}+w\frac{\partial w}{\partial z}\right)=-\frac{\partial P}{\partial z}+\eta^*\left[\frac{1}{r}\frac{\partial\left(r\frac{\partial w}{\partial t}\right)}{\partial r}+\frac{1}{r^2}\frac{\partial^2 w}{\partial \theta^2}+\frac{\partial^2 w}{\partial z^2}\right] \quad (5.20)$$

These are the equations that must be solved in order to calculate the force required to squeeze the fluid sinusoidally. However, the equations are mathematically intractable in their current form. In order to simplify the calculation, certain assumptions need to be made. The most obvious simplification is to assume that the flow is axisymmetric. This means that there is no flow in the angular direction and that the flow does not vary in this direction. This assumption is valid as long as the platens only move axially relative to each other, which is the case [149]. This simplifies the equations to:

$$\rho\left(\frac{\partial u}{\partial t}+u\frac{\partial u}{\partial r}+w\frac{\partial u}{\partial z}\right)=-\frac{\partial P}{\partial r}+\eta^*\left[\frac{\partial^2 u}{\partial r^2}+\frac{1}{r}\frac{\partial u}{\partial r}+\frac{\partial^2 u}{\partial z^2}-\frac{u}{r^2}\right]$$

$$\rho\left(\frac{\partial w}{\partial t}+u\frac{\partial w}{\partial r}+w\frac{\partial w}{\partial z}\right)=-\frac{\partial P}{\partial z}+\eta^*\left[\frac{\partial^2 w}{\partial r^2}+\frac{1}{r}\frac{\partial w}{\partial r}+\frac{\partial^2 w}{\partial z^2}\right] \quad (5.21)$$

We can also non-dimensionalise the equations. This allows for the easy comparison between the various forces [149]. It is well known that if the Reynolds number is small, the inertial forces can be neglected; the validity of this assumption will be discussed later. Neglecting the inertial forces further simplifies the equations to:

$$0 = -\frac{\partial P}{\partial r} + \eta^* \left[\frac{\partial^2 u}{\partial r^2} + \frac{1}{r}\frac{\partial u}{\partial r} + \frac{\partial^2 u}{\partial z^2} - \frac{u}{r^2} \right]$$

$$0 = -\frac{\partial P}{\partial z} + \eta^* \left[\frac{\partial^2 w}{\partial r^2} + \frac{1}{r}\frac{\partial w}{\partial r} + \frac{\partial^2 w}{\partial z^2} \right] \tag{5.22}$$

One of the stipulations of being able to use eq. 5.2 (and subsequently eq. 5.16) is that the strain and the strain rate are infinitesimally small. Therefore the upper platen is constrained to move thus:

$$h(t) = \bar{h} + \varepsilon e^{i\omega t} \tag{5.23}$$

As ε is small ($\varepsilon \ll \bar{h}$), the velocity components will have the form [150]:

$$u = Ue^{i\omega t} \quad and \quad w = We^{i\omega t} \tag{5.24}$$

The relative magnitude of the velocities is based on a further assumption. In order to simplify the flow calculation, it is assumed that the fluid material planes parallel to the platens remain parallel to the platens throughout the duration of the flow [151]. This assumption that the material planes do not 'buckle' is based on the fact that the flow is predominately radial in nature. It is an assumption that is valid provided that the aspect ratio between the gap and the radius is small [149, 151], a constraint that is maintained throughout this thesis (this is known as the lubrication approximation [149]).

The reason why this concept is useful is because we can now use the principle of the conservation of volume to calculate the relative magnitudes of the velocities. To do this, consider an elemental cylinder (see Fig. 5.8). If the upper platen moves a distance dh axially in time dt, the volume of the cylinder decreases at a rate of:

$$Q_z = \pi r^2 \frac{dh}{dt} = \pi r^2 w \tag{5.25}$$

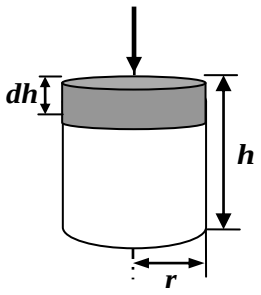

Fig. 5.8: An elemental cylinder being squashed.

From the assumption that the flow is predominantly radial, fluid must flow out of the cylinder at a rate of (see Fig. 5.9):

$$Q_r = 2\pi r \bar{h} \frac{dr}{dt} = 2\pi r \bar{h} \bar{u} \tag{5.26}$$

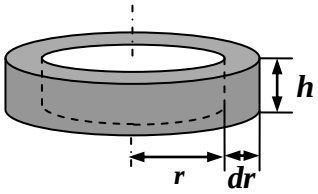

Fig. 5.9: The elemental cylinder with fluid flowing out of the sides.

From the principle of the conservation of volume, we can equate these rates together giving a relationship for the relative magnitude of the fluid velocities:

$$u = -\frac{r}{2h} w \tag{5.27}$$

Therefore we can assume a velocity profile of the form [150]:

$$u = \frac{r}{2}\frac{df(z,t)}{dz} \quad and \quad w = -f(z,t) \tag{5.28}$$

Substituting into eq. 5.22 gives the equation:

$$\frac{d^4 f(z,t)}{dz^4} = 0 \tag{5.29}$$

This can be solved by direct integration using the following boundary conditions:

$$\begin{aligned} f(0,t) &= 0, \quad f(\bar{h},t) = i\varepsilon\omega \\ \frac{df(0,t)}{dz} &= 0, \quad \frac{df(\bar{h},t)}{dz} = 0 \end{aligned} \tag{5.30}$$

The first two conditions state that the bottom platen is stationary while the upper platen is oscillating as stated in eq. 5.23. The second two conditions is the no-slip condition. Integrating eq. 5.29 and applying the boundary conditions gives:

$$f(z,t) = \frac{z^2}{\bar{h}^2}\left(2\frac{z}{\bar{h}} - 3\right)(i\varepsilon\omega) \tag{5.31}$$

Combining this equation with eqs 5.24 and 5.28 gives the velocity profile within a fluid undergoing squeeze flow. The force required to squeeze the fluid sinusoidally is calculated by integrating the stress acting in the direction of the force over the surface of the upper platen, or:

$$F = \int_0^{2\pi}\int_0^R \sigma_{zz} r dr d\theta \tag{5.32}$$

Where the axial stress is defined as:

$$\sigma_{zz} = -P\delta_{zz} + T_{zz} \tag{5.33}$$

Where the additional stress is defined as:

$$T_{zz} = 2\eta^* \frac{dw}{dz} \tag{5.34}$$

Substituting eq. 5.28 into eq. 5.22 gives the pressure as eq. 5.35 and the added stress as eq. 5.36:

$$P = 3\eta^* \left(\frac{r^2}{\bar{h}^3} - \frac{\bar{R}^2}{\bar{h}^3} \right) i\varepsilon\omega e^{i\omega t} \tag{5.35}$$

$$T_{zz} = 12\eta^* \frac{z}{\bar{h}^3} \left(\bar{h} - z \right) i\varepsilon\omega e^{i\omega t} \tag{5.36}$$

Substituting into Eq. 5.32 and integrating gives the force:

$$F = \frac{3\pi\eta^* \bar{R}^4}{2\bar{h}^3} i\varepsilon\omega e^{i\omega t} \tag{5.37}$$

Comparing this equation to the original Stefan-Reynolds equation for constant velocity squeeze flow [152] shows the validity of this equation.

5.7. Assumptions and Corrections

While this is the solution to the Navier-Stokes equations for viscoelastic sinusoidal squeeze flow, there are some issues. The first is the assumption that the radius of the fluid remains constant. This is because in the derivation it is implied that the platens are completely submerged with fluid and so the cross-sectional area of the fluid being squeezed is the same as the radius of the platens. In our case this is not so, as it is a discrete constant volume of fluid that is being squeezed. Therefore the radius will vary sinusoidally and this needs to be taken into account. Recalling in Chapter 4 that it was shown that the

root mean square of the bridge profile is a valid approximation for the bridge radius, we can define the radius to be:

$$R = \sqrt{\frac{Vol}{\pi h(t)}} \tag{5.38}$$

Substituting this and eq. 5.23 into eq. 5.37 gives:

$$F = \frac{3\eta^* Vol^2}{2\pi \bar{h}^5 \left(1 + \frac{\varepsilon}{\bar{h}} e^{i\omega t}\right)^2} i\varepsilon\omega e^{i\omega t} \tag{5.39}$$

As it can be shown that provided that x is small:

$$\frac{1}{(1+x)^2} \simeq (1-x)^2 \tag{5.40}$$

Eq. 5.39 can be simplified to:

$$F = \frac{3\eta^* Vol^2}{2\pi \bar{h}^5} \left(1 - \frac{\varepsilon}{\bar{h}} e^{i\omega t}\right)^2 i\varepsilon\omega e^{i\omega t} \tag{5.41}$$

Expanding gives:

$$F = \frac{3\eta^* Vol^2}{2\pi \bar{h}^5} \left(1 - 2\frac{\varepsilon}{\bar{h}} e^{i\omega t} + \frac{\varepsilon^2}{\bar{h}^2} e^{i2\omega t}\right) i\varepsilon\omega e^{i\omega t} \tag{5.42}$$

As ε is small, we can ignore all higher powers leaving us with:

$$F = \frac{3\eta^* Vol^2}{2\pi \bar{h}^5} i\varepsilon\omega e^{i\omega t} \tag{5.43}$$

Another issue is the lubrication approximation. Throughout this section it has been stated that if the ratio between the gap and the radius is sufficiently small, the flow is predominantly radial. This implies that the stresses do not vary axially. However upon inspection eq. 5.36 is a function of z and is a maximum at $h/2$. Therefore, we need to integrate eq. 5.32 at $h/2$ instead of at the platen surface as otherwise the force will be underestimated. This gives a solution of:

$$F = \frac{3\pi\eta^* \bar{R}^4}{2\bar{h}^3}\left(1+2\frac{\bar{h}^2}{\bar{R}^2}\right)i\varepsilon\omega e^{i\omega t} \tag{5.44}$$

It is easy to see that if the gap to radius ratio is vanishingly small, this equation reduces back to eq. 5.37. This equation can also be put into the constant volume form by using the same method as above giving:

$$F = \frac{3\eta^* Vol^2}{2\pi\bar{h}^5}\left(1+\frac{\pi\bar{h}^3}{V}\right)i\varepsilon\omega e^{i\omega t} \tag{5.45}$$

This may seem to be unnecessary, but because while it can be ensured that the gap to radius ratio is small, it cannot be made as small as we may like. This is because as the fluid get thinner, the force required to squeeze it increases significantly. Therefore in order to reduce the force the rheometer has to supply, the lubrication approximation has to be relaxed a little. This can be done by using eq. 5.45 which will maintain accuracy.

Eq. 5.45 can be expanded into its viscous and elastic components by using the relationship given in eq. 5.16.

$$\frac{3\eta' Vol^2}{2\pi\bar{h}^5}\left(1+\frac{\pi\bar{h}^3}{Vol}\right)\frac{dx}{dt}+\frac{3G' Vol^2}{2\pi\bar{h}^5}\left(1+\frac{\pi\bar{h}^3}{Vol}\right)x = Fe^{i\omega t} \tag{5.46}$$

This is the same form as eq. 5.17 so that it is clearly seen that the coefficients that will go into the main dynamic equation are:

$$C_1 = \frac{3\eta' Vol^2}{2\pi \bar{h}^5}\left(1+\frac{\pi \bar{h}^3}{Vol}\right) \quad and \quad K_1 = \frac{3G' Vol^2}{2\pi \bar{h}^5}\left(1+\frac{\pi \bar{h}^3}{Vol}\right) \tag{5.47}$$

It can be seen that due to the approximations given above that these coefficients are indeed constant. This is an assumption which is valid provided that the constraint that ε is small is true.

5.8. Inertia

It has always been stated that the inertia of the fluid is going to be neglected. This assumption was purely made to simplify the solution of the Navier-Stokes equations (eq. 5.21). Bell et al. [150] did solve the full equation to include inertia and gave the result in their paper. The full solution given was a very complex solution and was not amenable to be adapted for use here. There were simplifications given in the same paper, but it was decided that they won't be used. Quite simply, it was discovered that the frequency that the rheometer would have to be driven at in order to make inertia significant, was outside the range the rheometer would operate in. To show this, we define the Reynolds number to be:

$$\mathbf{Re} = \frac{\bar{h}^2 \rho \omega}{\eta'} \tag{5.48}$$

It can be shown that if **Re** is kept below 0.1, inertia can be neglected. For example if we were to want to test a low viscosity fluid of 1 Pa.s the maximum frequency we can go to is around 5 kHz given typical geometries and still maintain accuracy (see Fig. 5.10) (for more viscous fluids (say 30 Pa.s fluids) this value can be around 1MHz).

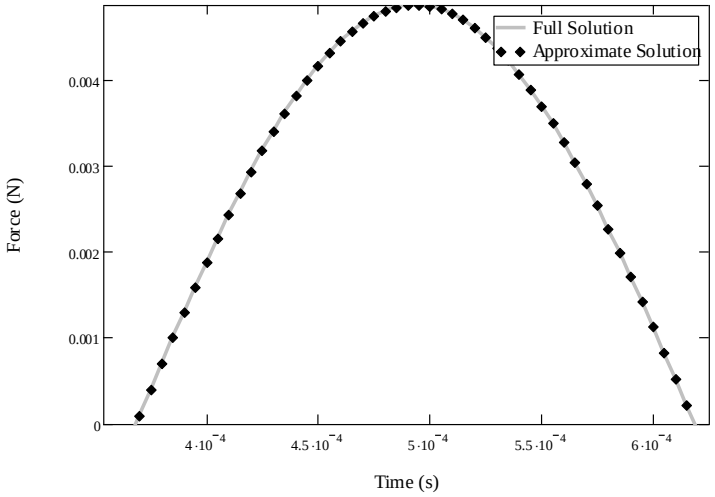

Fig. 5.10: A comparison between the full solution (inertia included) given in [150] and the solution given here (inertia neglected).

If we were to operate the rheometer at a frequency that would make **Re** much higher, the accuracy would decrease (see Fig. 5.11). However, as the rheometer is designed to operate at around 1 kHz, the inertia correction is not necessary.

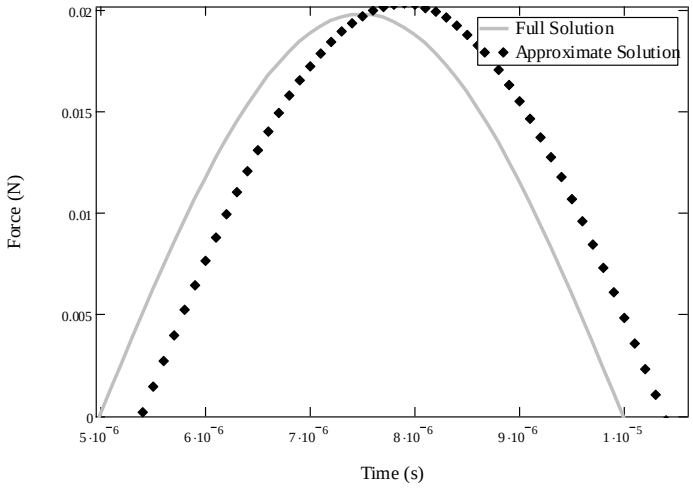

Fig. 5.11: The same fluid as in Fig. 10 being tested at 100 kHz, giving a Re of 2.5. Note how the two solutions no longer match.

5.9. Conclusion

In this chapter the theory of viscoelasticity has been explained and applied to the squeeze flow problem. Using the Maxwell model an effective viscosity coefficient incorporating both viscous and elastic terms was derived and used in the solution of the Navier-Stokes equation. Through this method the Stefan-Reynolds equation for sinusoidal viscoelastic fluids was found. This solution was improved further by including the effects of having a constant volume and the effect of having a geometry that approaches the limit for the lubrication approximation. This improved solution was then split into its component parts to form the coefficients to be used in Chapter 3. The effects of inertia were discussed and a limit for the frequency was imposed to maintain accuracy.

6. THE MICRORHEOMETER

In this chapter the mechanical and electrical behaviour of the microrheometer is discussed. Firstly, the proposed design is reviewed to remind the reader how the device is to be piezoelectrically actuated. Then in order to facilitate the subsequent analysis, the theory behind the piezoelectric effect is explored, specifically with a view of determining the piezoelectrical material to be used and its material properties. This information is then used to calculate the mechanical response of the rheometer, including its stiffness and inertia, as a function of the applied voltage and the fluid properties. Once the mechanical response of the rheometer is established, the resultant induced voltage is found. Once this is understood, it is discussed how the fluid properties can be calculated given the amplitude and phase of the induced voltage. Finally, a brief discussion into the practicalities of measuring the induced voltage is performed.

6.1. The Design

It was decided in Chapter 2 that a piezoelectric rheometer was the design that had the most potential. And it was shown in Chapter 3 that the rheometer is to be made from two parts: the active layer containing the quartz disc and a passive layer which just has the lower platen and other features to allow for easy assembly and the alignment of the platens (see Fig. 6.1 and 6.2). It is 30mm by 30mm by 1mm in size. The other dimensions are disclosed in the discussion below.

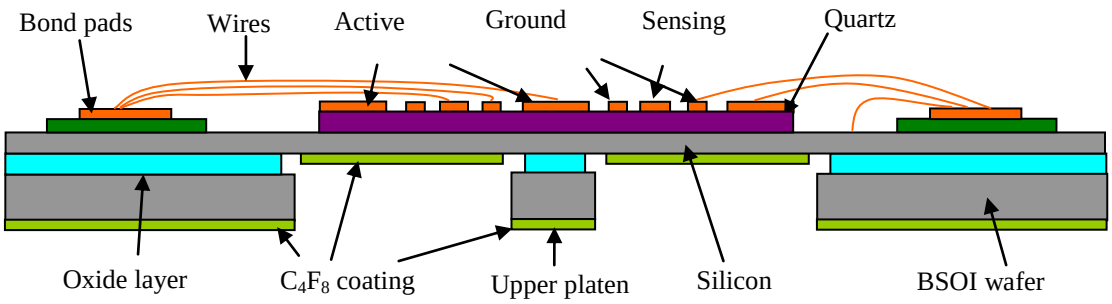

Fig. 6.1: Schematic of the active layer of the microrheometer.

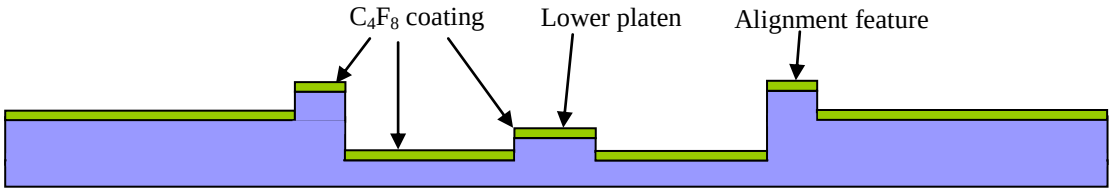

Fig. 6.2: Schematic of the passive layer of the microrheometer.

The passive layer as shown in Fig. 6.2 is to be fabricated from a single crystal silicon wafer. The wafer has been etched to three stages of different depths. The first stage supports the active layer. It has been etched to expose a concentric annulus (the alignment feature) which will help to locate the active layer and the upper platen. The second stage exposes the lower platen and sets the gap between the platens. The last stage allows the lower platen to stand above the bottom of the passive layer. This is to allow excess liquid to flow away from the platen and the sample being analysed. The entire layer is coated with C_4F_8 to help keep the sample in place (see Chapter 4).

In Fig. 6.1 it can be seen that the active layer is made up of several components, namely the silicon diaphragm, the quartz, the electrodes, the bond wires and the bond pads. The basis of the active layer is a BSOI wafer. The quartz is bonded to the device layer and the

handle wafer etched away to release the diaphragm. The electrodes are then deposited onto the quartz and the bond pads and wires attached. For convenience, the details for each component are given again below:

- The silicon diaphragm
    - The diaphragm is made out of single crystal silicon and has a low resistivity (~0.001Ωcm) and also acts as the ground electrode for the piezoelectric material.
    - The diaphragm has a diameter of 11.5mm and is 50μm thick.
- The quartz disc
    - This is made out of X-cut quartz (see section 6.3 for more details on different cuts of quartz and their associated constants.)
    - It has been cut into a disc with a 10mm diameter and 100μm thickness.
    - It is assumed that it has a Young's modulus of 40.14GPa, Poisson's ratio of 0.322 (calculated values - see below) and a piezoelectric coupling coefficient (d_{11}) of -0.934×10^{-12} C/N.
- The electrodes
    - The electrodes comprise of a 10nm e-beam evaporated layer of titanium (for adhesion) under a 200nm layer of thermally evaporated gold.
    - The electrodes have been deposited onto the quartz in five concentric circles:
        - The inner electrode is an active electrode in that the input voltage will be directly applied to it. It is a circle of radius 3mm.

- The second electrode is a ground electrode to shield the sensing electrode from the applied electric field. It is an annulus of inner radius 3.25mm and outer radius 3.75mm.
- The third electrode is the sensing electrode. It is an annulus of inner radius 4mm and outer radius 6mm.
- The fourth electrode is another ground electrode. It is an annulus with inner radius 6.25mm and outer radius 6.75mm.
- The last electrode is another active electrode. It is an annulus of inner radius 7mm and outer radius 10mm.

- The platen has a radius of 250μm with a set gap between the platens of 20 μm. Similar to the passive layer the entire bottom surface of the active layer is coated with C_4F_8.

The two layers are simply placed onto top of each other for assembly purposes (see Fig. 6.3). If the microrheometer is to be used to analyse some liquid, a drop of the sample is to be placed on the lower platen prior to assembly (the details of this is given in Chapter 8).

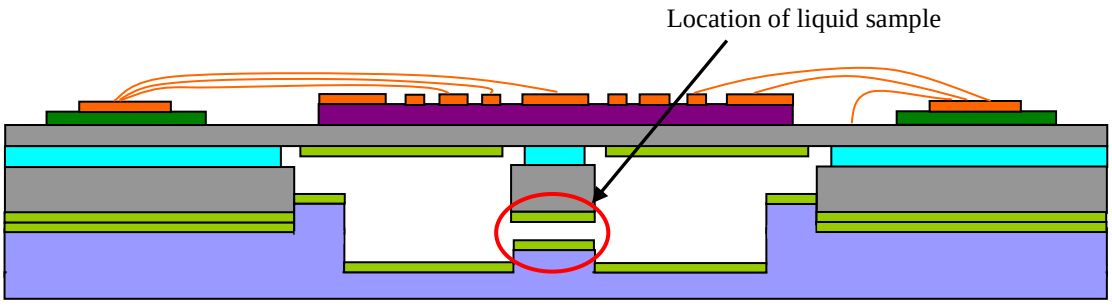

Fig. 6.3: Schematic of the assembled microrheometer.

6.2. The Piezoelectric Effect

Piezoelectricity is the ability of some materials to produce a voltage in response to an applied mechanical load [153]. This effect is caused in materials such as quartz because when stress is applied to the crystal lattice, the individual atoms in the material are displaced. This results in a charge separation as the positive and negative charge centres are displaced by differing amounts causing electric polarization within the crystal. This concentration of charge causes an electric field in a way analogous to that found in a parallel plate capacitor. This electric field in turn means there is a potential difference across the material due to the applied stress. This is known as the piezoelectric effect.

The piezoelectric effect is reversible in that materials exhibiting the direct piezoelectric effect (the production of electricity when stress is applied) also exhibit the converse piezoelectric effect (the production of stress and/or strain when an electric field is applied). Many crystalline materials exhibit piezoelectric behaviour. A number of materials exhibit the phenomenon strongly enough to be used in applications that take advantage of their properties. These include quartz, Rochelle salt, lead titanate zirconate ceramics (e.g. PZT-4, PZT-5A, etc.), barium titanate, and polyvinylidene fluoride (a polymer film) [153].

Mathematically, piezoelectricity is described by the material's constitutive equations, which describe how the material's stress (***T***), strain (***S***), charge-density displacement ($\boldsymbol{D_i}$), and electric field (***E***) interact. In strain-charge form the piezoelectric constitutive equations are given as [154]:

$$\begin{aligned} \boldsymbol{S} &= \boldsymbol{s}_E \cdot \boldsymbol{T} + \boldsymbol{d}^t \cdot \boldsymbol{E} \\ \boldsymbol{D}_i &= \boldsymbol{d} \cdot \boldsymbol{T} + \boldsymbol{\varepsilon}_{0T} \cdot \boldsymbol{E} \end{aligned} \tag{6.1}$$

The matrix $\boldsymbol{d}$ contains the piezoelectric coupling coefficients for the material, and it appears twice in the constitutive equation (the subscript *E* indicates a zero, or constant, electric field; the subscript *T* indicates a zero, or constant, stress field; and the superscript *t* stands for transposition of a matrix). $\boldsymbol{\varepsilon}_{0T}$ is the permittivity of the material and $\boldsymbol{s}$ is its compliance.

The strain-charge form of the constitutive equations for a standard simple piezoelectric material (such as a poled piezoelectric ceramic, e.g. PZT) may be written as [153]:

$$\begin{bmatrix} \boldsymbol{S}_1 \\ \boldsymbol{S}_2 \\ \boldsymbol{S}_3 \\ \boldsymbol{S}_4 \\ \boldsymbol{S}_5 \\ \boldsymbol{S}_6 \end{bmatrix} = \begin{bmatrix} \boldsymbol{s}_{11} & \boldsymbol{s}_{12} & \boldsymbol{s}_{13} & \boldsymbol{0} & \boldsymbol{0} & \boldsymbol{0} \\ \boldsymbol{s}_{12} & \boldsymbol{s}_{11} & \boldsymbol{s}_{13} & \boldsymbol{0} & \boldsymbol{0} & \boldsymbol{0} \\ \boldsymbol{s}_{13} & \boldsymbol{s}_{13} & \boldsymbol{s}_{33} & \boldsymbol{0} & \boldsymbol{0} & \boldsymbol{0} \\ \boldsymbol{0} & \boldsymbol{0} & \boldsymbol{0} & \boldsymbol{s}_{44} & \boldsymbol{0} & \boldsymbol{0} \\ \boldsymbol{0} & \boldsymbol{0} & \boldsymbol{0} & \boldsymbol{0} & \boldsymbol{s}_{55} & \boldsymbol{0} \\ \boldsymbol{0} & \boldsymbol{0} & \boldsymbol{0} & \boldsymbol{0} & \boldsymbol{0} & \boldsymbol{s}_{66} \end{bmatrix} \begin{bmatrix} \boldsymbol{T}_1 \\ \boldsymbol{T}_2 \\ \boldsymbol{T}_3 \\ \boldsymbol{T}_4 \\ \boldsymbol{T}_5 \\ \boldsymbol{T}_6 \end{bmatrix} + \begin{bmatrix} \boldsymbol{0} & \boldsymbol{0} & \boldsymbol{d}_{31} \\ \boldsymbol{0} & \boldsymbol{0} & \boldsymbol{d}_{31} \\ \boldsymbol{0} & \boldsymbol{0} & \boldsymbol{d}_{33} \\ \boldsymbol{0} & \boldsymbol{d}_{15} & \boldsymbol{0} \\ \boldsymbol{d}_{15} & \boldsymbol{0} & \boldsymbol{0} \\ \boldsymbol{0} & \boldsymbol{0} & \boldsymbol{0} \end{bmatrix} \begin{bmatrix} \boldsymbol{E}_1 \\ \boldsymbol{E}_2 \\ \boldsymbol{E}_3 \end{bmatrix} \tag{6.2}$$

This simply states that the strain in a piezoelectric material is given as the sum of the strain due to mechanical stress and the strain due to the electrical displacement of the atoms. This can be expanded to give:

$$\begin{bmatrix} \boldsymbol{S}_1 \\ \boldsymbol{S}_2 \\ \boldsymbol{S}_3 \\ \boldsymbol{S}_4 \\ \boldsymbol{S}_5 \\ \boldsymbol{S}_6 \end{bmatrix} = \begin{bmatrix} \boldsymbol{s}_{11}\boldsymbol{T}_1 + \boldsymbol{s}_{12}\boldsymbol{T}_2 + \boldsymbol{s}_{13}\boldsymbol{T}_3 + \boldsymbol{d}_{31}\boldsymbol{E}_3 \\ \boldsymbol{s}_{12}\boldsymbol{T}_1 + \boldsymbol{s}_{11}\boldsymbol{T}_2 + \boldsymbol{s}_{13}\boldsymbol{T}_3 + \boldsymbol{d}_{31}\boldsymbol{E}_3 \\ \boldsymbol{s}_{13}\boldsymbol{T}_1 + \boldsymbol{s}_{13}\boldsymbol{T}_2 + \boldsymbol{s}_{33}\boldsymbol{T}_3 + \boldsymbol{d}_{33}\boldsymbol{E}_3 \\ \boldsymbol{s}_{44}\boldsymbol{T}_4 + \boldsymbol{d}_{15}\boldsymbol{E}_2 \\ \boldsymbol{s}_{55}\boldsymbol{T}_5 + \boldsymbol{d}_{15}\boldsymbol{E}_1 \\ \boldsymbol{s}_{66}\boldsymbol{T}_6 \end{bmatrix} \tag{6.3}$$

Thus, if a voltage was applied in the z-direction (i.e. in the E_3 direction) then a PZT disc would increase in size in all directions. As the disc is thin, this would mean the disc will expand radially. If the disc was bonded onto a silicon diaphragm such as is the case in the microrheometer, this radial expansion would cause the diaphragm to deflect. It is this effect which we take advantage of to squeeze the fluid.

In the microrheometer, we wish to use the piezoelectric material as both an actuator and a sensor. To do this, the piezoelectric disc is only partially coated with active electrodes and an area is left passive. It is in this passive area that the induced voltage is to be measured and related to the properties of the fluid. This is possible because as is shown in eq. 6.1b, if the stress in the disc is known, the induced charge-density displacement is known, which is linked to the induced voltage.

6.3. Quartz

In the previous section PZT was used to describe how the piezoelectric disc can be used as an actuator and a sensor. This is because PZT is the most isotropic piezoelectric material with the simplest constitutive equations allowing the subsequent discussions to be most easily understood. However, as was discussed in the first section, quartz is to be used as the piezoelectric material.

PZT is by far the most commonly used piezoelectric material and the use of PZT would mean the mathematics is simpler. PZT would also be beneficial as its piezoelectric coefficients [153] mean that the silicon diaphragm would deflect significantly more for a

given voltage as compared to an equivalent disc of quartz [155]. However, the decision to use quartz is borne out of several considerations:

1. PZT is a man-made polycrystalline ceramic. Therefore when a disc of PZT is oscillating, the crystals rub together resulting in significant hysteretic losses [156, 157]. This is an issue because the purpose of the rheometer is to measure the losses in the fluid which may be masked by the losses in the PZT. These losses can be quantified, but it is not a simple relationship. It was shown in [156] that the losses are a function of voltage amplitude, deflection and frequency, and as we are using the piezoelectric disc to measure deflection, we would need to calibrate for the entire range of amplitudes, deflections and frequencies which is a formidable task and would probably lead to inaccuracies. Quartz, on the other hand, is a single crystal material. Therefore hysteresis and internal losses are much less pronounced [158, 159] and this should lead to a more accurate reading.
2. The properties of PZT mean that it is an excellent actuator as a large stress can be induced in the PZT by a relatively small applied voltage. It is this fact that makes it a poor sensor [160] in that it requires a large applied stress to induce a measurable voltage. Remembering that there will be electrical noise in the system, it is important to induce as large a voltage as possible. It is shown [160] that quartz is the best choice for this reason.
3. PZT is a polycrystalline material and as such is a brittle material. This macroscopically implies a statistical distribution of its ultimate strength, because defects, such as pores or cracks are responsible for the initiation of the specimen failure especially along grain boundaries [161]. This means that it is much more

prone to failure and will have a shorter working life as compared to quartz which is single crystal.

4. The rheometer is to be fabricated by bonding the quartz to a silicon diaphragm. The bonding of quartz is now a well known process and can be carried out with great success [162-164]. Quartz is silicon dioxide and bonds readily to silicon without any intermediate layers. PZT on the other hand does not bond as readily. For bonding PZT to silicon a thick intermediate layer of gold is required. This first covers any surface discrepancies caused by the polycrystalline nature of the PZT and allows for the eutectic bonding to the silicon [165]. This additional layer results in more losses and a reduction in the possible deflection [166]. The more common and simpler alternative to bonding PZT is to use an adhesive [167] but this method only exacerbates the problems just mentioned.
5. Another significant advantage is that quartz can be bought commercially in the exact size required. PZT is usually sold ready packaged as an actuator and it is not easy to find in its raw form. It can be made using various methods such as the sol-gel method [168, 169], but the development of an integrated PZT process is beyond this research.

Given that quartz is to be used, it is necessary to deduce which ‘cut’ is needed (being single crystal, the properties of the quartz disc depends on the orientation of the disc to the orientation of the crystal lattice). To decide this, consider the constitutive equations for quartz [170]:

$$\begin{bmatrix} S_1 \\ S_2 \\ S_3 \\ S_4 \\ S_5 \\ S_6 \end{bmatrix} = \begin{bmatrix} s_{11} & s_{12} & s_{13} & s_{14} & 0 & 0 \\ s_{12} & s_{11} & s_{13} & -s_{14} & 0 & 0 \\ s_{13} & s_{13} & s_{33} & 0 & 0 & 0 \\ s_{14} & -s_{14} & 0 & s_{44} & 0 & 0 \\ 0 & 0 & 0 & 0 & s_{55} & s_{56} \\ 0 & 0 & 0 & 0 & s_{56} & s_{66} \end{bmatrix} \begin{bmatrix} T_1 \\ T_2 \\ T_3 \\ T_4 \\ T_5 \\ T_6 \end{bmatrix} + \begin{bmatrix} d_{11} & 0 & 0 \\ -d_{11} & 0 & 0 \\ 0 & 0 & 0 \\ d_{14} & 0 & 0 \\ 0 & -d_{14} & 0 \\ 0 & d_{26} & 0 \end{bmatrix} \begin{bmatrix} E_1 \\ E_2 \\ E_3 \end{bmatrix} \quad (6.4)$$

This can be expanded to:

$$\begin{bmatrix} S_1 \\ S_2 \\ S_3 \\ S_4 \\ S_5 \\ S_6 \end{bmatrix} = \begin{bmatrix} s_{11}T_1 + s_{12}T_2 + s_{13}T_3 + s_{14}T_4 + d_{11}E_1 \\ s_{12}T_1 + s_{11}T_2 + s_{13}T_3 - s_{14}T_4 - d_{11}E_1 \\ s_{13}T_1 + s_{13}T_2 + s_{33}T_3 \\ s_{14}T_1 - s_{14}T_2 + s_{44}T_4 + d_{14}E_1 \\ s_{55}T_5 + s_{56}T_6 - d_{14}E_2 \\ s_{56}T_5 + s_{66}T_6 + d_{26}E_2 \end{bmatrix} \quad (6.5)$$

This shows that applying a voltage in the z-direction will not cause any deflection in the quartz. Instead, from eq. 6.5 it can be seen that a cut of quartz where a voltage can be applied in the x-direction (remember this in the crystallographic coordinate system not the laboratory system) is the only cut that will result in the expansion of the quartz. From Fig. 6.4 it is obvious the only possible cut of quartz is the X-cut as it is orthogonal to the x-axis.

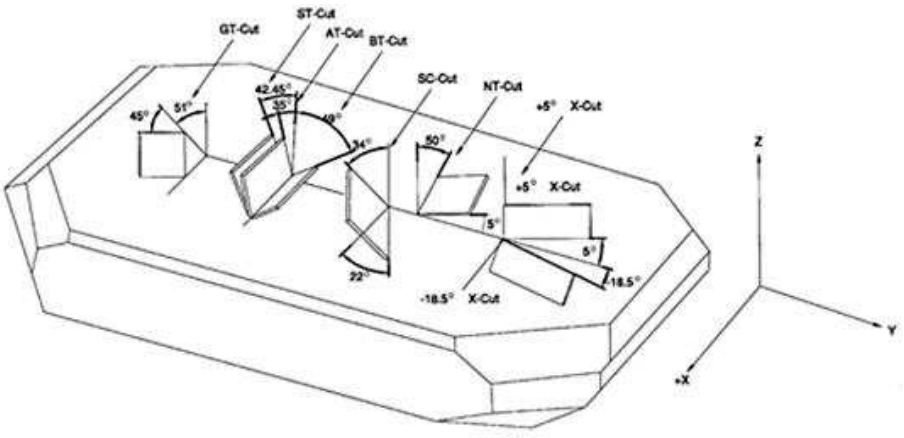

Fig. 6.4: Schematic of a quartz crystal, representing all the cuts [170].

Another issue with the constitutive equations for quartz is that they are orthotropic. This is because quartz has a trigonal symmetry (class 32) as it is made up of a lattice of silica (SiO_2) tetrahedra [170]. Dealing with such orthotropic systems is mathematically difficult and it is unlikely that the results will be sufficiently tractable to be useful in any subsequent analysis. Fortunately it has been shown that such orthotropic crystalline materials have compliance matrices that can be simplified to an isotropic matrix plus a small orthotropic part [171,172]. This means quartz can be modelled as an isotropic material (see Appendix A).

As calculated in Appendix A, the equivalent Young's modulus of the quartz is E = 40.191 GPa and its Poisson's ratio is ν = 0.322. These are the properties of quartz which are to be used in the subsequent analysis. From this point onwards quartz will be treated as an isotropic material to simplify analysis.

6.4. Laminated Plate Theory

The model for the microrheometer is derived using classical laminated plate theory (CLPT). CLPT is essentially based on the Kirchhoff's plate theory wherein a multi-layered heterogeneous plate structure is reduced to a kinematically equivalent single layer, thereby simplifying a 3D elasticity problem to an equivalent 2D problem [173]. The full derivations and proofs for CLPT are lengthy and won't be covered in full here; instead the reader is referred to the many excellent texts covering the subject [173, 175]. The advantage of using CLPT is that it allows sufficient simplicity in the expressions and can

lead to closed form solutions in most cases. These solutions are in a much more convenient form than the numerical results obtained by earlier researchers [176-182].

CLPT is used here to arrive at the closed form solutions for the deflection and induced strain for a multi-layered circular piezoelectric actuator and sensor under voltage and point force loading conditions. In a similar style to that used in [183], the approach is as follows: general solutions for the transverse and lateral deflections of a circular axisymmetric laminate comprised of *n* number of uniformly thick material layers of equal radii, where one or more of these layers are piezoelectric are derived from the CLPT. Then the general solutions are used to obtain closed form solutions for the transverse deflections of the rheometer where the diameter of the substrate is partially covered by the quartz, which in turn is partially coated with active electrodes.

Since the derivations are based on the CLPT, the final results must retain all of the assumptions involved in the CLPT formulation [174]. The assumptions are: (i) the layers are perfectly bonded to each other, (ii) the material of each layer is linearly elastic and transversely isotropic, (iii) each layer has uniform thickness, (iv) the strains and deflections are small, (v) plane stress conditions apply and (vi) the transverse shear to the top and bottom surfaces of the laminate are zero.

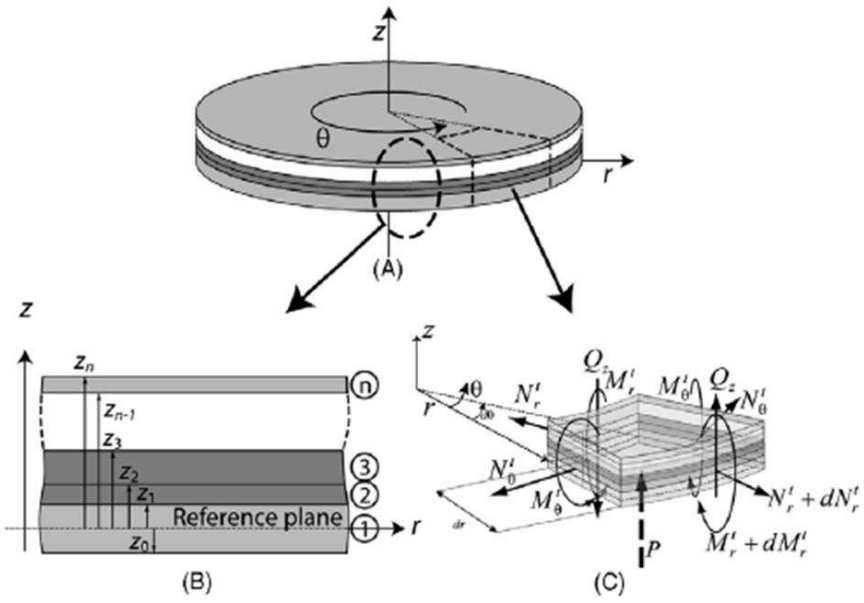

Fig. 6.5: The conventions used for the coordinate systems and the directions of the forces etc [183].

The kinematic relations of the laminate in Fig. 6.5 are defined in polar ($\boldsymbol{r,\theta,z}$) coordinates where the reference plate is located on the mid-plane of the bottommost layer and the z-axis is taken upward from the reference plane. The *k*th layer in the laminate is located between the points $\boldsymbol{z = z_{k-1}}$ and $\boldsymbol{z = z_k}$ in the thickness direction. From Kirchhoff's theory, the strain and the curvature for the plate at the reference plane can be expressed in terms of the lateral and transverse deflections of points in that plane as:

$$\begin{Bmatrix} \varepsilon_{rr}^0 \\ \varepsilon_{\theta\theta}^0 \end{Bmatrix} = \begin{Bmatrix} \dfrac{\partial u_0(r)}{\partial r} \\ \dfrac{u_0(r)}{r} \end{Bmatrix} \tag{6.13}$$

and,

$$\begin{Bmatrix} \kappa_r^0 \\ \kappa_\theta^0 \end{Bmatrix} = \begin{Bmatrix} -\dfrac{\partial^2 w_0(r)}{\partial r^2} \\ -\dfrac{1}{r}\dfrac{\partial w_0(r)}{\partial r} \end{Bmatrix} \tag{6.14}$$

Since the CLPT assumes a linear distribution of strain along the thickness direction, the transversely isotropic elastic strain in any *k*th layer of the structure at a distance z_k from the reference plane is described in terms of the strain and curvature of the reference plane as:

$$\begin{Bmatrix} \varepsilon_{rr}^{k} \\ \varepsilon_{\theta\theta}^{k} \end{Bmatrix} = \begin{Bmatrix} \varepsilon_{rr}^{0} \\ \varepsilon_{\theta\theta}^{0} \end{Bmatrix} + z_k \begin{Bmatrix} \kappa_{r}^{0} \\ \kappa_{\theta}^{0} \end{Bmatrix} - E_f^k \begin{Bmatrix} d_{11}^{k} \\ d_{11}^{k} \end{Bmatrix} \tag{6.15}$$

If the *k*th layer is piezoelectric (i.e. the quartz layer) E_f^k is the applied electric field across that layer and d_{11}^k is the transverse piezoelectric constant. However if the layer is not piezoelectric then these values are set to zero.

The linear isotropic constitutive relations for the *k*th layer in polar coordinates are:

$$\begin{Bmatrix} \sigma_{rr}^{k} \\ \sigma_{\theta\theta}^{k} \end{Bmatrix} = \left[Q_k\right] \begin{Bmatrix} \varepsilon_{rr}^{k} \\ \varepsilon_{\theta\theta}^{k} \end{Bmatrix} = \left[Q_k\right] \left(\begin{Bmatrix} \varepsilon_{rr}^{0} \\ \varepsilon_{\theta\theta}^{0} \end{Bmatrix} + z_k \begin{Bmatrix} \kappa_{r}^{0} \\ \kappa_{\theta}^{0} \end{Bmatrix} - E_f^k \begin{Bmatrix} d_{11}^{k} \\ d_{11}^{k} \end{Bmatrix} \right) \tag{6.16}$$

Where $\left[Q_k\right]$ is the plane stress-reduced stiffness matrix of the kth layer expressed in terms of engineering constants as:

$$\left[Q_k\right] = \frac{E_k}{\left(1-\upsilon_k^2\right)} \begin{bmatrix} 1 & \upsilon_k \\ \upsilon_k & 1 \end{bmatrix} \tag{6.17}$$

The net force, ***N***, and the net moment, ***M***, acting on the structure across the entire plate thickness is obtained by integrating the stresses through the thickness of each layer of the plate and then summing the forces and moments (as given in Fig. 6.5) over all the layers as:

$$N = \begin{Bmatrix} N_r^k \\ N_\theta^k \end{Bmatrix} = \sum_{k=1}^{n} \int_{z_{k-1}}^{z_k} \begin{Bmatrix} \sigma_{rr} \\ \sigma_{\theta\theta} \end{Bmatrix} dz = A \begin{Bmatrix} \varepsilon_{rr}^0 \\ \varepsilon_{\theta\theta}^0 \end{Bmatrix} + B \begin{Bmatrix} \kappa_r^0 \\ \kappa_\theta^0 \end{Bmatrix} - \begin{Bmatrix} N_r^P \\ N_\theta^P \end{Bmatrix} \tag{6.18}$$

$$M = \begin{Bmatrix} M_r^k \\ M_\theta^k \end{Bmatrix} = \sum_{k=1}^{n} \int_{z_{k-1}}^{z_k} \begin{Bmatrix} \sigma_{rr} \\ \sigma_{\theta\theta} \end{Bmatrix} z dz = B \begin{Bmatrix} \varepsilon_{rr}^0 \\ \varepsilon_{\theta\theta}^0 \end{Bmatrix} + D \begin{Bmatrix} \kappa_r^0 \\ \kappa_\theta^0 \end{Bmatrix} - \begin{Bmatrix} M_r^P \\ M_\theta^P \end{Bmatrix} \tag{6.19}$$

A, *B* and *D* are the extensional stiffness matrix, extensional-bending coupling stiffness matrix and bending stiffness matrix, respectively, expressed as:

$$A = \begin{bmatrix} A_{11} & A_{12} \\ A_{12} & A_{11} \end{bmatrix} = \sum_{k=1}^{n} \int_{z_{k-1}}^{z_k} \left[Q_k \right] dz = \begin{bmatrix} \sum_{k=1}^{n} \frac{E_k}{\left(1-\upsilon_k^2\right)} \left(z_k - z_{k-1}\right) & \sum_{k=1}^{n} \frac{\upsilon_k E_k}{\left(1-\upsilon_k^2\right)} \left(z_k - z_{k-1}\right) \\ \sum_{k=1}^{n} \frac{\upsilon_k E_k}{\left(1-\upsilon_k^2\right)} \left(z_k - z_{k-1}\right) & \sum_{k=1}^{n} \frac{E_k}{\left(1-\upsilon_k^2\right)} \left(z_k - z_{k-1}\right) \end{bmatrix} \tag{6.20}$$

$$B = \begin{bmatrix} B_{11} & B_{12} \\ B_{12} & B_{11} \end{bmatrix} = \sum_{k=1}^{n} \int_{z_{k-1}}^{z_k} \left[Q_k \right] z dz = \frac{1}{2} \begin{bmatrix} \sum_{k=1}^{n} \frac{E_k}{\left(1-\upsilon_k^2\right)} \left(z_k^2 - z_{k-1}^2\right) & \sum_{k=1}^{n} \frac{\upsilon_k E_k}{\left(1-\upsilon_k^2\right)} \left(z_k^2 - z_{k-1}^2\right) \\ \sum_{k=1}^{n} \frac{\upsilon_k E_k}{\left(1-\upsilon_k^2\right)} \left(z_k^2 - z_{k-1}^2\right) & \sum_{k=1}^{n} \frac{E_k}{\left(1-\upsilon_k^2\right)} \left(z_k^2 - z_{k-1}^2\right) \end{bmatrix} \tag{6.21}$$

$$D = \begin{bmatrix} D_{11} & D_{12} \\ D_{12} & D_{11} \end{bmatrix} = \sum_{k=1}^{n} \int_{z_{k-1}}^{z_k} \left[Q_k \right] z^2 dz = \frac{1}{3} \begin{bmatrix} \sum_{k=1}^{n} \frac{E_k}{\left(1-\upsilon_k^2\right)} \left(z_k^3 - z_{k-1}^3\right) & \sum_{k=1}^{n} \frac{\upsilon_k E_k}{\left(1-\upsilon_k^2\right)} \left(z_k^3 - z_{k-1}^3\right) \\ \sum_{k=1}^{n} \frac{\upsilon_k E_k}{\left(1-\upsilon_k^2\right)} \left(z_k^3 - z_{k-1}^3\right) & \sum_{k=1}^{n} \frac{E_k}{\left(1-\upsilon_k^2\right)} \left(z_k^3 - z_{k-1}^3\right) \end{bmatrix} \tag{6.22}$$

N_r^P and N_θ^P are the radial and tangential equivalent piezoelectric forces, and M_r^P and M_θ^P are the radial and tangential equivalent piezoelectric moments generated by the piezoelectric layer when a voltage is applied across it. These are expressed as:

$$\begin{Bmatrix} N_r^P \\ N_\theta^P \end{Bmatrix} = \sum_{k=1}^{n} \int_{z_{k-1}}^{z_k} [Q_k] E_f^k \begin{Bmatrix} d_{11}^k \\ d_{11}^k \end{Bmatrix} dz = \begin{Bmatrix} \sum_{k=1}^{n} \frac{(1+\upsilon_k) E_k}{(1-\upsilon_k^2)} E_f^k d_{11}^k (z_k - z_{k-1}) \\ \sum_{k=1}^{n} \frac{(1+\upsilon_k) E_k}{(1-\upsilon_k^2)} E_f^k d_{11}^k (z_k - z_{k-1}) \end{Bmatrix} \quad (6.23)$$

$$\begin{Bmatrix} M_r^P \\ M_\theta^P \end{Bmatrix} = \sum_{k=1}^{n} \int_{z_{k-1}}^{z_k} [Q_k] E_f^k \begin{Bmatrix} d_{11}^k \\ d_{11}^k \end{Bmatrix} z dz = \frac{1}{2} \begin{Bmatrix} \sum_{k=1}^{n} \frac{(1+\upsilon_k) E_k}{(1-\upsilon_k^2)} E_f^k d_{11}^k (z_k^2 - z_{k-1}^2) \\ \sum_{k=1}^{n} \frac{(1+\upsilon_k) E_k}{(1-\upsilon_k^2)} E_f^k d_{11}^k (z_k^2 - z_{k-1}^2) \end{Bmatrix} \quad (6.24)$$

It is readily seen that the contribution to the equivalent piezoelectric forces and moments from the non-piezoelectric layers would be zero since $d_{11}^k = 0$ for such layers.

The net force and moment acting on the laminate structure, N and M, hold the structure in static equilibrium, which for axisymmetrically loaded conditions can be expressed as [183]:

$$\frac{dN_r^k}{dr} + \frac{N_r^k - N_\theta^k}{r} = 0 \quad (6.25)$$

$$\frac{dM_r^k}{dr} + \frac{M_r^k - M_\theta^k}{r} = Q_z \quad (6.26)$$

where Q is the local shear force. As seen in Fig. 6.5. Combining eqs. 6.18-6.26, the following differential equations are obtained:

$$\left[\frac{\partial^2 u_0(r)}{\partial r^2} + \frac{1}{r} \frac{\partial u_0(r)}{\partial r} - \frac{u_0(r)}{r^2} \right] A_{11} + \left[-\frac{\partial^3 w_0(r)}{\partial r^3} - \frac{1}{r} \frac{\partial^2 w_0(r)}{\partial r^2} + \frac{1}{r^2} \frac{\partial w_0(r)}{\partial r} \right] B_{11} = 0$$

(6.27)

$$\left[\frac{\partial^2 u_0(r)}{\partial r^2}+\frac{1}{r}\frac{\partial u_0(r)}{\partial r}-\frac{u_0(r)}{r^2}\right]B_{11}+\left[-\frac{\partial^3 w_0(r)}{\partial r^3}-\frac{1}{r}\frac{\partial^2 w_0(r)}{\partial r^2}+\frac{1}{r^2}\frac{\partial w_0(r)}{\partial r}\right]D_{11}=Q_z$$

(6.28)

Combining these two equations by eliminating $u_0(r)$, a differential equation entirely in terms of the transverse deflection $w_0(r)$ is obtained:

$$\left[-\frac{\partial^3 w_0(r)}{\partial r^3}-\frac{1}{r}\frac{\partial^2 w_0(r)}{\partial r^2}+\frac{1}{r^2}\frac{\partial w_0(r)}{\partial r}\right]\left(\frac{A_{11}D_{11}-B_{11}^2}{A_{11}}\right)=Q_z \tag{6.29}$$

The shear force due to a point load is given as [174]:

$$Q_z=-\frac{P_0}{2\pi r} \tag{6.30}$$

Therefore the equation to solve is:

$$\left[-\frac{\partial^3 w_0(r)}{\partial r^3}-\frac{1}{r}\frac{\partial^2 w_0(r)}{\partial r^2}+\frac{1}{r^2}\frac{\partial w_0(r)}{\partial r}\right]\left(\frac{A_{11}D_{11}-B_{11}^2}{A_{11}}\right)=-\frac{P_0}{2\pi r} \tag{6.31}$$

The general solution for the transverse deflection $w_0(r)$ is obtained by integrating eq. 6.31 three times and can be seen to be:

$$w_0(r)=\left(\frac{A_{11}}{A_{11}D_{11}-B_{11}^2}\right)\frac{P_0}{8\pi}r^2\left(\ln(r)-1\right)+C_1\frac{r^2}{4}+C_2\ln(r)+C_3 \tag{6.32}$$

Substituting eq. 6.32 into eq. 6.27 gives the differential equation for the lateral deflection $u_0(r)$:

$$\left[\frac{\partial^2 u_0(r)}{\partial r^2}+\frac{1}{r}\frac{\partial u_0(r)}{\partial r}-\frac{u_0(r)}{r^2}\right]=\left(\frac{B_{11}}{A_{11}D_{11}-B_{11}^2}\right)\frac{P_0}{2\pi r} \tag{6.33}$$

Solving eq. 6.33 gives the lateral deflection $u_0(r)$ as:

$$u_0(r) = \left(\frac{B_{11}}{A_{11}D_{11} - B_{11}^2} \right) \frac{P_0}{8\pi} r\left(2\ln(r) - 1\right) + C_4 \frac{r}{2} + C_5 \frac{1}{r} \tag{6.34}$$

Eqs. 6.32 and 6.34 can be used as working equations to compute the transverse and lateral deflections, respectively, of a circular laminate with layers of equal diameters in closed form in terms of applied voltage and a point load after solving for the constants of integration through appropriate boundary conditions. Although the applied voltage does not appear explicitly in eqs. 6.32 and 6.34, it will appear in the final equations within the constants of integration.

The microrheometer can be divided into four concentric sections (see Fig. 6.6). The first section, α, is the inner section as defined by the central active electrode. The next section, β, has the same cross-section but the voltage is not applied here. Therefore the piezoelectric forces and moments are zero. The next section, γ, is another active area and the last section, δ, is the bare silicon diaphragm.

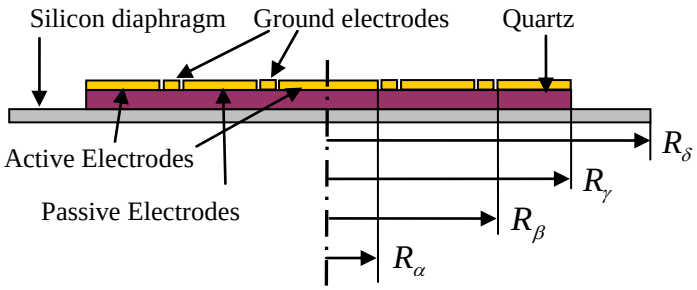

Fig. 6.6: The concentric sections of the microrheometer as denoted by their radii as given by R_α etc.

As the properties of the plate vary throughout the different sections, analytical solutions are required for each section. These solutions are obtained by applying the relations given by eqs. 6.32 and 6.34 for all continuous sections separately and then connecting them through matching continuity and equilibrium conditions at the interface of the various sections as illustrated in Fig. 6.7, an approach similar to that used in [183].

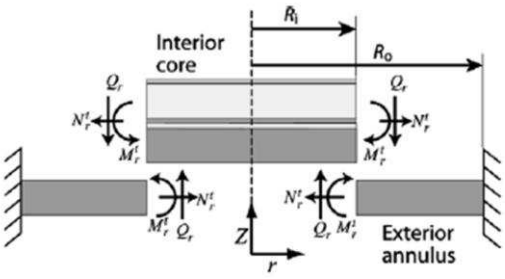

Fig. 6.7: The force and moment continuity relationships for a partially laminated plate. For clarity only two sections are displayed.

As there are four expressions for the lateral deflection (one for each section) and four for the transverse deflection, there are twenty constants of integration to solve for. Therefore the reader is referred to Appendix B for the pertinent continuity and boundary conditions. The conditions that need to be satisfied are:

1. The transverse deflection in the centre of the plate must be finite.
2. The lateral deflection in the centre of the plate must be zero.
3. The edges of the plate are fixed so the transverse and lateral deflections at the edge must be zero.
4. Similarly, the gradient of the transverse deflection must be zero at the edge.
5. At the interfaces between the sections, the deflections and gradients must be consistent.
6. Also the normal forces and bending moments acting on the interfaces must be consistent for each section.

These conditions result in the eighteen expressions given in Appendix B. These equations are too lengthy and numerous to be solved algebraically within a sensible time-frame but can be solved very quickly on a computer in matrix form to give the constants of integration. Given these constants the deflection equations can be solved (see Fig. 6.8).

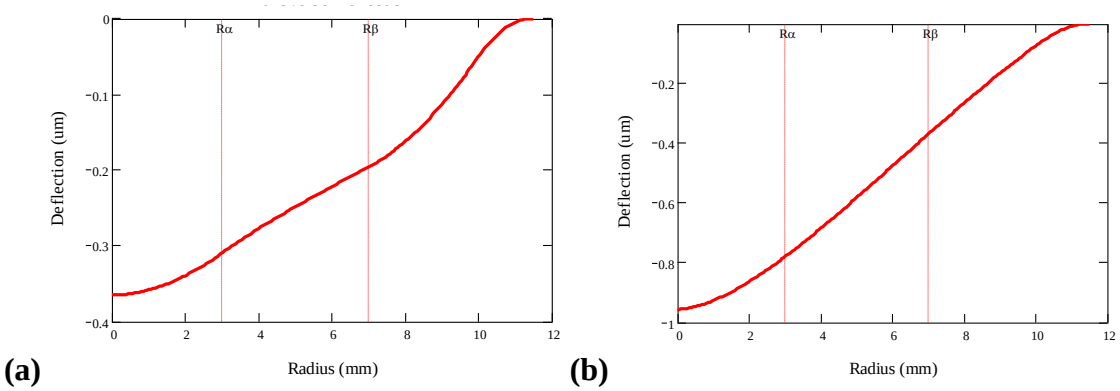

Fig. 6.8: Transverse deflections of the rheometer under an applied (a) 100V and (b) 5mN point load.

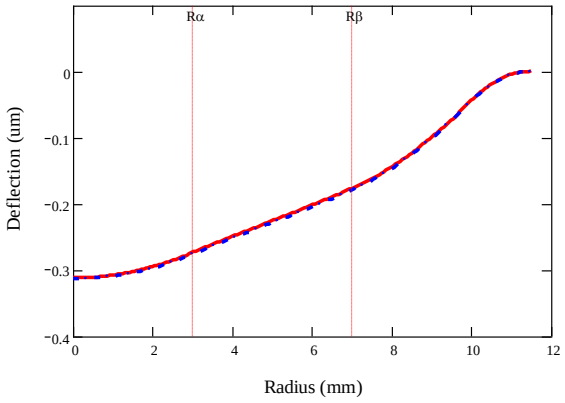

Fig. 6.9: Comparison between the solution of eq. 6.32 and the FEA solution for the transverse deflections of the rheometer under an applied 100V. Note the solutions are very similar.

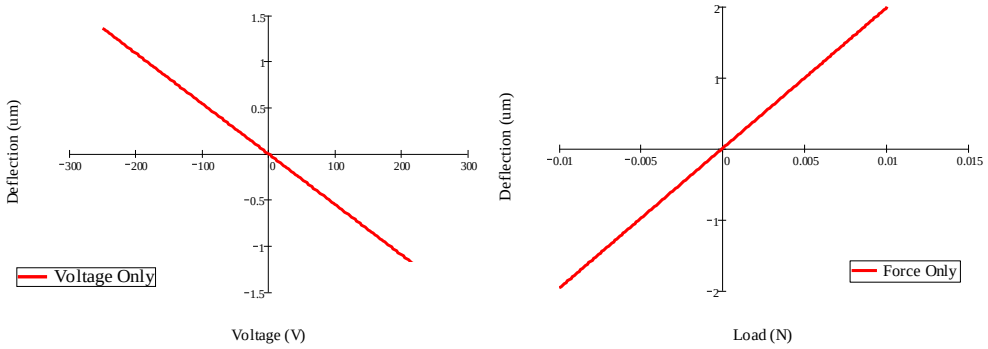

Fig. 6.10: Maximum deflection of the rheometer as a function of (a) voltage and (b) load. Note how the deflection is a linear function of the applied voltage and force.

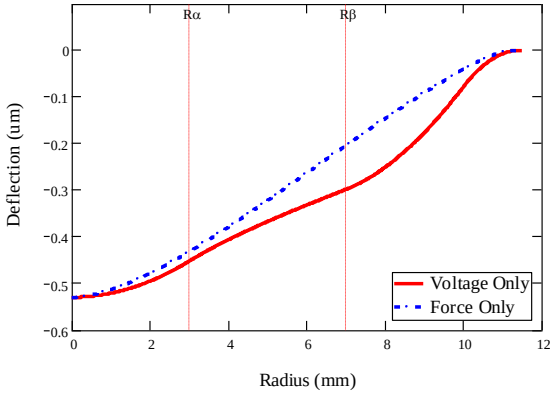

Fig. 6.11: Deflection of the rheometer as a function of voltage and load to show that movement of upper platen due to an applied voltage is indistinguishable from that of an applied load.

In Fig. 6.9 it is clear that the solution of eq. 6.32 is sufficiently accurate to allow its use in the subsequent analysis. Fig. 6.10 shows that the deflection is a linear function of both the applied voltage and the applied load. This means that we can give the voltage the form of an equivalent applied load. Doing this means the resultant force which determines the central deflection can be defined as the sum of the equivalent force due to the applied voltage and the resistive force due to the liquid. It is important to remember that when calculating strains and induced voltages it is still necessary to treat the applied voltage as a voltage. This is because it can be seen in Fig. 6.11 that the deflection profile varies

depending on whether a voltage or a load has been applied and hence the strain would be dependent too.

6.5. Plate Dynamics

These equations give the static deflection of the plate. However for the purposes of rheology, it is intended that a sinusoidal voltage and point load (the resisting force due to the fluid) is to be applied to the plate. This means the plate will oscillate and the dynamic equations of the plate will need to be considered. This is given as [174]:

$$D\Delta^2\Delta^2 w(r,t) = P(r,t) - \rho h_p \frac{\partial^2 w(r,t)}{\partial t^2} \tag{6.35}$$

P(r, t) is the effective sinusoidal force due to the sum of the applied voltage and point load. The derivation of eq. 6.35 is a simple extension of the static case made by adding the inertial forces to the plate that result from the accelerations of the mass of the plate. For the purposes of this model we will neglect damping as it is assumed that internal damping will be small compared to the damping due to the liquid.

An exact solution of eq. 6.35 in closed form is possible only for a limited number of cases regarding a plate's geometry and its boundary conditions [174]. Such a solution is certainly impractical for a plate with boundary conditions as complicated as that given here. Therefore an approximate method is required. As oscillations are small, the plate can be modelled as a sinusoidally oscillating mass on a spring. Therefore the dynamic equations can instead be shown to be:

$$\boldsymbol{M\frac{\partial^2 w_0(t)}{\partial t^2} + K_{Plate} w_0(t) = P(t)} \quad (6.36)$$

As we are assuming a sinusoidal response of the plate, this equation is easy to solve. However, the mass ($\boldsymbol{M}$) and the stiffness ($\boldsymbol{K_{Plate}}$) of the plate needs to be deduced. The stiffness is quite easy to calculate. From eq. 6.36 it can be seen that the central deflection of the plate due to the applied voltage and point load is given by the constant c_{18} – see Appendix B. It can also be seen in Fig. 6.10 that this deflection varies linearly with the applied load and point force. Therefore an effective stiffness of the plate can be found by dividing the effective force that has been applied to the plate by the deflection as given by c_{18}. It can be shown that $\boldsymbol{K_{Plate}}$ = 5252 N/m.

To calculate the inertia of the plate, first the natural frequency of the plate has to be found. Again due the complicated nature of the plate, the exact answer is difficult to find, but the Rayleigh method can be used to a reasonable accuracy [184]. Rayleigh's method for finding the natural frequency of the plate is based on the following statement:

'*if the vibrating system is conservative, then the maximum kinetic energy, K_{max}, must be equal to the maximum potential (strain) energy, U_{max}'.*

Applying this principle, consider the plate as a system with one degree of freedom undergoing free vibrations. We can present the above principle as follows:

$$\boldsymbol{U_{max} = K_{max}} \quad (6.37)$$

The kinetic energy of the plate is [174]:

$$K = \frac{1}{2}\iint_A \rho h\left[\frac{\partial w_0(r,t)}{\partial t}\right]^2 r dr d\theta \tag{6.38}$$

Assuming that the plate is undergoing harmonic oscillations, the deflection of the vibrating neutral axis of the plate can be approximated by:

$$W_0(r,t) = w_0(r)\sin\omega t \tag{6.39}$$

Where $W_0(r,t)$ is a given continuous function that represents the shapes of the plate's deflected neutral axis as a function of time and ω is the frequency we wish to find. Substituting eq. 6.39 into eq. 6.38 for the kinetic energy, we obtain:

$$K = \frac{\omega^2}{2}\cos^2\omega t\iint_A \rho h w_0(r)^2 r dr d\theta \tag{6.40}$$

It is evident that the kinetic energy is a maximum when $\cos\omega t = 1$. Thus we have:

$$K_{\max} = \frac{\omega^2}{2}\iint_A \rho h w_0(r)^2 r dr d\theta \tag{6.41}$$

Similarly the maximum strain energy for a plate can be given as:

$$U_{\max} = \iint_A \frac{D_p}{2}\left[\frac{\partial^2 w_0(r)}{\partial r^2} + \frac{1}{r}\frac{\partial w_0(r)}{\partial r}\right]^2 r dr d\theta \tag{6.42}$$

Equating eq. 6.41 and eq. 6.42 as in eq. 6.37 and solving for the frequency gives:

$$\omega^2 = \frac{\iint_A D_p\left[\frac{\partial^2 w_0(r)}{\partial r^2} + \frac{1}{r}\frac{\partial w_0(r)}{\partial r}\right]^2 r dr d\theta}{\iint_A \rho h w_0(r)^2 r dr d\theta} \tag{6.43}$$

As r continues through all four sections, these integrals need to be solved for all the sections separately and summed together. The solution is quite lengthy and won't be given here, suffice to state that the natural frequency was given as f = 2.667 kHz.

This was verified using FEA (see Fig. 6.12). Standard eigenvalue analysis was performed using the actual properties of quartz (i.e. the full anisotropic case). The value calculated for the natural frequency was f = 2.698 kHz. This means this approach is reasonably accurate and so valid. As the frequency can be defined as:

$$\omega = \sqrt{\frac{K_{Plate}}{M}} \tag{6.44}$$

The effective mass of the plate can be shown to be $\boldsymbol{M}$ = 2.376x10^{-5} kg or 18.3% of the total mass of the diaphragm and quartz which is 1.3x10^{-4}kg.

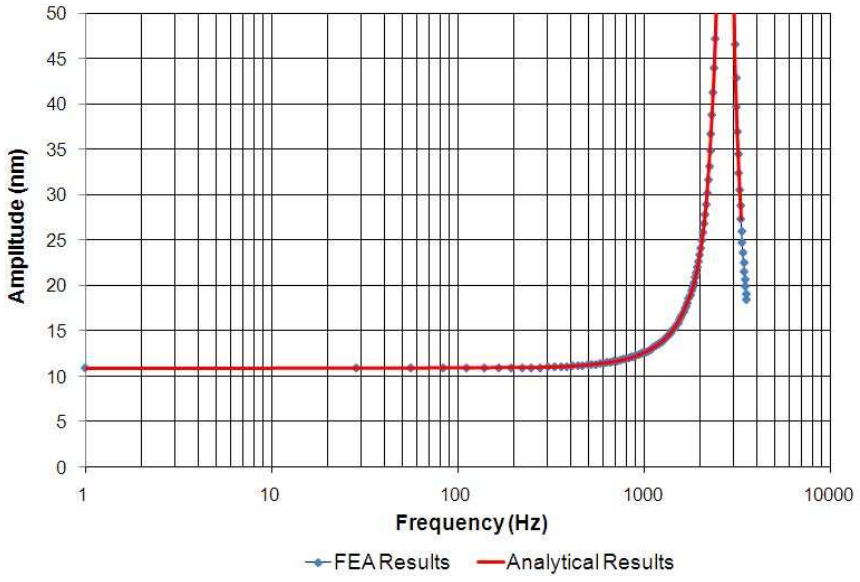

Fig. 6.12: A comparison between the FEA calculated frequency response of the microrheometer (without liquid) and the analytical solution of eq. 6.36.

6.6. Induced Voltage

Recalling the governing differential equation for this microrheometer from Chapter 3, and remembering x is the displacement of the upper platen (i.e. $x(t) = w(0,t)$):

$$M\frac{d^2x(t)}{dt^2} + C_1\frac{dx(t)}{dt} + K_1x(t) + K_{Plate}x(t) - K_{Cap}x(t) + \chi_{Cap} = F_0\sin\omega t \qquad (6.45)$$

And the solution:

$$x(t) = \sqrt{\frac{F_0^2}{(B^2 + \omega^2 C_1^2)}}\sin\left(\omega t + \tan^{-1}\left(\frac{\omega C_1}{B}\right)\right) - \frac{\chi_{Cap}}{K_{Plate} - K_{Cap}} \qquad (6.46)$$

Where:

$$B = -\omega^2 M + K_1 + K_{Plate} - K_{Cap} \qquad (6.47)$$

If the results from Chapter 4 and 5 are brought forward it can be seen that we have all the necessary coefficients to use this equation. What remains to be done is to relate the voltage induced in the plate to the response given by eq. 6.46. To do this we need to know the phase and amplitude of the resistive force. This resistive force due to the fluid is made up of several components such as the viscoelastic force and the capillary force and acts as a pressure over the area of the fluid in contact with the upper platen. As this area is small compared to the size of the plate, and as the upper platen is rigid, these forces can be assumed to act as a single point load on the centre of the plate. Similarly, for reasons given above, the applied voltage can be assumed to act as a single point load on the centre of the platen. Therefore it can be seen that the response (eq. 6.46) is just the result of having these combined forces act on the plate. This means the equations of motion can be presented in this form:

$$F_0 \sin \omega t + P_0 \sin(\omega t + \alpha) + \chi_{Cap} = x(t)\left(K_{Plate} - K_{Cap}\right) \tag{6.48}$$

This can be read as the applied voltage plus the resistive force plus the static capillary force equals the force required to deflect the plate. Substituting eq. 6.46 into this equation gives:

$$F_0 \sin \omega t + P_0 \sin(\omega t + \alpha) = X_0 \sin(\omega t + \varphi) \tag{6.49}$$

Where we let:

$$X_0 = \varepsilon\left(K_{Plate} - K_{Cap}\right) \tag{6.50}$$

X_0 can be considered to be the resultant force acting on the plate. As eq. 6.49 is just the sum of sines, the phase and amplitude of the resisting force can be given as:

$$P_0 = \sqrt{F_0^2 + X_0^2 - 2F_0 X_0 \cos\varphi} \tag{6.51}$$

$$\alpha = \tan^{-1}\left(\frac{X_0 \sin\varphi}{-F_0 + X_0 \cos\varphi}\right) \tag{6.52}$$

The validity of this approach is shown in Fig. 6.13.

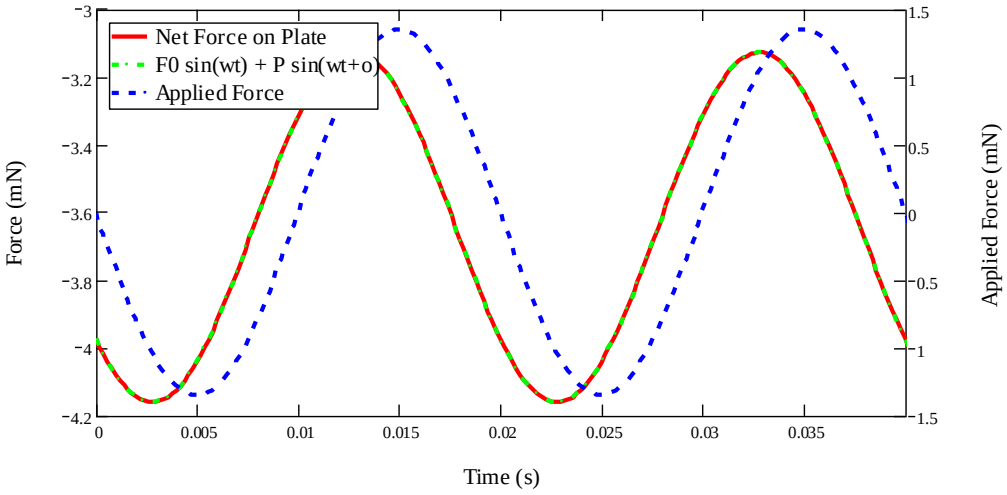

Fig. 6.13: Comparison between the applied load and the resultant load for a typical experiment. As the net force is the same as the sum of the applied load and the resisting load, eq. 6.49 is valid.

As we now know the forces acting on the plate we can calculate its deflection. This is done by substituting the forces given in the LHS of eq. 6.49 (the first term can be given as a voltage or the equivalent force) into the plate equations. As indicated in eq. 6.48 the constants need to be scaled by $\frac{K_{Plate}}{K_{Plate} - K_{Cap}}$ in order to take into account the spring effect of the surface tension acting on the plate. As this gives the deflection in the plate during an experiment equal to the response given in eq. 6.46 (see Fig. 6.14), we know the profile of the plate at any given time.

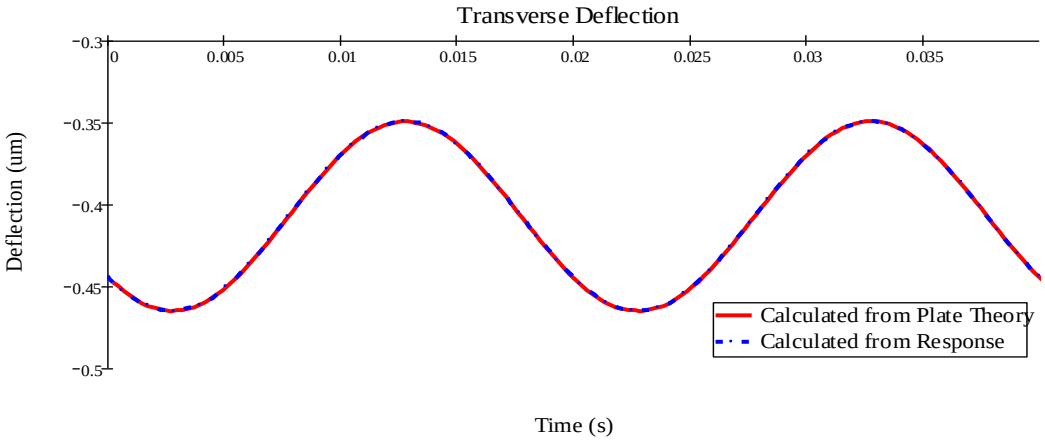

Fig. 6.14: Comparison between the deflection of the plate given by c_{18} and the response given by eq. 6.46 for a typical experiment. Note they are equal.

As the deflection and hence the profile of the plate is known at any given time, we can calculate the strain in the plate using eq. 6.15. In order to calculate the induced voltage, the strain in the quartz, specifically in section β, needs to be found. The radial and tangential strain can be defined as (refer to Appendix B for definition of constants):

$$\varepsilon_{rr}^{0} = \left(E' - z_k F'\right)\frac{P}{8\pi}\left(2\ln(r)+1\right) + \frac{1}{2}\left(c_{14} - c_{11}z_k\right) - \frac{\left(c_{15} - c_{12}z_k\right)}{r^2} \tag{6.53}$$

$$\varepsilon_{\theta\theta}^{0} = \left(E' - z_k F'\right)\frac{P}{8\pi}\left(2\ln(r)-1\right) + \frac{1}{2}\left(c_{14} - c_{11}z_k\right) + \frac{\left(c_{15} - c_{12}z_k\right)}{r^2} \tag{6.54}$$

Where ***E'*** and ***F'*** can be thought of as the lateral and transverse flexural compliances of the plate in section β and are defined as:

$$E' = \frac{B_{1,1}^{\beta}}{A_{1,1}^{\beta} D_{1,1}^{\beta} - \left(B_{1,1}^{\beta}\right)^2} \tag{6.55}$$

$$F' = \frac{A_{1,1}^{\beta}}{A_{1,1}^{\beta} D_{1,1}^{\beta} - \left(B_{1,1}^{\beta}\right)^2} \tag{6.56}$$

With a closed form solution for the strain, we can use the alternative form of the piezoelectric constitutive equations to calculate the electric field generated in the passive area of the quartz as given in eq. 6.57:

$$E = -q \cdot S + \varepsilon_s^{-1} \cdot D_i \tag{6.57}$$

Where:

$$q = g.s_D^{-1} \tag{6.58}$$

And:

$$g = \varepsilon_T^{-1} \cdot d \tag{6.59}$$

If the material is isotropic, the radial and tangential strains can be placed directly into eq. 6.57 without any coordinate transformation of the material properties matrices to give (under plane stress conditions):

$$\begin{bmatrix} E_r \\ E_\theta \\ E_z \end{bmatrix} = \begin{bmatrix} q_{11} & q_{11} & 0 & 0 & 0 & 0 \\ 0 & 0 & 0 & 0 & 0 & 0 \\ 0 & 0 & 0 & 0 & 0 & 0 \end{bmatrix} \begin{bmatrix} \varepsilon_{rr} \\ \varepsilon_{\theta\theta} \\ 0 \\ 0 \\ 0 \\ 0 \end{bmatrix} \tag{6.60}$$

Or:

$$E_z = q_{11}\left(\varepsilon_{rr}^0 + \varepsilon_{\theta\theta}^0\right) = q_{11}\left[\left(E' - z_k D\right)\frac{P\ln r}{2\pi} + \left(c_{14} - z_k c_{11}\right)\right] \tag{6.61}$$

The electric field can be defined in terms of a potential difference between two surfaces as:

$$E_z(z) = \frac{dV}{dz} \tag{6.62}$$

Therefore the induced voltage can be given as (remember the silicon diaphragm is acting as a ground electrode):

$$v_{in} = \int_{z_1}^{z_1+t_q} E_z(z)dz \tag{6.63}$$

Integrating gives:

$$v_{in} = q_{11}t_q\left[\left(E' - \left(z_1 + \frac{t_q}{2}\right)F\right)\frac{P\ln r}{2\pi} + \left(c_{14} - \left(z_1 + \frac{t_q}{2}\right)c_{11}\right)\right] \tag{6.64}$$

This is the same as integrating the electric field over just the thickness of the quartz by assuming a constant strain field equal to that found in the centre plane of the quartz, i.e.:

$$v_{in} = \int_0^{t_q} E_z\left(z_1 + \frac{t_q}{2}\right)dz \tag{6.65}$$

In eq. 6.64 part of the induced voltage is in phase with the resistive force, P_0, and part is in phase with the applied voltage. This means the induced voltage will be of the form:

$$v_{in}(t) = A_{Vout}\sin\left(\omega t + \beta\right) \tag{6.66}$$

However, the constants $\boldsymbol{c_{11}}$ and $\boldsymbol{c_{14}}$ are a function of the resistive force and the applied voltage. They are calculated by solving the boundary conditions and continuity equations given in Appendix B. Despite the apparent complexity, the calculation simplifies to this:

$$[c] = [M_p]^{-1}[N_p] \tag{6.67}$$

Where **[*c*]** is the vector of the 18 constants to be found, **[M_p]** is the 18 by 18 matrix made up of functions based on the known geometry and material properties and can be considered to be a set of known constants and **[N_p]** is the vector which is a function of the force and applied voltage. This system can be simplified by recognising that the **[N_p]** vector can be split into two parts, namely one vector which is a function of the force **[F_p]** and another which contains the piezoelectric normal forces and bending moments **[*Pz*]**. This is useful because now the constants can be expressed as:

$$[c] = [M_p]^{-1}\{[F_p]+[Pz]\} = [M_p]^{-1}\{[F']P_0 + [Pz']V_{app}\} \tag{6.68}$$

Where **[*F'*]** and **[*Pz'*]** are simply vectors filled with known constants defined by the boundary conditions and continuity equations based on the known geometry and material properties. This means that the constants c_{11} and c_{14} are defined as:

$$[c] = [M_p]^{-1}[F']P + [M_p]^{-1}[Pz']V = C^1_{11,14}P_0 + C^2_{11,14}V \tag{6.69}$$

Where $\boldsymbol{C^1_{11,14}}$ and $\boldsymbol{C^2_{11,14}}$ are simply constants found by solving the above equation. Therefore the voltage induced due the resistive force is defined as:

$$v^P_{in} = q_{11}t_q\left[\left(E - \left(z_1 + \frac{t_q}{2}\right)F\right)\frac{P\ln r}{2\pi} + \left(C^1_{14}P - \left(z_1 + \frac{t_q}{2}\right)C^1_{11}P\right)\right] \tag{6.70}$$

And the voltage induced due to the applied voltage is defined as:

$$v_{in}^{V} = q_{11} t_q \left(C_{14}^2 V - \left(z_1 + \frac{t_q}{2} \right) C_{11}^2 V \right) \tag{6.71}$$

Then the amplitude of the induced voltage is defined as:

$$A_{Vout} = \sqrt{\left(v_{in}^{P}\right)^2 + \left(v_{in}^{V}\right)^2 + 2 v_{in}^{P} v_{in}^{V} \cos\alpha} \tag{6.72}$$

And the phase of the induced voltage is defined as:

$$\beta = \tan^{-1}\left(\frac{v_{in}^{P} \sin\alpha}{v_{in}^{V} + v_{in}^{P} \cos\alpha} \right) \tag{6.73}$$

6.7. Determination of the Fluid Properties

The purpose of this chapter is to determine: 'given the measured voltage induced by the rheometer, what are the properties of the fluid?' We are now at the position to answer that question. Given the induced voltage of the form of eq. 6.66 with amplitude as given in eq. 6.72 and phase as given in eq. 6.73 the mechanical phase of the response can be shown to be:

$$\varphi = \tan^{-1}\left(\frac{P_0 \sin\alpha}{F_0 + P_0 \cos\alpha} \right) \tag{6.74}$$

where the phase of the resistive force in terms of the induced voltage is defined as:

$$\alpha = \sin^{-1}\left(\frac{A_{Vout} \sin\beta}{v_{in}^{P}} \right) \tag{6.75}$$

The mechanical amplitude of the response can be shown to be:

$$\varepsilon = c_{18}\left(\frac{K_{Plate}}{K_{Plate} - K_{Cap}}\right) \tag{6.76}$$

To calculate ε and φ we need to know the amplitude, P_0, of the resistive force in terms of the induced voltage. This is done by solving eq. 6.32 at a given instance of time. That is, at any one instant the applied voltage and the induced voltage are known. Therefore solving eq. 6.32 with the applied voltage and a range of possible resistive forces will give the induced voltage as a function of the applied load (see Fig. 6.15). It is then a simple interpolation against the actual induced voltage to deduce the amplitude of the applied load. Given the solution of eq. 6.72 and eq. 6.73, the fluid properties can be found.

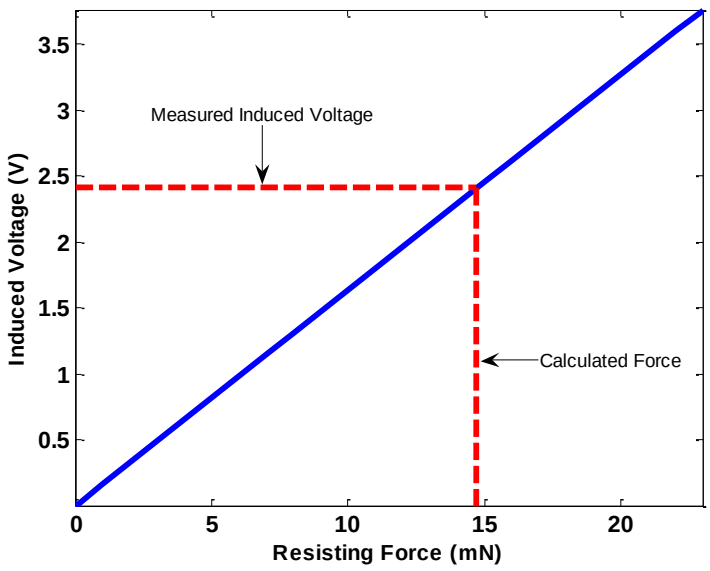

Fig. 6.15: The induced voltage as a function of applied load at a known instant of time.

To recap, in order calculate the fluid properties from the induced voltage, the following procedure needs to be followed:

1. Calculate the constants used in eq. 3.2.

2. Calculate the amplitude of the induced voltage using eq. 6.64 for a range of resisting forces, P_0, and interpolate using the measured amplitude of the induced voltage to find the actual force as in Fig. 6.15.
3. Use eq. 6.70 to find the component of the induced voltage in phase with the force and use eq. 6.75 to find the phase of the resisting force.
4. Given the phase and amplitude of the resisting force, calculate the phase and amplitude of the mechanical response using eq. 6.74 and 6.76 respectively. Solve eq. 6.67 to find $\boldsymbol{c_{18}}$.
5. Calculate the storage and loss moduli using eq. 3.7 and 3.8.

6.8. Electrical Considerations

The voltage induced by the quartz is not the voltage that will actually be measured. This is because the quartz electrodes, the oscilloscope and the intermediate wiring will affect the impedance of the circuit. The main effect will be due to the parasitic capacitance between the passive electrodes and the ground (there are also smaller capacitances caused by the potential between the passive electrode and the other electrodes as well). The basic (non-resonant) circuit for the system will look like:

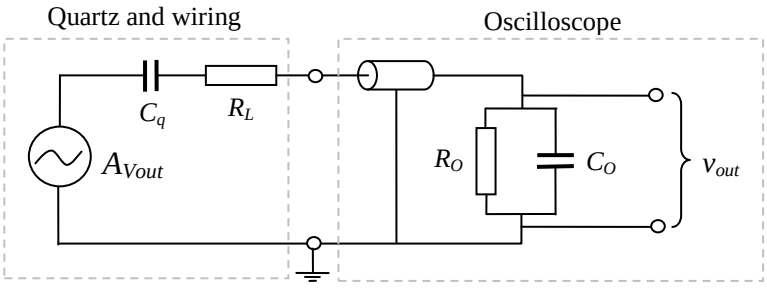

Fig. 6.16: A schematic of the basic circuit consisting of the quartz connected to an oscilloscope. The cylinder represents the input to the oscilloscope.

In this circuit the quartz is the voltage source with output described above, C_q is the capacitance of the electrodes, R_L represents the internal losses of the quartz and the wiring, R_O represents the input resistance of the oscilloscope and C_O is the capacitance of the input of the oscilloscope against its internal ground. v_{out} is the voltage that will actually be measured. To calculate the measured voltage, v_{out}, consider the impedances of the different sections of the circuit. The input impedance of the oscilloscope is given as:

$$\boldsymbol{Z_O = \frac{1}{\frac{1}{R_O} + i\omega C_O} = \frac{R_O}{1 + i\omega C_O R_O}} \tag{6.77}$$

Similarly, the load impedance of the quartz (and other losses due to wiring) is:

$$\boldsymbol{Z_q = R_L + \frac{1}{i\omega C_q}} \tag{6.78}$$

This means the circuit in fig. 6.16 can be redrawn as:

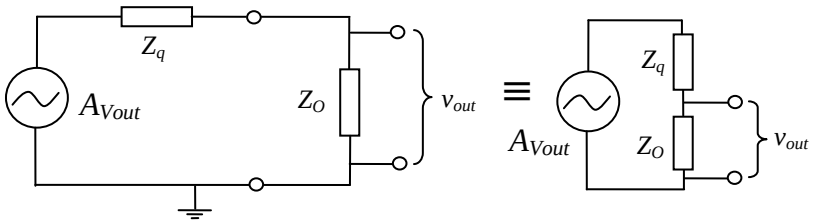

Fig. 6.17: A simplification of the basic circuit depicting how it acts as a potential divider.

Which shows the circuit acts as a potential divider and so the measured voltage is calculated as:

$$\boldsymbol{v_{out} = A_{Vout} \frac{Z_O}{Z_O + Z_q}} \tag{6.79}$$

Therefore the measured voltage will be proportional to the frequency response of the circuit which will have the form of:

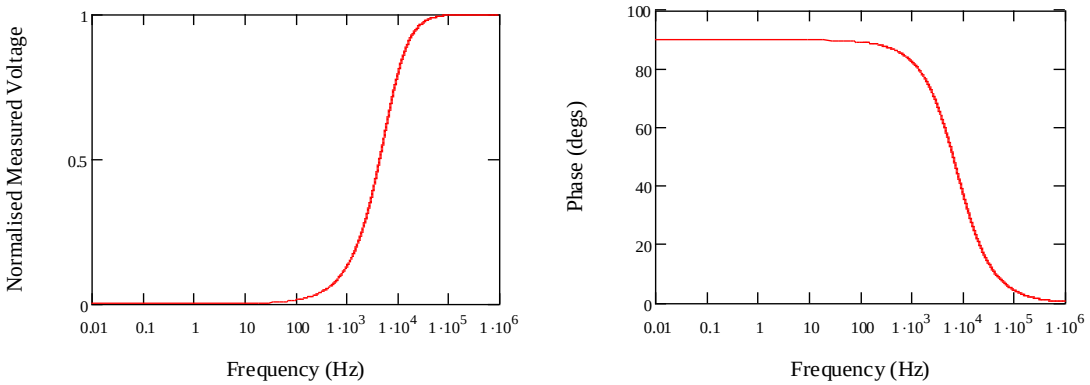

Fig. 6.18: The frequency response of the circuit for a given input signal of constant amplitude.

This means that the signal will not be measurable at low frequencies. It can be seen in eq. 6.76 that the way to improve the situation is to ensure the input impedance of the oscilloscope is high compared to the impedance of the quartz. This has to be done fairly carefully because if, for example, a large resistor was simply placed in the circuit to increase the load impedance, the cut-off frequency would be decreased but so would the amplitude of the voltage which is clearly undesirable. What is needed is a high impedance component which does not decrease the amplitude of the signal. A unity gain op-amp (or buffer) can be used because its input impedance is very high (for example the input impedance for the LF351 op-amp is 1 TΩ). The modified circuit will be equivalent to:

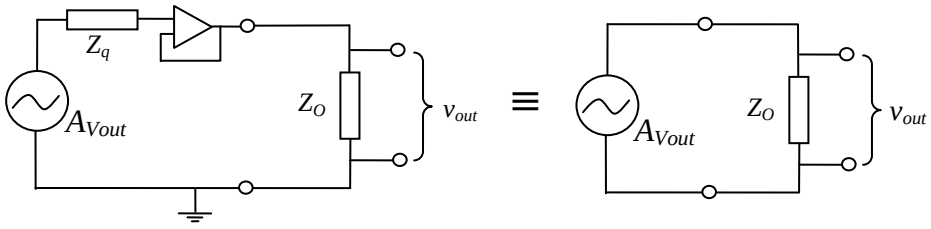

Fig. 6.19: A schematic of the improved circuit.

As the input impedance is high, no current can flow into the buffer amplifier. This means the voltage drop across the impedance of the quartz is zero, and therefore the input voltage into the amplifier is v_{in}. As the amplifier has unity gain, the voltage across the oscilloscope is also v_{in} which means the measured voltage equals the induced voltage, negating the frequency dependency of the quartz.

6.9. Conclusion

In this chapter the mechanics of the rheometer has been discussed. It was shown in Chapters 4 and 5 that the force due to the surface tension effects and the viscoelasticity of the liquid acts as a sinusoidal point load in the centre of the rheometer. This force was built into the model of the rheometer whereby the static deflection of the rheometer due to an applied voltage and the resistive force was derived. The resulting equations were used to calculate the stiffness and inertia of the plate for use in the solution of the governing differential equation of motion for the rheometer as used in Chapter 3. The deflection equations were used to calculate the strain induced in the quartz during operation in order to deduce the induced voltage which is to be measured. It was then shown that this induced voltage could be related back to the properties of the fluid.

7 FABRICATION

In this chapter, the various methods used in the construction in the microrheometer will be discussed. Initially the basic techniques (such as photolithography etc.) will be briefly explained so that they can be referred to in the subsequent sections. The specific recipes relating to the actual parameters (such as etch times etc.) used in the fabrication of the different parts of the microrheometer will be described.

7.1 Basic Techniques

A number of different techniques are required to fabricate MEMS devices. In this section only the techniques that are important to the fabrication of the microrheometer will be discussed. As most of these techniques are now commonplace within the MEMS community, they will only be discussed briefly so that the reader can appreciate the specific fabrication steps described later on. Detailed descriptions of the processes can be found in the various references.

7.1.1 Photolithography

Photolithography is used to partially protect surfaces and so define the area to be etched prior to selectively removing parts of a substrate with etch processes [185, 186]. This is achieved by first coating the substrate with a light-sensitive polymer called photoresist, usually by pouring the photoresist onto the substrate and spinning it at a prescribed speed until it obtains a specific thickness. After spinning, the resist is then soft baked at about 75 to 100°C for a short while to remove any solvents and stress in the photoresist layer and to promote adhesion to the underlying substrate. The photoresist is then selectively exposed

to ultra-violet light by protecting parts of the photoresist using a mask (an opaque plate with holes or transparencies that allow light to shine through in a defined pattern) for example see Fig. 7.1. The UV radiation induces a chemical reaction in the exposed areas of the photoresist, altering its solubility in a developer.

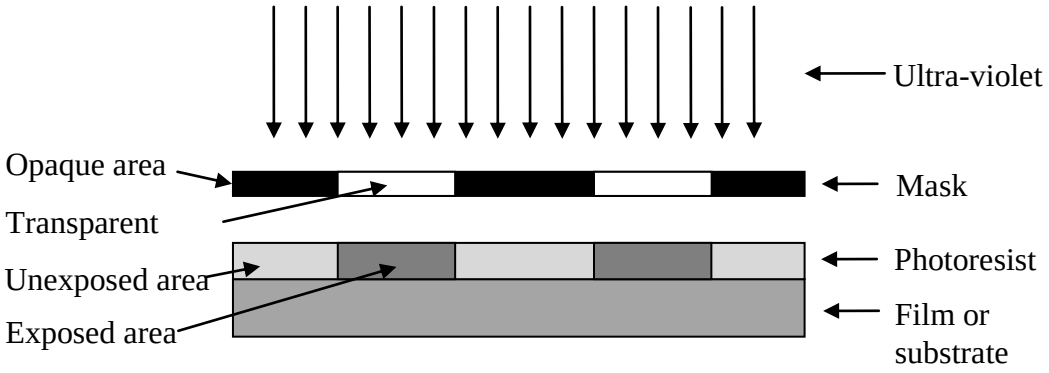

Fig. 7.1: A schematic of the exposure process that takes place during photolithography.

Development transforms the latent image formed during exposure into a relief image (see Fig. 7.2) which will serve as a mask during any subsequent fabrication steps. Developing essentially means that selective dissolving of the photoresist by using solvent takes place. The mechanism that allows this depends on the photoresist used, but fundamentally the exposure to UV light causes the molecules in the photoresist to change by either promoting cross-linking or chain scission or by converting the initially insoluble sensitizer into a soluble acid product. In practice, developing is achieved by submerging the whole substrate and photoresist in a specific solvent for a prescribed time with agitation. The substrate is then rinsed with de-ionised water, dried using compressed nitrogen and hard baked. Hard baking involves heating the photoresist above its glass transition temperature. This enables the photoresist to anneal into its most stable state. This results in a 1:1 relief image of the entire mask in the photoresist.

Fig. 7.2: A schematic of the substrate after photolithography. Note how part of the substrate is exposed.

7.1.2 DRIE

After being patterned using photolithography, the substrate is usually etched. A common type of etching is DRIE etching. DRIE (or Deep Reactive Ion Etching) is a highly anisotropic etch process used to create deep, steep-sided holes and trenches in wafers (see Fig. 7.3). It uses chemically reactive plasma to remove material from exposed substrates (hence this process is preceded by the photolithography process which specifies the area to be etched). The substrate is then etched by physically bombarding it with ions or chemically by a chemical reaction with the reactive high-energy ions at the surface (or commonly, a combination of these two mechanisms) [187, 188].

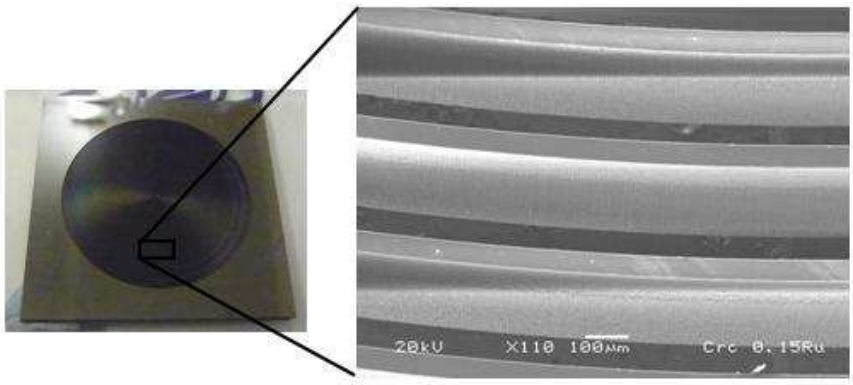

Fig. 7.3: A typical example of deep reactive ion etching. Here the back of the silicon diaphragm of the rheometer has been etched – see Fig. 7.11 for details.

A DRIE system typically consists of a vacuum chamber, with a (electronically isolated) wafer platter situated in the bottom portion of the chamber (see Fig. 7.4). Gas enters through small inlets in the top of the chamber, and exits to the vacuum pump system

through the bottom [189]. The type and amount of gas used varies depending upon the etch process; for instance, sulphur hexafluoride is commonly used for etching silicon. Gas pressure is typically maintained in a range between a few millitorr and a few hundred millitorr by adjusting gas flow and/or adjusting an exhaust orifice. The etcher used for the fabrication of the microrheometer (A STS Multiplex ICP DRIE etcher (STS Plc., UK)) has the additional feature of utilising an inductively couple plasma (ICP). In this type of system the plasma is generated with an RF powered magnetic field which increases the etch rate (but may enhance the isotropic nature of the etch). The field is set to a frequency of 13.56 megahertz, at a few hundred watts. The oscillating electric field ionizes the gas molecules by stripping them of electrons, creating plasma.

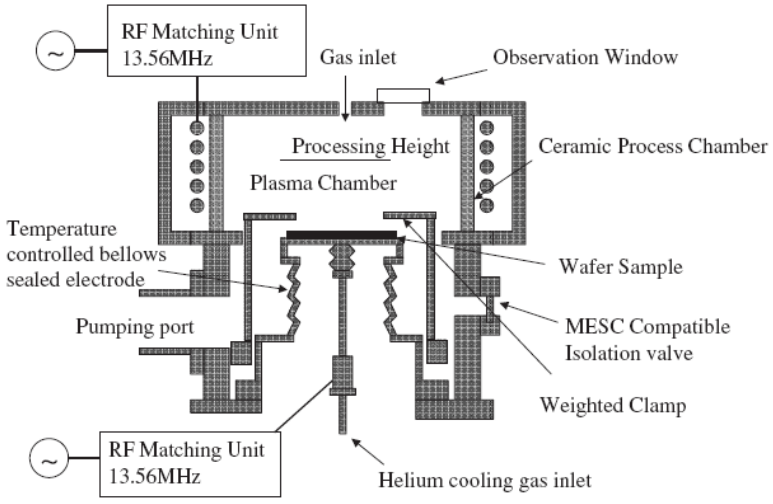

Fig. 7.4: A schematic of the STS ICP etcher [190].

In each cycle of the field, the electrons are electrically accelerated up and down in the chamber, sometimes striking both the upper wall of the chamber and the wafer. At the same time, the much more massive ions move relatively little in response to the RF electric field. When electrons are absorbed into the chamber walls they are simply fed out to ground and do not alter the electronic state of the system. However, electrons absorbed

into the wafer cause it to build up charge due to its DC isolation. This charge build up develops a large negative voltage on the platter, typically around a few hundred volts. The plasma itself develops a slightly positive charge due to the higher concentration of positive ions compared to free electrons. Because of the large voltage difference, positive ions tend to drift toward the wafer platter, where they collide with the samples to be etched. The ions react chemically with the materials on the surface of the samples, and can also knock off (sputter) some material by transferring some of their kinetic energy to the atoms in the substrate. Due to the mostly vertical delivery of reactive ions, reactive ion etching can produce very anisotropic etch profiles, which contrast with the typically isotropic profiles of wet chemical etching [188].

The anisotropy of the etch, and etch depth is improved by utilising the Bosch process. Also known as pulsed or time-multiplexing etching [189], the Bosch process alternates repeatedly between two modes to achieve nearly vertical structures. The first mode is the standard plasma etch already described. The other is the deposition of a chemically inert passivation layer. In this case C_4F_8 is the source gas used. Each phase lasts for several seconds. The passivation layer protects the entire substrate from further chemical attack and prevents further etching. However, during the etching phase, the directional ions that bombard the substrate attack the passivation layer at the bottom of the trench (but not on the walls). They collide with it and sputter it off, exposing the substrate to the chemical etchant, which removes material from the bottom of the structure but not off the side walls. This produces a highly anisotropic etch.

These etch/deposit steps are repeated many times, resulting in a large number of very small isotropic etch steps taking place only at the bottom of the etched pits. To etch through a 0.5

mm silicon wafer, for example, 100–1000 etch/deposit steps are needed. The two-phase process causes the sidewalls to undulate with an amplitude of about 100–500 nm (see Fig. 7.5). The cycle time can be adjusted: short cycles yield smoother walls, and long cycles yield a higher etch rate.

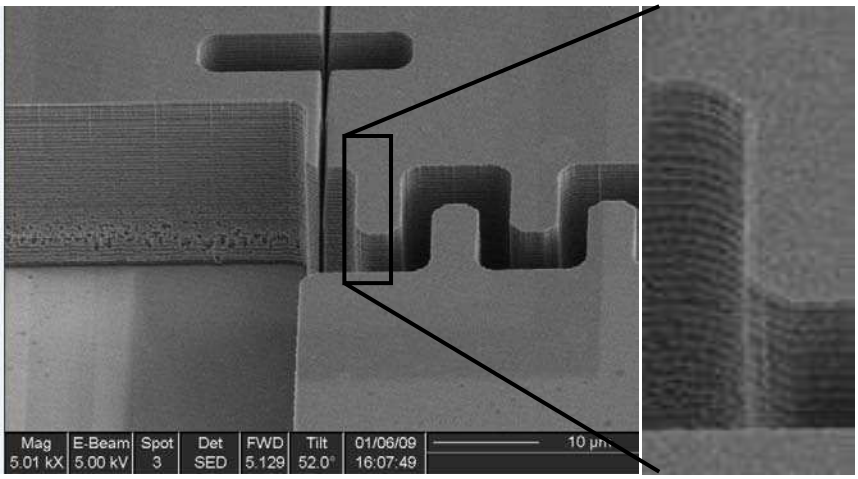

Fig. 7.5: An example of the scalloping effect caused by the Bosch process (insert is a close-up). Picture courtesy of Dr. Emma Carter.

7.1.3 HF Etching

As well as DRIE, another type of etching is wet etching. Wet etching has many uses, but in this context it will be used as part of a sacrificial process, whereby a material (the oxide layer in the BSOI) is used purely to facilitate fabrication but is then removed from the final device.

As will be shown later, the active part of the microrheometer (the silicon membrane) was fabricated from a BSOI (Bonded Silicon on Insulator) wafer. These wafers consist of a thin silicon device layer of specific thickness and conductivity, bonded to a thin oxide layer which has been grown onto a much thicker silicon handle wafer. The advantages of using

such a wafer over a standard wafer are the result of the drastic difference in the chemical and electrical properties of the silicon to its oxide. Specifically, the oxide layer can resist deep reactive ion etching far better than silicon. Therefore it can be used as an etch stop and then selectively removed using HF. For example, later it will be described how the handle wafer was patterned using photolithography and then etched using DRIE through to the oxide leaving the diaphragm unharmed.

The oxide layer in this case is no longer desirable after it has achieved its purpose as an etch stop and needs to be removed, leaving the silicon membrane behind. This is possible because the chemistry of the oxide is sufficiently different, i.e. it is chemically selective, from the silicon that it can be etched away using HF (Hydrogen Fluoride) which attacks silicon dioxide but not silicon, i.e. the oxide layer has been sacrificed. Here, as the etched silicon acts as a mask, the oxide can be removed by simply submerging it in the HF in a Teflon container. The etch is isotropic and will undercut the silicon. Normally, stiction is an issue when using HF to remove a sacrificial oxide layer. This is because surface tension can cause released silicon structures to collapse and stick to each other, therefore HF vapour is frequently used [191]. In this case stiction can not occur and so a standard wet etch procedure was used. A typical process involves using a solution of HF in water with a concentration of 1:10. This gives an etch rate of around 0.45µm /min at room temperature [192].

7.1.4 Metal Deposition

The quartz in the microrheometer is a piezoelectric material. As such it needs to be placed between two electrodes with a potential difference placed across them for it to actuate the microrheometer. As the quartz is bonded to a silicon membrane with high conductivity, it

is only its upper surface that requires an extra electrode. This is achieved by coating the quartz with a conductive material. The natural choice for the electrode material is gold as it is highly conductive. To improve adhesion, a thin layer (around 20nm) of another metal with low electron deficiency (usually Cr, Al, Ti etc.) is deposited onto the quartz prior to gold deposition.

As gold has a relatively low melting temperature [193] it can be thermally evaporated. Thermal evaporation (also called filament or resistive evaporation) is the simplest method of evaporating metals. Here metal sources are placed on filaments (made from a material of high melting temperature such as tungsten or molybdenum) and heated under vacuum to their melting points by passing a current through the filament until metal source sublimates. The liquid metal gives off a vapour; the atoms of which have kinetic energy proportional to the melt temperature. The metal atoms then travel in a straight line from the source to the sample. The metal vapour then condenses on the cooler surface of the sample, forming the desired metal layer.

For the metals used in the adhesive layer, the temperature produced in the filament is usually not high enough to cause evaporation. For this reason electron beam (e-beam) evaporation is used [187]. Here a high-intensity electron gun (5 keV) is magnetically directed onto the metal source. The metal is kept in a water-cooled crucible and is heated by the directed electrons until the metal melts, evaporates and is deposited on the substrate.

7.1.5 Lift-off Process

In the photolithographic process, not all photons strike the resist film in an orthogonal fashion. Diffraction at the substrate/resist interface causes a broadening of the exposed

region. The diffracted radiation profile for a positive resist (especially pronounced with overexposure) can lead to a lip or overcut in the profile of the remaining resist (see Fig. 7.6a), which can lead to shadow masking. This can be taken advantage of in the so-called lift-off process [187]. Here after photolithography, instead of etching the substrate, metal is deposited onto the resist in a manner described above. Then a solvent is used to dissolve the remaining resist underneath the metal, starting at the lip of the resist and 'lifts-off' the excess metal in the process. This leaves areas of patterned metal on the substrate, such as those required in the electrodes of the quartz. The process is shown schematically in Fig. 7.6.

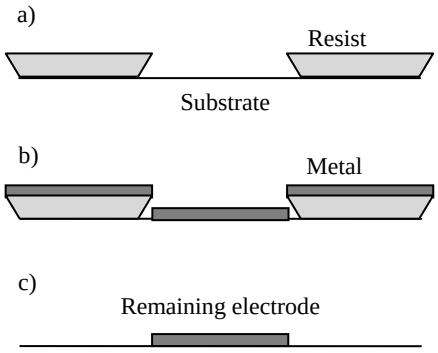

Fig. 7.6: A schematic of the lift-off process; a) define photoresist, b) deposit metal and c) remove excess resist.

7.1.6 Direct Bonding

Direct wafer bonding technology is a technique used to fuse two wafers together by heat. Typically it is used to bond two Si wafers or two SiO_2 wafers. The technique is becoming increasingly common because of its versatile application. For example two silicon wafers of varying conductivity can be joined to form the P-N junction in a diode with little further processing [194]. In the fabrication of the microrheometer, this process is used to bond the quartz piezoelectric layer to the silicon membrane. As silicon readily forms a native oxide

at room temperature (approximately 20Å thick) this bond can be considered as though it was between two SiO_2 substrates.

For the bonding of two wafers to be successful, they have to be very clean and very flat. This allows for the SiO_4 tetrahedra on the surface of the substrates to be able to be brought into intimate contact so they can form a stable bond. In order to control the flatness of the quartz wafer and so promote bond strength, AML (Applied Microengineering Ltd, the company contracted to perform the bonding) has developed a tool called a 'pin chuck' [195]. The chuck consists of spring pins of decreasing height from the centre outwards which gradually dissipates a force across the entire bonding area (see Fig. 7.7). In this system the second wafer is held inverted above the lower pin chuck wafer. An actuator pin is used to bow the second wafer, changing its curvature from a flat wafer to over 200µm (depending on the thickness/stiffness of the wafer).The actuator pin contracts as the wafers come into contact. This ensures that the bond starts from the centre of the wafers, and more importantly that the rate and direction of the bond propagation can be controlled. This eliminates the chance of multiple bond fronts intersecting and trapping voids in the bond.

Fig. 7.7: The AML pin chuck. Reproduced from [195].

The original theory for the bonding of two surfaces of SiO_2 was developed by Lasky [196]. According to this theory, the wafer bonding process occurs when the gaseous oxygen trapped between the two wafers is converted to the silicon dioxide by the oxidation of silicon. The bonding mechanism is depicted in Fig. 7.8 which shows the state of the wafers immediately preceding the bond. It is well known that the surface of an oxidised silicon wafer terminates at the Si dangling bonds. These bonds react rapidly with water (either atmospherically or during wafer cleaning etc.) to form SiOH groups. Therefore, the surface of an oxidised wafer normally contains silicon hydroxyl groups (as shown in Fig. 7.8). When the wafers are pressed together and heated, the two opposite OH groups interact forming H_2O and the Si-O-Si siloxane bond. This reaction can be described by the equation:

$$\text{Si-OH + HO-Si} \rightarrow H_2O + \text{Si-O-Si}$$

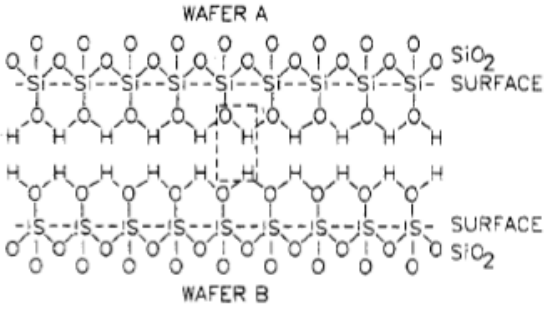

Fig. 7.8: A representation of the hydroxyl groups on oxidized silicon wafers prior to bonding (reproduced from [197].

As quartz crystal (SiO_2) has a large thermal expansion coefficient ($14.5 - 16.9\times10^{-6}$) compared to that of silicon (4.9×10^{-6}), low-temperature bonding is necessary in order to avoid excessive thermal strain. It has been known for some time that high strength wafer

bonding can be achieved by exposure to oxygen plasmas for a few minutes followed by a 200°C, 60 minute anneal step (compared to the conventional process which uses a 1000°C annealing process without plasma [194]). However it can be shown that the plasma can cause excessive ion bombardment which can cause a roughening of the wafer surface, decreasing bond strength. AML have developed a new process similar to plasma activation using radicals [198, 199]. It uses mesh electrodes to create a field-free space surrounding the wafers, ensuring that the radicals that approach the wafers are neutral and with negligible perpendicular velocity. This ensures that any impact with the wafers is minimal - preventing etching of the surface. The process as used by AML is therefore:

1. Load wafers onto top and bottom platens of the aligner-bonder
2. Pump down to a base pressure of 5×10^{-5} mBar
3. Introduce wet oxygen and maintain a dynamic pressure of 1 mBar
4. Strike discharge and maintain a voltage of 500 VDC
5. Switch off discharge and pump down to base pressure
6. Bond wafers in-situ at base pressure
7. Remove wafers and anneal

7.2 Specific Recipes

In this section it will be shown how the above techniques were utilised in the fabrication of the microrheometer. There are two main parts to the microrheometer as discussed in previous chapters. These include the base plate and the upper active plate. There are three different versions of the active plate: one comprised of a prefabricated thin quartz disc glued to the silicon membrane, one of a PZT disc glued to the membrane and finally, the one which uses whole wafer bonding methods. All four parts of the microrheometer will

be discussed separately below. As some processes are repeated, where possible they will be discussed once and the reader will be referred back where applicable.

7.2.1 Base Plate

This is the chip which contains the static lower platen. It also contains features which allow for the aligning of the upper and lower platens, a sunken section to allow excess fluid to run away from the platens and vias which allow the free movement of air (which prevents extra damping due to trapped air). The schematic is shown in Fig. 7.9 below:

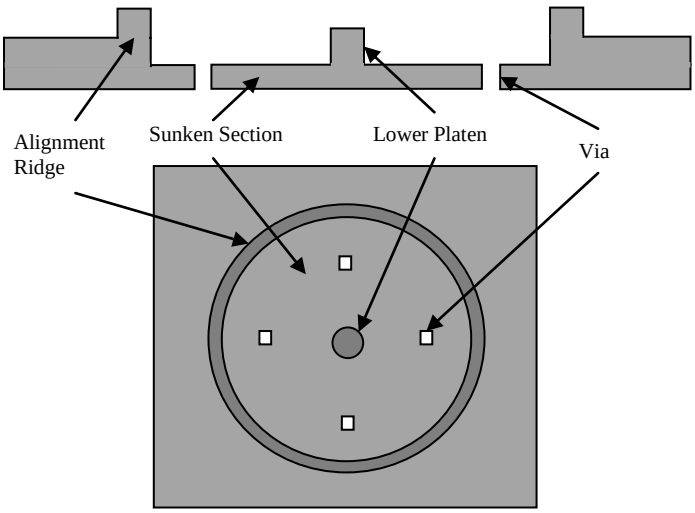

Fig. 7.9: A schematic of the base plate from the side and from the top showing the general arrangement of the features.

The base plate is made from a standard single crystal silicon wafer. As can be seen from Fig. 7.9, the features are defined by etching down into the wafer to four different heights.

The procedure is outlined below:

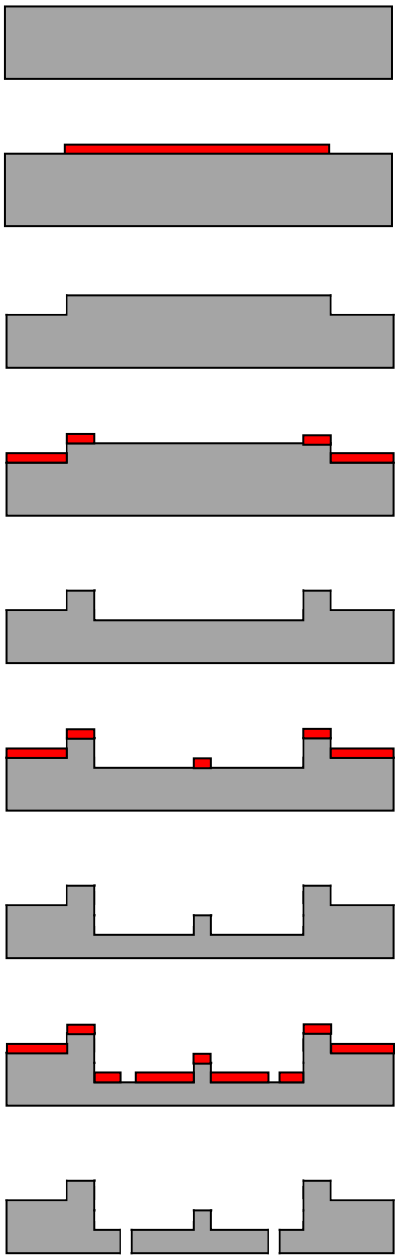

- Start with a single crystal silicon wafer, 525µm thick, 100mm diameter.
- Spin on SPR 220-7 (Chestech, UK) photoresist and pattern (see Table 7.1 for complete process)
- DRIE etch down 100µm to define the outside of the alignment ridge (see Table 7.2 for etcher parameters).
- Spin on SPR 220-7 photoresist and pattern (see Table 7.1 for complete process)
- DRIE etch down 120µm to define the inside of the alignment ridge and to set gap between platens (see Table 7.2 for etcher parameters).
- Spin on SPR 220-7 photoresist and pattern (see Table 7.1 for complete process)
- DRIE etch down 200µm to define the lower platen and sunken region (see Table 7.2 for etcher parameters).
- Spin on SPR 220-7 photoresist and pattern (see Table 7.1 for complete process)

Fig. 7.10: Fabrication steps for the passive layer.

This last step obviously shows that the wafer now has holes through it. This meant that the wafer had to be supported by a handle wafer in order to maintain the correct gas flow within the etcher chamber. The processed wafer was attached to the handle wafer using thermal tape (Nitto Denko, Japan). This allows for the simple and clean release of the processed wafer by heating of the handle wafer to above 120°C whereupon the adhesivity

of the tape is significantly reduced. It is also to be noted that after each etch, the photoresist was removed using oxygen plasma cleaning whilst the wafer was still in the etcher; the parameters of that procedure are displayed in Table 7.3. Similarly, after the last etch (and O_2 clean), the whole processed wafer was coated in C_4F_8 (the reasons for which have already been described in Chapter 4). The parameters of this process, which was also completed whilst the wafer was in the etcher, are given in Table 7.4.

Spin speed	Slow ramp to 500rpm for 10s, slow ramp to 2000rpm for 30s
Resist thickness	9µm
Soft bake	115°C for 90s
Exposure	45s (dose = 470mJ/cm^2)
Developer	Submerged in MF-26A (Chestech, UK) for 60s at room temp
Hard bake	115°C for 60min

Table 7.1: The procedure for the patterning of SPR220-7 (Chestech, UK) which is a positive photoresist.

	Etch Cycle	Passivate Cycle
SF_6 Flow Rate	100 sccm	0 sccm
C_4F_8 Flow Rate	0 sccm	85 sccm
Duration	12s	5s
13.56MHz Platen Power	800W	600W

Table 7.2: The parameters for the standard DRIE etch using the STS Multiplex ICP DRIE etcher (STS Plc., UK). Process divided into two according to the Bosch process (see above).

O_2 Flow Rate	100 sccm
Duration	10min
13.56MHz Platen Power	800W

Table 7.3: The parameters for the standard oxygen plasma clean using the STS Multiplex ICP DRIE etcher (STS Plc., UK).

C_4F_8 Flow Rate	85 sccm
Duration	1min 23s
Film Thickness	250nm
13.56MHz Platen Power	600W

Table 7.4: The parameters for the C_4F_8 (Pelchem, South Africa) deposition using the STS Multiplex ICP DRIE etcher (STS Plc., UK).

7.2.2 Mark I

The Mark I device was the earliest prototype of the active plate of the microrheometer. It comprised a thin quartz disc (bought ready cut to shape - MaTeck, Germany) glued to the silicon membrane. The use of glue is not ideal because the properties and thickness of the adhesive are not completely known and there is likely to be alignment issues as the quartz is attached by hand. Fortunately the adhesive layer only has a small effect on the overall stiffness of the rheometer. However, this method uses the least number of processes (and can be fabricated completely in house) and is the cheapest process. Therefore this prototype is used principally to test the feasibility of the microrheometer and to allow the testing of the electronics and mathematical models. The process is described below:

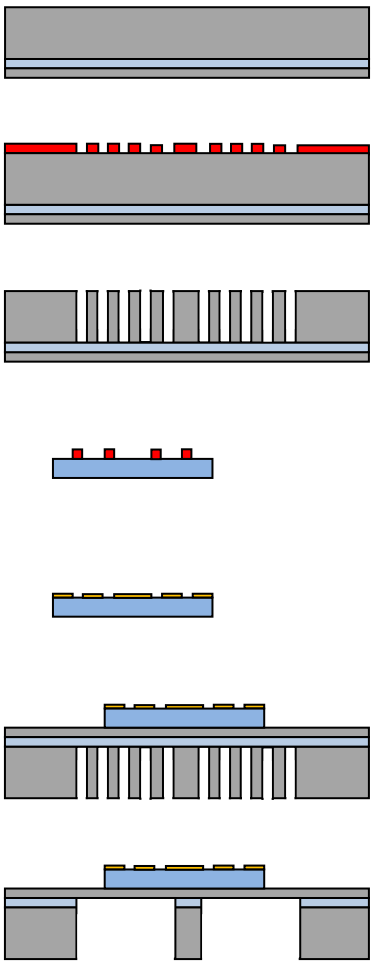

- Start with a 100mm diameter BSOI wafer with 50µm device layer, 1µm oxide layer and 500µm handle wafer.
- Spin on photoresist in a manner as described in Table 7.1.
- DRIE down through the handle wafer to the oxide layer (see discussion below).
- Take a 20mm diameter, 100µm thick X-cut quartz disc and pattern photoresist (see Table 7.1).
- E-beam evaporate 20nm titanium and thermally evaporate 200nm gold to form the electrodes and remove photoresist.
- Glue quartz disc onto silicon membrane.
- Remove the supporting silicon by HF etching the oxide layer away (see relevant section above).

Fig. 7.11: Fabrication steps for the Mark I active layer.

DRIE was used to etch through the handle wafer is used to define the upper platen and the edge of the silicon membrane. This was done in two stages. The first used the standard etch as described in Table 7.2. When the oxide layer was becoming exposed, the second etch process was implemented. The etch process is not completely homogenous across the entire wafer, especially after long etches (the etch rate achieved using the process used in Table 7.2 is about 2.5µm/min, therefore an etch of about 3hrs 15min is required to etch through the handle wafer). Therefore the outer edges of the silicon membrane tend to get etched a little quicker. This means the oxide gets exposed in this area first. At this point the standard etch is stopped and a low frequency etch is used. This produces plasma with less momentum than the standard etch process. Therefore the velocity at which the ions impinge on the oxide layer is reduced and so is the amount of back scattering which causes under cutting near the oxide layer. This process is only used at the last few minutes because it has a much slower etch rate and because it is a more isotropic etch as it precludes the use of the Bosch process.

The photoresist was patterned as to leave concentric rings of silicon behind after the DRIE etch. This was because in order to glue the disc to the membrane, significant pressure had to be applied to the disc to squeeze out excess glue. The membrane alone is not strong enough to support this process and so the silicon was left to support it whilst still allowing the HF access to the underlying oxide.

The photoresist was removed by using oxygen plasma as described in Table 7.3 and the last step was to coat the upper platen with C_4F_8 as described in Table 7.4.

7.2.3 Mark II

The Mark II microrheometer uses PZT as the piezoelectric layer instead of quartz. Similar to the Mark I device, the PZT is glued to the silicon membrane with the disadvantages already described. However, the decision to use PZT was based on the fact that it requires a lower voltage to achieve large displacements and is a more isotropic material than quartz and so is easier to model. Despite the disadvantages described previously and in Chapter 6, this prototype was fabricated to test the extent of the issues and see whether a successful microrheometer can still be made using PZT. The fabrication process is similar to the Mark I process and is described below:

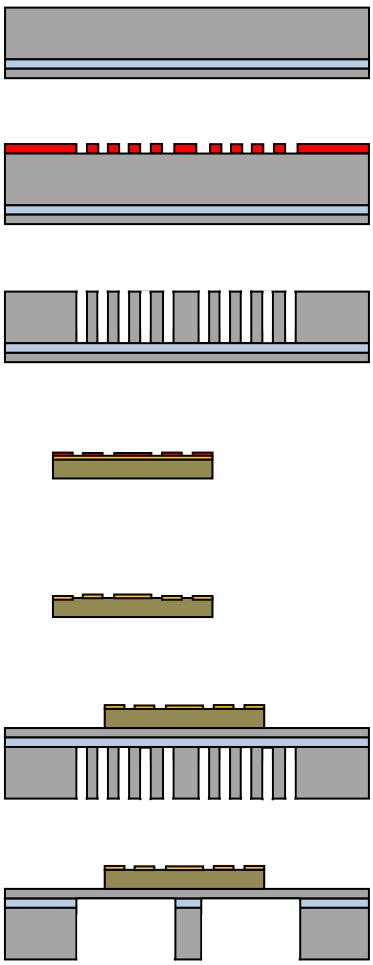

- Start with a 100mm diameter BSOI wafer with 50µm device layer, 1µm oxide layer and 500µm handle wafer.
- Spin on photoresist in a manner as described in Table 7.1.
- DRIE down through the handle wafer to the oxide layer (see discussion below).
- Take a 20mm diameter, 250µm thick PZT disc and pattern photoresist (see Table 7.1).
- Submerge disc in nitric acid for 60s to dissolve exposed silver coating leaving remaining silver for the electrodes.
- Glue PZT disc onto silicon membrane.
- Remove the supporting silicon by HF etching the oxide layer away (see relevant section above).

Fig. 7.12: Fabrication steps for the Mark II active layer.

It is obvious the processes used in the fabrication of the Mark I and II microrheometer are very similar. The only real difference is that the lift-off process is not required when using PZT. This is because PZT needs to be polarised during its fabrication in order to make it piezoelectric. To do this the PZT is coated on both sides with silver and a potential applied across the two surfaces to reorient the domains within the PZT in the correct direction. In the Mark II, this silver coating can be used for the electrodes but they need to be patterned using nitric acid to isolate the active electrodes and the passive electrodes.

7.2.4 Mark III

The Mark III microrheometer uses whole wafer bonding of a quartz wafer onto the silicon membrane. This means that there is no gap between the quartz and silicon and the properties of all materials are well defined. The processes used should also ensure that alignment is good and that the behaviour of the microrheometer is as close to ideal as is feasibly possible. It is however, a complicated process dependent on external companies to produce, but the process does show the possible commercialisation of the device. The process is described below:

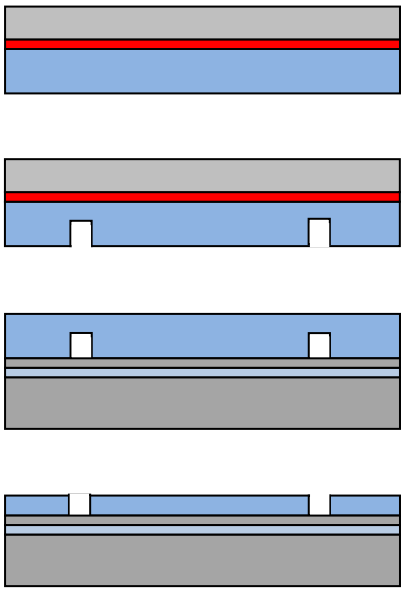

- Start with a 100mm diameter 500µm thick X-cut quartz wafer attached to a silicon handle wafer using PMMA.
- Powder blast (see discussion below) part way through the quartz to define disc shape.
- Use direct bonding (see applicable section above) to bond quartz to BSOI wafer and remove handle wafer.
- Use chemical mechanical polishing to thin quartz down to 100µm thickness.

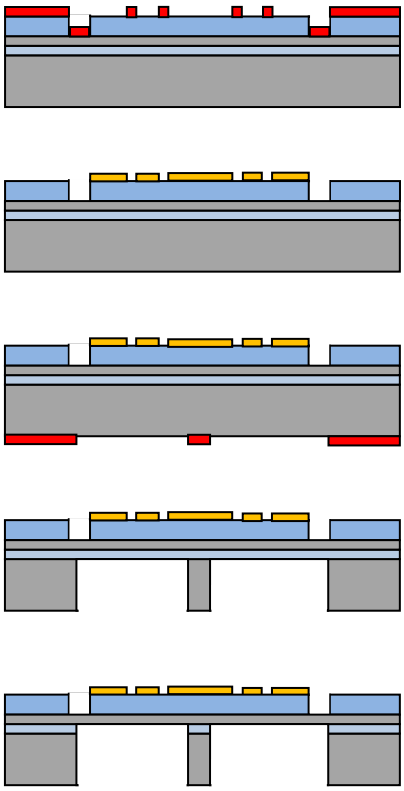

- Spin on and pattern photoresist according to Table 7.1.
- Use metal deposition and lift-off process as described above to pattern electrodes comprising of 20nm titanium and 200nm gold.
- Spin on photoresist in a manner as described in Table 7.1.
- DRIE down through the handle wafer to the oxide layer (see discussion below).
- Remove the any remaining silicon by HF etching the oxide layer away (see relevant section above).

Fig. 7.13: Fabrication steps for the Mark III active layer.

Powder blasting was not described before as it is such a simple process. Powder blasting, or abrasive jet machining (AJM), is a technique in which a particle jet is directed towards a target for mechanical material removal. It is a fast, cheap and accurate directional etch technique for brittle materials such as glass, silicon and ceramics but has limited resolution. It is another of the facilities offered by AML; therefore it was a natural choice for the milling of the quartz wafer prior to bonding. The reason for using full thickness quartz wafers and then polishing them down to thickness rather than simply purchasing pre-thinned wafers may be considered odd. In fact the latter method was attempted first, but it transpired that the thermal stresses incurred during the attaching of the handle wafer was so great as to cause the wafers to break, therefore thicker and stronger wafers were needed.

The chemical mechanical polishing is also a simple process whereby the top surface of a wafer is polished with the aid of slurry containing an abrasive grit suspended within reactive chemical agents. The polishing action is partly mechanical and partly chemical. The mechanical element of the process applied downward pressure while the chemical reaction that takes place increases the material removal rate and this is usually tailored to suit the type of material being processed.

7.3 Conclusion

In this chapter the fabrication of the microrheometer was discussed. First the basic techniques used were described. Then it was shown how these techniques were employed within the specific processes used in the fabrication of the various parts of the microrheometer.

8. EXPERIMENTAL RESULTS

In this chapter, the experiments used to verify the theory and the validity of the design are discussed. Initially, the C_4F_8 film used to change the surface chemistry of the rheometers platens was characterised so that it's mechanical, chemical and wetting properties could be ascertained. The film was also tested for chemical stability to ensure that the rheometer could be cleaned between experiments. Then the dynamic properties of the test fluid (various viscosities of PDMS) were measured using conventional cone and plate rheometry. The circuitry of the microrheometer was then tested to show its development and performance. Then each version of the rheometer was tested in order to measure their frequency response and their ability to measure fluid properties.

8.1. Properties of C_4F_8 Film

The purpose of using C_4F_8 is to ensure that the liquid placed on the platen forms a sessile drop, i.e. that the liquid does not perfectly wet the platens and simply flow off them. To ensure this, the wetting properties of the C_4F_8 film needs to be determined.

Plasma-polymerised C_4F_8 films were deposited onto the polished side of single crystal N-type Si (100) wafers (IDB Technologies, UK) using a STS Multiplex ICP DRIE etcher (STS Plc., UK), utilising C_4F_8 gas (Pelchem, South Africa). The gas flow rate was 85 sccm (standard cubic centimetres per minute). Wafers were used as received, with any visible dust or debris being removed by sweeping the surface with N_2 gas. All sample handling was carried out using tweezers (Agar Scientific, UK) to minimise the risk of sample

contamination. Deposition times were 1, 2 and 3 minutes with each deposition being prepared on a new wafer.

8.1.1. Assessment of Surface Wetting Properties by Dynamic Contact Angle Measurements

To determine the spreadability of fluids on the film, dynamic and static contact angles were measured using a purpose-built apparatus employing a Charge-Coupled Device (CCD) KP-M1E/K camera (Hitachi, UK) and FTA Video Analysis software v2.0 (First Ten Angstroms, UK). A 25 µL gastight syringe (Hamilton, UK) was used for changing the volume of the droplet, which was released onto the sample surface from a blunt-ended needle of ~1 mm diameter (Hamilton, UK). All data were collected at room temperature and pressure under ambient humidity conditions. Frames for the video analysis were captured at a rate of 12.5 Hz, usually yielding a minimum of ten frames for both the advancing contact angle and the receding contact angle. Data for the advancing contact angle were selected only when the droplet width was increasing. Similarly, data for the receding contact angle were only chosen when the droplet width was decreasing. The calculated contact angles for each frame during the advancing or receding droplet movement were averaged to give mean values for both the advancing and receding contact angle behaviour of the surface. 1Pa.s PDMS (Dow Corning, UK) was used as the probe fluid as PDMS of various viscosities was to be used as a test fluid for subsequent experiments. It was found that the static contact angle (θ_S) for PDMS was 40° while it's advancing (θ_A) and receding (θ_R) contact angles are 35° and 83° respectively.

A Zisman plot (Fig. 8.1) [200] was performed in order to calculate the surface energy of the C_4F_8 film, whereby the static contact angles of a range of fluids is plotted versus the fluid surface tension. These data can be extrapolated until the contact angle equals zero, revealing the critical surface energy of the C_4F_8 – this is the energy at which the fluid will perfectly wet the surface. This is useful because if the surface tension of the fluid is greater than this value then it will form a sessile drop on the solid facilitating experimentation in the rheometer. The fluids employed here ranged in surface tension from 18.4 mN/m to 28.5 mN/m and were hexane (Fisher Scientific, UK), propan-2-ol (Fisher Scientific, UK), ethanol (Fisher Scientific, UK), acetone (Fisher Scientific, UK), hexan-1-ol (Fisher Scientific, UK), tetrahydrofuran (Fisher Scientific, UK), chloroform (Fisher Scientific, UK), hexadecane (Fisher Scientific, UK) and toluene (Fisher Scientific, UK).

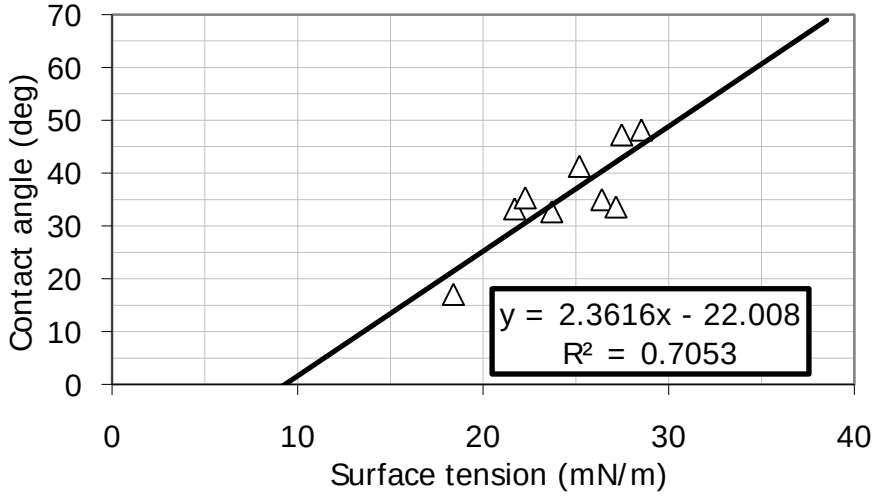

Fig. 8.1: A Zisman plot for the C_4F_8 film.

It can be seen that the critical surface tension for C_4F_8 is 9.32mN/m. This means PDMS, which has a surface tension (γ_{LV}) of 20.5mN/m, will form a sessile drop on C_4F_8. This effect can be also quantified by calculating the spreadability, *S*, of the fluid. In general, if

the intermolecular attractive forces between surface molecules of the fluid and the solid are equal to, or greater than, the forces of cohesion between the fluid molecules themselves, good adhesion should theoretically occur and the fluid will wet the solid. The spreadability is given as [201]:

$$S = W_A - W_C$$

W_A is the work of adhesion and is given by:

$$W_A = \gamma_{SV} + \gamma_{LV} - \gamma_{LS}$$

While W_C is the work of cohesion and is given by:

$$W_C = 2\gamma_{LV}$$

This means the spreadability is shown to be:

$$S = \gamma_{SV} - \gamma_{LV} - \gamma_{LS}$$

Or, using Young's equation (eq. 4.1) it is shown to be:

$$S = \gamma_{LV}\left(\cos(\theta_S) + 1\right) - 2\gamma_{LV}$$

For PDMS, S = -0.0197 and for water S = -0.0936. This expression is only approximate as it only applies to non-polar liquids (PDMS is but water isn't). Negative spreadability indicates that these liquids will not spread perfectly on the C_4F_8 film. The values for PDMS and water are also consistent in that the contact angle for water ($\theta_S \approx 90^\circ$) is higher than for PDMS and so exhibits higher cohesive strength giving it a larger negative spreadability.

8.1.2. Determination of Film Thickness by Spectroscopic Ellipsometry

In order to determine the thickness of the C_4F_8 films after various deposition times and therefore determine deposition rates, ellipsometry measurements were taken of each of the three deposited samples. The ellipsometry measurements were performed using a spectroscopic ellipsometer (Jobin-Yvon/Horiba, UK) operating with DeltaPsi2 v2.0.8 software. The angle of incidence was set to 70^o. The wavelength range for the incident light was 250-800 nm. All measurements were made under conditions of ambient temperature, pressure and humidity. Mean film thicknesses were obtained from a minimum of five measurements at different locations on the substrate. Precautions were taken to avoid performing measurements on visibly defective locations on the sample. Calculation of the C_4F_8 film thickness was performed for each measurement, based on a four-phase ambient/C_4F_8 film/SiO_2/Si model, in which the C_4F_8 film was assumed to be isotropic. The C_4F_8 film was modelled using a simple classical layer model, whose initial thickness was varied using a multiguess iterative calculation procedure. The single outcome of each iteration process was the result with the lowest χ^2, which is a measure of the error between the measured data and the calculated model. A minimum of twenty different initial values for the film thicknesses were chosen for each film measurement. Those results with the lowest χ^2 for each measurement made were averaged to give a mean film thickness. The thicknesses obtained from ellipsometry are given in Table 8.1.

Deposition time (min)	Mean thickness (nm)	St. Err. (nm)
1	160.17	2.80
2	382.08	1.80
3	595.31	3.84

Table 8.1: The film thicknesses as measured by ellipsometry.

This result is plotted in Fig. 8.2. It can be clearly seen that with deposition times above 1 minute, film thickness increases linearly with time. These values were used to ensure the gap between the platens was known.

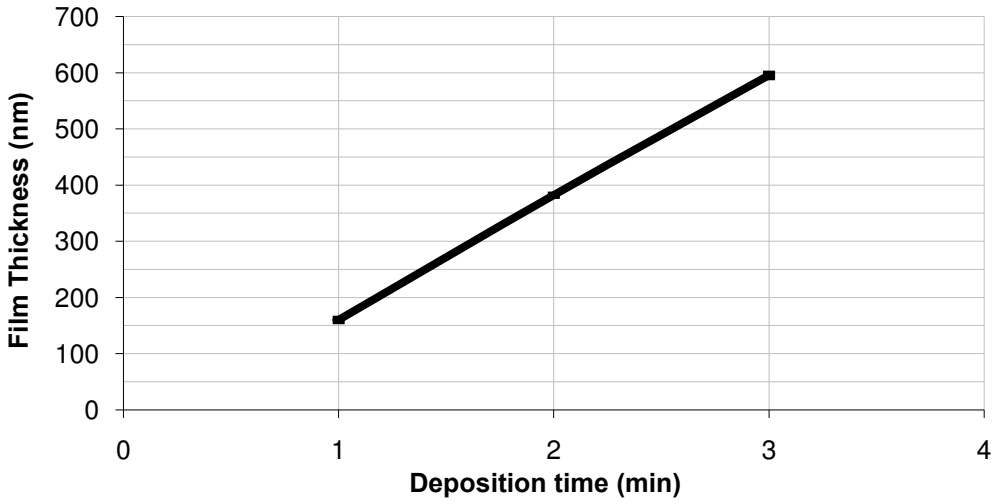

Fig. 8.2: Film thickness as a function of deposition time.

8.1.3. Assessment of Surface Topography by Atomic Force Microscopy

To assess the roughness of the C_4F_8 surface, atomic force microscopy (AFM) images were acquired using a Dimension 3100 Nanoscope AFM (Veeco, UK) and a MultiMode AFM with 'E' scanner, both housed on vibration isolation tables. Nanoscope v5.12 software (Veeco, UK) was used throughout for both real-time analysis and post-capture image processing. All images were acquired while operating in Contact Mode under ambient conditions, using triangular 100 μm length pyramidal-tipped Si_3N_4 cantilevers with oxide-sharpened tips (Veeco, UK). These cantilevers had nominal spring constants of 0.58 N m^{-1} and analysis of the tip shape using an aluminium oxide grid (Agar Scientific, UK) revealed tip diameters of 50 ± 5 nm. All images were acquired at scan rates between 0.5-1.5 Hz, each image being composed of 512 x 512 pixels. All images (for example see Fig. 8.3)

were subsequently analysed to find the roughness of the surface. The root-mean-square roughness (r_{RMS}) of the film can be shown to be around 1nm for the three samples while the average roughness (r_a) and the z-range is around 1nm and 5nm respectively. However in Fig. 8.3b, it can be seen that a small amount of organic matter may have settled on the surface. When this is taken into account, the roughness changes accordingly to have values of $r_{RMS} \approx 3.5$nm, $r_a \approx 2.5$nm and z-range $\approx$ 50nm. This shows that the C_4F_8 surface is essentially smooth and will not affect the flow of the fluid.

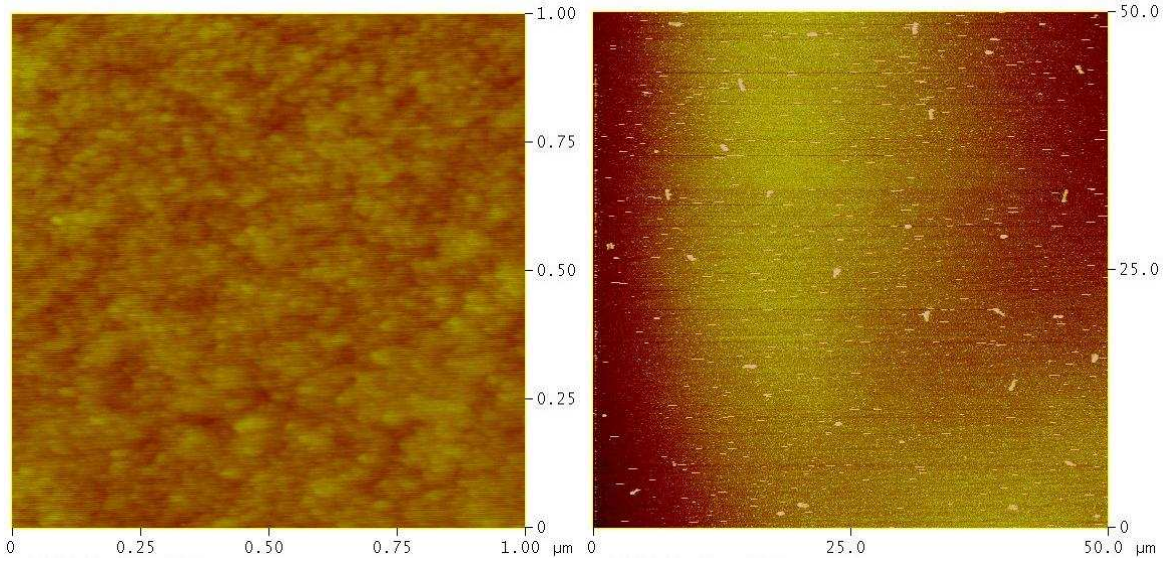

Fig. 8.3: Typical AFM images of the C_4F_8 film. Both images are from a film that was deposited in 3 minutes. (a) is a close-up of the film and (b) shows potential surface deposits.

8.1.4. Assessment of Surface Composition by X-Ray Photoelectron Spectroscopy

To ensure the silicon was effectively coated by the C_4F_8, XPS analysis was performed using an Escalab 250 system (Thermo VG Scientific, UK) operating with Avantage v1.85 software. An Al Kα X-ray source was used, providing a monochromatic X-ray beam with incident energy of 1486.68 eV. The measurements were made at a pressure of ~5 x 10^{-9}

mbar and with a circular spot size of ~0.2 mm^2. Samples were immobilised onto stainless steel sample holders using double-sided carbon sticky tape (Shintron tape, Shinto Paint Company, UK). Low resolution survey spectra were obtained using a pass energy of 150 eV over a binding energy range of -10 to 1,200 eV with 1 eV increments. Low resolution spectra would typically be obtained from an average of 5 scans. High resolution spectra were obtained using a pass energy of 20 eV over a binding energy range of 20-30 eV, centred around a chosen photoelectron binding energy with 0.1 eV increments. A dwell time of 20 ms was employed when collecting data from each binding energy increment for all measurements. High resolution spectra would typically be derived from an average of at least 10 scans. For C_4F_8 films spectra for the C 1s, F 1s, Si 2p and O 1s photoelectron peaks were obtained. Using the Avantage v1.85 software the area of each peak was calculated and subsequently divided by the relative sensitivity factor for that element, yielding a fractional atomic composition of the surface, which was 42.8 % C and 57.2 % F (compare Fig 8.4 to Fig. 8.5). This means that the C_4F_8 coated the silicon surface well.

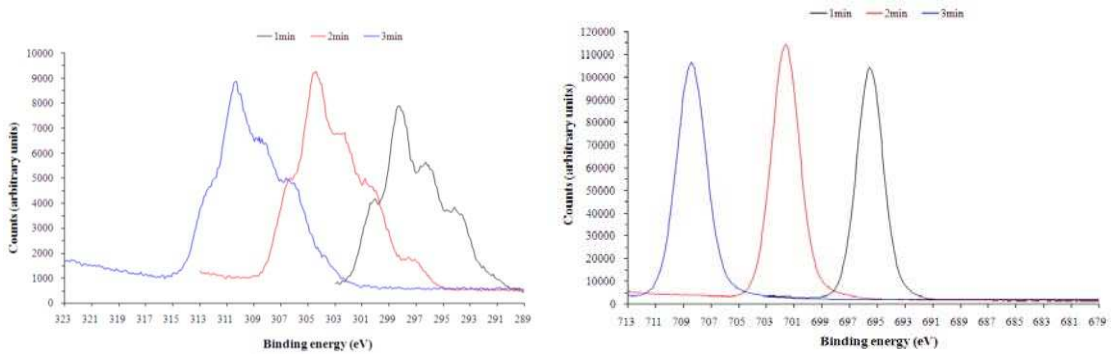

Fig. 8.4: XPS data showing the peaks for (a) C 1s and (b) F 1s for the three samples. The shifts in the peaks for the different samples are due to the increased charging of the surface as the thickness of the film increases.

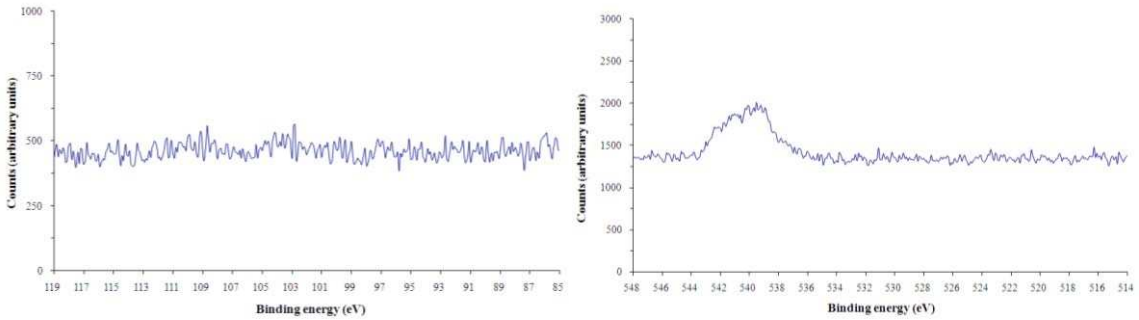

Fig. 8.5: XPS data showing the peaks for (a) Si 2p and (b) O 1s for a typical sample. Note that if the wafer was not completely coated, these elements would show large peaks. The lack of peaks proves that the C_4F_8 coats the wafers well.

8.1.5. Assessment of C_4F_8 Film Stability in Liquid Media

As the rheometer would need to be cleaned between experiments, C_4F_8 films (of 1 minute deposition times) were immersed in a range of liquid media for times up to 24 h in order to assess their stability to organic solvents, acids and bases. Acetone (Fisher Scientific, UK), chloroform (Fisher Scientific, UK), ethanol (Fisher Scientific, UK), propan-2-ol (Fisher Scientific, UK), tetrahydrofuran (Fisher Scientific, UK) and toluene (Fisher Scientific, UK) were the organic solvents investigated. The aqueous media investigated were HPLC grade water (Fisher Scientific, UK), a hydrochloric acid solution prepared at pH 2.60, sodium hydroxide solutions of pH 8.40 and 10.37, as well as MF26a (Shipley Europe Ltd., UK), a developer used in the preparation of MEMS devices, which had a pH of 10.37. Hydrochloric acid (Fisher Scientific, UK) and sodium hydroxide pellets (Fisher Scientific, UK) were used as received and diluted with HPLC grade water. All pH measurements were performed using an IQ150 pH meter (IQ Scientific Instruments) following calibrations with buffer solutions (Fisher Scientific, UK) of pH 4.0, 7.0 and 9.18.

The C_4F_8 films which were immersed in the organic solvents acetone, chloroform, ethanol, propan-2-ol, tetrahydrofuran and toluene showed no degradation after 24 h exposure, with AFM and XPS employed to assess any levels of film degradation. Similarly, C_4F_8 films which were immersed in water and aqueous solutions at pH 2.0, 8.4 and 10.4 showed no degradation after 24 h exposure. However, C_4F_8 films which were immersed in the MF26a developer were found to degrade after an immersion time of only 1 minute, with the loss of fragments of the C_4F_8 film resolved by AFM analysis of the surface. MF26a developer is an aqueous solution of pH 10.4 containing tetramethylammonium hydroxide (TMAH) which is often used for the etching of Si [202-203]. After a 5 minute immersion time there was additional surface degradation with additional loss of C_4F_8 film fragments and evidence of a secondary process taking place underneath the C_4F_8 film, evidenced in the form of raised patches of film, resembling blisters (see Fig. 8.6). After a 10 minute immersion time only a small amount of the C_4F_8 film remained, and that which did remain exhibited further blistering underneath the film. At immersion times greater than 10 minutes no significant amount of C_4F_8 film was found to remain on the Si surface upon inspection by AFM, although small C 1s and F 1s photoelectron peaks could be observed by XPS for immersion times up to 2 hours. AFM images suggest that the film always fractured in a unit of the full thickness of the deposited film, and never in a laminar fashion. The mechanics of fragmentation of the C_4F_8 film is an area currently under further investigation. Exposure of the C_4F_8 film to an aqueous solution of sodium hydroxide at pH 10.4 caused no degradation to the film, which suggests that the TMAH is responsible for the removal of the film.

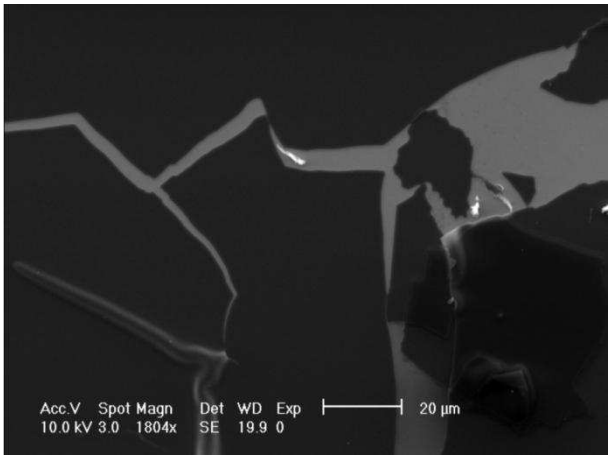

Fig. 8.6: Evidence of degradation of C4F8 film due to submersion in TMAH. Note how the film does not appear to have been dissolved, merely fractured and peeled away, suggesting that it's the underlying substrate that's being attacked.

It is therefore apparent that generally the organic solvents tested will pose no threat to the stability of the C_4F_8 film. In particular, as PDMS was the fluid used to test the microrheometer, toluene was used as the solvent to clean the platens.

8.1.6. Determination of Elastic Modulus by Nanoindentation

The elastic modulus of the C_4F_8 film was investigated using a nanoindentation cantilever (Veeco, UK) housed in a MultiMode AFM (Veeco, UK). The cantilever had a calibrated spring constant of 190 N/m and a triangular diamond tip. An applied force of 45 μN produced an indentation of 39.2 nm depth. By applying the method outlined by Fischer-Cripps [204] the elastic modulus of the C_4F_8 film was calculated to be 6.48 GPa. This figure is likely to be much higher than the elastic modulus of the complex fluids that will be tested in the microrheometer and so it will be considered to be non-compliant in subsequent analysis.

8.2. Results of Conventional Rheometry

In order to check the accuracy of the microrheometer it was necessary to compare the results to those obtained by conventional oscillatory rheometry. Therefore, the storage and loss moduli of PDMS of various viscosities were obtained using an AR2000 cone and plate rheometer (TA instruments, USA). PDMS was used as it is a well known polymer consisting of a linear molecule which can be accurately and repeatably reproduced to the required viscosity. A 20mm stainless steel truncated cone with a 4° side wall angle was used to manipulate the liquid. A frequency sweep from 0.1 hz to 100 hz (where possible) was performed with logarithmic increments. The amplitude of the applied strain (angle of twist multiplied by the radius of the sample divided by average height) was kept constant at 1%. The sample volume was approximately 0.15ml and the sample temperature was set to 25°C (maintained by a Peltier plate).

Typical results are shown in Figs 8.7 and 8.8 for the storage and loss moduli for various viscosity PDMS samples. From these values the dynamic viscosity was found (see Fig. 8.9). This viscosity is commonly used to determine whether a liquid is Newtonian, viscoelastic etc. This is more easily seen in Fig. 8.10 which shows the normalised dynamic viscosity. As can be seen, the dynamic viscosity of PDMS below 10 Pa.s doesn't show frequency dependency and can be considered to be Newtonian, whereas PDMS above 10 Pa.s shows more viscoelastic behaviour as indicated by the apparent decrease of viscosity with frequency. However the data in Fig. 8.4 suggests that using the microrheometer to probe the higher frequency response may yield hereto unknown information and may change these definitions.

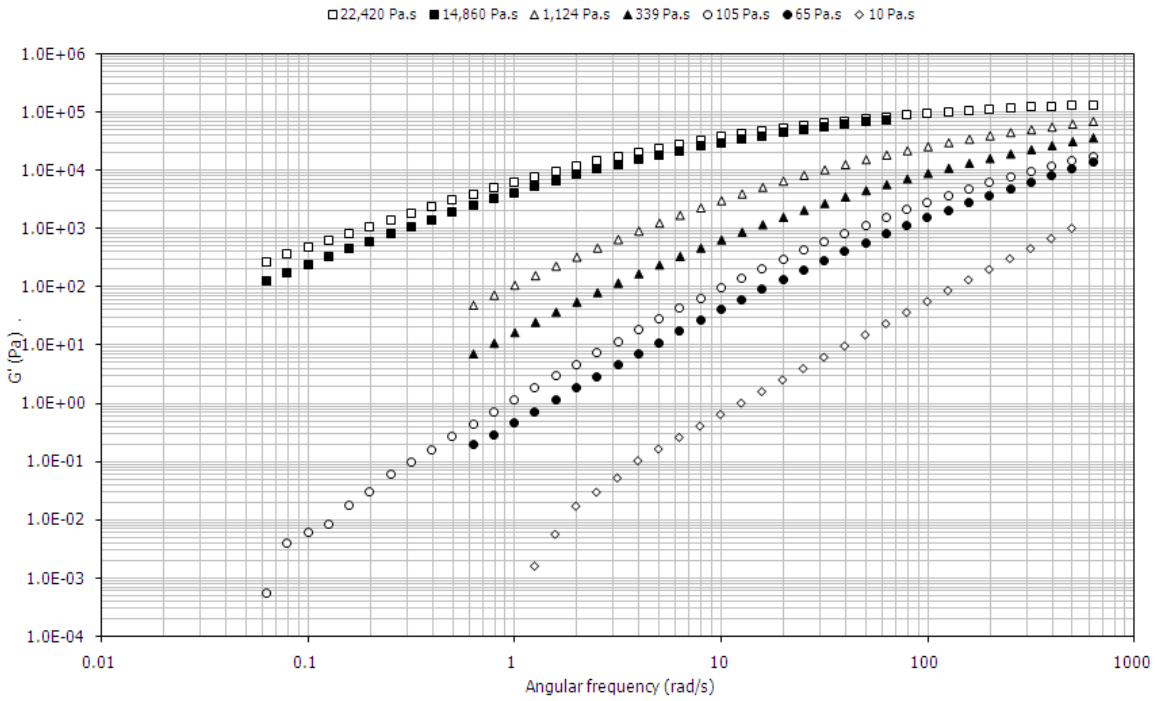

Fig. 8.7: The storage moduli for various shear viscosities of PDMS.

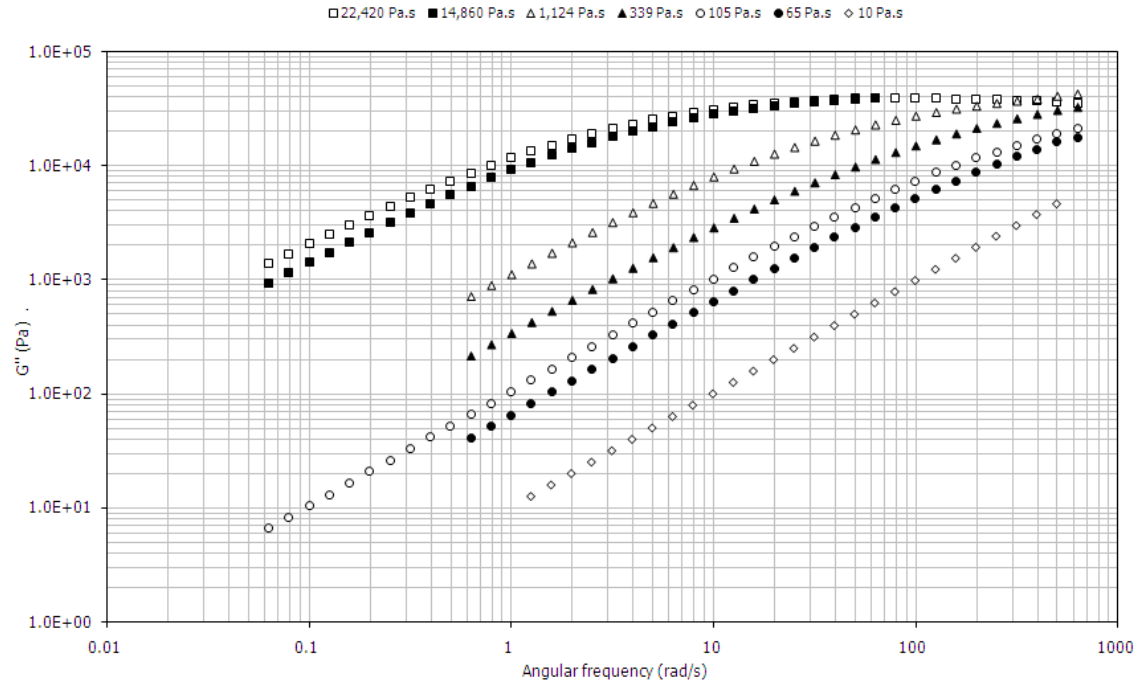

Fig. 8.8: The loss moduli for various shear viscosities of PDMS.

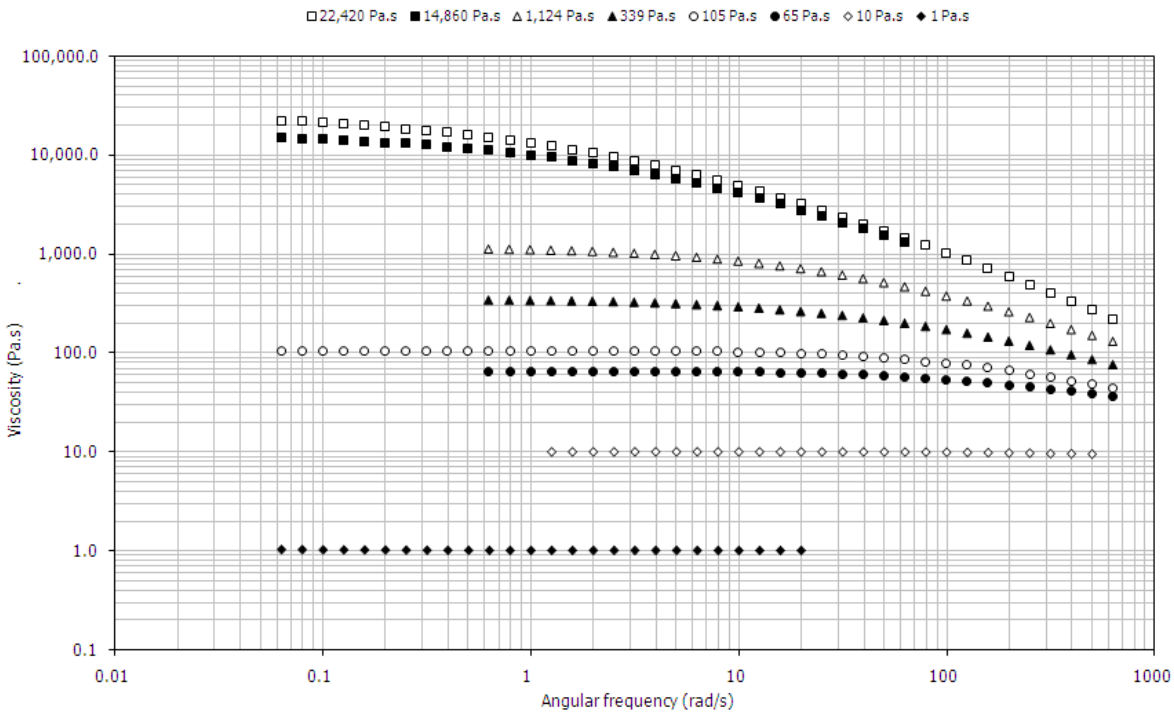

Fig. 8.9: The dynamic viscosity for various shear viscosities of PDMS.

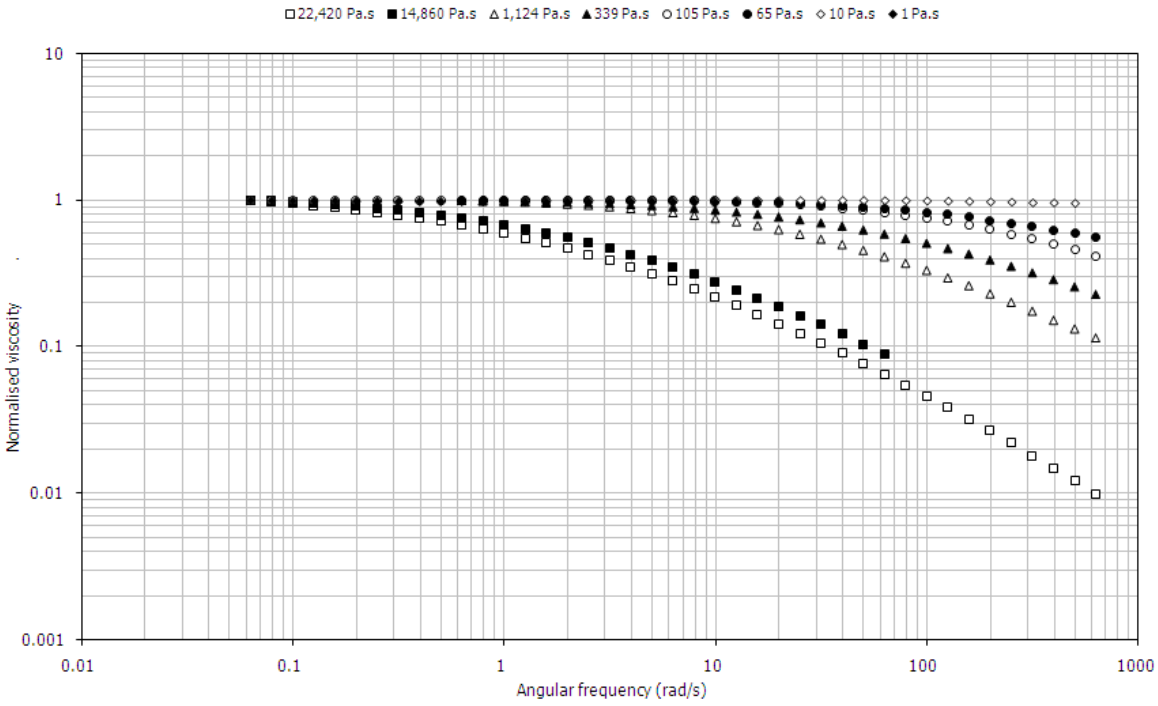

Fig. 8.10: The normalised dynamic viscosity for various shear viscosities of PDMS.

The data given by the cone and plate experiments was used to calculate the parameters used in the generalised Maxwell model (see Chapter 5) using a least-square method of curve fitting. The values found were then used to predict the properties of the fluid at frequencies higher than can be measured using cone and plate rheometry. The calculated Maxwell parameters are shown in Table 8.2.The data shows that each fluid tested can be treated as a Maxwell fluid i.e. they are all viscoelastic. The low viscosity fluids are adequately represented by a single element, but the higher viscosity fluids exhibit more relaxation processes and require more elements.

Fluid	Parameter	Element 1	Element 2	Element 3	Element 4	Element 5
22420 Pa.s PDMS	η (Pa.s)	500.406	115.257	5718.239	10952.473	1970.870
	G (Pa)	42556.314	56359.994	24901.393	8223.983	38217.453
	λ (s)	0.0118	0.00205	0.229	1.332	0.0516
14860 Pa.s PDMS	η (Pa.s)	514.255	81.303	4477.220	6764.894	1775.168
	G (Pa)	60690.83	4387.400	20163.24	5284.194	35223.704
	λ (s)	0.00847	0.0185	0.222	1.280	0.0504
1124 Pa.s PDMS	η (Pa.s)	368.108	437.843	72.652	180.199	-
	G (Pa)	15989.160	3872.033	72610.939	31777.068	-
	λ (s)	0.0230	0.113	0.00100	0.00567	-
340 Pa.s PDMS	η (Pa.s)	63.018	91.753	71.774	72.591	-
	G (Pa)	62854.046	2313.821	13743.306	4681.638	-
	λ (s)	0.00100	0.0397	0.00522	0.0155	-
30 Pa.s PDMS	η (Pa.s)	26.426	-	-	-	-
	G (Pa)	10891.387	-	-	-	-
	λ (s)	0.00242	-	-	-	-
10 Pa.s PDMS	η (Pa.s)	9.773	-	-	-	-
	G (Pa)	21138.806	-	-	-	-
	λ (s)	0.0004624	-	-	-	-

Table 8.2: The calculated Maxwell properties for a range of liquids (see Chapter 5 for more details). η is the dynamic viscosity, G is the shear modulus and λ is the relaxation time. Each column pertains to an equivalent spring and dashpot element in the generalised Maxwell model. For example 30 Pa.s PDMS is weakly viscoelastic and can therefore be represented mathematically by a single spring and dashpot. 22420 Pa.s PDMS is very viscoelastic and so requires five spring and dashpots to represent its dynamics.

8.3. Analysis of the Microrheometer Circuitry

In this section the electrical response of the microrheometer was tested. It was from the phase and amplitude of this response that the fluid properties of the fluid were calculated. Initially the response of the uncompensated microrheometer was measured to emphasise the impedance effects of the piezoelectric material and the need to include extra circuitry. This was then compared to the response of the buffered microrheometer to show the improvements the circuit provided.

8.3.1. Experimental Set-up

The various versions of the rheometer were tested by placing the rheometer onto a breadboard to which the circuitry was attached (see Fig. 8.11). The breadboard was housed in a cast aluminium box which was grounded via coaxial cables to the function generator and the ADC-212 Picoscope (a virtual oscilloscope by Pico Inc.). This enables the cast aluminium box to act as a Faraday cage which should protect the rheometer and associated circuitry from external sources of electronic noise.

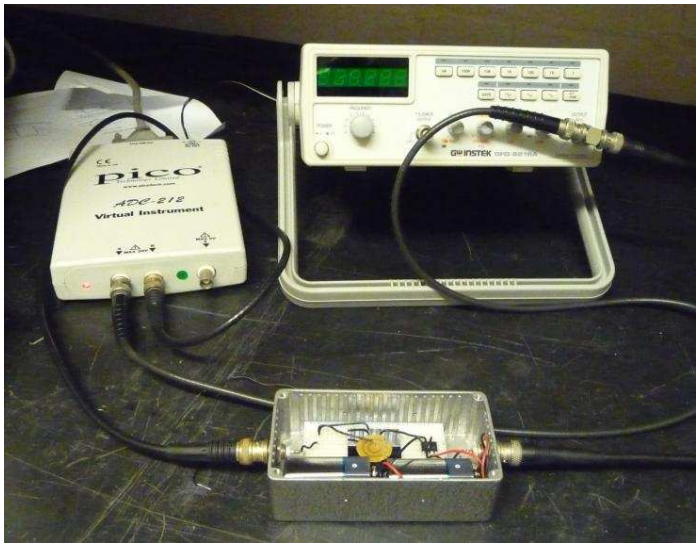

Fig. 8.11: The experimental set-up.

The function generator supplied a sinusoidal voltage with constant amplitude (depending on which rheometer was being tested). The frequency was varied on a logarithmic scale from 1Hz to 5000Hz. The voltage was applied directly to the rheometer by placing probes attached to the coaxial cable onto the active electrodes on the piezoelectric material on the rheometer (see Fig. 8.12). The amplitude and frequency of the input voltage was maintained by attaching the function generator directly to the Picoscope and adjusting the function generator accordingly. The voltage induced by the rheometer was monitored by placing a probe on the passive electrode on the piezoelectric layer. This probe was either attached directly to the Picoscope via the coaxial cable or indirectly via the buffer circuitry. The input voltage and induced voltage were recorded simultaneously by the Picoscope. The data was then analysed to find the amplitude of the induced voltage and phase difference between the input and induced voltage as a function of frequency and input voltage amplitude.

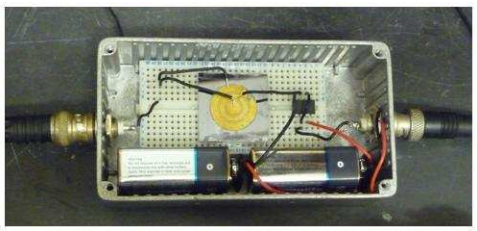

Fig. 8.12: The rheometer set-up.

8.3.2. Uncompensated Electrical Response

It was previously described in Chapter 6 that the load impedance of the quartz and oscilloscope would cause the basic circuit (Fig. 6.16) to be equivalent to a voltage divider giving a response similar to that given in Fig. 6.18. To check this assumption, an AC voltage frequency scan was applied to the Mark I microrheometer without any

compensating circuitry. As can be seen below in Figs. 8.13 and 8.14, the response is similar to that given in Fig. 6.18. This confirms that compensating circuitry was definitely needed as these impedance effects will mask any response changes due to altering the fluid properties of the sample.

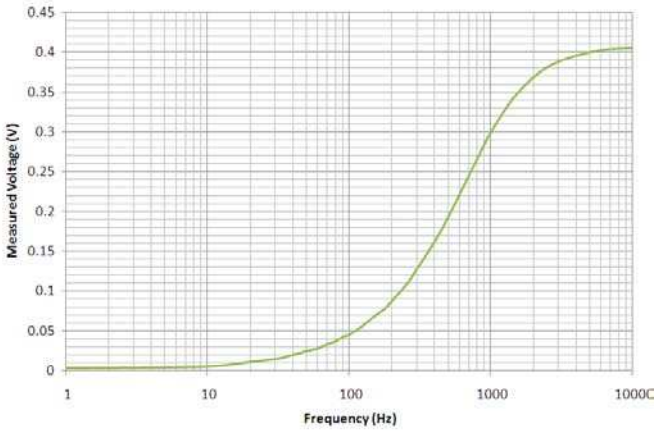

Fig. 8.13: The amplitude of the induced voltage of the dry Mark I microrheometer.

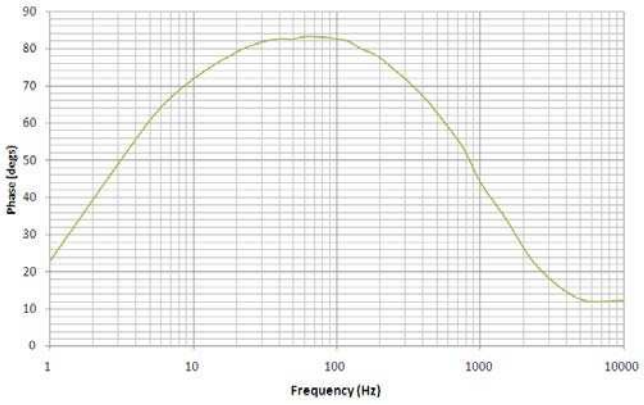

Fig. 8.14: The phase of the induced voltage of the dry microrheometer.

8.3.3. Electrical Response with Simple Buffer Amplifier

In the last section of Chapter 6 it was shown that a unity gain buffer amplifier (or voltage follower) can be used to negate the impedance effects of the piezoelectric layer (Fig. 6.19). In this circuit the inverting terminal of the op-amp was connected directly to the output

terminal and the signal from the quartz was applied directly to the non-inverting terminal. The output voltage now follows the input, giving the circuit a gain of 1. The reason for doing this was that the buffer amplifier has very high input impedance and very low output impedance. This means that current was essentially prevented from flowing from the microrheometer and so there is no voltage drop due to parasitic capacitance. The response of the microrheometer with the buffer amplifier in the circuit is shown in Fig 8.15 and 8.16.

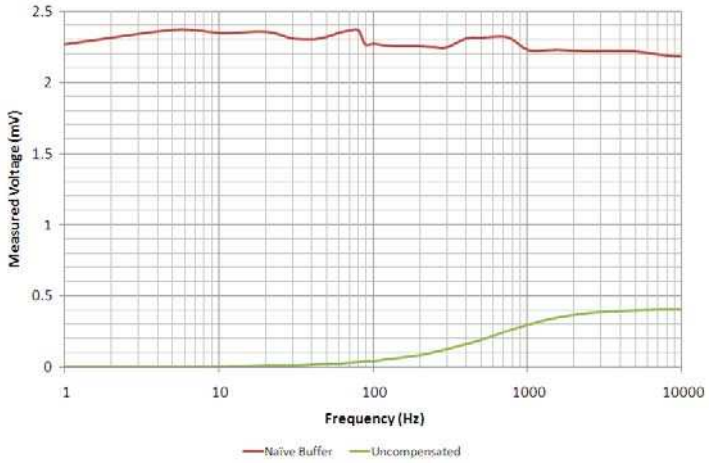

Fig. 8.15: The amplitude of the response of the buffered circuit as compared to the original response.

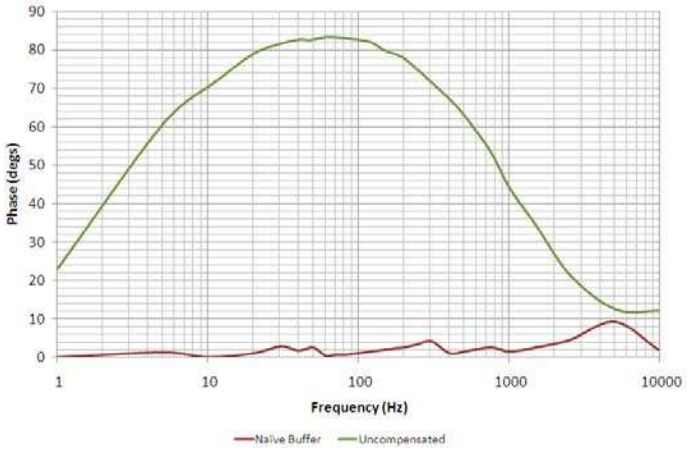

Fig. 8.16: The phase of the response of the buffered circuit as compared to the original response.

As can be seen in Figs 8.15 and 8.16 it seems that the simple buffer has negated most of the impedance effects of the quartz. It shows that the amplitude is almost constant and the phase is practically zero. Theoretically these should be constant and zero respectively for the case when the rheometer is ran without any fluid present and away from resonance. However, whilst it is an improvement, the circuit is still not suitable for measuring fluid properties. This is because, as can be seen above, the response is not smooth as it should be. This is because the circuit used will only work effectively if the op-amp was ideal – hence the name of naïve buffer amplifier.

In the real world there are a few extra factors that need to be considered:

1. Stray capacitances at the inputs of the op-amp. In this case a TL071CN op-amp was used as the buffer amplifier as it is a low noise J-FET op-amp. This means it has a high input impedance of 1TΩ. However if the stray capacitance between the inputs and ground is 3pF, the impedance of the stray capacitance is 53MΩ. Since this is much smaller than the input impedance given, the effective input impedance of the circuit can be much lower than stated. This is an issue because the buffer amplifier is only of use when its input impedance is much higher than the impedance of the quartz.

2. Extra components mean extra noise. The TL071CN op-amp has an equivalent input noise voltage of 15 nV/√Hz. The equation for the added noise is given as [205]:

$$noise\ added = \sqrt{f(e_n^2)}$$

Where f is the bandwidth (10kHz) and e_n is 15 nV/√Hz (as given in the TL071CN data sheet). This gives the added noise as 1.5µV. This is small enough to be neglected.

3. The present circuit can be considered to be capacitor-coupled at the input due to the piezoelectric layer. This is acceptable because we only wish to amplify AC voltages. However this capacitance may interrupt the bias current paths to the op-amp input terminals preventing the op-amp from working properly. The TL071CN only requires an input bias current of 20nA and so a resistor to ground at the inverting input should suffice. This should also allow any stray capacitances at the input to discharge.

8.3.4. Modified Circuit

It has been shown that the circuit of Fig. 6.19 is affected by the capacitance of the piezoelectric layer. As capacitors are reactive devices, they affect the phase of the signal and cause instabilities, even oscillations, in the performance of the op-amp. What is needed is a circuit that can react to the capacitive load and adjust itself accordingly. The circuit shown in Fig. 8.17 is designed to do just that.

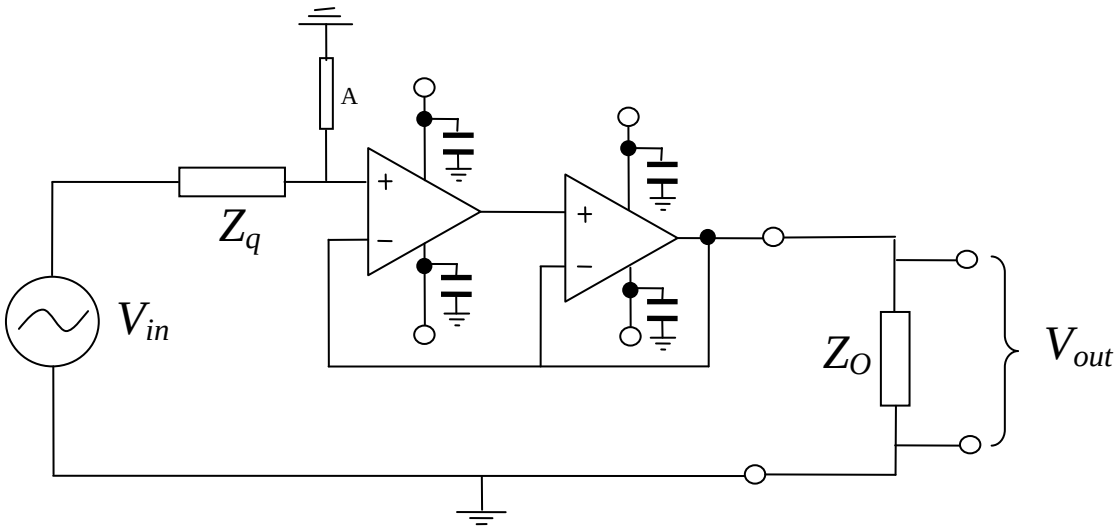

Fig. 8.17: The modified circuit. The capacitors all have values of 0.1µF as recommended by the op-amp manufacturer. Resistor A has a value of 10 MΩ – see point 3 above for details.

This circuit uses the TL072CN op-amp. This is similar to the TL071CN op-amp except that it is a dual op-amp with uses well-matched J-FET inputs and takes up less space than using two TL071CN op-amps. By cascading the two unity gain amplifiers and adding the extra phase compensation components the stability of the circuit has been much improved. As feedback along supply lines is another source of instability, supply-decoupling capacitors have been connected from each terminal to ground close to the IC terminals. The result of all these modifications can be seen in Figs. 8.18 and 8.19.

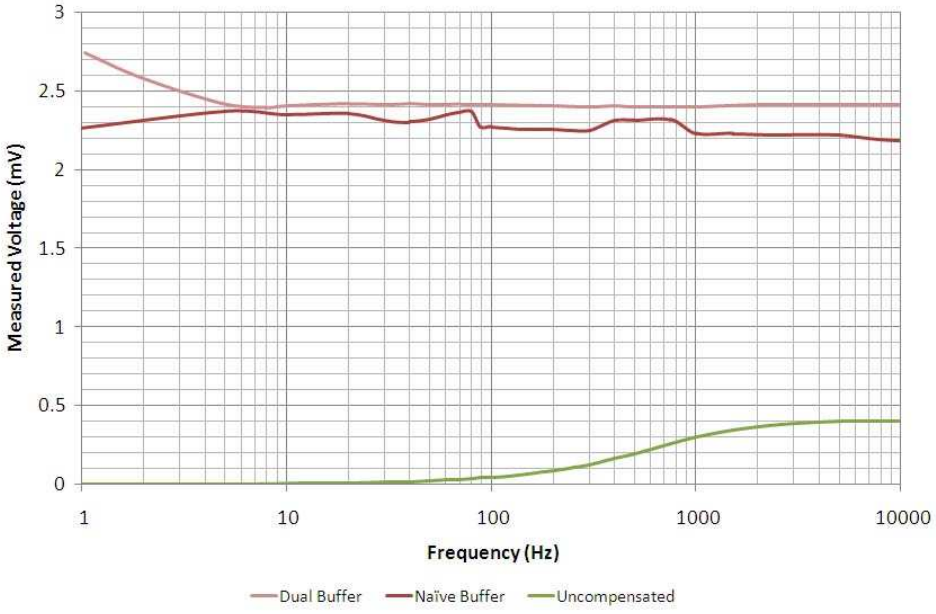

Fig. 8.18: The amplitude of the response of the dual-buffered circuit as compared to the original response and the single buffered circuit.

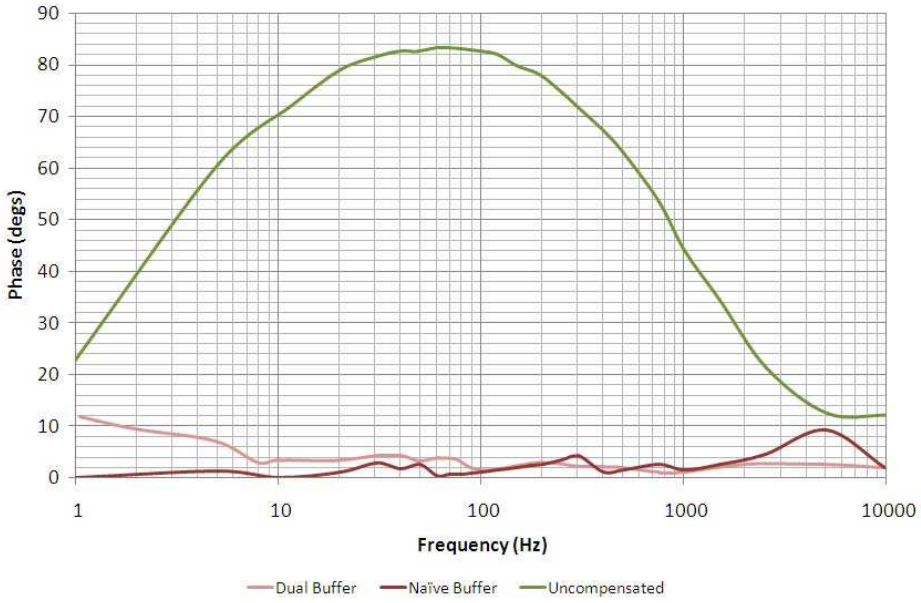

Fig. 8.19: The phase of the response of the dual-buffered circuit as compared to the original response and the single buffered circuit.

As can be seen above, the response is indeed smoother, although there appears to be a roll-off in performance below 10Hz. This is probably due to capacitance effects discussed previously. The noise in the phase response is still present. The source of the noise in the

phase response is unclear as the circuit should have reduced it. It may be due to the use of the breadboard instead of a more efficient and less noisy bespoke printed circuit board. For example if the rheometer is replaced in the circuit with the function generator set at a constant 5 V amplitude, there is still some degree of noise, see Fig. 8.20, suggesting that at least some of the noise is inherent in the circuitry. However, whilst the noise will reduce the accuracy of the rheometer, the circuitry is sufficient to allow testing of the rheometer with different fluids.

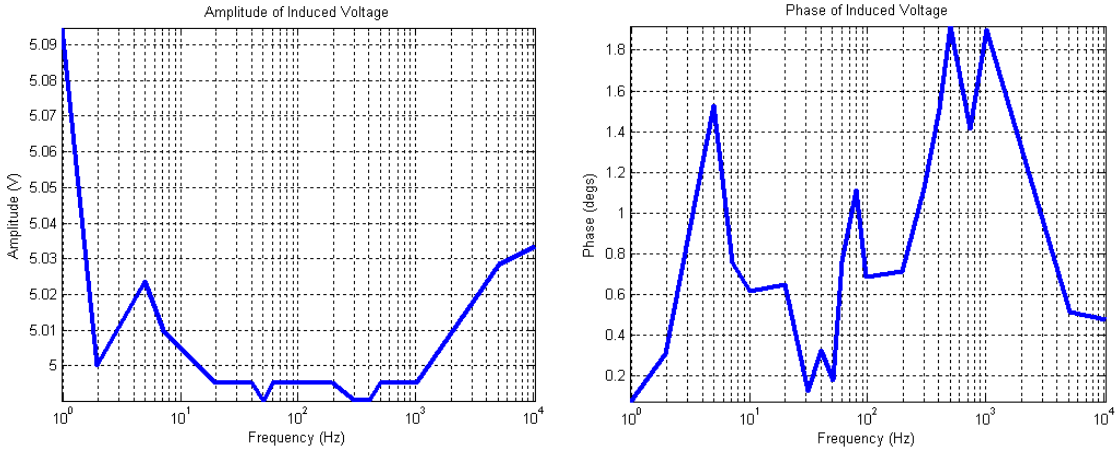

Fig. 8.20: The frequency response of the circuit using the function generator as the voltage source. Note how there is still noise in the circuit, even when the rheometer is not present.

8.4. Analysis of the Microrheometer

In the last section it was shown that the impedance effects of the quartz were negated permitting testing of the rheometer. In this section, the electrical response of the microrheometers under the influence of various fluids was measured and used to calculate the storage and loss moduli of the liquid.

The experimental procedure was the same for all the microrheometers. The base plate was placed under a microscope and a drop applied to the lower platen by dipping a glass rod into the liquid and placing the liquid onto the platen (see Fig. 8.21). The active plate was then assembled onto the base plate and the electrical probes were placed in contact with the pertinent electrodes. The lid of the aluminium box was then screwed into place thus isolating the rheometer. The sinusoidal voltage was applied by the function generator and the Picoscope monitored the induced voltage. The measured electrical response was then used to calculate the mechanical response of the rheometer and then the dynamic properties of the fluid being tested.

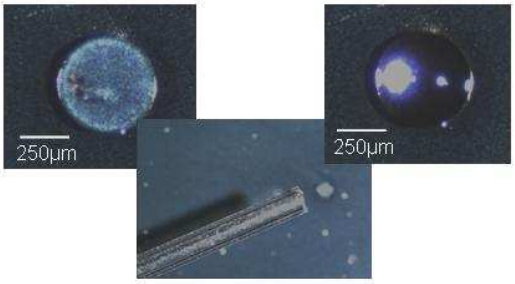

Fig. 8.21: The application of the liquid onto the lower platen.

8.4.1. The Mark I Rheometer

The Mark I rheometer was fabricated by gluing a thin quartz disc onto the silicon membrane (see Fig. 8.22).

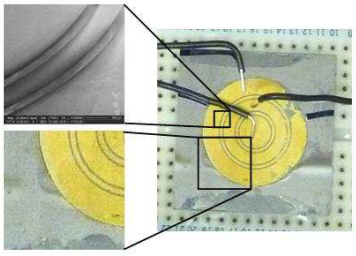

Fig. 8.22: The Mark I rheometer.

The rheometer was first tested mechanically by placing the rheometer (without any liquid) under an AFM cantilever (Veeco, UK) operating in Contact Mode under ambient conditions. The Si_3N_4 cantilevers (Veeco, UK) were rectangular and 100 μm in length and had 5 μm diameter SiO_2 colloidal probes. The cantilever had a nominal spring constant of 10 N m^{-1}. The colloidal probe was positioned directly on the centre of the quartz layer. The rheometer was oscillated by applying a sinusoidal voltage of 5V amplitude for a range of frequencies to the active electrodes. The amplitude of the mechanical movement of the rheometer was then measured by monitoring the deflection of the cantilever. The results are shown in Fig. 8.23. Finite element analysis of the structural mechanics of the rheometer was also carried out and compared to the analytically calculated and the AFM measured response in Fig. 8.23.

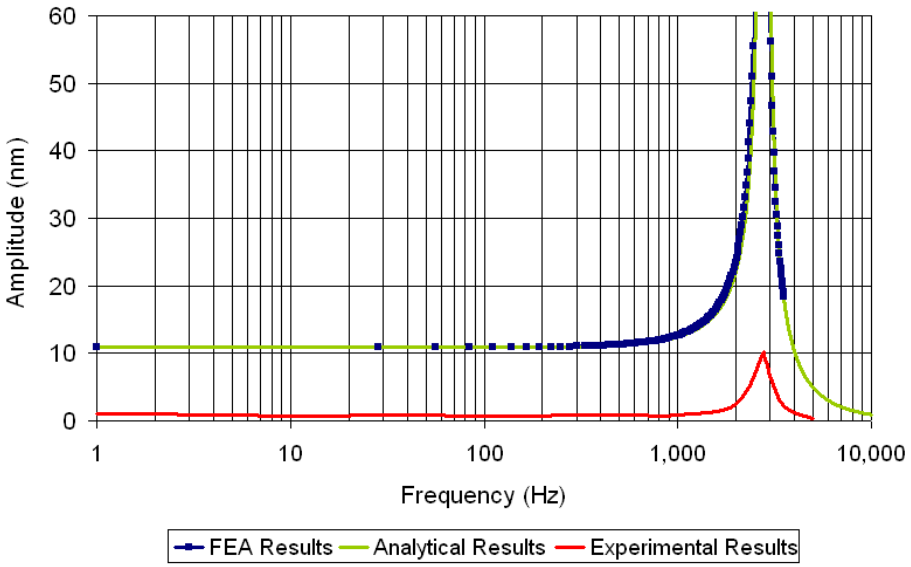

Fig. 8.23a: The mechanical amplitude of the dry rheometer. Note how the FEA and analytical results are practically equal. The experimental results show the same resonant frequency as that calculated although the amplitude was lower than expected.

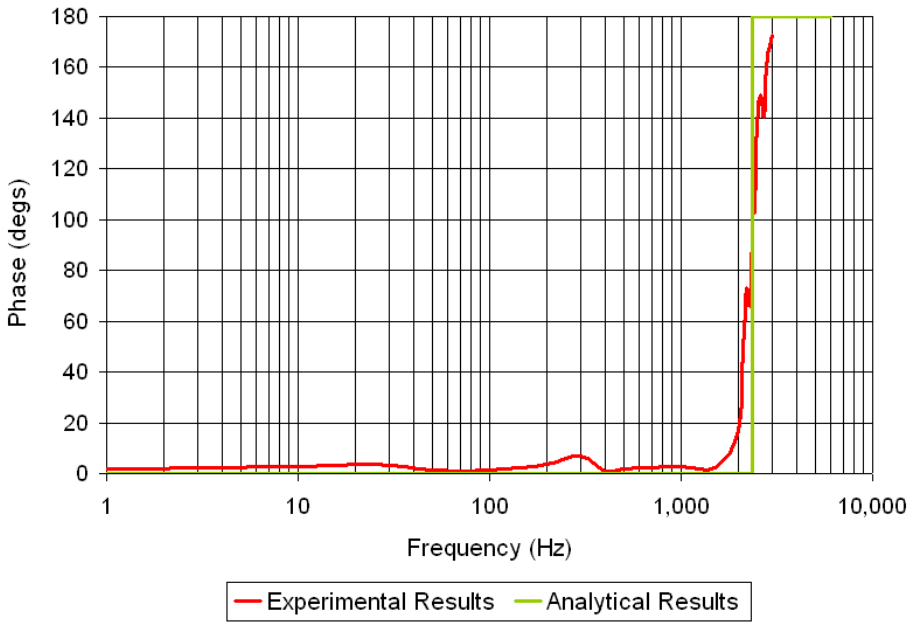

Fig. 8.23b: The mechanical phase of the dry rheometer.

In Fig. 8.23 it can be seen that the FEA results and the analytical results for the mechanical response are practically identical and predict an amplitude of 10.5 nm and resonant frequency of around 2667 Hz. However, while the AFM measured a similar resonant frequency, the measured amplitude was lower than expected. The phase difference was also shown to be noisy when it should have been zero. This may mean that the noise in the phase detected in the circuitry earlier may be mechanical noise not electrical.

The reduced amplitude suggests either the force being applied is not what is expected, or the stiffness is not what was calculated. This may be due to the quartz being thicker than expected but the quoted tolerances (100µm ±5µm) suggest that this isn't the cause. It is possible that the quartz was misaligned but FEA analysis of the rheometer suggests that the stiffness is not too sensitive to the alignment with a variation of only 1% of the nominal stiffness provided that the quartz is within 1mm (radially) of the correct position. Another concern is the adhesion of the electrodes to the quartz surface. Even though

titanium was used as the adhesive layer as it has the correct electron negativity, in some areas the gold had a tendency to scratch off (see Fig. 8.22). It is possible that even though the adhesion seemed to be adequate in most areas, the electrical contact between the gold and the quartz might not be completely sufficient. However, it should be noted that during the various experiments the AFM cantilever did on occasion drift out of contact with the rheometer, suggesting that there may be issues with this method of measuring the mechanical response rather than an issue with the rheometer itself.

The experiment was repeated with a sample of 30 Pa.s PDMS included. It can be seen in Fig. 8.24 that the fluid has a definite effect on the mechanical behaviour of the rheometer. The response of the rheometer due to the liquid was compared to the theoretical response in Fig. 8.25. The measured response is qualitatively similar to the theoretical response. However, the amplitude of the theoretical response had to be normalised to facilitate comparison. The theoretical response predicts an amplitude of around 10 nm (i.e. quite similar to the dry theoretical response), instead the measured amplitude was much lower. The phase response, on the other hand, was very close to what was predicted.

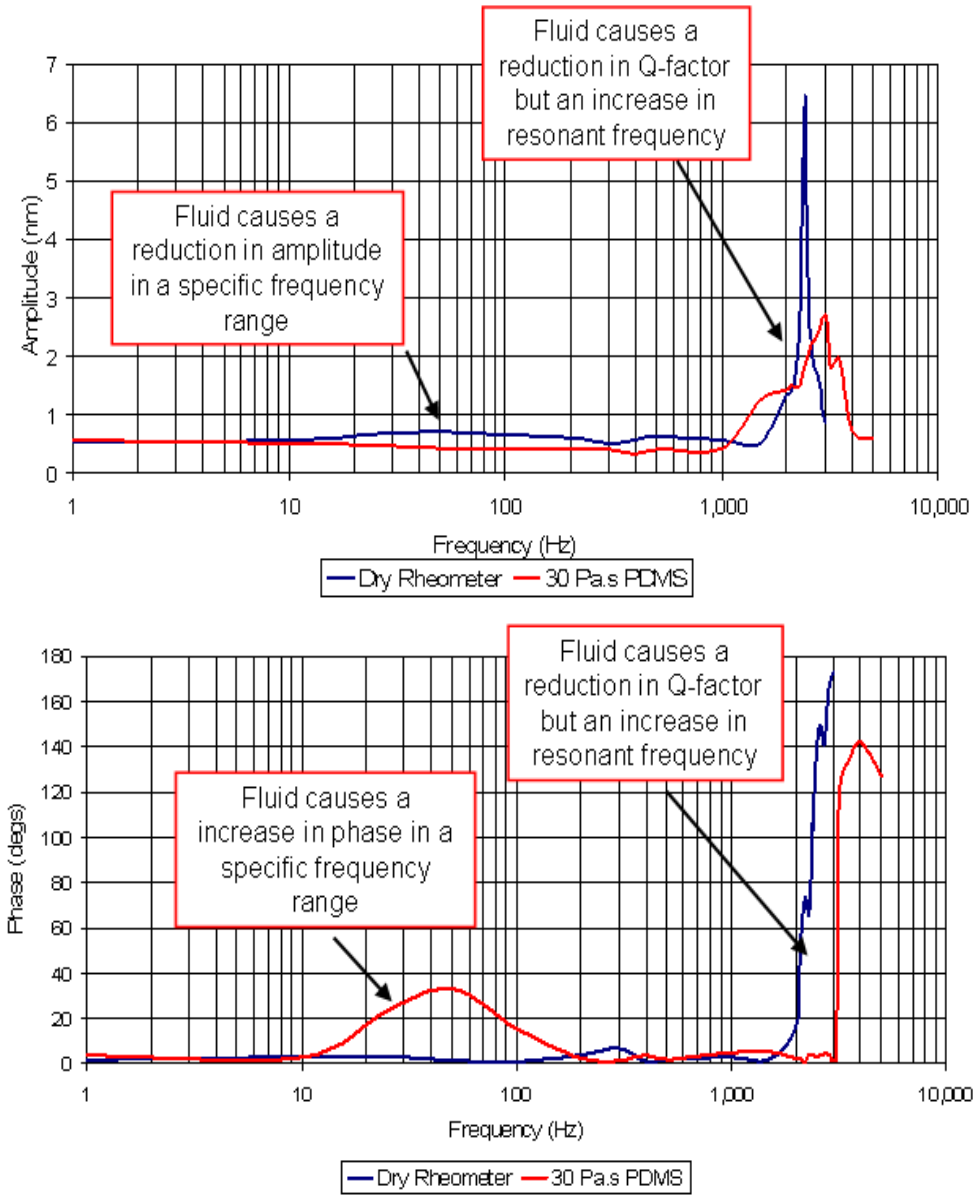

Fig. 8.24: Putting the 30Pas sample in the rheometer changes the response.

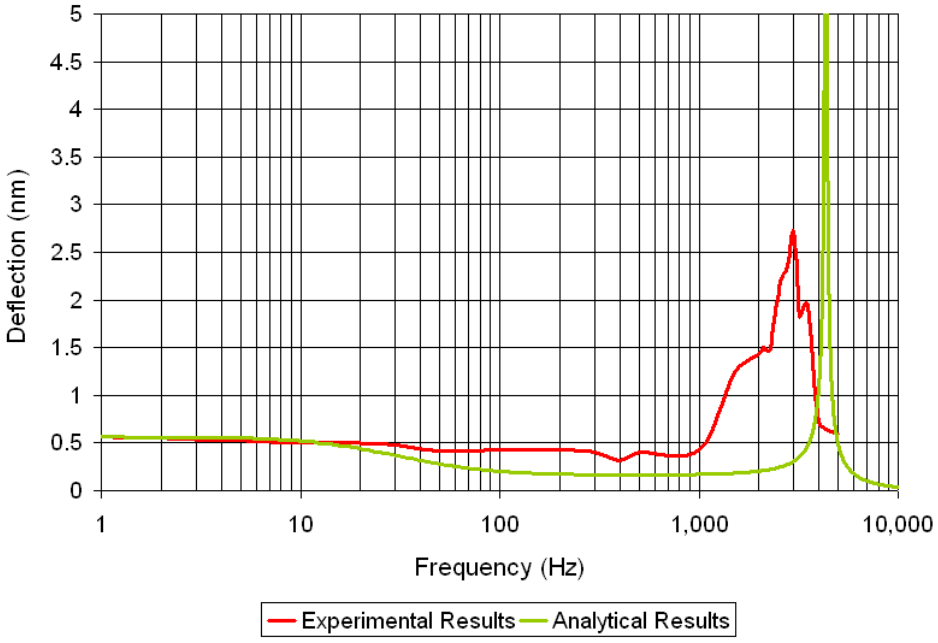

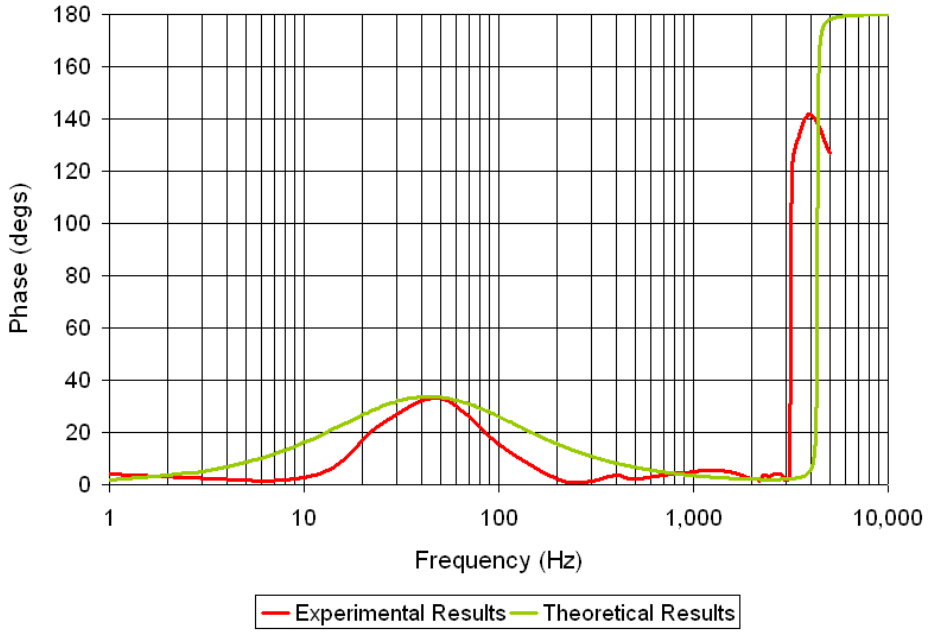

Fig. 8.25: Comparison between the theoretical results and the experimental results for the mechanical response for the 30Pas.

These experiments showed that the Mark I rheometer oscillated under the effect of an applied AC voltage. The results also show that the response of the rheometer is dependent on the properties of the fluid inside. Next it is important to ascertain whether the electrical response changes when the fluid is changed. A series of experiments were carried out in which the induced voltage was monitored as the frequency of the applied voltage was

varied (the amplitude was maintained at 5V). PDMS liquids with viscosities of 1 Pa.s, 10 Pa.s, 30 Pa.s and 340 Pa.s were used as the test samples. An example of how the phase and amplitude of the induced voltage changes with fluid is shown in Fig. 8.26.

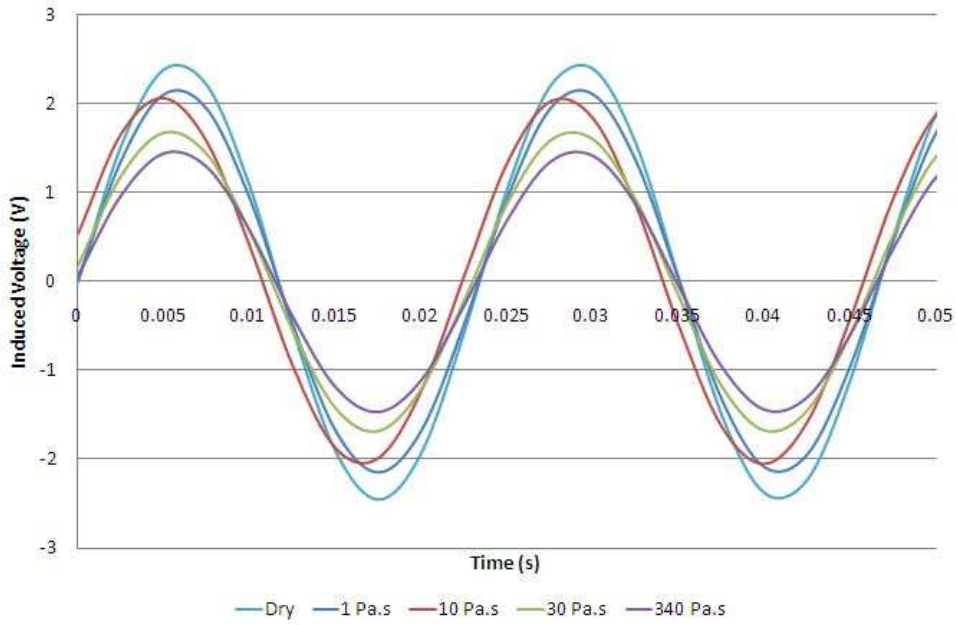

Fig. 8.26: The electronic response of the Mark I rheometer for PDMS of various viscosities at 40 Hz.

In Fig. 8.26 it is clearly seen that the response is dependent on the liquid properties, and that the phase and amplitude is a function of the relative magnitude of the fluid's storage and loss moduli. How the variation of these properties with frequency affects the response of the rheometer is more clearly shown in the frequency response graphs for the amplitude and phase of the induced voltage as given in Figs. 8.27 and 8.28 respectively.

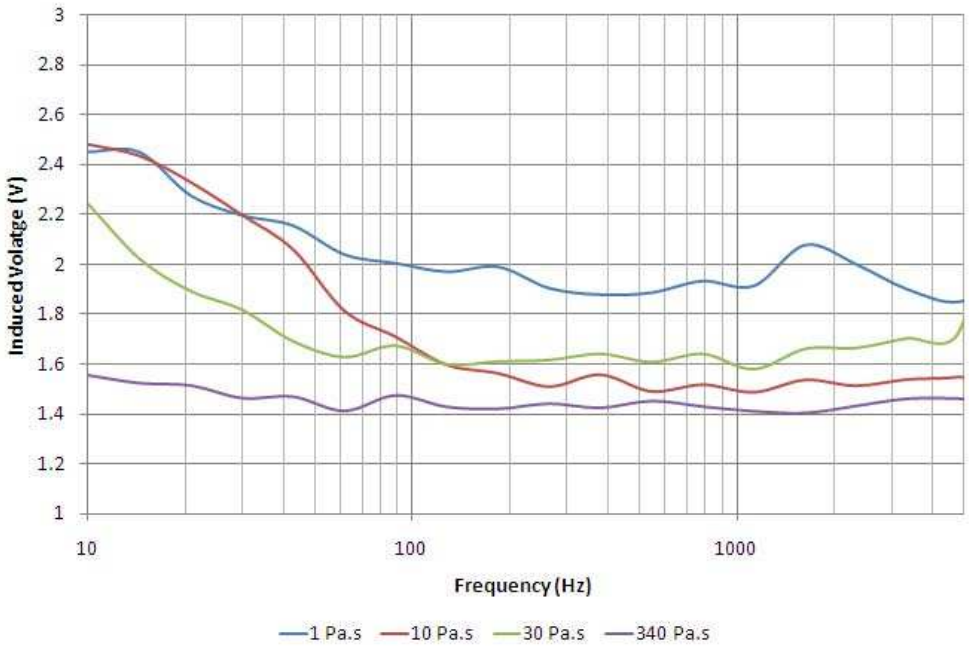

Fig. 8.27: The electrical amplitude frequency response of the Mark I rheometer for PDMS of various viscosities.

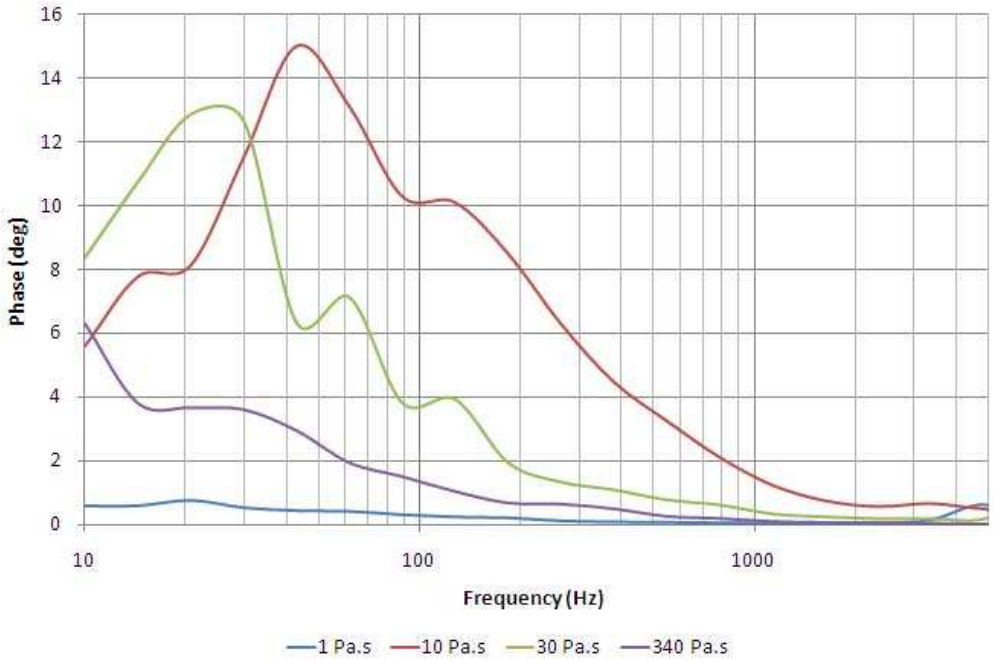

Fig. 8.28: The electrical phase frequency response of the Mark I rheometer for PDMS of various viscosities.

These frequency response curves clearly show that the liquids can be easily distinguished. This data was used to calculate the storage and loss moduli of the liquids. The results are shown in Figs. 8.29 and 8.30.

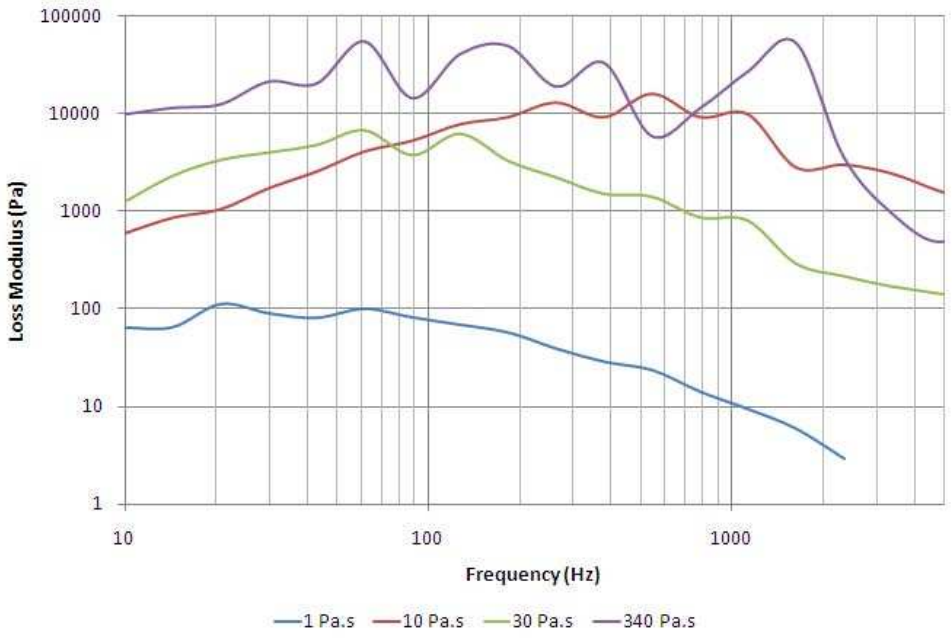

Fig. 8.29: The loss moduli for the various liquids as calculated from the data given in Figs. 8.27 and 8.28.

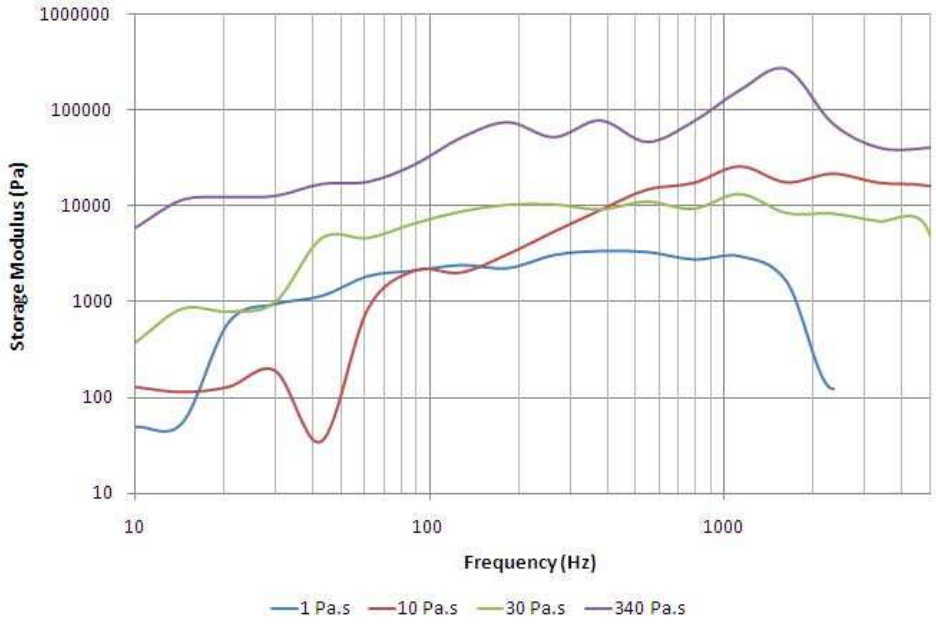

Fig. 8.30: The storage moduli for the various liquids as calculated from the data given in Figs. 8.27 and 8.28.

The trends given in the above graphs clearly show the expected increase in the values in the storage and loss moduli as the fluid viscosity increases. In order to assess the accuracy of these measurements, they are compared to the theoretical values given in Table 8.1 as calculated using cone and plate rheometry as discussed earlier. The results for the 10 Pa.s, 30 Pa.s and 340 Pa.s are shown below. This comparison could not be carried out for the 1 Pa.s as the storage and loss moduli were too small to be measured consistently with the cone and plate rheometer. The noise may be either electrical or mechanical (see Fig. 8.20). The electrical noise is due to instabilities in the circuitry which could probably be removed with more detailed design. There are a few potential sources for the mechanical noise and perhaps for the apparent reduced mechanical amplitude that the Mark I rheometer experienced. In Appendix C, there is an analysis of the potential effects of the surrounding air. Two main effects that air can have were considered. These were the viscous dissipation due to the squeezing of the entrained air inside the rheometer and the added mass due to the pressure waves being pushed through the air on the outside. It can be seen that the Mark I and III rheometers are potentially sensitive to pressure effects. The results shown in the appendix are theoretical results for static air. However as the quartz is so sensitive, it may be possible that air currents or pressure fluctuations may negatively affect the performance of the rheometer and increase noise.

The results shown in Figs 8.31 to 8.33 confirm that the Mark I rheometer does respond to the fluid properties reasonably accurately. It is evident however that the noise in the phase and amplitude of the induced voltage can result in significant errors in the measurement of the storage and loss modulus.

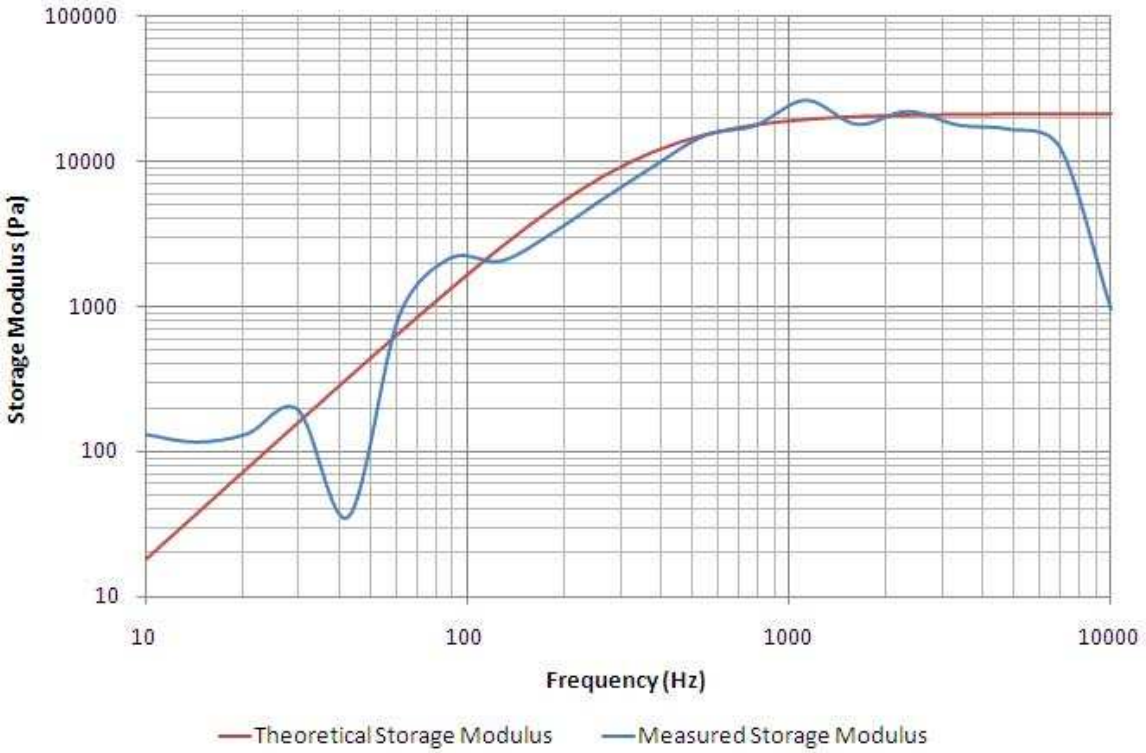

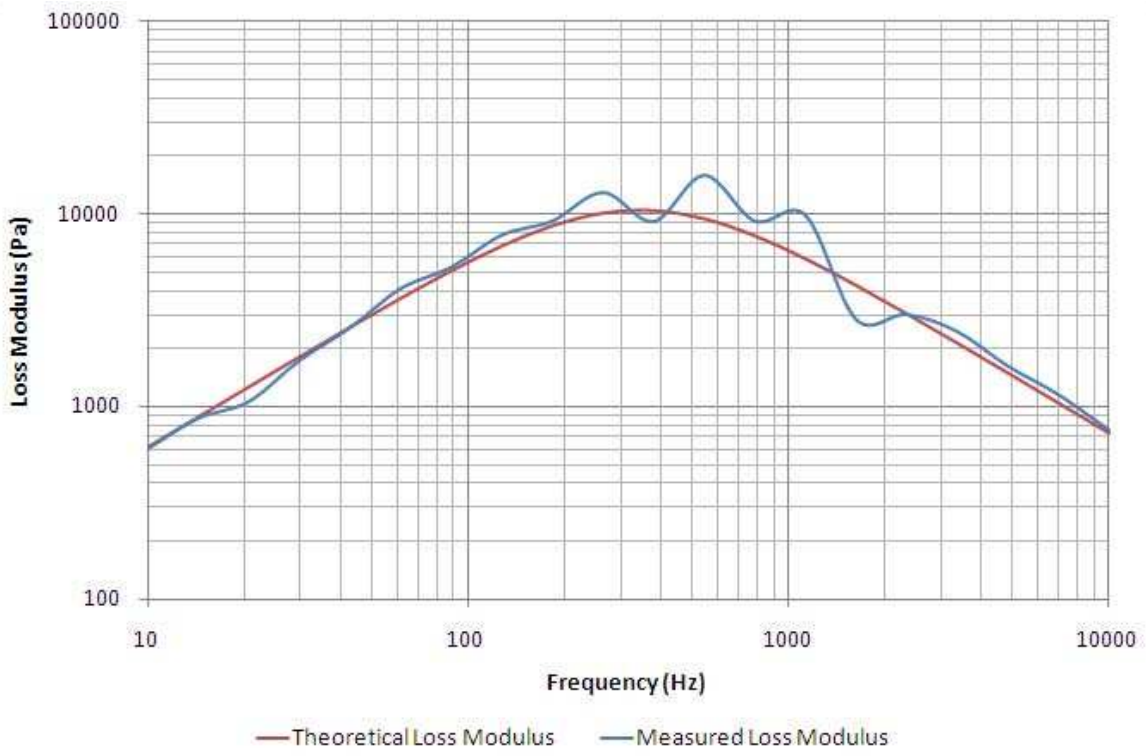

Fig. 8.31: A comparison between the measured storage and loss moduli for 10 Pa.s PDMS and the theoretical values calculated from the data in Table 8.1.

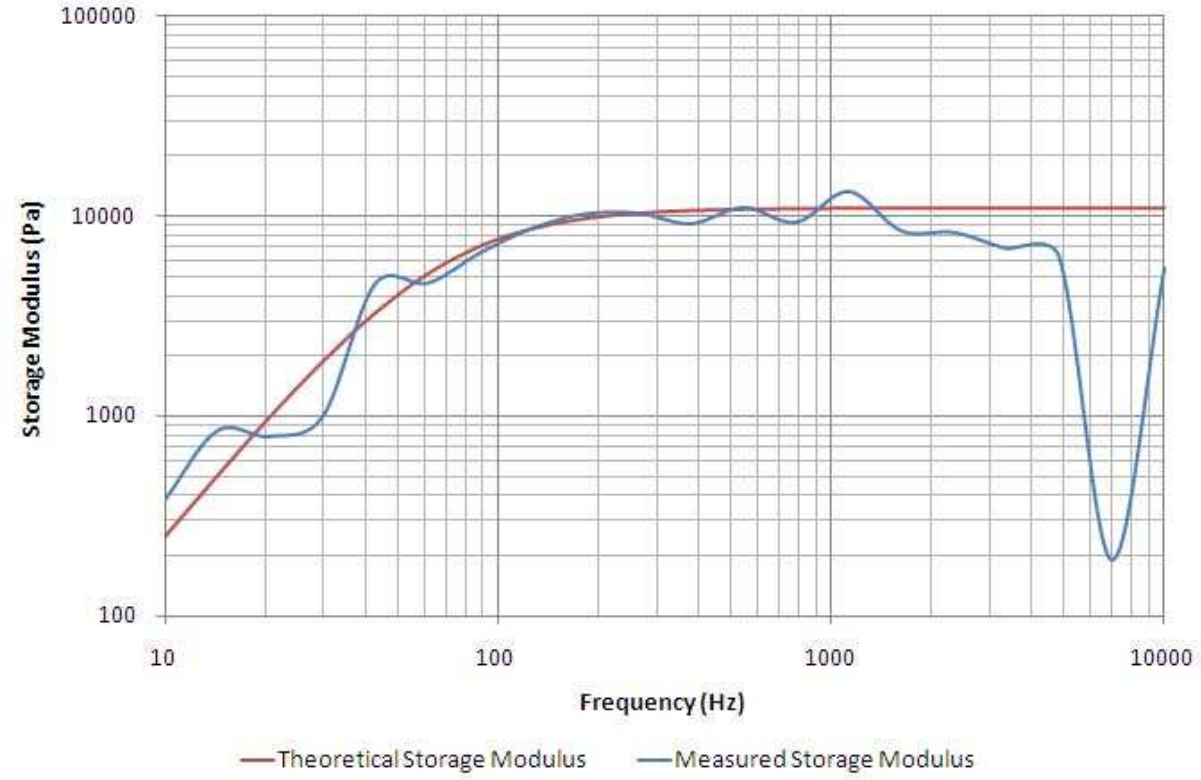

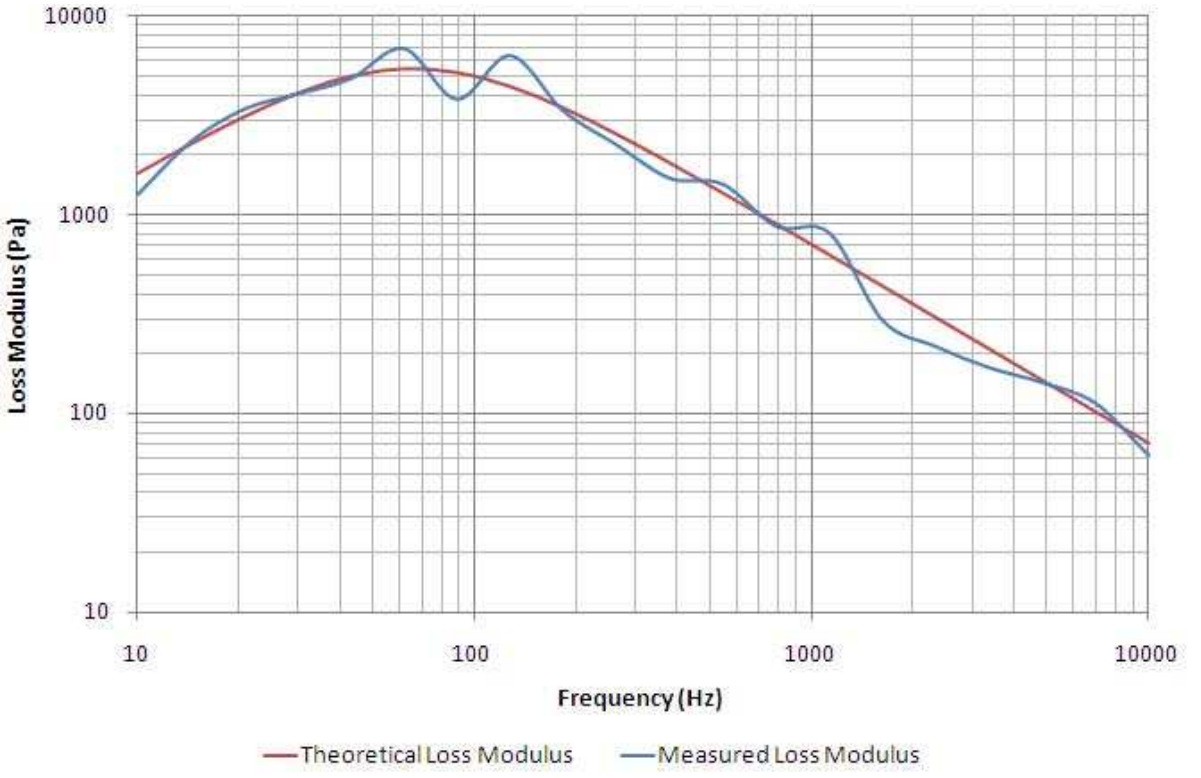

Fig. 8.32: A comparison between the measured storage and loss moduli for 30 Pa.s PDMS and the theoretical values calculated from the data in Table 8.1.

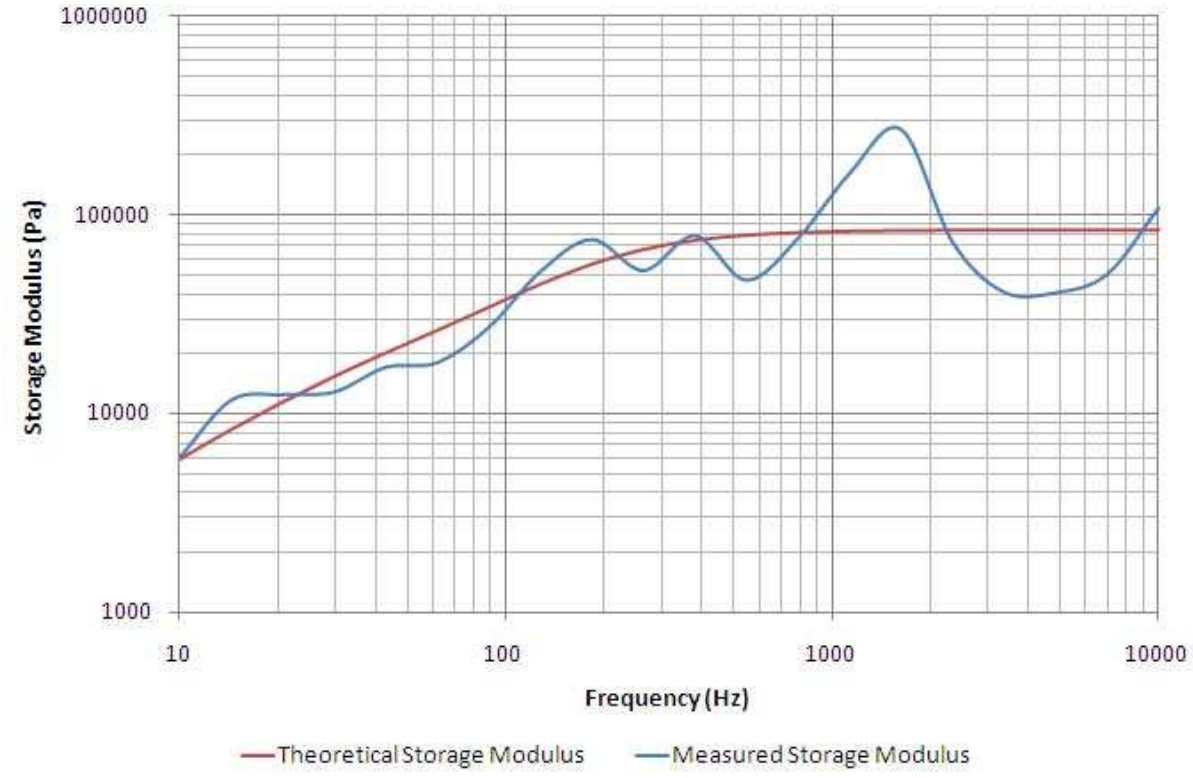

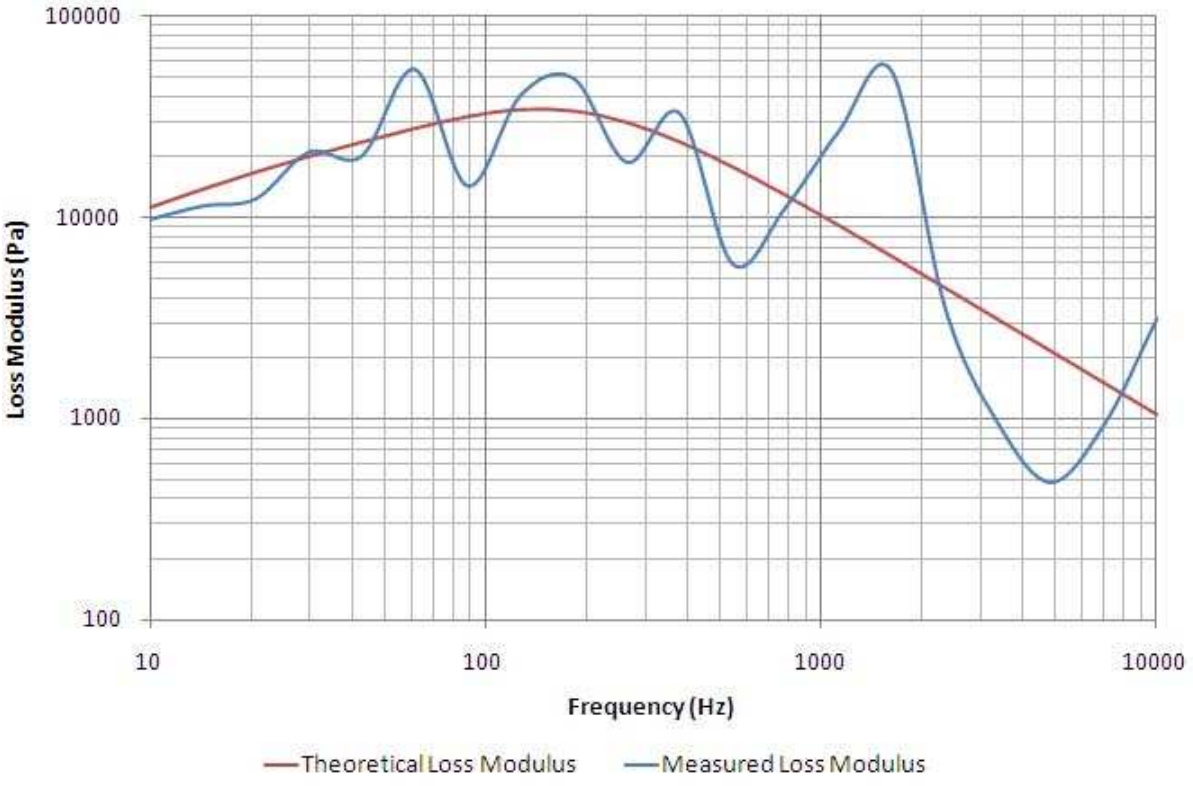

Fig. 8.33: A comparison between the measured storage and loss moduli for 340 Pa.s PDMS and the theoretical values calculated from the data in Table 8.1.

8.4.2. The Mark II Rheometer

The Mark II rheometer uses PZT-5H (Physik Instrumente GmbH & Co.) as the piezoelectric layer (see Fig. 8.34). PZT-5H is a widely used piezoelectric ceramic made from doped lead zirconate titanate, with typical constants, Young's modulus 62 GPa and d_{11} -274x10^{-12} C/N [207]. This had the advantage that the piezoelectric coupling constant is larger, meaning that the deflection of the rheometer will be larger for a given applied voltage but the induced voltage will be lower. This means a larger force can be applied extending the range of viscosities that the rheometer can handle. However, the electrical response becomes non-linear at higher voltages – a phenomenon not experienced with the quartz rheometers.

Fig. 8.34: The Mark II rheometer.

For example, compare the electronic response curves in Fig. 8.35. Here a voltage of amplitude 1 V, 5 V and 10 V and frequency 100 Hz was applied to the Mark II rheometer whilst dry. As can be seen, when the applied voltage is low, the response is linear, however as the applied voltage increases the response becomes more non-linear. Also the amplitude of the induced voltage does not increase as much as can be expected at the higher applied voltages. This suggests that, when large voltages are applied to the PZT second order effects and/or hysteresis become significant, affecting the response. The current model for the PZT does not take these effects into account and therefore the amplitude of the applied voltage will be maintained at 1 V for the Mark II rheometer. At

this voltage, a mechanical amplitude of 161 nm is expected, compared to the 11 nm of the quartz at 5 V.

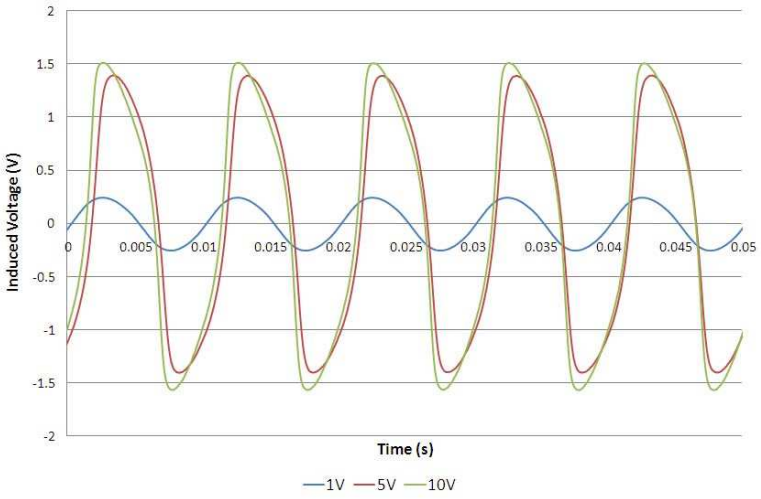

Fig. 8.35: The electronic responses of the Mark II rheometer as voltages of different amplitudes are applied. Note how at higher applied voltages the response is non-linear.

Various liquids were tested in the Mark II rheometer. The frequency response for each of the liquids is shown in Figs. 8.36 and 8.37. As can be seen there is a change in the amplitude and phase of the electronic response as the viscosity of the liquid increases.

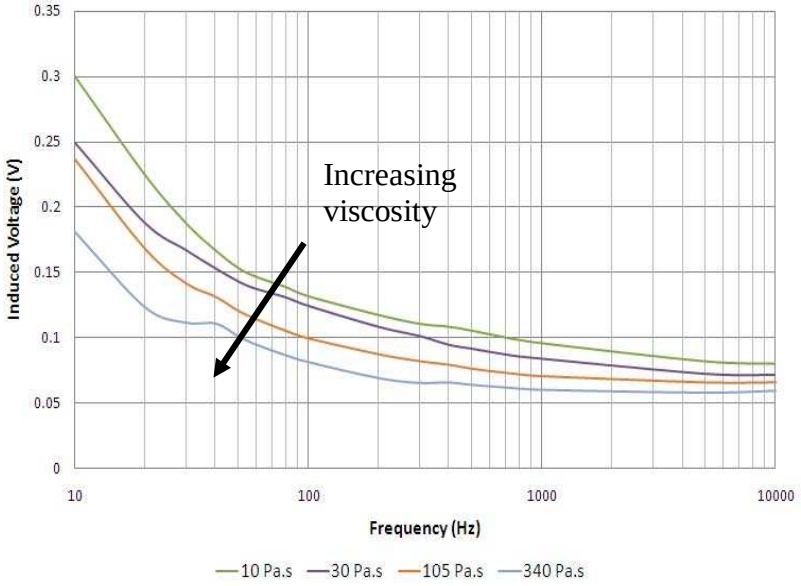

Fig. 8.36: The electronic amplitude frequency response for a range of fluids.

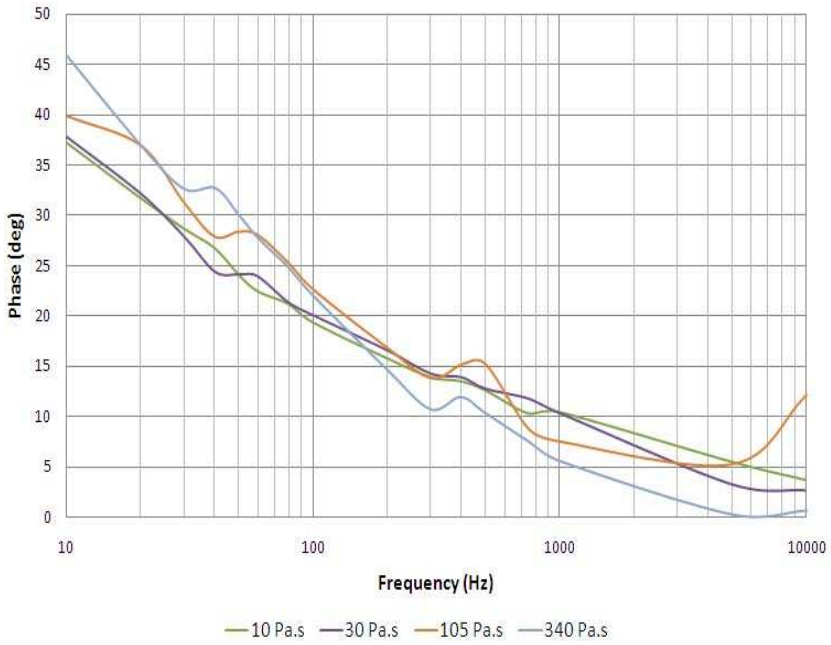

Fig. 8.37: The electronic phase frequency response for a range of viscoelastic fluids.

The model developed in previous chapters was then applied to these responses in order to find the measured storage and loss moduli for the various liquids. The results are shown below in Figs. 8.38 and 8.39:

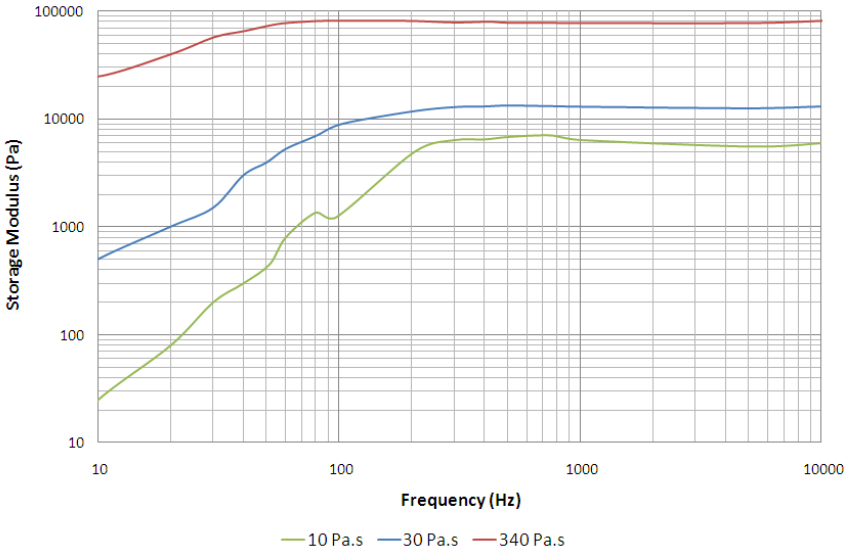

Fig. 8.38: The storage modulus for PDMS of various viscosities as calculated from the electronic response shown in Fig. 8.36 and 8.37.

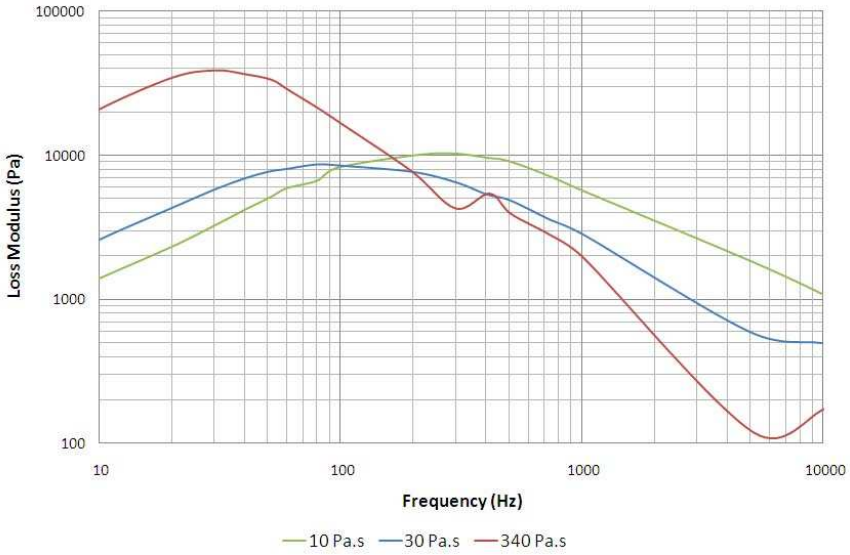

Fig. 8.39: The loss modulus for PDMS of various viscosities as calculated from the electronic response shown in Fig. 8.36 and 8.37.

These storage and loss moduli can be compared to the theoretical values to be found in Table 8.1 as calculated from the cone and plate rheometry. Note that the conventional cone and plate rheometry only tests the region up to 100 Hz. It is also important to note that while the moduli have been tested up to 10kHz, the frequencies above the resonant frequency of the rheometer (~1.6kHz) should be considered with care as above this frequency other mode shapes of the silicon diaphragm are becoming dominant and so may affect the curvature of the rheometer and so the electronic response. The results of this comparison can be seen in Figs. 8.40 to 8.42.

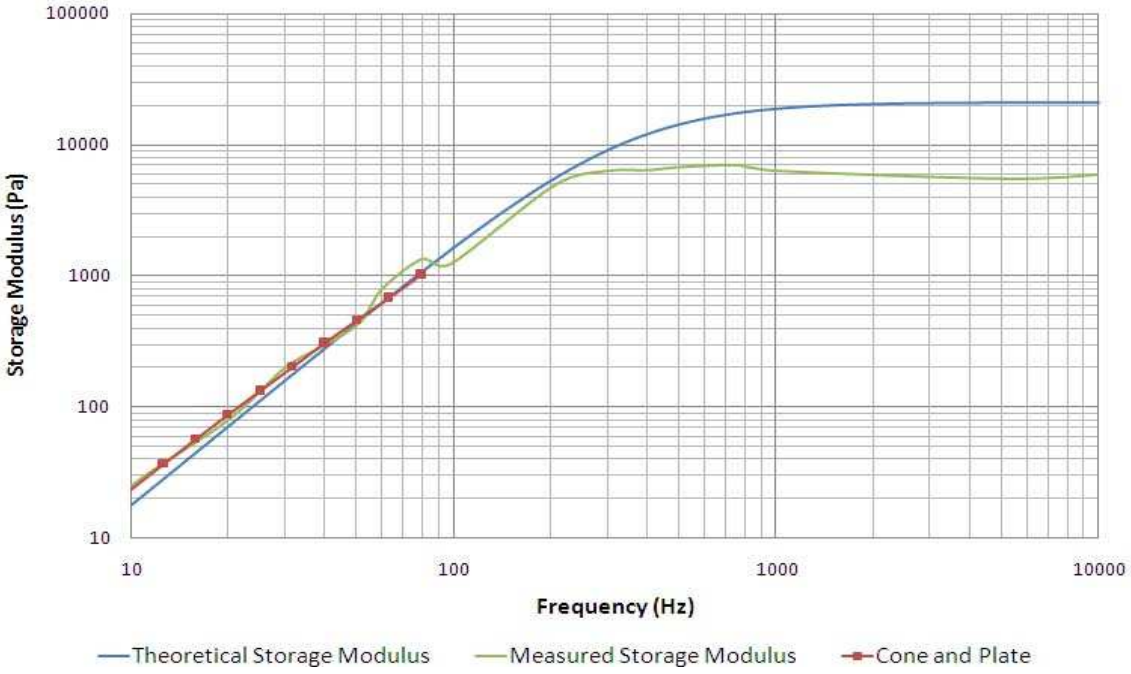

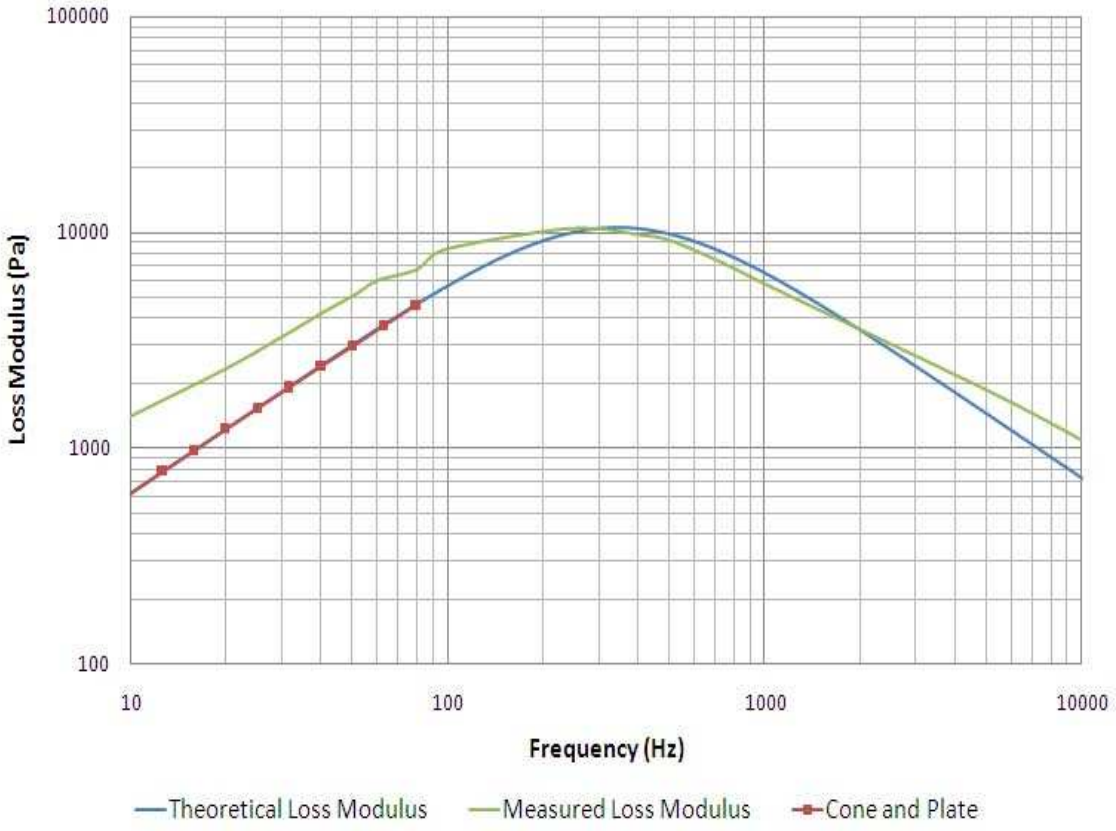

Fig. 8.40: The storage and loss moduli for 10 Pa.s PDMS as measured by the Mark II device as compared to the theoretical results and cone and plate rheometry.

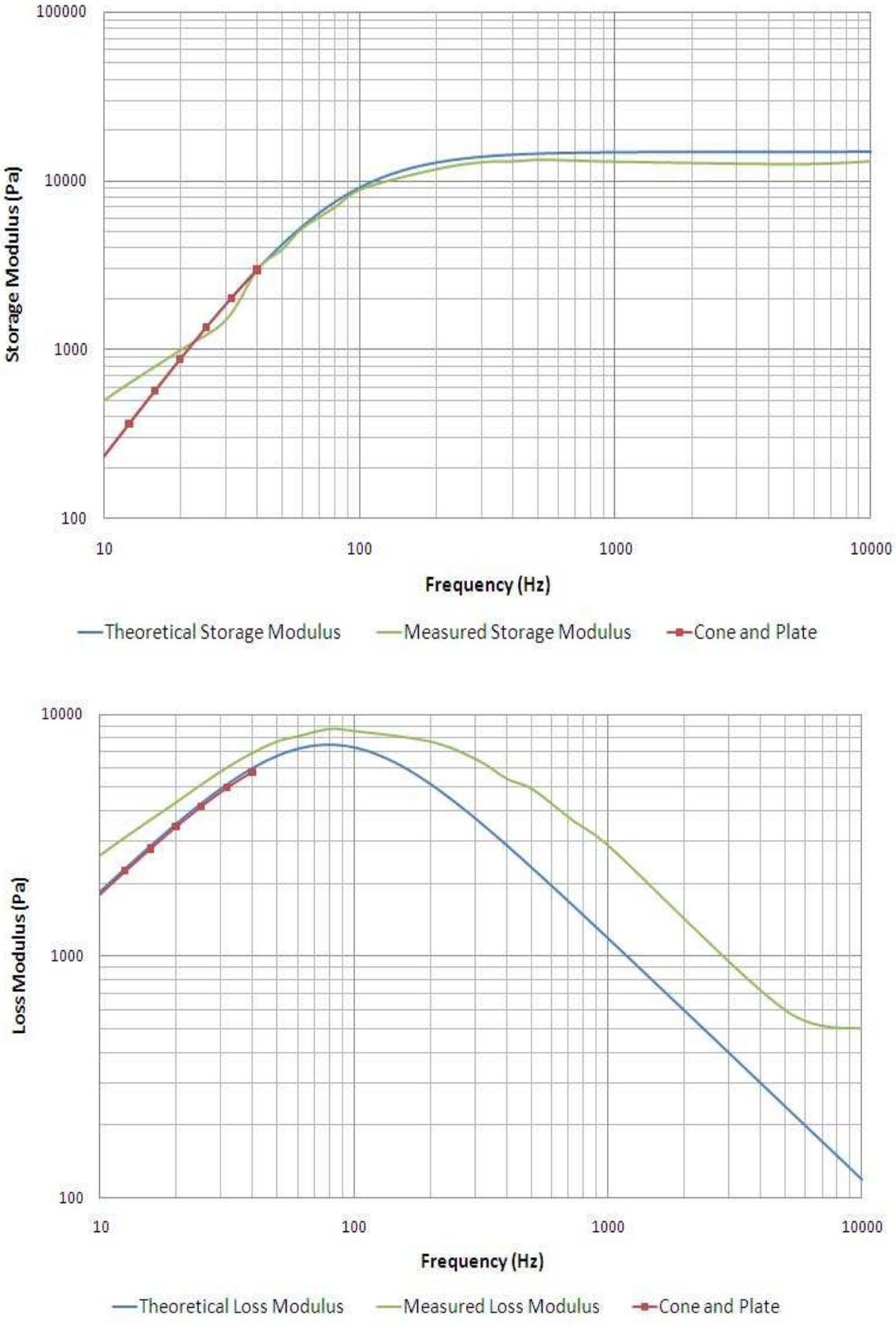

Fig. 8.41: The storage and loss moduli for 30 Pa.s PDMS as measured by the Mark II device as compared to the theoretical results and cone and plate rheometry.

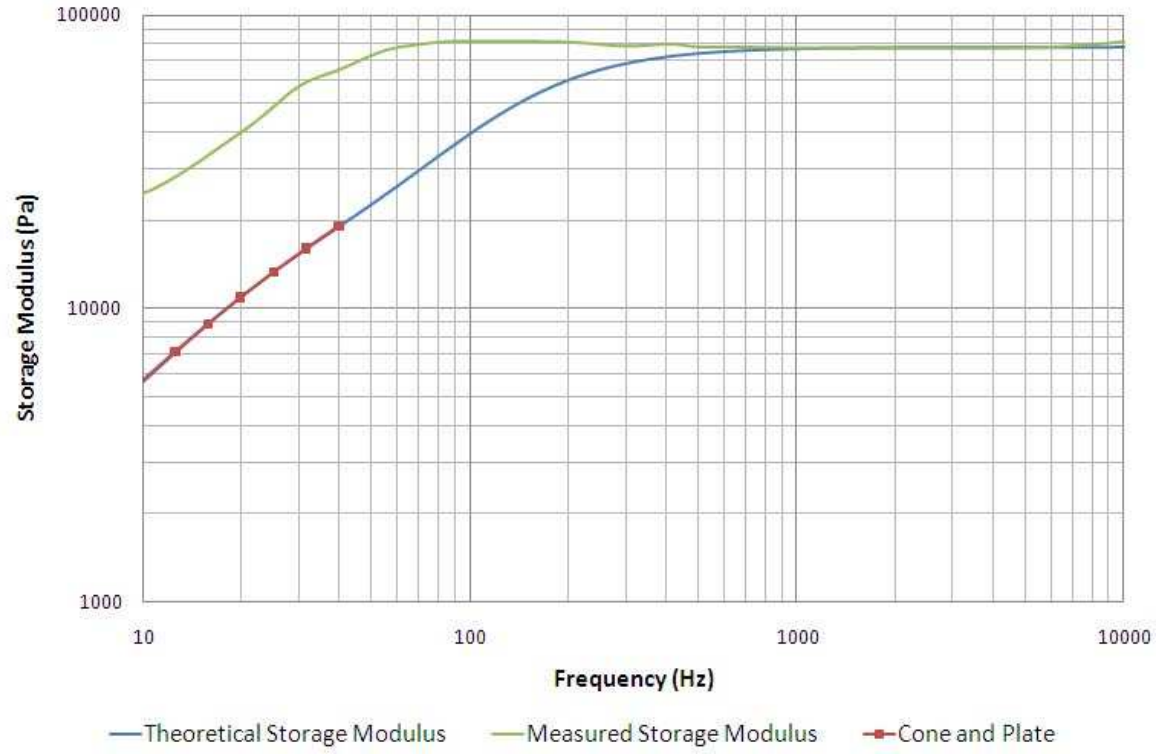

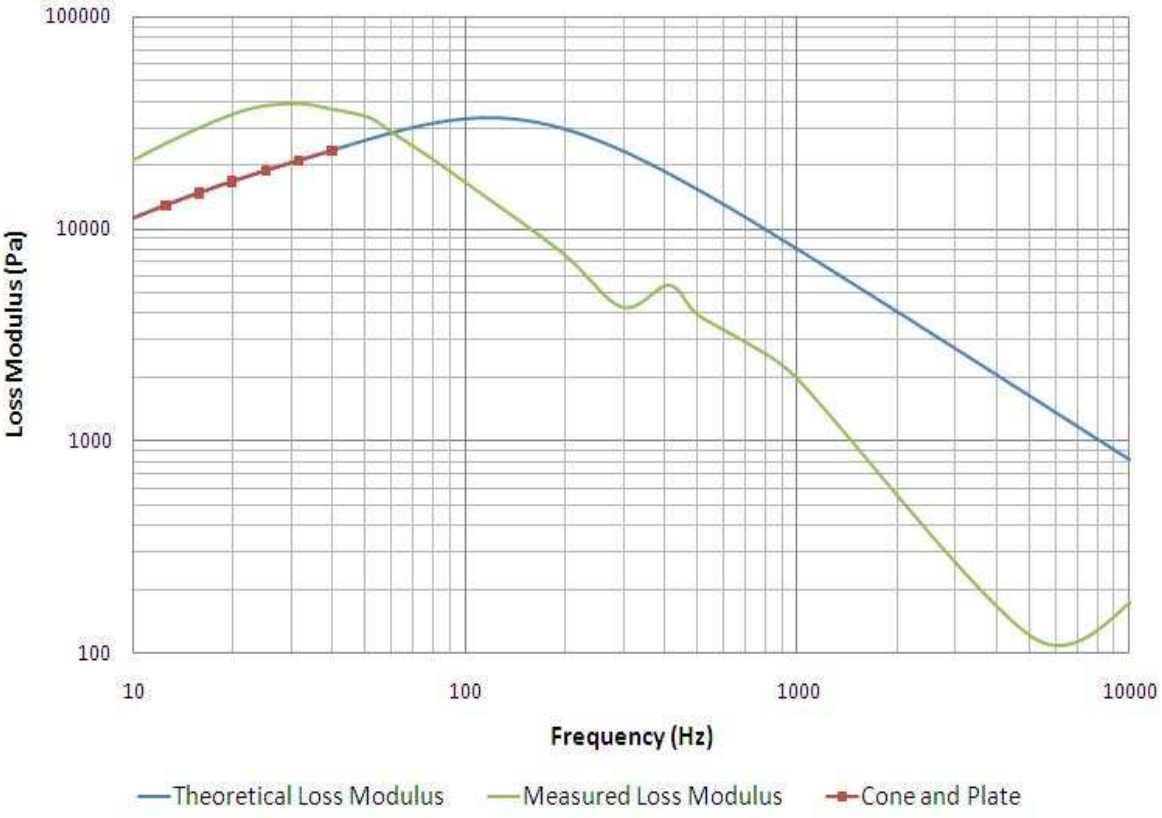

Fig. 8.42: The storage and loss moduli for 340 Pa.s PDMS as measured by the Mark II device as compared to the theoretical results and cone and plate rheometry.

The comparisons show excellent agreement between theoretical and experimental results for the 10 and 30 Pa.s PDMS. The 340 Pa.s PDMS results show some discrepancy. However if the frequency of the peak of the loss modulus is considered, the Mark II rheometer shows that this frequency should decrease with viscosity. The results from the cone and plate rheometry do not show this trend. This may suggest some inconsistency in the cone and plate rheometry rather than the Mark II rheometry. Either way the results show that the Mark II rheometer shows great potential.

Two further lower viscosity Newtonian liquids were also tested. These were Glycerol (viscosity 1.5 Pa.s) and 5 Pa.s PDMS. These cannot be tested on a cone and plate rheometer normally because their viscosity is so low that they tend to flow away from the cone instead of forming a bridge. An advantage of the microrheometer is that the gap is so small that most liquids can be held in place by their own surface tensions. This isn't true of volatile liquids which will tend to evaporate too quickly, owing to the small sample volume, a problem which can be rectified by using the rheometer under saturated vapour conditions. The frequency response is shown in Fig. 8.43 and their corresponding storage and loss moduli are shown in Fig. 8.44. Interestingly, the liquids displayed a small elastic component when normally the fluids are considered to be purely viscous. Further testing is required in order to ascertain whether this is just an artefact of the microrheometer.

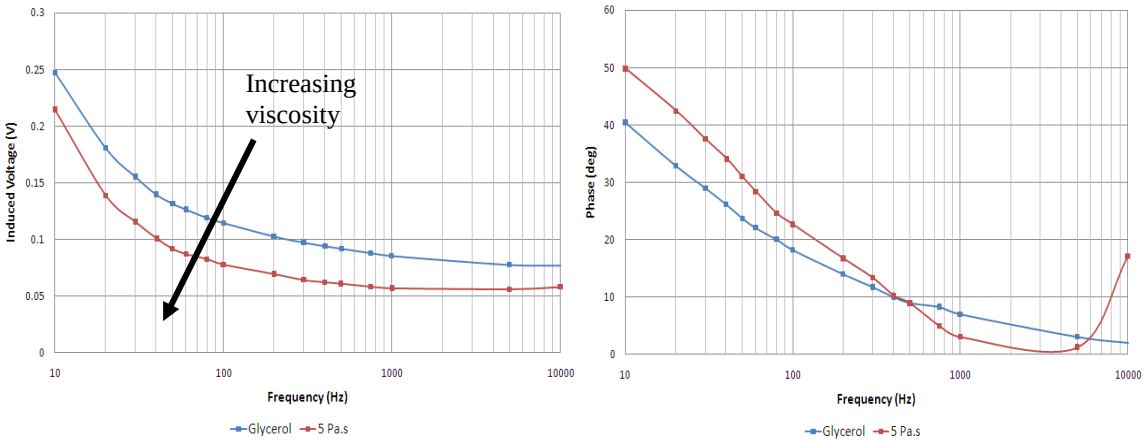

Fig. 8.43: The frequency response of the Mark II rheometer for glycerol and 5 Pa.s PDMS. Note how the trend is similar to that shown by the more viscoelastic material.

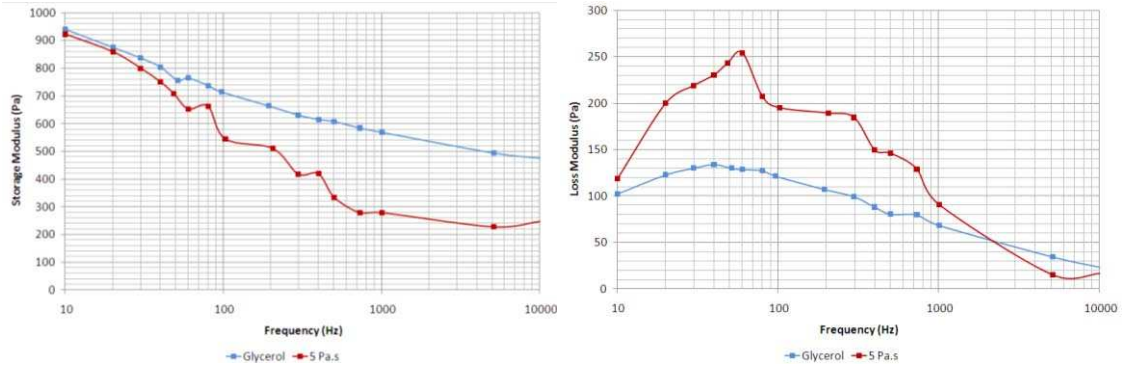

Fig. 8.44: The storage and loss moduli of glycerol and 5 Pa.s PDMS as measured by the Mark II rheometer.

8.4.3. The Mark III Rheometer

The Mark III rheometer was designed to have been fabricated by directly bonding a patterned quartz wafer to the silicon membrane. The quartz was then to be polished to the required thickness before the silicon was processed, see Chapter 7 for details. The powder blasting process, which was used to pattern the quartz to form the piezoelectric disc on the active plate, seems to have been very successful as seen in Fig. 8.45. This suggests that this is a good way of patterning quartz prior to bonding.

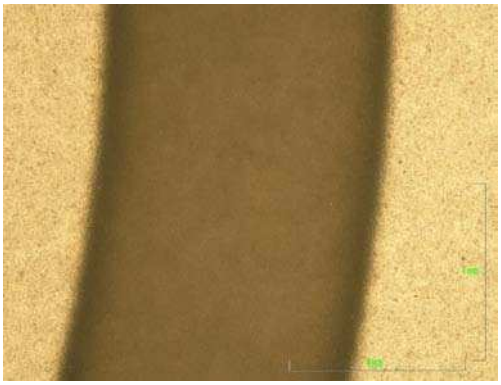

Fig. 8.45: A close-up of an area of quartz etched using the powder-blasting technique. Note that the edges are reasonably smooth.

However upon bonding, the quartz and BSOI wafer cracked. The principal reason is due to the thermal expansion mismatch between the X-cut quartz and the silicon membrane. Normally quartz bonds well to silicon, for example see Fig. 8.46. However it seems that usually it is a temperature-insensitive cut of quartz (such as AT-cut quartz) that is bonded. But these cuts tend to only actuate in shear not radially as is required for the rheometer.

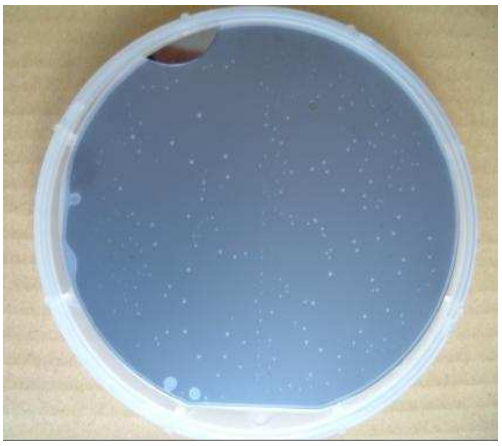

Fig. 8.46: A AT-cut quartz wafer bonded to silicon. Note that the bond is of a good quality with no cracks. The white areas are voids but these can be omitted using careful processing.

X-cut quartz does expand radially but expands significantly with temperature causing the silicon substrate to crack. For instance, a silicon wafer bonded to X-cut quartz is shown in

Fig. 8.47. Even though only a small area was bonded the stress was enough to crack the wafer (it is thought that the bond area was so small due to the concavity of the two wafers). This happened to all the wafers, even at the minimum temperature that the bond process works.

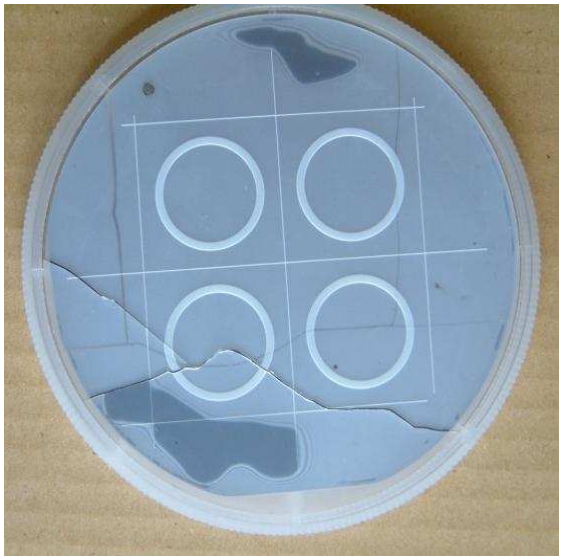

Fig. 8.47: An example of bonded X-cut quartz (in this case after the powder blasting process). Note the dark bonded areas and the crack.

Different methods were tried so that the benefits of direct bonding could still be taken advantage of. The first was to use a thinner quartz wafer (100μm thick), as it was thought that it may be more compliant and put less stress on the silicon, but the quartz was too delicate and still cracked. Thin quartz discs such as those used in the fabrication of the Mark I rheometer were also tried. However it was found that these discs were too flimsy to survive the cleaning process (the wafers to be bonded are cleaned using piranha etch) and were generally too rough to get a strong enough bond.

There are alternative processes that may counteract the thermal mismatch issue. It is possible that using two thin X-cut quartz wafers orientated and bonded perpendicularly to

each other could counteract the other wafers anisotropy giving the pair a useable thermal expansion coefficient. Another method is to use an intermediate adhesive layer which would absorb the stress. Whether this would result in permanent induced stress in the rheometer it is not known. However this method would negate some of the advantages of using the bonding process such as having no gap between the quartz and the silicon diaphragm. That said, if the adhesive layer was spun on to an accurate and small thickness and the quartz/PZT aligned accurately, this method may at least remove some sources of error which may occur in the fabrication of the Mark I and II devices. For example the topology of the underside of the silicon diaphragm of one of the Mark II devices was measured using interferometry (ADE Phase Shift MicroXAM-2 optical interferometric profiler) (see Fig. 8.48). It can be seen that there is some latent curvature in the silicon diaphragm which is most likely due to the use of adhesive. Moreover the stress seems to vary over the diaphragm surface as shown by the roughness of the surface. The effect of this is not known, but still it is preferable if the issue can be neglected all together using a better fabrication technique.

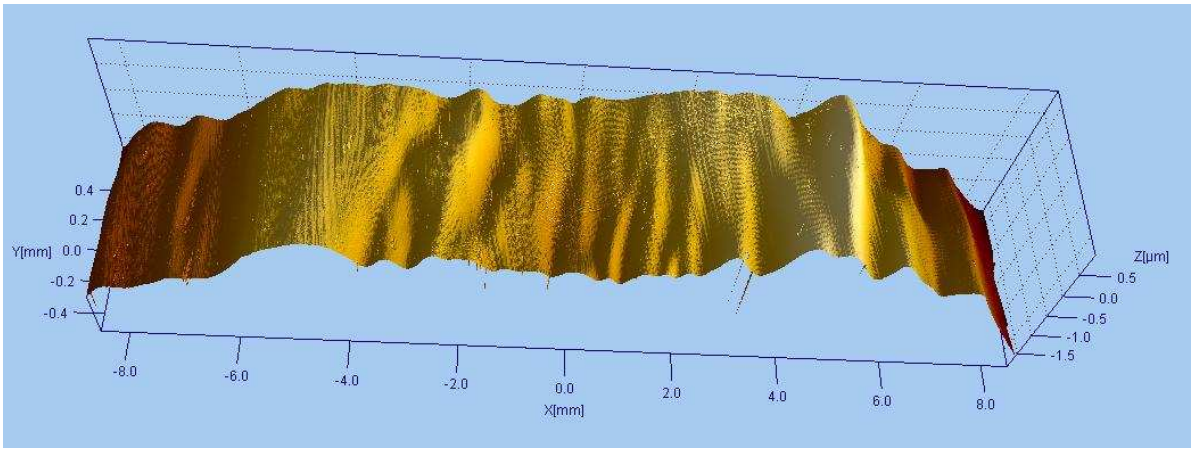

Fig. 8.48: A cross-section of the topology of the underside of the silicon diaphragm of a Mark II device after fabrication. Ideally this should be completely flat.

Further investigations will certainly involve seeing whether one of the methods described can be used to make a successful Mark III device.

8.5. Conclusion

In this chapter the experimental results pertaining to the testing of the microrheometer have been discussed. Cone and plate rheometry has been used to gather storage and loss moduli data on a range of different PDMS liquids. The generalised Maxwell model was then applied to this data to find the parameters which were then used to test the accuracy of the microrheometer. It has been shown that the use of C_4F_8 allows for the testing of fluids by ensuring that they form a sessile drop on the platen rather than flowing away. It has also been shown that the C_4F_8 is stable and can be cleaned without issue. The electronic circuit used to gather data from the microrheometer was then analysed. Deficiencies in the original circuit were recognised and the circuit was duly improved to an extent that it could be used successfully for experimental purposes.

Finally the different versions of the microrheometer were tested in order. It was found that whilst the Mark I rheometer was sensitive to noise, it could, along with the Mark II rheometer, be successfully used to measure the storage and loss moduli of a range of liquids with good accuracy compared to the data gathered from conventional rheometry. It was also shown that the rheometer was able to test liquids at frequencies at least one order of magnitude higher than conventional rheometry and with volumes in the nanolitre range. This satisfies the goal of the project set out in Chapter 1.

9 CONCLUSION AND FURTHER WORK

In this thesis a micro squeeze flow rheometer was developed and tested. This chapter presents a summary of the need for such a device as well as the goals of the project. Following this, an overview of the proposed design, especially its novel aspects, will be given before detailing how the design was modelled and tested experimentally. Finally a summary will be made of the project before discussing possible directions for future research.

9.1 Conclusion

In this section, the different aspects of the project will be reviewed in order to assess the success of the project and to highlight the achievements made.

There are many industries such as the pharmaceutical, cosmetic and food industries, that are actively involved in the development of novel, often complex, liquids. Naturally, in order to provide the best product, these liquids need to be analysed in order to ascertain their rheological properties. Traditionally this analysis was performed using the conventional rheometers discussed in Chapter 1. These rheometers are often large and require large volumes of liquid in order to get reliable results and are limited to low frequencies. However, the nature of research that is taking place in industry and academia often means that only small volumes of liquid can be produced. This is especially true in medical and biological research when samples cannot be artificially produced. There is also a drive to test these fluids at higher and higher frequencies so that the fundamental

processes that occur within the fluid at short times scales can be analysed. This has led to the development of microrheometric techniques. At present many of these techniques require sophisticated equipment and in many techniques the physics is often not completely understood to within the necessary accuracy. It is apparent that there is a need for a microrheometer that can be made cheaply and easily and can be modelled accurately.

The proposed design consists of a central platen supported by a circular silicon membrane partially covered by a piezoelectric disc. The piezoelectric disc has specifically placed electrodes so that when a sinusoidal voltage is applied to the active electrodes the piezoelectric disc will oscillate radially, causing the platen to move up and down squeezing the liquid. These oscillations cause a voltage to be induced which can be measured at the passive electrode. The phase and amplitude of the induced voltage are a function of the fluid's properties.

This design has a number of advantages over existing rheometers:

1. It can measure the properties of a wide range of liquids. The range of liquids that was tested had viscosities that ranged over 1 Pa.s to 340 Pa.s. The storage and loss moduli that could be measured covered the range from 5 Pa to over 100000 Pa.

2. It is very small and cheap. The overall size of the rheometer was only 30 mm by 30 mm by 1mm, without circuitry. This means that research centres could employ a number of these rheometers to perform parallel testing for high

throughput screening. This will help improve efficiency and costs when prototyping new materials.

3. It only requires small volumes of liquid. The proposed design, which had platens with a radius of 250 μm and a separation distance of 20 μm, only required 4 nanolitres of liquid to produce accurate data whereas conventional rheometers require millilitre volumes. Even other squeeze flow rheometers (see Chapter 1) currently need more than 100 μl. There is also the possibility to vary the dimensions of the platens during the fabrication stage to facilitate testing of exotic materials such as cells. This means more tests can be performed on the same volume of liquid than previously, reducing the cost of development.

4. It can operate at frequencies in the kHz range. The Mark I rheometer had a resonant frequency of 2700 Hz and the Mark II rheometer had a resonant frequency of 1600 Hz. The theory behind the rheometer assumes that it is operated below resonance and so it was assumed that the Mark I rheometer was accurate below 2 kHz and the Mark II rheometer below 1 KHz. Most conventional rheometers can only work reliably up to frequencies of the order of 100Hz. This rheometer has lower inertia, allowing it to oscillate at higher frequencies without being unstable.

5. It has only one active component. Most rheometers require a number of actuators and sensors that need to be assembled carefully making them expensive.

The rheometer was fully modelled analytically. This was done by coupling together the capillary effects, including contact angle hysteresis, the viscoelasticity of the liquid, the piezoelectric effects and the plate mechanics of the rheometer. The model allows the calculation of the storage and loss modulus of the liquid as a function of frequency given the phase and amplitude of the induced voltage. This was achieved by making the initial assumption that if the amplitude of the mechanical oscillations were small enough, the dynamics of the rheometer could be modelled with a linear second order differential equation, the constants for which were determined through analysis of the individual forces.

It was shown that the capillary force was nonlinear because of contact angle hysteresis at the solid/liquid/vapour interface. This force was first calculated by solving the Young-Laplace equation numerically, but this method was inconvenient. A closed form solution for the capillary force was found using the toroidal approximation. Using this model it was shown that if the gap oscillated with small amplitude that the contact line did not slip – allowing the force to be linearised. Using conventional cone and plate rheometry, it was shown that the fluid could be modelled accurately by assuming the generalised Maxwell model was its constitutive equation. This allowed a complex viscosity to be defined. This simplified the rheology and allowed the viscous and elasticity constants for the fluid to be deduced.

The analysis showed that the force exerted on the rheometer by the fluid is a sinusoidal force with the same frequency as the rheometer as determined by the applied voltage. Therefore an analytical model of the rheometer as a partially laminated piezoelectrically

actuated plate under the influence of an applied voltage and a central point load was found. From this result, the stiffness, the effective mass of the rheometer and the effective force due to the applied voltage was found. Combining these constants in the initial differential equation meant that dynamics of the rheometer was known.

Knowing the forces acting on the rheometer as a function of time meant that the strain and hence the voltage induced in the rheometer could be calculated using the plate equations developed earlier. This analysis led to the model of the rheometer whereby the storage and loss moduli of the liquid can be found from the induced voltage from the rheometer.

The rheometers were fabricated using the process discussed in Chapter 7. Upon testing, however, it was found that the impedance of the piezoelectric layer masked the effects of the fluid on the induced voltage. To negate this impedance a unity gain buffer amplifier was built into the circuit. This removed the impedance effects but the response was still noisy. The circuit was improved further by adding in phase compensation components which made the response smoother. Two versions of the rheometer were tested. One used quartz as the piezoelectric layer and the other used PZT. The quartz rheometer (Mark I) was shown to be more sensitive producing a larger voltage but exhibited more noise in its response. The amplitude of the induced voltage whilst dry was 2.45 V ± 0.1 V when the applied voltage had an amplitude of 5 V and the noise in the phase was ± 2°. The PZT rheometer (Mark II) had a smoother response but was less sensitive and was shown to display signs of nonlinearity at high applied voltages. The dry amplitude was 0.3 V ± 0.01 V when 1 V was applied the noise in the phase was the same as the Mark I rheometer. Several liquids were tested in the two rheometers. These were PDMS of different

viscosities. Both versions of the rheometer had a different electrical response for each of the liquids showing that the response was dependent on the fluid properties. Using the model developed in the previous chapters, the data was used to calculate the storage and loss modulus for each of the fluids. The responses from both rheometers gave results that were similar to those predicted by the cone and plate rheometry. This shows that the model was valid and that the design can be used to measure the storage and loss moduli of nanolitre volumes of liquid at high frequencies.

9.1.1 Summary

The project was to design, model, fabricate and test a novel microrheometer capable of measuring the storage and loss modulus of small volumes of fluid at frequencies higher than conventional rheometers can manage. This thesis has shown that this was achieved. The volume required for analysis is of the order of nano-litres several orders of magnitude less than conventional rheometry. The rheometer operates at frequencies approaching the kHz range, an order of magnitude greater than conventional rheometry. Therefore it has been shown that the rheometer can measure the storage and loss modulus of fluids at volumes and frequencies that at present no other device of such small size and simplicity can achieve. While there are still a few details to be investigated, it is apparent that the device has the potential to be of great use in rheological research be it for industry or academia.

9.2 Future Work

The work undertaken during the project as discussed in this thesis shows that there is potential for this rheometer to be improved further to the point where it can be industrially useful. At this point it has been shown that the premise and theory behind the rheometer are valid and that it can indeed be used to measure the dynamic properties of small volumes of fluids at frequencies above those of conventional rheometers as stipulated in the original brief disclosed in Chapter 1. However there are a few issues, such as robustness and the circuitry, that need to be resolved before any commercialisation can be considered. To this end, the work that needs to be done in the future is discussed below:

9.2.1 Full Systematic Study of Potential Uses

The rheometer was tested with a range of PDMS and other simple Newtonian liquids. This was in order to see whether the model worked and the design was feasible; it was necessary to use simple fluids that behaved in a simple manner, in that they can be treated as viscoelastic or Newtonian as applicable. However, it is apparent that the rheometer can be used for much more. Areas to be investigated may include:

- The squeezing of cells to measure their multiphase mechanical properties.
- The measuring of polymers and other structured fluids/soft solids.
- The measuring of biological material that is inherently only available in small quantities.
- Emulate real lubrication conditions. There are many examples of situations where the rheology of materials may be affected by their surroundings. However, the platens in the rheometer can be coated with a variety of different materials to see

the effect of charge, surface chemistry etc. on the lubricity of fluids. For example, it is possible to grow/deposit bone cells on the platens and test synovial liquid and hence emulate synovial joints such as the knee or hip. Alternatively, due to the small size of the rheometer, it can be placed in warm, cold or humid conditions to see if this has an effect on the fluid properties.

9.2.2 Impedance of Air

It was shown that the rheometers may be sensitive to the effects of the impedance of the air. It seemed that air can negatively affect the performance of the rheometer, potentially introducing noise and decrease accuracy. These effects weren't included in the full model as the issue only became apparent late in the project. However, a more extensive study could be made and either the effects should be built into the model and compensated for, or the experimental rig should be redesigned to negate them.

9.2.3 Anisotropy of Quartz

As discussed in the previous chapter, the Mark III rheometer was not fabricated successfully. This was due to thermal expansion mismatch between the quartz layer and the silicon diaphragm. This is a shame because if this was successful, the Mark III would have been more sensitive and more accurate than the previous versions. There are alternative methods that should be investigated in the future. One is the use of an intermediate adhesive layer which will help reduce the stress and hopefully prevent cracking. Another is the use of two layers of quartz with their crystallographic planes placed perpendicularly to each other. This will have the additional advantage of negating the anisotropy of the quartz, simplifying analysis and improving accuracy. This will

however make the rheometer thicker, unless a method of bonding very thin quartz discs together is found (use of Van der Waals forces perhaps?). However, it is likely there will still be a thermal expansion mismatch between the quartz and silicon and so it may be that an investigation into alternative bonding methods or alternative diaphragm materials such as nitrides or metals will yield beneficial results.

9.2.4 Electronics

For the purposes of negating the impedance of the piezoelectric layer and facilitating the measuring of the fluid's dynamic properties, a bespoke circuit was designed and used. However, the circuit was still quite basic owing to the author's inexperience and it is quite apparent that it can be developed to improve its noise and stability characteristics.

Appendix A: Calculation of Material Properties for Quartz

The compliance matrix for quartz is given as [170]:

$$s_E = \begin{bmatrix} 12.77 & -1.79 & -1.22 & -4.5 & 0 & 0 \\ -1.79 & 12.77 & -1.22 & 4.5 & 0 & 0 \\ -1.22 & -1.22 & 9.6 & 0 & 0 & 0 \\ -4.5 & 4.5 & 0 & 20.04 & 0 & 0 \\ 0 & 0 & 0 & 0 & 20.04 & -9 \\ 0 & 0 & 0 & 0 & -9 & 29.1 \end{bmatrix} \cdot 10^{-12} \frac{m^2}{N} \tag{6.6}$$

The orthonormal fourth-order tensors for the pertinent symmetry classes are given as [171]:

$$A^I = \frac{1}{3}\begin{bmatrix} 1 & 1 & 1 & 0 & 0 & 0 \\ 1 & 1 & 1 & 0 & 0 & 0 \\ 1 & 1 & 1 & 0 & 0 & 0 \\ 0 & 0 & 0 & 0 & 0 & 0 \\ 0 & 0 & 0 & 0 & 0 & 0 \\ 0 & 0 & 0 & 0 & 0 & 0 \end{bmatrix}, \quad A^{II} = \frac{1}{6\sqrt{5}}\begin{bmatrix} 4 & -2 & -2 & 0 & 0 & 0 \\ -2 & 4 & -2 & 0 & 0 & 0 \\ -2 & -2 & 4 & 0 & 0 & 0 \\ 0 & 0 & 0 & 3 & 0 & 0 \\ 0 & 0 & 0 & 0 & 3 & 0 \\ 0 & 0 & 0 & 0 & 0 & 3 \end{bmatrix} \tag{6.7}$$

The groups of matrix elements are defined as:

$$M_1 = \sum_{i=1}^{3} s_{ii}, \quad M_2 = \sum_{i=4}^{6} s_{ii}, \quad M_3 = \sum_{i=1}^{3}\sum_{j=1}^{3} s_{ij} \tag{6.8}$$

The formulas for computing inner products are defined as:

$$(c, A^I) = \frac{1}{3} M_3, \quad (c, A^{II}) = \frac{1}{3\sqrt{5}}\left[3M_1 + 6M_2 - M_3\right] \tag{6.9}$$

The nearest isotropic tensor is therefore:

$$s^0_{ijkl} = \sum_{K=I}^{II} (c, A^K) A^K_{ijkl} \tag{6.10}$$

Or:

$$\boldsymbol{s_E} = \begin{bmatrix} \mathbf{24.912} & \mathbf{-8.009} & \mathbf{-8.009} & \mathbf{0} & \mathbf{0} & \mathbf{0} \\ \mathbf{-8.009} & \mathbf{24.912} & \mathbf{-8.009} & \mathbf{0} & \mathbf{0} & \mathbf{0} \\ \mathbf{-8.009} & \mathbf{-8.009} & \mathbf{24.912} & \mathbf{0} & \mathbf{0} & \mathbf{0} \\ \mathbf{0} & \mathbf{0} & \mathbf{0} & \mathbf{16.461} & \mathbf{0} & \mathbf{0} \\ \mathbf{0} & \mathbf{0} & \mathbf{0} & \mathbf{0} & \mathbf{16.461} & \mathbf{0} \\ \mathbf{0} & \mathbf{0} & \mathbf{0} & \mathbf{0} & \mathbf{0} & \mathbf{16.461} \end{bmatrix} \cdot \mathbf{10^{-12}} \frac{\boldsymbol{m^2}}{\boldsymbol{N}} \quad (6.11)$$

As the compliance matrix is now in isotropic form, the material properties of quartz can be found. If the stress-strain relationship is defined thus:

$$\begin{bmatrix} \boldsymbol{S_1} \\ \boldsymbol{S_2} \\ \boldsymbol{S_3} \\ \boldsymbol{S_4} \\ \boldsymbol{S_5} \\ \boldsymbol{S_6} \end{bmatrix} = \begin{bmatrix} \mathbf{1/E} & \mathbf{-\nu/E} & \mathbf{-\nu/E} & \mathbf{0} & \mathbf{0} & \mathbf{0} \\ \mathbf{-\nu/E} & \mathbf{1/E} & \mathbf{-\nu/E} & \mathbf{0} & \mathbf{0} & \mathbf{0} \\ \mathbf{-\nu/E} & \mathbf{-\nu/E} & \mathbf{1/E} & \mathbf{0} & \mathbf{0} & \mathbf{0} \\ \mathbf{0} & \mathbf{0} & \mathbf{0} & \mathbf{1/G} & \mathbf{0} & \mathbf{0} \\ \mathbf{0} & \mathbf{0} & \mathbf{0} & \mathbf{0} & \mathbf{1/G} & \mathbf{0} \\ \mathbf{0} & \mathbf{0} & \mathbf{0} & \mathbf{0} & \mathbf{0} & \mathbf{1/G} \end{bmatrix} \begin{bmatrix} \boldsymbol{T_1} \\ \boldsymbol{T_2} \\ \boldsymbol{T_3} \\ \boldsymbol{T_4} \\ \boldsymbol{T_5} \\ \boldsymbol{T_6} \end{bmatrix} \quad (6.12)$$

The Young's modulus of the quartz can therefore be shown to be E = 40.191 GPa and its Poisson's ratio to be ν = 0.322.

Appendix B: The Boundary Conditions and Continuity Equations for the Rheometer

Here twenty equations representing the boundary conditions and the continuity equations ensuring consistency (in the deflections, gradients, normal forces and bending moments) between the sections of the rheometer as defined in Fig. 6.6 are given. It is intended that these simultaneous linear equations are solved in matrix form in order to give the constants required to solve eqs. 6.32 and 6.34 for the deflection of the rheometer.

- At $r = 0,$ w and u must be finite:

  Therefore c_{17} and c_{20} must equal zero

- At $r = R_\delta, w_\delta = 0$ therefore:

$$c_1 \frac{R_\delta^2}{4} + c_2 \ln\left(R_\delta\right) + c_3 = \frac{A_{\delta_{11}}}{A_{\delta_{11}} D_{\delta_{11}} - B_{\delta_{11}}^2} \frac{P}{8\pi} R_\delta^2 \left(\ln\left(R_\delta\right) - 1\right)$$

- At $r = R_\delta, \frac{dw_\delta}{dr} = 0$ therefore:

$$c_1 \frac{R_\delta}{2} + c_2 \frac{1}{R_\delta} = \frac{A_{\delta_{11}}}{A_{\delta_{11}} D_{\delta_{11}} - B_{\delta_{11}}^2} \frac{P}{8\pi} R_\delta \left(2\ln\left(R_\delta\right) - 1\right)$$

- At $r = R_\delta, u_\delta = 0$ therefore:

$$c_4 \frac{R_\delta}{2} + c_5 \frac{1}{R_\delta} = \frac{B_{\delta_{11}}}{A_{\delta_{11}} D_{\delta_{11}} - B_{\delta_{11}}^2} \frac{P}{8\pi} R_\delta \left(2\ln\left(R_\delta\right) - 1\right)$$

- At $r = R_\gamma, w_\delta = w_\gamma$ therefore:

$$c_1 \frac{R_\gamma^2}{4} + c_2 \ln\left(R_\gamma\right) + c_3 - c_6 \frac{R_\gamma^2}{4} - c_7 \ln\left(R_\gamma\right) - c_8 =$$
$$\left[\left(\frac{A_{\gamma_{11}}}{A_{\gamma_{11}} D_{\gamma_{11}} - B_{\gamma_{11}}^2}\right) - \left(\frac{A_{\delta_{11}}}{A_{\delta_{11}} D_{\delta_{11}} - B_{\delta_{11}}^2}\right)\right] \frac{P}{8\pi} R_\gamma^2 \left(\ln\left(R_\gamma\right) - 1\right)$$

- At $r = R_\gamma, \frac{dw_\delta}{dr} = \frac{dw_\lambda}{dr}$ therefore:

$$c_1 \frac{R_\gamma}{2} + c_2 \frac{1}{R_\gamma} - c_6 \frac{R_\gamma}{2} - c_7 \frac{1}{R_\gamma} =$$
$$\left[\left(\frac{A_{\lambda_{11}}}{A_{\lambda_{11}} D_{\lambda_{11}} - B_{\lambda_{11}}^2}\right) - \left(\frac{A_{\delta_{11}}}{A_{\delta_{11}} D_{\delta_{11}} - B_{\delta_{11}}^2}\right)\right] \frac{P}{8\pi} R_\gamma \left(2\ln\left(R_\gamma\right) - 1\right)$$

- At $r = R_\lambda, u_\delta = u_\gamma$ therefore:

$$c_4 \frac{R_\gamma}{2} + c_5 \frac{1}{R_\gamma} - c_9 \frac{R_\gamma}{2} - c_{10} \frac{1}{R_\gamma} =$$
$$\left[\left(\frac{B_{\gamma_{11}}}{A_{\gamma_{11}} D_{\gamma_{11}} - B_{\gamma_{11}}^2}\right) - \left(\frac{B_{\delta_{11}}}{A_{\delta_{11}} D_{\delta_{11}} - B_{\delta_{11}}^2}\right)\right] \frac{P}{8\pi} R_\gamma \left(2\ln\left(R_\gamma\right) - 1\right)$$

- At $r = R_y, N_{r_\delta} = N_{r_\gamma}$ therefore:

$$\left(\frac{B_{\delta_{11}} + B_{\delta_{12}}}{-2}\right) c_1 + \left(\frac{B_{\delta_{11}} - B_{\delta_{12}}}{R_\gamma^2}\right) c_2 + \left(\frac{A_{\delta_{11}} + A_{\delta_{12}}}{2}\right) c_4 + \left(\frac{A_{\delta_{12}} - A_{\delta_{11}}}{R_\gamma^2}\right) c_5 +$$
$$\left(\frac{B_{\gamma_{11}} + B_{\gamma_{12}}}{2}\right) c_6 - \left(\frac{B_{\gamma_{11}} - B_{\gamma_{12}}}{R_\gamma^2}\right) c_7 - \left(\frac{A_{\gamma_{11}} + A_{\gamma_{12}}}{2}\right) c_9 - \left(\frac{A_{\gamma_{12}} - A_{\gamma_{11}}}{R_\gamma^2}\right) c_{10} =$$
$$\left[\left(\frac{A_{\gamma_{12}} B_{\gamma_{11}} - A_{\gamma_{11}} B_{\gamma_{12}}}{A_{\gamma_{11}} D_{\gamma_{11}} - B_{\gamma_{11}}^2}\right) - \left(\frac{A_{\delta_{12}} B_{\delta_{11}} - A_{\delta_{11}} B_{\delta_{12}}}{A_{\delta_{11}} D_{\delta_{11}} - B_{\delta_{11}}^2}\right)\right] \frac{P}{8\pi} \left(2\ln\left(R_\gamma\right) - 1\right) - N_r^P$$

- At $r = R_\gamma, M_{r_\delta} = M_{r_\gamma}$ therefore:

$$\left(\frac{D_{\delta_{11}}+D_{\delta_{12}}}{-2}\right)c_1+\left(\frac{D_{\delta_{11}}-D_{\delta_{12}}}{R_\gamma^2}\right)c_2+\left(\frac{B_{\delta_{11}}+B_{\delta_{12}}}{2}\right)c_4+\left(\frac{B_{\delta_{12}}-B_{\delta_{11}}}{R_\gamma^2}\right)c_5+$$
$$\left(\frac{D_{\gamma_{11}}+D_{\gamma_{12}}}{2}\right)c_6-\left(\frac{D_{\gamma_{11}}-D_{\gamma_{12}}}{R_\gamma^2}\right)c_7-\left(\frac{B_{\gamma_{11}}+B_{\gamma_{12}}}{2}\right)c_9-\left(\frac{B_{\gamma_{12}}-B_{\gamma_{11}}}{R_\gamma^2}\right)c_{10}=$$
$$\left[\left(\frac{B_{\gamma_{11}}B_{\gamma_{11}}-A_{\gamma_{11}}D_{\gamma_{11}}}{A_{\gamma_{11}}D_{\gamma_{11}}-B_{\gamma_{11}}^2}\right)-\left(\frac{B_{\delta_{11}}B_{\delta_{11}}-A_{\delta_{11}}D_{\delta_{11}}}{A_{\delta_{11}}D_{\delta_{11}}-B_{\delta_{11}}^2}\right)\right]\frac{P}{8\pi}\left(2\ln\left(R_\gamma\right)+1\right)+$$
$$\left[\left(\frac{B_{\gamma_{11}}B_{\gamma_{12}}-A_{\gamma_{11}}D_{\gamma_{12}}}{A_{\gamma_{11}}D_{\gamma_{11}}-B_{\gamma_{11}}^2}\right)-\left(\frac{B_{\delta_{11}}B_{\delta_{12}}-A_{\delta_{11}}D_{\delta_{12}}}{A_{\delta_{11}}D_{\delta_{11}}-B_{\delta_{11}}^2}\right)\right]\frac{P}{8\pi}\left(2\ln\left(R_\gamma\right)-1\right)-M_r^P$$

- At $r=R_\beta, w_\gamma=w_\beta$ therefore:

$$c_6\frac{R_\beta^2}{4}+c_7\ln\left(R_\beta\right)+c_8-c_{11}\frac{R_\beta^2}{4}-c_{12}\ln\left(R_\beta\right)-c_{13}=$$
$$\left[\left(\frac{A_{\beta_{11}}}{A_{\beta_{11}}D_{\beta_{11}}-B_{\beta_{11}}^2}\right)-\left(\frac{A_{\gamma_{11}}}{A_{\gamma_{11}}D_{\gamma_{11}}-B_{\gamma_{11}}^2}\right)\right]\frac{P}{8\pi}R_\beta^2\left(\ln\left(R_\beta\right)-1\right)$$

- At $r=R_\beta, \frac{dw_\gamma}{dr}=\frac{dw_\beta}{dr}$ therefore:

$$c_6\frac{R_\beta}{2}+c_7\frac{1}{R_\beta}-c_{11}\frac{R_\beta}{2}-c_{12}\frac{1}{R_\beta}=$$
$$\left[\left(\frac{A_{\beta_{11}}}{A_{\beta_{11}}D_{\beta_{11}}-B_{\beta_{11}}^2}\right)-\left(\frac{A_{\lambda_{11}}}{A_{\lambda_{11}}D_{\lambda_{11}}-B_{\lambda_{11}}^2}\right)\right]\frac{P}{8\pi}R_\beta\left(2\ln\left(R_\beta\right)-1\right)$$

- At $r=R_\beta, u_\gamma=u_\beta$ therefore:

$$c_9\frac{R_\beta}{2}+c_{10}\frac{1}{R_\beta}-c_{14}\frac{R_\beta}{2}-c_{15}\frac{1}{R_\beta}=$$
$$\left[\left(\frac{B_{\beta_{11}}}{A_{\beta_{11}}D_{\beta_{11}}-B_{\beta_{11}}^2}\right)-\left(\frac{B_{\gamma_{11}}}{A_{\gamma_{11}}D_{\gamma_{11}}-B_{\gamma_{11}}^2}\right)\right]\frac{P}{8\pi}R_\beta\left(2\ln\left(R_\beta\right)-1\right)$$

- At $r = R_\beta, N_{r_\gamma} = N_{r_\delta}$ therefore:

$$\left(\frac{B_{\gamma_{11}} + B_{\gamma_{12}}}{-2}\right)c_6 + \left(\frac{B_{\gamma_{11}} - B_{\gamma_{12}}}{R_\beta^2}\right)c_7 + \left(\frac{A_{\gamma_{11}} + A_{\gamma_{12}}}{2}\right)c_9 + \left(\frac{A_{\gamma_{12}} - A_{\gamma_{11}}}{R_\beta^2}\right)c_{10} +$$
$$\left(\frac{B_{\beta_{11}} + B_{\beta_{12}}}{2}\right)c_{11} - \left(\frac{B_{\beta_{11}} - B_{\beta_{12}}}{R_\beta^2}\right)c_{12} - \left(\frac{A_{\beta_{11}} + A_{\beta_{12}}}{2}\right)c_{14} - \left(\frac{A_{\beta_{12}} - A_{\beta_{11}}}{R_\beta^2}\right)c_{15} =$$
$$\left[\left(\frac{A_{\beta_{12}}B_{\beta_{11}} - A_{\beta_{11}}B_{\beta_{12}}}{A_{\beta_{11}}D_{\beta_{11}} - B_{\beta_{11}}^2}\right) - \left(\frac{A_{\gamma_{12}}B_{\gamma_{11}} - A_{\gamma_{11}}B_{\gamma_{12}}}{A_{\gamma_{11}}D_{\gamma_{11}} - B_{\gamma_{11}}^2}\right)\right]\frac{P}{8\pi}\left(2\ln\left(R_\beta\right) - 1\right) + N_r^P$$

- At $r = R_\beta, M_{r_\gamma} = M_{r_\beta}$ therefore:

$$\left(\frac{D_{\gamma_{11}} + D_{\gamma_{12}}}{-2}\right)c_6 + \left(\frac{D_{\gamma_{11}} - D_{\gamma_{12}}}{R_\beta^2}\right)c_7 + \left(\frac{B_{\gamma_{11}} + B_{\gamma_{12}}}{2}\right)c_9 + \left(\frac{B_{\gamma_{12}} - B_{\gamma_{11}}}{R_\beta^2}\right)c_{10} +$$
$$\left(\frac{D_{\beta_{11}} + D_{\beta_{12}}}{2}\right)c_{11} - \left(\frac{D_{\beta_{11}} - D_{\beta_{12}}}{R_\beta^2}\right)c_{12} - \left(\frac{B_{\beta_{11}} + B_{\beta_{12}}}{2}\right)c_{14} - \left(\frac{B_{\beta_{12}} - B_{\beta_{11}}}{R_\beta^2}\right)c_{15} =$$
$$\left[\left(\frac{B_{\beta_{11}}B_{\beta_{11}} - A_{\beta_{11}}D_{\beta_{11}}}{A_{\beta_{11}}D_{\beta_{11}} - B_{\beta_{11}}^2}\right) - \left(\frac{B_{\gamma_{11}}B_{\gamma_{11}} - A_{\gamma_{11}}D_{\gamma_{11}}}{A_{\gamma_{11}}D_{\gamma_{11}} - B_{\gamma_{11}}^2}\right)\right]\frac{P}{8\pi}\left(2\ln\left(R_\beta\right) + 1\right) +$$
$$\left[\left(\frac{B_{\beta_{11}}B_{\beta_{12}} - A_{\beta_{11}}D_{\beta_{12}}}{A_{\beta_{11}}D_{\beta_{11}} - B_{\beta_{11}}^2}\right) - \left(\frac{B_{\gamma_{11}}B_{\gamma_{12}} - A_{\gamma_{11}}D_{\gamma_{12}}}{A_{\gamma_{11}}D_{\gamma_{11}} - B_{\gamma_{11}}^2}\right)\right]\frac{P}{8\pi}\left(2\ln\left(R_\beta\right) - 1\right) + M_r^P$$

- At $r = R_\alpha, w_\beta = w_\alpha$ therefore:

$$c_{11}\frac{R_\alpha^2}{4} + c_{12}\ln\left(R_\alpha\right) + c_{13} - c_{16}\frac{R_\alpha^2}{4} - c_{18} =$$
$$\left[\left(\frac{A_{\alpha_{11}}}{A_{\alpha_{11}}D_{\alpha_{11}} - B_{\alpha_{11}}^2}\right) - \left(\frac{A_{\beta_{11}}}{A_{\beta_{11}}D_{\beta_{11}} - B_{\beta_{11}}^2}\right)\right]\frac{P}{8\pi}R_\alpha^2\left(\ln\left(R_\alpha\right) - 1\right)$$

- At $r = R_\alpha, \frac{dw_\beta}{dr} = \frac{dw_\alpha}{dr}$ therefore:

$$c_{11}\frac{R_\alpha}{2}+c_{12}\frac{1}{R_\alpha}-c_{16}\frac{R_\alpha}{2}=$$
$$\left[\left(\frac{A_{\alpha_{11}}}{A_{\alpha_{11}}D_{\alpha_{11}}-B_{\alpha_{11}}^2}\right)-\left(\frac{A_{\beta_{11}}}{A_{\beta_{11}}D_{\beta_{11}}-B_{\beta_{11}}^2}\right)\right]\frac{P}{8\pi}R_\alpha\left(2\ln\left(R_\alpha\right)-1\right)$$

- At $r=R_\alpha, u_\beta=u_\alpha$ therefore:

$$c_{14}\frac{R_\alpha}{2}+c_{15}\frac{1}{R_\alpha}-c_{19}\frac{R_\alpha}{2}=$$
$$\left[\left(\frac{B_{\alpha_{11}}}{A_{\alpha_{11}}D_{\alpha_{11}}-B_{\alpha_{11}}^2}\right)-\left(\frac{B_{\beta_{11}}}{A_{\beta_{11}}D_{\beta_{11}}-B_{\beta_{11}}^2}\right)\right]\frac{P}{8\pi}R_\alpha\left(2\ln\left(R_\alpha\right)-1\right)$$

- At $r=R_\alpha, N_{r_\beta}=N_{r_\alpha}$ therefore:

$$\left(\frac{B_{\beta_{11}}+B_{\beta_{12}}}{-2}\right)c_{11}+\left(\frac{B_{\beta_{11}}-B_{\beta_{12}}}{R_\alpha^2}\right)c_{12}+\left(\frac{A_{\beta_{11}}+A_{\beta_{12}}}{2}\right)c_{14}+\left(\frac{A_{\beta_{12}}-A_{\beta_{11}}}{R_\alpha^2}\right)c_{15}+$$
$$\left(\frac{B_{\alpha_{11}}+B_{\alpha_{12}}}{2}\right)c_{16}-\left(\frac{A_{\alpha_{11}}+A_{\alpha_{12}}}{2}\right)c_{19}=$$
$$\left[\left(\frac{A_{\alpha_{12}}B_{\alpha_{11}}-A_{\alpha_{11}}B_{\alpha_{12}}}{A_{\alpha_{11}}D_{\alpha_{11}}-B_{\alpha_{11}}^2}\right)-\left(\frac{A_{\beta_{12}}B_{\beta_{11}}-A_{\beta_{11}}B_{\beta_{12}}}{A_{\beta_{11}}D_{\beta_{11}}-B_{\beta_{11}}^2}\right)\right]\frac{P}{8\pi}\left(2\ln\left(R_\alpha\right)-1\right)-N_r^P$$

- At $r=R_\alpha, M_{r_\beta}=M_{r_\alpha}$ therefore:

$$\left(\frac{D_{\beta_{11}}+D_{\beta_{12}}}{-2}\right)c_{11}+\left(\frac{D_{\beta_{11}}-D_{\beta_{12}}}{R_\alpha^2}\right)c_{12}+\left(\frac{B_{\beta_{11}}+B_{\beta_{12}}}{2}\right)c_{14}+\left(\frac{B_{\beta_{12}}-B_{\beta_{11}}}{R_\alpha^2}\right)c_{15}+$$

$$\left(\frac{D_{\alpha_{11}}+D_{\alpha_{12}}}{2}\right)c_{16}-\left(\frac{B_{\alpha_{11}}+B_{\alpha_{12}}}{2}\right)c_{19}=$$

$$\left[\left(\frac{B_{\alpha_{11}}B_{\alpha_{11}}-A_{\alpha_{11}}D_{\alpha_{11}}}{A_{\alpha_{11}}D_{\alpha_{11}}-B_{\alpha_{11}}^2}\right)-\left(\frac{B_{\beta_{11}}B_{\beta_{11}}-A_{\beta_{11}}D_{\beta_{11}}}{A_{\beta_{11}}D_{\beta_{11}}-B_{\beta_{11}}^2}\right)\right]\frac{P}{8\pi}\left(2\ln\left(R_\alpha\right)+1\right)+$$

$$\left[\left(\frac{B_{\alpha_{12}}B_{\alpha_{11}}-A_{\alpha_{11}}D_{\alpha_{12}}}{A_{\alpha_{11}}D_{\alpha_{11}}-B_{\alpha_{11}}^2}\right)-\left(\frac{B_{\beta_{11}}B_{\beta_{12}}-A_{\beta_{11}}D_{\beta_{12}}}{A_{\beta_{11}}D_{\beta_{11}}-B_{\beta_{11}}^2}\right)\right]\frac{P}{8\pi}\left(2\ln\left(R_\alpha\right)-1\right)-M_r^P$$

Appendix C: Mechanical Impedance Due to Air

There are two main ways air can affect the mechanical response of the micro rheometer. The first is due to the squeezing of the entrained air inside the rheometer and the other is due to the pressure waves radiated out through the air on the outside. Due to the complex geometry of the rheometer whilst it is oscillating, the complete analysis of the mechanical-acoustic coupling is prohibitively difficult. However, an approximate solution can be found by treating the rheometer as an equivalent piston vibrating in air [208, 209] (see Fig. C.1). The primary assumption in the analysis is that all parts of the piston vibrate in phase (i.e. the piston is rigid). This is satisfied when the rheometer oscillates below its resonant frequency and so is dominated by its fundamental mode shape.

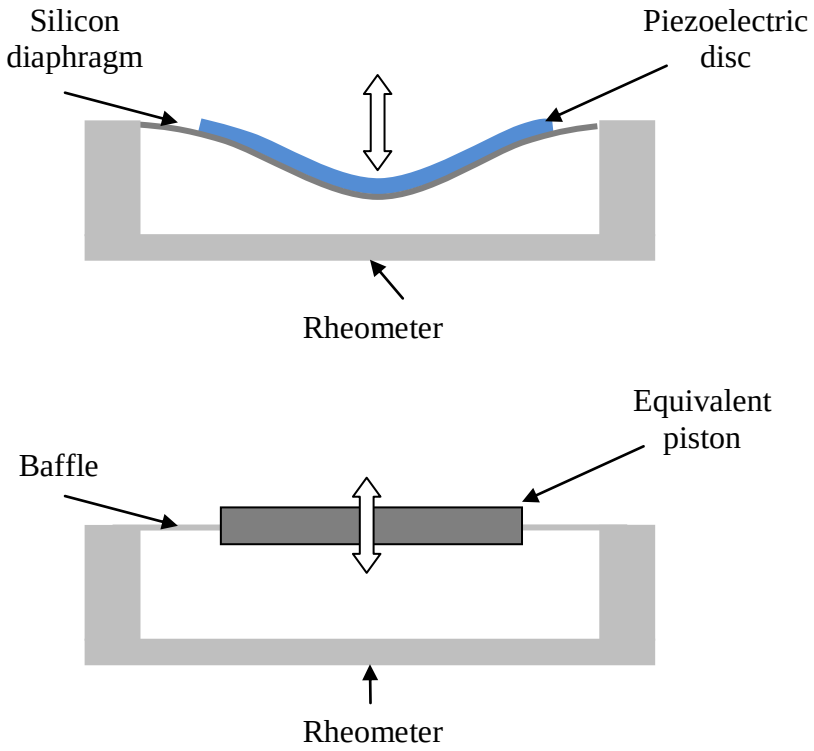

Fig. C.1: (a) A schematic of the rheometer as it is oscillating and (b) the equivalent piston.

The analysis requires the calculation of the area of the equivalent piston referred to the centre displacement of the silicon diaphragm. Thus calculation of the volume velocity of the diaphragm is necessary. From this the radius of the piston, R_p, is calculated and then the known solution of a vibrating piston in air is applied [209].

Recall that the deflection of the diaphragm is given by (eq. 6.39):

$$w(r,t) = w_0(r)\sin(\omega t)$$

The instantaneous velocity of the diaphragm is:

$$\dot{w}(r,t) = \omega w_0(r)\cos(\omega t)$$

Therefore the volume velocity, $U(t)$ is written as:

$$U(t) = \int_0^{2\pi}\int_0^{R_\delta} \omega w_0(r)\cos(\omega t) r dr d\theta$$

For simplicity we confine ourselves to the maximum values of displacements and velocities. And due to the circular symmetry, the maximum volume velocity U_{max} can be given as:

$$U_{max} = 2\pi\omega \int_0^{R_\delta} w_0(r) r dr$$

$w_0(r)$ is given by eq. 6.32 (recalling that this equation needs to be applied over all four sections of the rheometer) so that:

$$U_{max} = 2\pi\omega \int_0^{R_\delta} \left[\left(\sum_{i=1}^{3} A_i r^2(\ln(r) - 1) + B_i r^2 + C_i \ln(r) + D_i \right) + A_4 r^2(\ln(r) - 1) + B_4 r^2 + D_4 \right] r dr$$

Where $i = 1$ is equivalent to the portion of the diaphragm with radius $R_\delta \leq r \leq R_\gamma$, $i = 2$ is equivalent to the portion of the diaphragm with radius $R_\gamma \leq r \leq R_\beta$, $i = 3$ is equivalent to the portion of the diaphragm with radius $R_\beta \leq r \leq R_\alpha$, $i = 4$ is equivalent to the portion of the diaphragm with radius $R_\alpha \leq r \leq 0$. The constants $A_i, B_i, C_i \; and \; D_i$ can be gleaned from eq. 6.32. This can be integrated to give:

$$U_{max} = 2\pi\omega \sum_{i=1}^{4} \frac{A_i}{16}[5(R_{i+1}^4 - R_i^4) + 4(R_i^4 lnR_i - R_{i+1}^4 lnR_{i+1})] + \frac{B_i}{4}(R_i^4 - R_{i+1}^4) + \frac{C_i}{4}[(R_{i+1}^2 - R_i^2) + 2(R_i^2 lnR_i - R_{i+1}^2 lnR_{i+1})] + \frac{D_i}{2}(R_i^2 - R_{i+1}^2)$$

The maximum centre velocity of the plate as it passes through the equilibrium position is:

$$\dot{w}_c = \dot{w}(0) = \omega w_0(0)$$

The area of the equivalent piston is therefore:

$$A_p = \frac{U_{max}}{\dot{w}_c}$$

And the radius of the equivalent piston is:

$$R_p = \sqrt{\frac{A_p}{\pi}}$$

This radius is calculated to be 7.526mm for the Mark I and III rheometers where the applied voltage has amplitude of 5V and 1.506mm for the Mark II rheometer where the applied voltage has amplitude of 1V (note that the radius of the piezoelectric disc was 10mm and the radius of the silicon diaphragm was 11.5mm). The difference in the radii of the various equivalent pistons may seem odd given that the rheometers have a similar geometry, but it should be kept in mind that the Mark II rheometer uses PZT which deflects more and so has a larger curvature. This means that a smaller fraction of the mass is moving at near the maximum velocity, hence the smaller equivalent piston radius.

C.1 Impedance Due to the Squeezing of Air

As the air film is thin and the bounding surfaces are thermally conductive, the expansion and contraction of the air takes place isothermally, and the excess pressure due to simple compression is $P_{air}\left(x_p/h_p\right)$ in which P_{air} is the atmospheric pressure (taken as 101.325 kPa). The excess pressure can be equated to the viscous resistance of the air flow to give [208]:

$$\frac{d^2p}{dr^2}+\frac{1}{r}\frac{dp}{dr}=\frac{\kappa}{P_{air}}\frac{dp}{dt}$$

Where:

$$\kappa=\frac{12\mu_{air}}{{h_p}^2}$$

This can be solved to give the effective damping, $c_{air\,1}$, and stiffness, k_{air}, coefficients caused by the squeezing of air:

$$c_{air\,1} = \frac{2\pi P_{air} R_p}{\omega h_p \alpha}\left(\frac{bei(\alpha R_p)bei'(\alpha R_p) - ber(\alpha R_p)ber'(\alpha R_p)}{ber^2(\alpha R_p) + bei^2(\alpha R_p)}\right)$$

$$k_{air} = \frac{\pi P_{air} {R_p}^2}{h_p}\left(1 - \frac{2}{\alpha R_p}\frac{ber(\alpha R_p)bei'(\alpha R_p) - ber'(\alpha R_p)bei(\alpha R_p)}{ber^2(\alpha R_p) + bei^2(\alpha R_p)}\right)$$

Where:

$$\alpha = \sqrt{\frac{\omega\kappa}{P_{air}}}$$

And:

$$\kappa = \frac{12\mu_{air}}{{h_p}^2}$$

μ_{air} is the viscosity of air taken to be 18.27x10^{-6} Pa.s (at room temperature). See [210] about ber and bei functions. When $\alpha R < 1$ (i.e. at frequencies below 324.7 kHz for the Mark I and III rheometers and 8.1 MHz for the Mark II rheometer), the elastic component of air vanishes and the damping coefficient becomes:

$$c_{air\,1} = \frac{3\pi\mu_{air} R_p^4}{2{h_p}^3}$$

This is of course similar to that given for the squeeze flow of liquids in Chapter 5.

C.2 Impedance Due to the Acoustics of Air

The impedance of the air load upon one side of the piston (assuming it is surrounded by an infinite baffle – which is similar to the geometry in question (see Fig. C.1)) and vibrating sinusoidally is [211]:

$$Z_{air} = \pi R_p^2 \rho_{air} c \left[1 - \frac{J_1(2k_c R_p)}{k_c R_p}\right] + i \frac{\pi \rho_{air} c}{2k_c^2} K_1(2k_c R_p)$$

Where ρ_{air} is the density of air (taken to be 1.205 kg/m^3 at room temperature), c is the speed of sound in air (taken to be 340.29 m/s), k_c is the wave number (taken as ω/c) and J_1 is the first kind of Bessel function. K_1 is given by the series:

$$K_1(2k_c R_p) = \frac{2}{\pi}\left[\frac{(2k_c R_p)^3}{3} - \frac{(2k_c R_p)^5}{3^2 5} + \frac{(2k_c R_p)^7}{3^2 5^2 7} \ldots\right]$$

The real part is the resistance and can be defined as:

$$c_{air\,2} = \pi R_p^2 \rho_{air} c \left[1 - \frac{J_1(2k_c R_p)}{k_c R_p}\right]$$

And the imaginary part is equivalent to the added mass which can be defined as:

$$m_{air} = \frac{\pi \rho_{air} c}{2k_c^2} K_1(2k_c R_p)$$

Therefore the total damping due to air can be taken as:

$$c_{air} = c_{air\,1} + c_{air\,2} = \frac{3\pi \mu_{air} R_p^4}{2{h_p}^3} + \pi R_p^2 \rho_{air} c \left[1 - \frac{J_1(2k_c R_p)}{k_c R_p}\right]$$

Fig. C.2 shows how these impedances vary with frequency for the various rheometers.

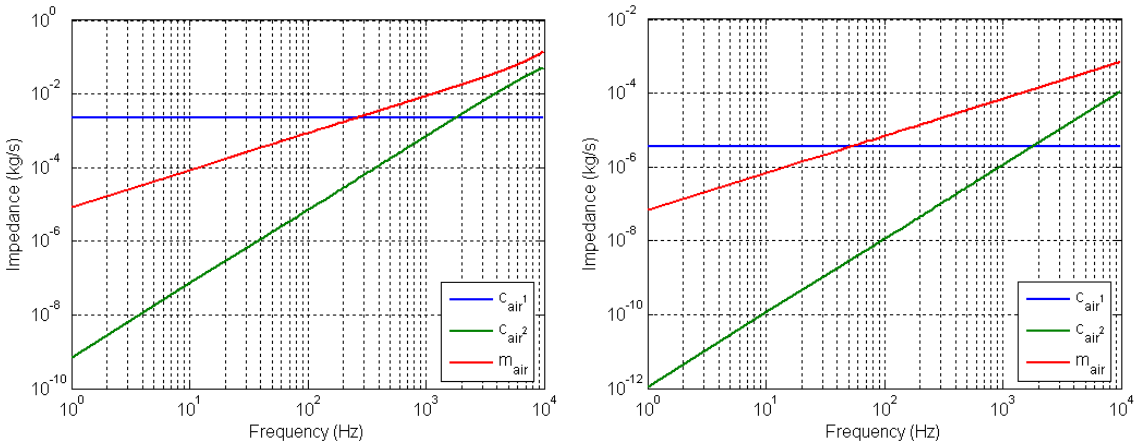

Fig. C.2: The impedance of air for (a) the Mark I and III rheometers and (b) the Mark II rheometer.

These impedances can be used to describe the effects air has on the rheometer. There are essentially two effects; one is the added mass due to air which can change the resonant frequency of the rheometer and secondly air can add extra damping to the system. In Fig. C.3 it can be seen that for the Mark I and III rheometers the added mass is small - but may still lead to a decrease of resonant frequency of the order of ~200Hz. However in the case of the Mark II rheometer, due to the small radius of the equivalent piston and the high density of the PZT the added mass should be negligible. As for the damping effects of air, it can be seen in Fig. C.4 that compared to the damping due to water (which is likely to be the lowest viscosity liquid to be tested in the rheometer) the effect of air is negligible in all cases.

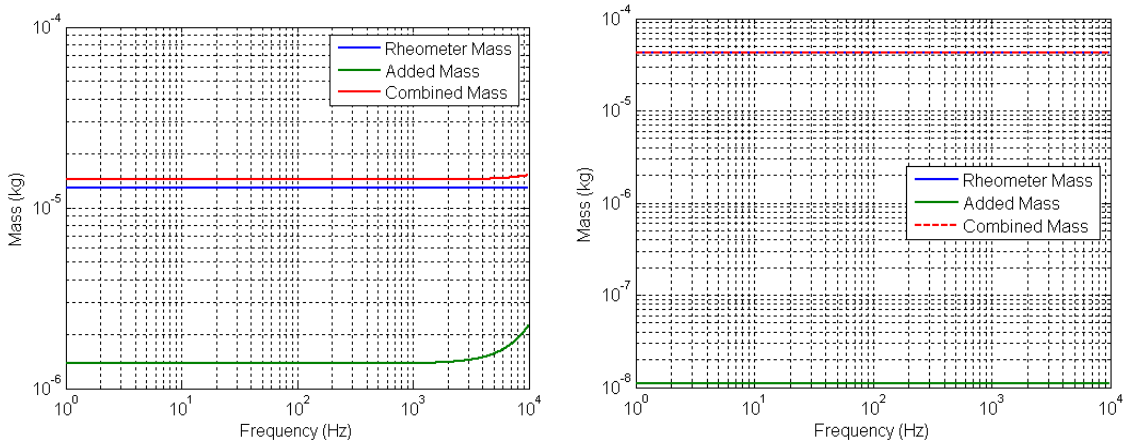

Fig. C.3: The added mass due to air for (a) the Mark I and III rheometers and (b) the Mark II rheometer.

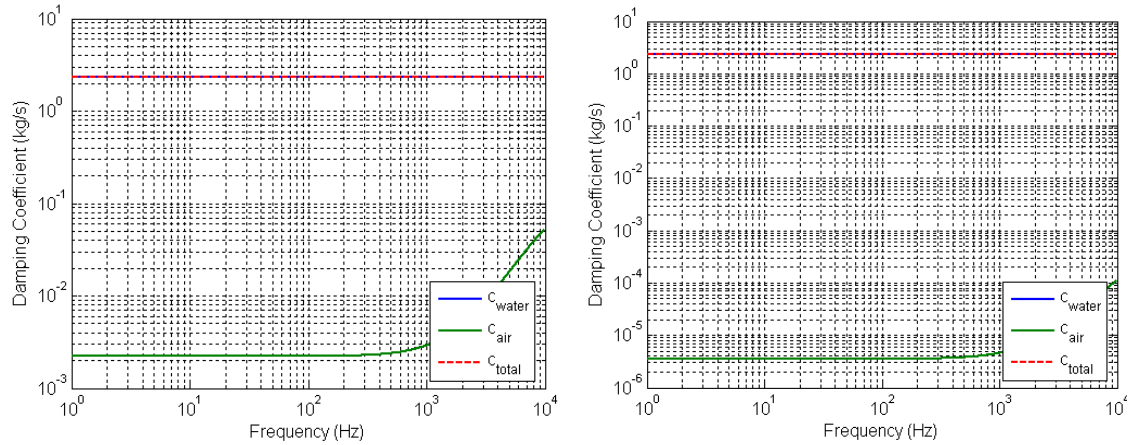

Fig. C.4: The damping coefficients of air for (a) the Mark I and III rheometers and (b) the Mark II rheometer as compared to the damping coefficient of water during a squeeze flow experiment.

References

Chapter 1 – Introduction

[1] Meyers, M. A. and Chawla, K. K., (1999), *Mechanical Behavior of Materials*, 2nd Ed., Cambridge University Press

[2] Waigh, T. A., (2005), *Microrheology of Complex Fluids*, Rep. Prog. Phys., Vol. 68, pp. 685-742

[3] Berg, H. C., (1993), *Random Walks in Biology*, Princeton University Press, Princeton, NJ

[4] Tabilo-Munizaga, G. and Barbosa-Canovas, G. V., (2005), *Rheology for the Food Industry*, J. Food Eng., Vol. 76, pp. 147-156

[5] Barbosa-Canovas, G. V., Kokini, J. L., Ma, L., and Ibarz, A., (1996), *The Rheology of Semiliquid Foods*, Adv. Food and Nutrition Res., Vol. 39, pp.1-69

[6] Brummer, R. and Godersky, S., (1999), *Rheological Studies to Objectify Sensations Occurring when Cosmetic Emulsions are applied to the Skin*, Colloids and Surfaces: A, Vol. 152, pp, 89-94

[7] Larson, R. G. (1999), *The Structure and Dynamics of Complex Fluids*, Oxford University Press, Oxford

[8] Hansen, C. and Quake, S. R., (2003), *Microfluidics in Structural Biology: Smaller, Faster . . . Better*, Curr. Opin. Struct. Biol., Vol. 13, pp. 538-544

[9] Venerus, D. C., (2007), *Free Surface Effects on Normal Stress Measurements in Cone and Plate Flow*, Appl. Rheol., Vol. 17, No. 3, pp. 36494-36499

[10] Willenbacher, N. and Oelschlaeger, C., (2007), *Dynamics and Structure of Complex Fluids from High Frequency Mechanical and Optical Rheometry*, Curr. Op. Coll. Int. Sci., Vol. 12, pp. 43-49

[11] Raha, S. et al., (1968), *Cone and Plate Rheometer for Polymer Melts*, J. Phys E: Sci. Instrum., Vol. 1, pp. 1113-1115

[12] Liptak, G. G., (2003), *Instrument Engineers' Handbook: Process Measurement and Analysis*, 4th Ed., CRC Press

[13] Giacomin, A. J., Samurkas, T. and Dealy, J. M., (1989), *A Novel Sliding Plate Rheometer for Molten Plastics*, Polym. Eng. Sci., Vol. 29, pp.449

[14] Xu, J. et al, (2007), *Use of a Sliding Plate Rheometer to Measure the First Normal Stress Difference at High Shear Rates*, Rheo. Acta, Vol. 46, No. 6, pp. 815-824

[15] Reimers, M. J. and Dealy, J. M., (1998), *Sliding Plate Rheometer Studies of Concentrated Polystyrene Solutions: Nonlinear Viscoelasticity and Wall Slip of*

Two High Molecular Weight Polymers in Tricresyl Phosphate, J. Rheo., Vol. 42, No. 3, pp.

[16] Clasen, C., et al, (2006), *The Flexure-based Microgap Rheometer (FMR)*, J. Rheo., Vol. 50, No. 6, pp. 883-905

[17] Clasen, C., et al, (2002), *A Sliding Plate Microrheometer for Monitoring Structure Evolution in Self-Assembling Peptide Solutions and Other Complex Fluids*, Proceedings of the 6th European Conference on Rheology (eurheo 2002), pp. 473-474

[18] Macosko, C.W., (1994), *Rheology: Principles, Measurements and Applications*, Wiley, NY

[19] Wendl, M.C., (1999), *General Solution for the Couette Flow Profile*, Phys. Rev. E, Vol. 60, pp. 6192-6194

[20] Jacobson, B. O., (1991), *Rheology and Elastohydrodynamic Lubrication*, Elsevier, Amsterdam

[21] Brydson, J. A., (1981), *Flow Properties of Polymer Melts*, George Godwin, London

[22] Carreau, P. J., De Kee, D. C. R. and Chhabra, R. P., (1997), *Rheology of Polymeric Systems; Principles and Applications*, Hanser, New York

[23] Morita, A. T., et al, (2005), *Low Cost Capillary Rheometer, Transfer Moulding and Die-drawing Module*, Poly. Test., Vol. 25, No. 2, pp. 197-202

[24] Sun, L. et al, (1999), *A Versatile Thermostatted Glass Tube MRI Rheometer*, Meas. Sci. Technol., Vol. 10, pp. 1272–1278

[25] Hanasaki, I. and Akihiro, N., (2006), *Water Flow through Carbon Nano-Tube Junctions as Molecular Convergent Nozzles*, Nanotech., Vol. 17, No. 11, pp. 2794-2804

[26] Corfield, G. M. et al, (1999), A *Critical Examination of Capillary Rheometry for Foods (Exhibiting Wall Slip)*, Food Bioprod. Proc., Vol. 77, No. C1, pp. 3-10

[27] Dukhin, A. S. and Goetz, P. J. (2002), *Ultrasound for Characterizing Colloids*, Elsevier

[28] Edwards, D. A., Brenner, H. and Wasan, D. T., (1991), *Interfacial Transport Processes and Rheology*; Butterworth-Heinemann: Boston

[29] Landau, L. D. and Lifshitz, E. M., (1959), *Fluid Mechanics*, Pergamon: Oxford

[30] Sacchetti, M., Yu, H. and Zografi, G. J., (1993), *Hydrodynamic Coupling of Monolayers with Subphase*, Chem. Phys., Vol.99, pp. 563-566

[31] Kurnaz, M. L. and Schwartz, D. K., (1997), *Channel Flow in a Langmuir Monolayer: Unusual Velocity Profiles in a Liquid-Crystalline Mesophase*, Phys. Rev. E., Vol. 56, pp. 3378-3384

[32] Gaub, H. E. and McConnell, H. M., (1986), *Shear Viscosity of Monolayers at the Air-Water Interface*, J. Phys. Chem., Vol. 90, pp. 6830-6832

[33] Abraham, B. M., et al (1983), *Anomalous Melting Properties of Some Classical Monolayer Systems*, Phys. Rev. Lett., Vol. 51, pp. 1975-1978

[34] Santini, E., et al (2007), *A Surface Rheological Study of Non-Ionic Surfactants at the Water–Air Interface and the Stability of the Corresponding Thin Foam Films*, Coll. Surf. A, in press

[35] Goodrich, F. C., Allen, L. H. And Poskanzer, A., (1975), A New Surface Viscometer of High Sensitivity: I. Theory, J. Coll. Int. Sci, Vol. 52, No. 2, pp. 201-212

[36] Brooks, C. F., et al (1999), *An Interfacial Stress Rheometer to Study Rheological Transitions in Monolayers at the Air-Water Interface*, Langmuir, Vol. 15, pp. 2450-2459

[37] Zhang, J., et al (2003), *Combined Scanning Electrochemical Microscopy–Langmuir Trough Technique for Investigating Phase Transfer Kinetics Across Liquid/Liquid Interfaces Modified by a Molecular Monolayer*, Electrochem. Comm., Vol. 5, No. 2, pp. 105-110

[38] Clint, J. H. and Quirke, N., (1993), *Contact Angles on Particles from Langmuir Trough Studies*, Coll. Surf. A, Vol. 78, pp. 277-278

[39] Ashkin, A., Dziedzic, J.M. and Bjorkholm, J.E., Chu, S., (1986). *Observation of a Single-beam Gradient Force Optical Trap for Dielectric Particles*, Opt. Lett., Vol. 11, pp. 288–290

[40] Wright, G. D., et al. (2005), *Optical Tweezer Micromanipulation of Filamentous Fungi*, Fungal Genetics and Bio, Vol. 44, pp. 1-13

[41] Fallman, E., et al. (2004), *Optical Tweezers Based Force Measurement System for Quantitating Binding Interactions: System Design and Application for the Study of Bacterial Adhesion*, Biosens. and Bioelect., Vol. 19, No. 11, pp. 1429-1437

[42] Finer, J. T., Simmons, R. M. and Spudich, J. A. (1994), *Single Myosin Molecule Mechanics: Piconewton Forces and Nanometre Steps*, Nature, Vol. 368, pp. 113–119

[43] Visscher, K., Schnitzer, M. J. and Block, S. M. (1999), *Single Kinesin Molecules Studied With a Molecular Force Clamp*, Nature, Vol. 400, pp. 184–189

[44] Yin, H., Wang, M. D., Svoboda, K., Landick, R., Block, S. M. and Gelles, J., (1995), *Transcription against an Applied Force*, Science, Vol. 270, pp. 1653–1657

[45] Dai, J. and Sheetz, M. P., (1999), *Membrane Tether Formation from Blebbing Cells*, Biophys. J., Vol. 77, pp. 3363–3370

[46] Furst, E. M., (2005), *Applications of Laser Tweezers in Complex Fluid Rheology*, Curr. Op. Coll. Int. Sci, Vol. 10, No. 1-2, pp. 79-86

[47] Perkins, T. T, Smith, D. E. and Chu, S., (1994), *Direct Observation of Tube-Like Motion of a Single Polymer Chain*, Science, Vol. 264, pp. 819–822

[48] Perkins, T. T., Quake, S. R., Smith, D. E. and Chu, S. (1994), *Relaxation of a Single DNA Molecule Observed By Optical Microscopy*, Science, Vol. 264, pp. 822– 826

[49] Perkins, T, T., Smith, D. E., Larson, R. G. and Chu, S., (1995), *Stretching of a Single Tethered Polymer in a Uniform Flow*, Science, Vol. 268, pp. 83–87

[50] Schnurr, B., Gittes, F., MacKintosh, F. C. and Schmidt, C. F. (1997), *Determining Microscopic Viscoelasticity in Flexible and Semiflexible Polymer Networks from Thermal Fluctuations*, Macromolecules, Vol. 30, pp. 7781–7792

[51] Mukhopadhyay, A. and Granick, S., (2001), *Micro- and Nanorheology*, Curr. Op. Coll. Int. Sci., Vol. 6, pp. 423-429

[52] Levine, A. J. and Lubensky, T. C., (2000), *One- and Two-particle Microrheology*, Phys. Rev. Lett., Vol. 85, No. 8, pp. 1774-1777

[53] Schnurr, B., Gittes, F., MacKintosh, F. C., Schmidt, C. F., (1997), *Determining Microscopic Viscoelasticity in Flexible and Semiflexible Polymer Networks from Thermal Fluctuations*, Macromolecules, Vol. 30, pp. 7781-7792

[54] Gittes, F., Schnurr, B., Olmsted, P. D., MacKintosh, F. C. and Schmidt C. F., (1997), *Microscopic Viscoelasticity: Shear Moduli of Soft Materials Determined from Thermal Fluctuations*, Phys. Rev. Lett., Vol. 79, pp. 3286-3289

[55] Crocker, J. C., et al, (2000), *Two-point Microrheology of Inhomogeneous Soft Materials*, Phys. Rev. Lett., Vol. 85, No. 4, pp. 888-891

[56] Solomon, M. J. and Lu, Q., (2001), *Rheology and Dynamics of Particles in Viscoelastic Media*, Curr. Op. Coll. Int. Sci., Vol. 6, pp. 430-437

[57] Glass, J. E. and Prud'homme, R. K., (1997), *Coating Rheology: Component Influence on the Rheological Response and Performance of Water-Borne Coatings in Roll Applications*. In: Kistler, S. F., Schweizer, P. M., editors. Liquid Film Coating. London: Chapman and Hall

[58] Larson, R. G., (1999), *The Structure and Rheology of Complex Fluids*, New York: Oxford University Press, 1999.

[59] Vaia, R. and Giannelis, E. P., (2001), *Polymer Nanocomposites: Status and Opportunities*, MRS Bull, Vol. 26, pp. 394-401

[60] Chu, B., (1992), *Laser Light Scattering: Basic Principles and Practice*, 2nd Edition. Academic Press

[61] Weitz, D. A. and Pine, D. J. (1993), *Diffusing-wave Spectroscopy*, In: Brown W, editor. Dynamic Light Scattering: the Method and some Applications. Oxford: Oxford University Press, pp. 652-720

[62] Maret, G., (1997), *Diffusing-wave Spectroscopy*, Curr. Op. Coll. Int. Sci., Vol. 2, pp. 251-257

[63] Harden, J. L. and Viasnoff, V., (2001), *Recent Advances in DWS-based Micro-Rheology*, Curr. Op. Coll. Int. Sci., Vol. 6, pp. 438-445

[64] Mason, T. G. and Weitz, D. A., (1995), *Optical Measurements of Frequency-Dependent Linear Viscoelastic Moduli of Complex Fluids*, Phys. Rev. Lett., Vol. 74, pp. 1250-1253

[65] Mason, T. G., Gang, H. and Weitz, D. A., (1996), *Rheology of Complex Fluids Measured by Dynamic Light Scattering*, J. Mol. Struct., Vol. 383, pp. 8190

[66] Sujatha, K. S., et al. (2008), *Modelling Step-strain Filament-stretching (CaBER-type) using ALE Techniques*, J. Non-Newtonian Fluid Mech., Vol. 148, pp. 109-121

[67] Willenbacher, N., (2004), *Elongational Viscosity of Aqueous Thicker Solutions from Capillary Break-up Elongational Rheometry (CaBER)*, in: Proc. XIVth Int. Cong. Rheol., Seoul, S. Korea

[68] McKinley, G.H. and Sridhar, T., (2002), *Filament-stretching Rheometry of Complex Fluids*, Annu. Rev. Fluid Mech., Vol. 34, pp. 375–415

[69] Rodd, L.E., et al., (2005), *Capillary Break-up Rheometry of Low-viscosity Elastic Fluids*, Appl. Rheol., Vol. 15, pp. 12–27

[70] Lin, Z.Q., et al., (2001), *Comparison of the Effects of Dimethyl and Dichloro Benzoate Counterions on Drag Reduction, Rheological Behaviors, and Microstructures of a Cationic Surfactant*, J. Rheol., Vol. 45, pp. 963–981.

[71] Bazilevsky, A.V., Entov, V.M. and Rozhkov, A.N., (1990) *Liquid Filament Micro Rheometer and some of its Applications*, Third European Rheology Conference, pp. 41–43

[72] Tirtaatmadja, V. and Sridhar, T., (1993), *A Filament Stretching Device for Measurement of Extensional Viscosity*, J. Rheol., Vol. 37, pp. 1081–1102

[73] Bonacccurso, E., Kappl, M. and Butt, H-J., (2008), *Thin Liquid Films Studied by Atomic Force Microscopy*, Curr. Op. Coll. Int. Sci, Vol. 13, pp. 107-119

[74] Morris, V. J., et al, (2001), *Atomic Force Microscopy as a Tool for Interpreting the Rheology of Food Biopolymers at the Molecular Level*, Lebensm.-Wiss. U.-Technol., Vol. 34, pp. 3-10

[75] MacKintosh, F. C. and Schmidt, C. F., (1999), *Microrheology*, Curr. Op. Coll. Int. Sci, Vol. 4, pp. 300-307

[76] Liu, H. and Bhushan, B., (2003), *Nanotribological Characterization of Molecularly Thick Lubricant Films for Applications to MEMS/NEMS by AFM*, Ultramicroscopy, Vol. 97, pp. 321-340

[77] Aime, J.P., Elkaakour, Z., Odin, C. et al, (1994), *Comments on the Use of the Force Mode in Atomic-Force Microscopy for Polymer-Films*, J. Appl. Phys., Vol. 76, pp. 754-762

[78] Nakajima, K., et al (1997), *Nanorheology of Polymer Blends Investigated by Atomic Force Microscopy*, Japan J. Appl. Phys. Part 1, Vol. 36, pp. 3850-3854

[79] DeVecchio, D. and Bhushan, B., (1997), *Localized Surface Elasticity Measurements Using an Atomic Force Microscope*, Rev. Sci. Instrum., Vol. 68, pp. 4498-4505

[80] Overney, R. M., et al, (1996), *Compliance Measurements of Confined Polystyrene Solutions by Atomic Force Microscopy*, Phys. Rev. Lett., Vol. 76, pp. 1272-1275.

[81] Burnham, N. A. and Colton, R. J., (1989), *Measuring the Nanomechanical Properties and Surface Forces of Materials Using an Atomic Force Microscope*, J. Vacuum Sci. Technol. A, Vol. 7, pp.2906-2913

[82] Bremmell, K. E., et al, (2006), *Deformation and Nano-Rheology of Red Blood Cells: an AFM Investigation*, Coll. Surf. B: Bioint., Vol. 50, pp. 43-48

[83] Friedenberg, M. C. and Mate, C. M., (1996), *Dynamic Viscoelastic Properties of Liquid Polymer Films Studied by Atomic Force Microscopy*, Langmuir, Vol. 12, pp. 6138-6142

[84] Overney, R. M. and Leta, D. P., (1995), *Friction and Elasticity on a Molecular Scale*, Trib. Lett., Vol. 1, No. 2-3, pp. 247-252

[85] Akari, S. O. et al, (1994), *Imaging of Single Polymer Chains Based on their Elasticity*, Appl. Phys. Lett., Vol.65, pp. 1915-1917

[86] Rajagopalan, R., (2000), *Atomic Force and Optical Force Microscopy: Applications to Interfacial Microhydrodynamics*, Coll. Surf. A, Vol. 174, pp. 253-567

[87] Ma, H., Jimenez, J. and Rajagopalan, R., (2000), *Brownian Fluctuation Spectroscopy Using Atomic Force Microscopes*, Langmuir, Vol. 16, pp. 2254-2261

[88] Chen, G. Y., et al. (1994), *Resonance Response of Scanning Force Microscopy Cantilevers*, Rev. Sci. Instrum. Vol. 65, pp. 2532-2537

[89] Field, J. S., Swain, M. V. and Phan-Thein, N., (1996), *An Experimental Investigation of the use of Random Squeezing to Determine the Complex Modulus of Viscoelastic Fluids*, J. Non-Newtonian Fluid Mech., Vol. 65, pp. 177-194

[90] Bell, D., Binding D. M. and Walters, K., (2005), *The Oscillatory Squeeze Flow Rheometer – Comprehensive Theory and a New Experimental Facility*, Rheologica Acta, Vol. 46, No.1, pp. 111-121

[91] Phan-Thien, N. and Low, H. T., (1988), *Squeeze-Film Flow of a Viscoelastic Fluid – a Lubrication Model*, J. of Non- Newtonian Fluid Mech., Vol. 28, pp. 129-148

[92] GBC Scientific Equipment Pty Ltd., 12 Monterey Rd., Dandenong VIC, 3175, Australia

[93] See, H., (2001), *Advances in Measuring Linear Viscoelastic Properties Using Novel Deformation Geometries and Fourier Transform Techniques*, Korea-Australia Rheology Journal, Vol. 13, No. 2, pp. 67-81

[94] Glassock, J. A., et al, (2003), *An In-line Micro-Fourier Rheometer*, Rev. Sci. Inst., Vol. 74, No. 11, pp. 4925-4929

[95] Larson, R. G., (1999), *The Structure and Rheology of Complex Fluids*, Oxford University Press, New York,

[96] Kirschenmann, L., (2003), Ph.D. thesis, Institut für Dynamische Materialprüfung (IdM), University of Ulm, 2003

[97] Crassous, J. J., et al, (2005), *Characterization of the Viscoelastic Behavior of Complex Fluids Using the Piezoelastic Axial Vibrator*, J. Rheo., Vol. 49, No. 4, pp. 851-863

[98] Meeten, G. H., (2002), *Constant-force Squeeze Flow of Soft Solids*, Rheol. Acta, Vol. 41, pp. 557-566

[99] Stefan, J., (1874), *Versuche Uber die Scheinbare Adhasion*, Sitz. Kais. Akad. Wiss. Math. Nat. Wien, Vol. 69, No. 2, pp. 713–735

[100] Chatraei, S., Macosko, C. W. and Winter, H. H., (1981) , *Lubricated Squeezing Flow: A New Biaxial Extensional Rheometer*, J. Rheol., Vol. 25, No. 4, pp. 433–443

[101] Campanella, O. H., Peleg, M., (2002), *Squeezing Flow Viscometry for Non-Elastic Semi-Liquid Foods—Theory and Applications*, Crit. Rev. Food Sci. Nutr., Vol. 42, No.3, pp. 241–264

[102] Shirodkar, P., Bravo, A. and Middleman, S., (1982), *Lubrication Flows In Viscoelastic Liquids. 2. Effect Of Slip*, Chem. Eng. Comm., Vol. 14, No. 3–6, pp. 151–175

[103] Hoffner, B., Gerhards, C. and Peleg, M., (1997), *Imperfect Lubricated Squeezing Flow Viscometry for Foods*, Rheol. Acta, Vol. 36, pp. 686–693

[104] Servais, C., Luciani, A. and Manson, J. A. E., (2002), *Squeeze Flow of Concentrated Long Fibre Suspensions: Experiments and Model*, J. Non-Newtonian Fluid Mech., Vol. 104, No. 2–3, pp. 165–184

[105] Reynolds, O., (1886), *On The Theory of Lubrication and its Application*, Phil. Trans. Royal Soc. Lond., Vol. 177, pp. 157–234

[106] Phan-Thien, N., Dudek, J., Boger D. V. and Tirtaatmadja, V., (1985), *Squeeze Film Flow of Ideal Elastic Liquids*, J. Non-Newtonian Fluid Mech, Vol. 18, pp. 227-254

[107] Phan-Thien, N. and Tanner, R. I., (1983), *Viscoelastic Squeeze-Film Flows - Maxwell Fluids*, J. Non-Newtonian Fluid Mech, Vol. 129, pp. 265-281

[108] Bell, D., Binding D. M., and Walters, K., (2005), *The Oscillatory Squeeze Flow Rheometer - Comprehensive Theory and a New Experimental Facility*, Rheologica Acta, Vol. 46, No. 1, pp. 111-121

[109] Barnes, H. A., (1995), *A Review Of The Slip (Wall Depletion) of Polymer Solutions, Emulsions and Particle Suspensions in Viscometers: Its Cause, Character and Cure*, J. Non-Newtonian Fluid Mech., Vol. 56, pp. 221–251

[110] Pearson, J. R. A. and Petrie, C. J. S, (1968), in *Polymer Systems: Deformation and Flow*, Eds. Wetton. R. E. and Whorlow, R. W., McMillan, London

[111] Laun, H. M., Rady, M. and Hassager, O., (1999), *Analytical Solutions for Squeeze Flow with Partial Wall Slip*, J. Non-Newtonian Fluid Mech., Vol. 81, pp. 1–15

[112] Scott, J. R., (1931), *Theory And Application Of The Parallel-Plate Plastometer*, Trans. Inst. Rubber Ind., Vol. 7, pp. 169–186

[113] Peek, R. L., (1932), *Parallel Plate Plastometry*, J. Rheol., Vol. 3, No. 3, pp. 345–372

[114] Lipscomb, G. G. and Denn, M. M., (1984), *Flow of Bingham Fluids in Complex Geometries*, J. Non-Newtonian Fluid Mech., Vol. 14, pp. 337–346

[115] Denn, M. M., (1998), *Are Plug-Flow Regions Possible in Fluids Exhibiting a Yield Stress?*, Dynam. Complex Fluids, pp. 372–378

[116] Klingbeil, W. W. and Shield, R. S., (1966), *Large-Deformation Analyses of Bonded Elastic Mounts*, ZAMP, Vol. 17, pp. 281–305

[117] Tanner, R. I., (1965), *Some Illustrative Problems in the Flow of Viscoelastic Non-Newtonian Lubricants*, Amer. Soc. Lub. Eng. Trans., Vol. 8, pp. 179-183

[118] Kramer, J. M., (1974), *Large Deformations of Viscoelastic Squeeze Films*, Appl. Sci. Res., Vol. 30, pp. 1-16

[119] Shirodkar, P. and Middleman, S., (1982), *Lubrication Flows in Viscoelastic Liquids. 1. Squeezing Flow between Approaching Parallel Rigid Planes*, J. Rheol., Vol. 26, No. 1, pp.1–17

[120] Zahorski, S., (1979), *Viscoelastic Properties in Axially Symmetric Squeeze-Film Flows*, Arch. Mech. Vol. 31, No. 3, pp. 431–444

[121] Mavridis, H. et al, (1991), *Deformation Patterns in the Compression of Polypropylene Disks: Experiments and Simulation*, J. Rheol., Vol. 36, No. 1, pp. 27–43

[122] Debbaut, B. (2001), *Non-Isothermal and Viscoelastic Effects in the Squeeze Flow between Infinite Plates*, J. Non-Newtonian Fluid Mech., Vol. 98, pp. 15–31

[123] Adams, M. J. et al, (1997), *A Finite Element Analysis of the Squeeze Flow of an Elasto-Viscoplastic Material*, J. Non-Newtonian Fluid Mech., Vol. 71, pp. 41–57

Chapter 2 – Design Options

[124] Madou, M., (2001), *The MEMS Handbook*, CRC Press, Boca Raton

[125] Kenny, T., (2001), *Nanometer-scale Force Sensing with MEMS Devices*, Sensors Journal, IEEE, Vol. 1, No. 2, pp. 148-152

[126] Drexler, E. K., (1992), *Nanosystems: Molecular Machinery, Manufacturing and Computation*, John Wiley and Sons Inc., New York

[127] Serrona, L. K. E. B. et al., (2003), *Structure and Magnetic Properties of High Coercive NdFeB Films with a Perpendicular Anisotropy*, App. Phy. Letts., Vol. 82, No. 11, pp. 1751-1760

[128] Cho, H. and Ahn, C., (2000), *A Novel Bi-directional Magnetic Microactuator using Electroplated Permanent Magnet Arrays with Vertical Anisotropy*, Micro Electr. Mech. Sys., MEMS 2000, pp. 686-689

[129] Gibbs, M. R. J., Hill, E. W. and Wright, P. J., (2004), *Magnetic Materials for MEMS Applications*, J. Phys. D: Appl. Phys., Vpl. 37, No. 22, pp. 237

[130] Devoe, D. L. and Pisano, A., (1997), *Modelling and Optimal Design of Piezoelectric Cantilever Microactuators*, J. Micromech. Sys., Vol. 6, No. 3, pp. 266-274

Chapter 3 – Design Concept

Chapter 4 – Capillary Effects

[131] Fowkes, F. M., (1968), *Calculation of Work of Adhesion by Pair Potential Summation*, J. Colloid Int. Sci., Vol. 28, No. 3-4, pp. 493-505

[132] K. W. Allen, (2003), *"At Forty Cometh Understanding": A Review of Some Basics of Adhesion over the Past Four Decades*, Int. J. Adhesion and Adhesives, Vol. 23, No. 2, pp. 87-93

[133] Neumann, A. W. et al. (1996), *Applied Surface Thermodynamics*, Surfactant science series; v. 63, M. Dekker (New York), ISBN: 0824790960

[134] T. D. Blake, (2006), *The Physics of Moving Wetting Lines*, J. Colloid Int. Sci., Vol. 199, pp. 1-13

[135] Willett, C. D., Adams, M. J., Johnson, S. A. and Seville, J. P. K., (2003), *Effects of Wetting Hysteresis on Pendular Liquid Bridges between Rigid Spheres*, Powder Tech., Vol. 130, pp. 63-69

[136] J. B. Freund, (2003), *The Atomic Detail of a Wetting/De-Wetting Flow*, Physics of Fluids, Vol. 15, No. 5, pp. 33-36

[137] D. Bell, D. M. Binding and K. Walters, (2005), *The Oscillatory Squeeze Flow Rheometer - Comprehensive Theory and a New Experimental Facility*, Rheologica Acta,

[138] B. Debbaut and K. Thomas, (2004), *Simulation and Analysis of Oscillatory Squeeze Flow*, J. of Non-Newtonian Fluid Mech., Vol. 124, pp. 77-91

[139] Orr, F. M., et al., (1975), *Pendular Rings between Solids: Meniscus Properties and Capillary Force*, J. Fluid Mech., Vol. 67, pp. 723-742

[140] Lian, G., et al., (1993), *A Theoretical Study of the Liquid Bridge Forces between Two Rigid Spherical Bodies*, J. Colloid and Int. Sci., Vol. 161, pp. 138-147

[141] Pepin, X., et al., (2000), *Modelling the Evolution and Rupture of Pendular Liquid Bridges in the Presence of Large Wetting Hysteresis*, J. Colloid and Int. Sci., Vol. 232, pp. 289–297

[142] Fisher, R. A., (1926), *On the Capillary Forces in an Ideal Soil; Correction of Formulae given by WB Haines*, J. Agric. Sci., Vol. 19, pp. 492-

[143] Willett, C. D., et al., *Handbook of Powder Technology*, Vol. 2, Chap. 28, Pendular Capillary Bridges

Chapter 5 – Viscoelasticity

[144] Ferry, J. D., (1980), *Viscoelastic Properties of Polymers*, 3rd Ed., Wiley New York, ISBN: 0471048941

[145] Hutton, J. F. et al., (1989), *An Introduction to Rheology*, Rheology Series, Vol. 3, ISBN: 0444871403

[146] Roscoe, R., (1950), *Mechanical Models for the Representation of Viscoelastic Properties*, Brit. J. Appl. Phys., vol. 1, pp. 171-173

[147] Alfrey, T. Jr, (1946), *Methods of Representing the Properties of Viscoelastic Materials*, Quart. Appl. Math. Vol. 3, pp. 143-150

[148] Walters, K. (1975), *Rheometry*, Chapman & Hall, London, ISBN: 0412120909

[149] O. Reynolds, (1886), *On the Theory of Lubrication and Its Application to Mr. Beauchamp Tower's Experiments, Including an Experimental Determination of the Viscosity of Olive Oil*, Philosophical Transactions of the Royal Society of London, Vol. 177, pp. 157-234

[150] D. Bell, D. M. Binding and K. Walters, (2005), *The Oscillatory Squeeze Flow Rheometer - Comprehensive Theory and a New Experimental Facility*, Rheol. Acta, Vol. 46, No. 1, pp. 111-121

[151] G. Brindley, J. M. Davies and K. Walters, (1976), *Elastico-Viscous Squeeze Films - Part 1*, Journal of Non-Newtonian Fluid Mechanics, Vol. 1, pp. 19-37

[152] J. J. Bikerman, (1946), *The Fundamentals of Tackiness and Adhesion*, Vol. 2, pp. 163-175

Chapter 6 – The Microrheometer

[153] Yang, J., (2005), *An Introduction to the Theory of Piezoelectricity*, Springer, New York, ISBN: 0387235736

[154] Ikeda, T., (1990), *Fundamentals of Piezoelectricity*, Oxford University Press, ISBN: 0198563396

[155] Johnston, I. D., Tracey, M. C., Davis, J. B. and Tan, C. K. L. (2005), *Microfluidic Solid Phase Suspension Transport with an Elastomer-Based, Single Piezo-Actuator, Micro Throttle Pump*, Lab on a Chip, Vol. 5, pp. 318-325

[156] Hsu, Y.-C., Wu, C.-C., Lee, C.-C., Cao, G. Z. and Shen, I. Y. (2004), *Demonstration and Characterization of PZT Thin-Film Sensors and Actuators for Meso- and Micro-Structures*, Sensors and Actuators A: Physical, Vol. 116, No. 3, pp. 369-377

[157] Shibata, T., Unno, K., Makino, E. and Shimada, S. (2004), *Fabrication and Characterization of Diamond AFM Probe Integrated with PZT Thin Film Sensor and Actuator*, Sensors and Actuators A: Physical, Vol. 114, No. 2-3, pp. 398-405

[158] Cho, N.-J., et al (2007), *Quartz Resonator Signatures under Newtonian Liquid Loading for Initial Instrument Check*, Journal of Colloid and Interface Science, Vol. 315, No. 1, pp. 248-254

[159] Sun, H.-T., et al (1994), *AT-Cut Quartz Resonators for Determination of Viscoelastic and Dielectric Properties of Water/Glycerol*, Sensors and Actuators A: Physical, Vol. 43, No. 1-3, pp. 208-212

[160] Veríssimo, M. I. S., et al (2003), *Suitability of PZT Ceramics for Mass Sensors Versus Widespread Used Quartz Crystals*, Sensors and Actuators B: Chemical, Vol. 95, No. 1-3, pp. 25-31

[161] Guillon, O., et al, (2005), *New Considerations About the Fracture Mode of PZT Ceramics*, Journal of the European Ceramic Society, Vol. 25, No. 12, pp. 2421-2424

[162] Eda, K., et al (2000), *Direct Bonding of Piezoelectric Materials and Its Applications*, IEEE Ultrasonics Symposium, Vol. No. pp. 299-309

[163] Xu, X.-L., et al, (1988), *Silicon on Quartz by Solid-State Diffusion Bonding (SSDB) Technology*, Electronics Letters, Vol. 24, No. 11, pp. 691-692

[164] Zhao, J., Shang Z. and Gao, L., (2007), *Bonding Quartz Wafers by the Atom Transfer Radical Polymerization of the Glycidyl Methacrylate at Mild Temperature*, Sensors and Actuators A: Physical, Vol. 135, pp. 257-261

[165] Tanaka, K., Konishi, T., Ide, M. and Sugiyama, S., (2006), *Wafer Bonding of Lead Zirconate Titanate to Si Using an Intermediate Gold Layer for Microdevice Application*, Journal of Micromechanics and Microengineering, Vol. 16, pp. 815-820

[166] Whitney, J. M., (1987), *Structural Analysis of Laminated Anisotropic Plates*, Technomic Pub. Co. Lancaster, USA, ISBN: 0877625182

[167] Johnston, I. D., et al, (2005), *Micro Throttle Pump Employing Displacement Amplification in an Elastomeric Substrate*, Journal of Micromechanics and Microengineering, Vol. 15, pp. 1831-1839

[168] Omori, T., et al, (2001), *Preparation of Piezoelectric PZT Micro-Discs by Sol-Gel Method*, Transactions of the IEEE Japan, Vol. 121, No. 9, pp. 488-492

[169] Shao, T.-Q., et al, (2003), *High Quality Silicon-Based PZT Thin Films for Memory Applications*, Microelectronic Engineering, Vol. 66, No. pp. 713-718

[170] Mason, W. P., (1950), *Piezoelectric Crystals and Their Application to Ultrasonics*, Van Nostrand, London

[171] Tu, Y., (1968), *Perturbation Solution of Plane Stress Problems in Anisotropic Elasticity*, SIAM Journal on Applied Mathematics, Vol. 16, No. 2, pp. 374-386

[172] Tu, Y., (1968), *The Decomposition of an Anisotropic Elastic Tensor*, Acta Crystallographica, Vol. 24, No. 2, pp. 273-282

[173] Ventsel, E., (2001), *Thin Plates and Shells: Theory, Analysis, and Applications*, Marcel Dekker, New York, ISBN: 0824705750

[174] Timoshenko, S. P., (1959), *Theory of Plates and Shells*, McGraw-Hill, London

[175] Reddy, J. N., (1999), *Theory and Analysis of Elastic Plates*, Taylor and Francis, London, ISBN: 1560327057

[176] Li, S. and Chen, S., (2003), *Analytical Analysis of a Circular PZT Actuator for Valveless Micropumps*, Sens. Act. A Phys., Vol. 104, pp. 151–161

[177] Adelman, N. T. and Stavsky, Y., (1980), *Flexural-extensional Behaviour of Composite Piezoelectric Circular Plates*, J. Acoust. Soc. Am., Vol. 67, pp. 819–822

[178] Dobrucki, A. B. and Pruchnicki, P., (1997), *Theory of Piezoelectric Axisymmetric Bimorph*, Sens. Act. A, Phys., Vol. 58, pp. 203–212

[179] Li, X., et al, (1999), *Electromechanical Behaviours of PZT/brass Plate Unimorph*, J. Am Ceram. Soc., Vol. 82, No. 7, pp. 1733–1740.

[180] Prasad, S., et al, (2002), *Two-Port Electroacoustic Model of a Piezoelectric Circular Composite Plate*, Proceedings of the 43rd AIAA/ASME/ASCE/AHS/ASC Structures, Structural Dynamics, and Materials Conference, Denver, CO, 22–25 April 2002, pp. 1–9

[181] Prasad, S., et al., (2006), *Analytical Electroacoustic Model of a Piezoelectric Composite Circular Plate*, J. AIAA, Vol. 44, No. 10, pp. 2311–2318

[182] Mo, C., et al, (2006), *Behaviour of a Unimorph Circular Piezoelectric Actuator*, Smart Mater. Struct., Vol. 15, pp. 1094–1102

[183] Deshpande, M. and Saggere, L. (2007), *An Analytical Model and Working Equations for Static Deflections of a Circular Multi-Layered Diaphragm-Type Piezoelectric Actuator*, Sensors and Actuators A: Physical, Vol. 136, pp. 673-689

[184] Kalnins, A. and Dym, C. L., (1976), *Vibration: Beams, Plates, and Shells*, Hutchinson and Press, New York, ISBN: 0879332433

Chapter 7 – Fabrication

[185] Moreau, W. M., (1988), *Semiconductor Lithography*, Plenum Press, New York

[186] Thompson, L. F., Willson, C. G. and Bowden, M. J., (1994), *Introduction to Microlithography*, American Chemical Society, Washington, DC

[187] Madou, M., (1997), *Fundamentals of Microfabrication*, CRC Press, New York

[188] Stansfield, B. L., Fujita, H. and Sugawara, M., (1989), *Plasma Etching: Fundamentals and Applications* (Series on Semiconductor Science and Technology, 7), Oxford University Press, USA

[189] May, G. S. and Spanos, C. J., (2006), *Fundamentals of Semiconductor Manufacturing and Process Control*, Wiley-IEEE Press

[190] Docker, P. T., Kinnell, P. and Ward, M. C. L., (2003), *A Dry Single-Step Process for the Manufacture of Released MEMS Structure*, J. Micromech. Microeng., Vol. 13, pp. 790–794

[191] Witvrouw, A., Du Bois, B., De Moor, P. et al., (2000), *A Comparison between Wet HF Etching and Vapour HF Etching for Sacrificial Oxide Removal*, Proceedings of the SPIE Micromachining and Microfabrication Process Technology VI; September 2000, Vol. 4174, pp. 130-141

[192] Miyata, N., Watanabe, H. and Ichikawa, M., (1998), *HF-chemical Etching of the Oxide Layer Near a SiO2/Si(111) Interface*, Appl. Phys. Lett., Vol. 73, pp. 3923

[193] Barnes, M. C., Kim, D.-Y. and Hwang, N. M., (2000), *The Mechanism of Gold Deposition by Thermal Evaporation*, J. Cer. Proc. Res., Vol. 1, No. 1, pp. 45-52

[194] Ristic, L., (1994), *Sensor Technology and Devices*, Artech House, London

[195] Aitken, N. and Rogers, T., (2006), *Discussion of Tooling Solutions for the Direct Bonding of Silicon Wafers*, Microsys. Tech., Vol. 12, No. 5, pp. 417-417

[196] Lasky, J. B., Stiffler, S. R., White, F.R. and Abernathey, J. R., (1985), *Silicon-on-insulator (SOI) by Bonding and Etch-back*, Electron Devices Meeting – 1985 International, Vol. 31, pp. 684- 687

[197] Lasky, J. B., (1986), *Wafer Bonding for Silicon-on-Insulator Technologies*, Appl. Phys. Lett., Vol. 48, pp. 78-80

[198] Braithwaite, N., Kowal, J. and Rogers, T., (2007), *A Plasma-Based Pre-Treatment for Low Temperature Bonding of Silicon Wafers*, 60th Gaseous Electronics Conference, Arlington, Virginia USA

[199] Aitken, N. and Rogers, T., (2006), *In-Situ Activation, Alignment and Bonding using Radical Activation*, presented at 9th Int. Symp. on Wafer Bonding, Cancun, Mexico

Chapter 8 – Experimental Results

[200] Zisman, W. A., (1964), *Relation of Equilibrium Contact Angle to Liquid and Solid Constitution*, Chapter 1 in Contact Angle, Wettability, and Adhesion, American Chemical Society

[201] Shaw, D. J., (1992), *Colloid and Surface Chemistry*, 4th Edition, Butterworth-Heinemann

[202] Sundaram, K. B., Vijayakumar, A. and Subramanian, G., (2005), *Smooth Etching of Silicon using TMAH and Isopropyl Alcohol for MEMS Applications*, Microelec. Eng., Vol. 77, pp. 230-241

[203] Biswas, K. and Kal, S., (2006), *Etch Characteristics of KOH, TMAH and Dual Doped TMAH for Bulk Micromachining of Silicon*, Microelec. J., Vol. 37, pp. 519-525

[204] Fischer-Cripps, A. C., (2004), *Nanoindentation*, 2nd Edition, Springer (New York)

[205] Bell, D. A., (1990), *Operational Amplifiers: Applications, Troubleshooting and Design*, Prentice Hall

[206] Ulaby, F.T., (2004), *Fundamentals of Applied Electromagnetics*, Prentice Hall

[207] Priya, S. and Inman, D. J., (2008), *Energy Harvesting Technologies*, Springer

Appendix

[208] Crandall, I. B., (1918), *The Air-Damped Vibrating System: Theoretical Calibration of the Condenser Transmitter*, Physical Review, Vol. 11, No. 6, pp. 449-460

[209] House, R. N. and Kritz, J., (1959), *An Analytic Study of the Vibrating Free Disk*, IRE Transactions on Ultrasonics Engineering, pp. 76-84

[210] Russell, (1909), *Methods of Computing ber and bei Functions etc*., Phil. Mag., pp. 524

[211] Beranek,L. L., (1986), *Acoustics*, American Institute of Physics